UNIVERSITY OF QUEBEC AT CHICOUTIMI

DISSERTATION PRESENTED TO THE
UNIVERSITY OF QUEBEC AT CHICOUTIMI
IN PARTIAL FULFILLMENT OF THE REQUIREMENT FOR THE
DEGREE OF DOCTOR OF PHILOSOPHY IN ENGINEERING

BY

HONORÉ KAMGUO KAMGA, M.Sc

INFLUENCE OF ALLOYING ELEMENTS IRON AND SILICON
ON MECHANICAL PROPERTIES OF ALUMINUM-COPPER
TYPE B206 ALLOYS

FEBRUARY 2010

UNIVERSITÉ DU QUEBEC À CHICOUTIMI

THÉSE PRÉSENTÉE À
L'UNIVERSITÉ DU QUEBEC À CHICOUTIMI
COMME EXIGENCE PARTIELLE
DU DOCTORAT EN INGÉNIERIE

PAR

HONORÉ KAMGUO KAMGA, M.Sc

INFLUENCE DES ÉLÉMENTS D'ADDITIONS FER ET
SILICIUM SUR LES PROPRIÉTÉS MÉCANIQUES DES
ALLIAGES ALUMINIUM-CUIVRE DE TYPE B 206

FÉVRIER 2010

To my late father Mr. *Kamga Samuel René*
who passed away during the course of this study

ABSTRACT

Aluminum alloys are gaining more ground as first choice materials, especially in the transportation industry where a high strength/weight ratio is of premium importance. Increased activity in the recycling of spent automobiles in order to reduce production costs, leads to pick-up of iron from remelted scrap and melting equipments. This iron which can not be readily removed from molten aluminum by conventional foundry treatments makes it expensive for the industry to produce low iron-containing alloys and limits their use. Aluminum B206 alloy whose nominal composition allows a maximum of 0.1% iron falls within this category. The main objective of this research study was therefore to optimize the iron content in B206 alloys without major loss in mechanical properties, so that it can be produced from recycled materials and become cost competitive. This was done by neutralizing iron by silicon, and achieved through studies on the effects of iron and silicon additions on solidification, hot tearing, and mechanical properties of B206 alloy.

Studies on solidification were conducted because mechanical properties of a material greatly depend on its microstructure in the as-cast condition and thereby its solidification history. Different levels of Fe/Si ratios and two cooling rates (low and high) were used, with the remaining minor alloying elements kept almost constant. For each Fe/Si ratio, two levels of copper content were used in order to assess its importance. Actual casting took place in small moulds which produced samples weighing about 80 grammes. Solidification data were evolution of temperature with time recorded by two thermocouples introduced in the liquid metal prior to the start of solidification at the center and close to the wall of the mould. Characterization techniques include thermal analysis and thermodynamic computation to determine the solidification path, electron probe microanalyser (EPMA), scanning electron microscopy (SEM), coupled with EDX and WDS facilities for phase identification, optical microscopy in conjunction with image analysis for quantification purposes, and differential scanning calorimetry (DSC) for determination of near equilibrium dissolution temperatures of phases and optimization of heat treatment conditions.

Studies on hot tearing were conducted because it is an inherent defect in aluminium-copper alloys and is deleterious to mechanical properties of the material. A Constrained Rod Casting (CRC) mould was used in this study. It is a permanent mould made of cast iron with a cavity capable of producing four 12.7mm diameter cylindrical constrained rods with nominal lengths of 50.8mm, 88.9mm, 127mm, and 165.1mm. Alloys used for these tests had chemical compositions very close to those used during solidification studies such that the differences could not significantly affects the results. Characterization techniques include physical determination of hot tear sensitivity of alloys through tear indexation and theoretical determination using the vulnerability range theory.

Mechanical properties were evaluated at room temperature through hardness, tensile and impact properties for both as-cast and heat treated conditions. The hardness measurements were carried out using a Clemex computer-controlled microhardness tester of 10-1000 gramme-force (gf) capacity which can produce Vickers and Knoop methods of

testing materials in compliance with ASTM E-384 standards. Tensile properties were determined using a Servohydraulic MTS Mechanical Testing machine. The impact properties were assessed using a Charpy instrumented impact testing machine. The same melts used for hot tearing characterization were poured in an ASTM B-108 permanent mould and a mild steel impact test mould to produce the necessary test samples for tensile and impact testing, respectively. Solution heat treatment times of 2, 3, 4, 5, 6, 8, and 16 hours were used followed by natural and/or artificial aging depending on the iron to silicon ratio of the alloy. Microhardness measurements were performed on samples prepared from fractured tensile specimens and which also served for microstructural characterization.

Results from solidification studies show that iron is precipitated mainly as either β(CuFe) or α(MnFe) phases, or both, depending on the iron and silicon content, as well as the cooling rate. It was found that in alloys having up to 0.3wt% Fe, the precipitation of β(CuFe) phase can be largely suppressed if the Fe/Si ratio is close to 1 and the cooling rate is moderately high. The low mobility of the large facets of the β(CuFe) platelets is likely the cause limiting the amount of this phase, especially when the iron atoms have the possibility to be captured by another phase, in this case, the α(MnFe) phase.

Results from hot tearing studies show that the susceptibility to hot tearing is highly influenced by the iron to silicon ratio and the nominal concentration of the single elements. This influence is exerted through the determination of the amount of liquid at the eutectic temperature and the times spent in the vulnerable regime. The best resistance is obtained with both a ratio close to one and low concentrations of iron and silicon. The resistance decreases as this ratio distances itself from one. The higher this ratio, the worse the resistance to hot tearing, especially at a ratio of about two and above.

Results from mechanical testing show that properties are highly influenced by the iron to silicon ratio and the nominal concentration of the single elements. The best properties were obtained with both a ratio close to one and low concentrations of iron and silicon, in agreement with results obtained during solidification and hot tearing studies. Two main parameters were found to determine the properties of heat treated samples, namely solubility of Al_2Cu phase and dendrite coarsening. Present experimental results show that there will not be a problem with natural aging (T4) to obtain the minimum of 7% elongation required by the automotive industry by doubling or tripling the present limit of 0.1%Fe in these alloys, while increasing the strength. From calculated maximum values of strain at T4, the loss compare to B206 alloy may be narrowed to 2.5% with a good casting practice. With artificial aging (T7), it will be very difficult, if not impossible, to reach the 7% elongation at 0.2%Fe and 0.2%Si, while at 0.3%Fe and 0.3%Si it is quite impossible. Impact energy data correlates well with tensile ductility. The results shows that most of the decrease in absorbed energy of alloys containing (0.2%Fe, 0.2%Si) and (0.3%Fe, 0.3%Si) in comparison to B206 alloy is related to the crack propagation energy.

Even though these alloys show lower ductility than the base B206 alloy in the present experimental conditions, they still stand far above some alloys such as A356 and A319 presently used by the automobile industry, and therefore need to be considered.

RÉSUMÉ

Les alliages d'aluminium gagnent un peu plus de terrain comme matériaux de premier choix et plus particulièrement dans les industries du transport où le rapport résistance mécanique/poids est de première importance. L'activité croissante dans le recyclage des automobiles usées en vue de diminuer les coûts de production conduit à la contamination du métal produit par le fer provenant des équipements de fonderie et du métal recyclé. Ce fer qui ne peut être immédiatement retiré de l'aluminium liquide par les méthodes conventionnelles de traitement en fonderie rend la production industrielle des alliages à faible teneur en fer cher et limite l'utilisation de ces derniers. L'alliage d'aluminium B206 dont la composition nominale maximise à 0.1% la teneur en fer rentre dans cette catégorie. L'objectif principal de ce travail de recherche était donc d'augmenter la teneur en fer dans cet alliage sans conséquences fatales sur les propriétés mécaniques afin qu'il puisse être produit par recyclage et devenir compétitif par rapport à son prix. Ceci à été fait en neutralisant le fer par le silicium et réalisé en étudiant l'influence des additions de fer et de silicium sur la solidification, la fissuration à chaud, et les propriétés mécaniques des alliages d'aluminium de type B206.

Les études sur la solidification ont été réalisées parce que les propriétés mécaniques finales d'un matériau dépendent grandement de sa microstructure tel que coulée, donc de son historique de solidification. Différents rapports de Fe/Si et deux vitesses de refroidissement (faible et élevé) ont été utilisés, les autres éléments mineurs d'alliage maintenus presque constant. Pour chaque rapport Fe/Si, deux teneurs en cuivre ont été utilisées afin d'évaluer son importance. Les coulées ont été réalisées dans des petits moules pouvant former des échantillons d'environ 80 grammes en poids. Les données de solidification étaient l'évolution de la température en fonction du temps fournies par deux thermocouples placés dans le métal liquide au centre et tout près du bord du moule avant le début de la solidification Les techniques de caractérisation utilisées inclus l'analyse thermique et la simulation thermodynamique pour déterminer le parcours de solidification. Pour l'identification des phases, nous avons réalisé des analyses par microsonde et microscopie électronique à balayage (MEB). La microscopie optique couplée à l'analyseur d'image a été utilisée pour la quantification. Afin d'optimiser les traitements thermiques, la calorimétrie différentielle à balayage (DSC) a été utilisée.

Les études sur la fissuration à chaud ont été réalisées parce que ce défaut est inhérent aux alliages aluminium-cuivre et préjudiciable aux propriétés mécaniques. Un moule à barres contraintes à été utilisé dans cette étude. C'est un moule en fonte dont la cavité est capable de produire quatre barres contraintes cylindriques de 12,7mm de diamètre avec des longueurs nominales de 50.8mm, 88.9mm, 127mm, et 165.1mm. Les compositions chimiques des alliages utilisés étaient assez similaires de celles utilisées lors de l'étude sur la solidification telles que la différence ne puisse significativement affectée le résultat. Les techniques de caractérisation utilisées inclus la détermination physique de la sensibilité à la fissuration à chaud des alliages par l'indexation des fissures et la détermination théorique par la méthode de l'intervalle de vulnérabilité des alliage.

Les propriétés mécaniques ont été évalués à température ambiante à travers les essais de dureté, de traction et d'impact sur les échantillons dans les conditions telles que coulée et traités thermiquement. Les mesures de dureté ont été réalisées à l'aide d'un microduromètre de type Clemex contrôlé par ordinateur, ayant une capacité de 10 à 10000 gf et pouvant produire des méthodes de test Vickers et Knoop en accord avec les standards ASTM E-384. Les propriétés en traction ont été déterminées à l'aide d'une machine servo-hydraulique de type MTS. Les propriétés en impact ont été évaluées en utilisant une machine de type Charpy. Le même métal liquide utilisé pour la caractérisation de la fissuration à chaud à été coulé dans un moule de type ASTM B-108 et un moule en acier doux pour la production des échantillons nécessaires aux tests respectivement de traction et d'impact. Les temps de mise en solution de 2, 3, 4, 5, 6, 8, et 16 heures ont été utilisés suivis du vieillissement naturel et/ou artificiel dépendamment du rapport Fe/Si dans l'alliage. Les mesures de dureté ont été réalisées sur les échantillons préparés à partir des barres fracturées lors du test de traction et qui ont aussi servies pour la caractérisation microstructurale.

Les résultats des études sur la solidification montrent que le fer est principalement précipité soit sous la forme de phase β(CuFe) ou α(MnFe) ou des deux dépendamment aussi bien de la teneur en fer et en silicium de l'alliage que du taux de refroidissement. Dans les alliages ayant une teneur massique en fer d'environ 0.3%, la précipitation de la phase β(CuFe) peut être largement supprimée si le rapport Fe/Si est de 1 et le taux de refroidissement modérément élevé. La faible mobilité de la large facette des plaquettes de la phase β(CuFe) est probablement la cause de sa faible quantité, plus particulièrement quand les atomes de fer ont la possibilité d'être capturés par une autre phase, dans ce cas la phase α(MnFe).

Les résultats des études sur la fissuration à chaud montrent que la susceptibilité dans ce cas est grandement influencée par le rapport Fe/Si et la concentration nominale de chacun de ces éléments. Cette influence est exercée par la détermination de la quantité de métal liquide présente à la température eutectique et le temps passé en régime vulnérable. La meilleure résistance est obtenue avec un rapport proche de 1 et des faibles concentrations de fer et de silicium. La résistance baisse lorsque ce rapport s'éloigne de 1. Plus le rapport est élevé, plus mauvais est la résistance à la fissuration à chaud, spécialement avec un rapport de deux et plus.

Les résultats des tests mécaniques montrent que les propriétés sont grandement influencées par le rapport Fe/Si et la concentration nominale de chacun de ces éléments. les meilleures propriétés étant obtenues avec un rapport Fe/Si proche de 1 et des faibles concentrations de fer et de silicium, en accord avec les résultats obtenus lors des études sur la solidification et la fissuration à chaud. Deux paramètres principaux ont été identifiés comme déterminants les propriétés des alliages traités thermiquement; la solubilité de la phase Al_2Cu et l'accroissement de l'espace inter-dendritiques. Les résultats des expériences présentes montrent qu'en doublant ou en triplant la limite actuelle de 0.1% de fer tout en gardant un rapport Fe/Si de 1, il n y aura aucune difficulté à atteindre au vieillissement naturel (T4) la ductilité minimale de 7% requise par l'industrie automobile tout en augmentant les résistances élastique et mécanique du matériau. Par rapport aux valeurs

maximales de déformation calculées, la perte en ductilité pourrait même être réduite à environ 2.5% avec une amélioration dans la pratique de coulée. Au vieillissement artificiel (T7), il sera très difficile voir impossible d'atteindre la ductilité minimale de 7% requise par l'industrie automobile avec 0.2%Fe et 0.2%Si, alors que avec 0.3%Fe et 0.3%Si c'est probablement impossible. L'énergie d'impact montre une bonne corrélation avec la ductilité en traction. les résultats montrent que la baisse en énergie absorbée par les alliages contenant environ (0.2%Fe, 0.2%Si) et (0.3%Fe, 0.3%Si) en comparaison à l'alliage B206 est reliée à l'énergie de propagation des fissures.

Dans les conditions expérimentales actuelles, ces alliages présentent une ductilité inferieure a celle de l'alliage de base B206, mais largement supérieure a celles de certains alliages tels que le A356 et le A319 présentement utilisés dans l'industrie automobile. A cet effet, ils méritent une certaine attention.

Acknowledgments

To my mother Mrs Kamga Rebecca Rosette, my brothers and their families: Dr. Job Ernerst Nkengne Kamga, Dr. Hubert Nwafo Kamga, Mr Emmanuel Euler Fotso Kamga and Mr Felix Kaptué Kamga, my sisters and their families: Mrs Marguerite Isabelle Motué Kamga, Albertine Maptoum Kamga, Elise Felecité Nono Kamga and Dr. Adolphine Momokyié Kamga. I say many thanks for their moral support. Finally but not the least to my wife Virginie and my daughter Vanessa for their patience and understanding, I simply want to tell you how much I love you.

LIST OF PUBLICATIONS

Five journals articles have been compiled from this research project. But due to the prolonged submission time for journal publications, one is accepted, one is submitted while the remaining will be submitted subsequently. The list of publications is as follows:

1- Solidification of Aluminum-Copper B206 Alloys with Iron and Silicon Additions. Metallurgical and Materials Transactions A. (Accepted, 2010-03-25)

2- Hot Tearing of Aluminum-Copper B206 Alloys with Iron and Silicon Additions. Materials Science and Engineering A. (Submitted, 2010-05-07)

3- Tensile properties of Aluminum-Copper B206 Alloys with Iron and Silicon Additions International Journal of Cast Metal Research (To be submitted, June 2010)

4- Solution Heat Treatment of Aluminum-Copper B206 Alloys with Iron and Silicon Additions
Metallurgical and Materials Transactions A (To be submitted, June 2010)

5- Hardness and Impact Toughness of Aluminum-Copper B206 Alloys with Iron and Silicon Additions
Scripta Materiala (To be submitted, July 2010)

TABLE OF CONTENTS

LIST OF FIGURES

LIST OF TABLES

CHAPTER 1
INTRODUCTION

CHAPTER 1
INTRODUCTION

1.0 Overview

Aluminum alloys are gaining more ground as first choice materials, especially in the transportation industry where a high strength/weight ratio is of premium importance. This tendency is likely to last for a very long time, as long as energy sources continue to diminish irreversibly and people's awareness about environmental pollution increases. As recycling has shown to be a good alternative solution to saving energy, one can believe that the foundry industry will continue to play a key role for the well being of mankind in the future.

Metal casting offers an economical and simple route to the production of one or several parts weighing from a few grams to several hundred tons. Simple to complex parts can be produced with proper selection of the casting process, which is in turn dictated by the size, quantity and properties of the final casting. A wide variety of casting processes have been developed over time, sand and die casting being the most used for aluminum alloys. However, there are certain drawbacks of casting including the formation of defects such as porosity, hot tears and segregation. They could be potential crack initiators during service operation. [1,2] These defects can be minimized by proper design of the mould, proper melt

treatment (cleaning, degassing and refining), good optimization of the casting parameters such as melt temperature at pouring, mould preheating temperature and cooling rate, and most importantly the material chemistry. [3-7]

Aluminum is alloyed primarily to increase strength, although improvement of other properties are also very important. Most of the metallic elements readily alloy with aluminum, but just a few of them, individually or in combination, are important major alloying ingredients (Cu, Si, Mg, Zn, Sn) in commercial aluminum based casting alloys. Nevertheless, an appreciable number of other elements serve as supplementary alloying additions for improving alloy properties and characteristics and/or to suppress the effect of some undesirable impurity elements. Impurities and alloying elements, in general, partly go into solution in the matrix and partly form intermetallic particles during the solidification process.

Al-Si alloys with small amounts of magnesium and/or copper have become the chief support of the aluminum casting industry because of their good casting characteristics. However, aluminum copper alloys are well known to be distinguished among the other aluminum foundry alloys by their excellent strength and toughness, which are obtained through artificial or natural age-hardening. In contrast to the good mechanical properties, they have poor castability, poor resistance to corrosion, and a marked susceptibility to hot tearing. [8,9] The term castability is not precisely defined. It is generally used to estimate the suitability of a composition for solidification in a specific process to produce castings without major defects. [10] Different casting processes will generate different casting defects and castability will therefore have a different meaning. Notwithstanding, the recurrent

important castability properties are fluidity, feedability and hot cracking resistance. [11]

Fluidity is most strongly affected by temperature above the liquidus or degree of superheat and is defined as the ability of a metal to flow into regions of the casting that have small cross sections and that are far from the casting ingate without freezing. According to Jorstad, [12] metal flow is restricted by sludge during casting. Feedability is defined as the ability to feed liquid metal to compensate for solidification shrinkage and thus avoid porosity in the casting. According to Arnberg et al.,[11] the size and morphology of intermetallic particles may affect the formation of porosity and the resistance to feeding. Hot cracking resistance is defined as the ability of a metal to withstand cracking during solidification due to thermal contraction of the solid metal.

1.1 Motivation

The solubility of iron in aluminum is very low (0.052% in pure aluminum). The presence of copper lowers this solubility by almost five times, [13] and it is generally present in aluminum copper alloys as intermetallic compounds (mainly as the Al_7FeCu_2 phase). These iron-bearing compounds potentially decrease the strength and ductility of the alloy and the reduction of soluble copper that results from their formation establishes the acceptable iron as the lowest possible, say less than 0.1% in B206 alloy. The automobile industry is one of the main consumers of 206 alloys. Increased activity in the recycling of spent automobiles in order to reduce production costs, has led to pick-up of iron from remelted scrap and melting equipments. This iron which can not be readily removed from molten aluminum by conventional foundry treatments makes 206 alloys expensive for the

industry and limits their use. Many efforts have been carried out to better understand and improve alloy A206, the majority of them focussing on casting parameters such as cooling rate, gating system, casting geometry, etc. [7,14-17] Just a few of the published studies discuss the effects of iron content on microstructure and mechanical properties. [18-20] Tseng et al. [19] studied *the effect of iron content on microstructure and mechanical properties of A206 alloy*. Their study was carried out on alloys in the T7 condition. They concluded that a typical solidification structure is composed of a network of Al_2Cu and needle-like Al_7FeCu_2, and that the tensile strength and elongation linearly decreases with increasing iron content. Major and Sigworth [18,20] studied the chemistry/properties relationships, but related directly the chemistry and heat treatment response to mechanical properties without proper reference to microstructural constituents. However, based on their literature survey, they revealed the possibility to increase Fe and Si limits in 206 alloys in the T4 temper to 0.2% each, resulting in only a small loss of ductility. Also, they pointed out that the Fe/Si ratio is important in these alloys although there is disagreement about what is the best ratio to have.

It is well known that the formation of solid solutions and heterogeneous constituents (quantity, size, form and distribution) determine the physical, mechanical and technical properties of an alloy. Plausible responsibilities of intermetallics phases in pre-cited drawbacks of aluminum-copper alloys were earlier highlighted. Unfortunately, they seem to have not been clearly studied and established.

1.2 Objectives

The main objective of this research study was to optimize the iron content in B206 alloys without major loss in mechanical properties, so that it can be produced from recycled materials and become cost competitive. This was done by neutralizing iron by silicon, and achieved in the following sequence.

1- *Study on solidification behaviour*

Since the mechanical properties of a material greatly depend on its microstructure in the as-cast condition and therefore its solidification history, the first part of this research focused on the combined effects of iron and silicon additions as well as the cooling rate on solidification and microstructure of aluminum type B206 alloys. Also, due to the wide range of allowable copper in B206 alloys (4.2-5%), two different levels of copper were used to assess the importance of copper content.

2- *Study on hot tearing behaviour*

Aluminum-copper alloys are known to have poor castability due to their high susceptibility to hot tearing. Hot tearing is therefore an inherent defect in these alloys and is deleterious to their mechanical properties. The second part of this research focused on the combined effects of iron and silicon additions on the hot tearing behaviour of aluminum type B206 alloys, to establish an optimal Fe/Si ratio for a better resistance to hot tearing.

3- *Study on mechanical properties*

The third and final part of this research focused on the combined effects of iron and silicon additions as well as heat treatment on themechanical properties of aluminum B206 type alloys. Properties investigated were tensile, impact toughness and microhardness. Tension

testing is the main test method and is used to determine the Fe/Si ratios that satisfy automobile and aerospace requirements. Microhardness is used to assess the contribution of dissolved elements to the overall strengthening of alloys. It is also used for qualitative evaluation of phase evolution during heat treatment. Impact toughness which can also be used to assess the ductility of a material is carried out only on optimized Fe/Si ratios in order to correlate results with those obtained during tensile testing and have a better understanding of the failure history of the material.

1.3 Statement of originality

Although Major and Sigworth [18,20] pointed out the importance of Fe/Si ratio in 206 alloys as previously mentioned, a detailed study in this regard seems to be absent in the published literature. This work establishes unambiguously, through a detailed and careful study using different levels of iron and silicon, the effect of Fe/Si ratio on solidification characteristics, hot tearing behaviour, and mechanical properties of aluminum type B206 alloys with additions of iron and silicon. Therefore, the current research work contains a high degree of originality and references are provided where previous works are cited.

1.4 Structure of the thesis

This dissertation discusses the combined effects of iron and silicon additions on solidification behaviour, hot tearing behaviour, and mechanical properties of B206 alloys. It is subdivided into six chapters presented in the following order:

- Chapter 1 essentially presents our motivations to carry out this research work and our main objective.

- Chapter 2 starts with a brief presentation of 206 alloys (history, application and properties), and focuses on a survey of previous studies on solidification and heat treatment of aluminum-copper alloys, and their effects on mechanical properties. Also, the estimation of the quality of a casting by quality index charts is discussed.

- Chapter 3 focuses on solidification studies. Experimental methods are presented. Results are discussed and findings are summarized.

- Chapter 4 focuses on hot tearing studies. Experimental methods are presented. Results are discussed and findings are summarized.

- Chapter 5 focuses on mechanical properties studies. Experimental methods are presented. Results are discussed and findings are summarized.

- Chapter 6 presents an overall conclusion of the findings of this research study and describes further suggestions for future studies.

CHAPTER 2
LITERATURE REVIEW

CHAPTER 2
LITERATURE REVIEW

2.0 Introduction

The mechanical properties of a part produced by casting depend mainly on its solidification history, *i.e.*, its properties in the as-cast condition. In heat treatable alloys such as aluminum-copper alloys, these properties can be substantially improved by the application of a proper heat treatment to the part after removal from the mould. This chapter is devoted to the investigation of previous studies on solidification and heat treatment of aluminum-copper alloys, and their effects on mechanical properties. Since the alloy is primarily identified by its chemistry, the direct impact of alloying elements on mechanical properties is also investigated. Finally the estimation of the quality of a casting by quality index charts is presented. A brief presentation of aluminum 206 alloys is given in the next section.

2.1 History, applications and properties of 206 alloys

The 206 aluminum alloy family is the newest of an important group of the Aluminum-Copper-Magnesium-Manganese (Al-Cu-Mg-Mn) system. Like alloy 201.0 (formerly KO-1), alloy 206.0 is a modification of the French alloy AU5GT-T4 which has been in use for 80 years. [14,15] The American equivalent of this French alloy is registered with the Aluminum

Association as 204.0-T4. 201.0 alloy has been in use for 44 years and is considered as the strongest cast aluminum alloy, but it contains 0.7 wt.% Ag which renders the alloy very expensive and useful only where material costs are not a prime consideration such as in military and similar applications. 206.0 alloy was registered by the Aluminum Association (AA) in 1976.[15] The purpose of the alloy 206.0 development was to preserve as much of the ductility and mechanical properties of alloy 201.0, while reducing alloy costs to a level comparable to other premium casting alloys. As a consequence, the commercial grade 206.0 alloy may be characterized as a silverless 201.0 alloy. [14]

Its typical uses include applications where high tensile and yield strengths and high fracture toughness are needed, some examples of which are structural castings in heat-treated temper for automotive and aerospace applications. The aerospace industry is the other main consumer of this alloy, besides the automotive industry earlier mentioned. These two markets have markedly different requirements. The aerospace market in which the use of high purity alloys is easily justified calls for high strength, but requires the ductility to exceed a minimum range of only 3 to 5%, depending on the location within the casting. [21] In such applications, strength is at a premium but only moderate ductility is required. The automotive industry in which economy of process and material dominates favours crashworthy alloys and therefore calls for higher ductility, where elongations of 7% or greater are typically required. [18]

Today, two more versions of the alloy have been registered. [20] A206.0 is the higher purity version commonly used in aerospace applications and which has also been used in automotive suspension components such as knuckles. [22] It is significantly strong and

ductile, but is difficult to cast because of its tendency for hot tearing. [7,16] B206.0 is a recently registered alloy. [18] It differs from the other alloys primarily in the lower titanium limit which is claimed to improves the alloy behaviour with respect to hot tearing by increasing its response to Ti-B based grain refiners for Ti-B additions in the range of 10-30 ppm boron. This claim was confirmed by Wannasin *et al.* [16] who studied hot tearing susceptibility and fluidity of semi-solid gravity cast Al-Cu alloys at 5% fraction solid. Registered 206 Alloy compositions and mechanical properties of A206 alloys are presented in Tables 2.1 and 2.2, respectively.

2.2 Solidification of aluminum-copper alloys

Solidification theory has gained great development in the last four decades. [1,24] This has led to a better understanding of solidification phenomena and mechanisms, and improved quality control of ingot and casting production. The major progress achieved in this field, both experimental and theoretical, includes the theory of liquid/solid interface stability,[25-27] as well as the theories of cellular, dendritic and eutectic structure growth. [11, 28-36] From these studies, it is clearly established that in aluminum alloys, constitutional supercooling is essential in destabilizing the solidification front, resulting in dendritic growth.

The general nature of dendritic solidification was reasonably well understood at the start of the 1900's. Rosenhain [37] described the growth of dendrites as being similar to the way in which children's building blocks might be piled up to cover a given area. Even the effect of solidification rate upon the dendrite structure was observed as early as 1920, [38]

Table 2. 1: Registered AA 206 Alloy Compositions [18]

Alloy	Si	Fe	Cu	Mn	Mg	Ti	Zn	Others	
								Each	Total
206.0	0.10	0.15	4.2-5.0	0.20-0.50	0.15-0.35	0.15-0.30	0.10	0.05	0.15
206.2	0.10	0.10	4.2-5.0	0.20-0.50	0.20-0.35	0.15-0.25	0.05	0.05	0.15
A206.0	0.05	0.10	4.2-5.0	0.20-0.50	0.15-0.35	0.15-0.30	0.10	0.05	0.15
A206.2	0.05	0.07	4.2-5.0	0.20-0.50	0.20-0.35	0.15-0.25	0.05	0.05	0.15
B206.0	0.05	0.10	4.2-5.0	0.20-0.50	0.15-0.35	0.10	0.10	0.05	0.15
B206.2	0.05	0.07	4.2-5.0	0.20-0.50	0.20-0.35	0.05	0.05	0.05	0.15

Table 2. 2: Mechanical properties of A206 alloys [23]

Properties	Sand casting		Permanent mould casting	
	T4	T71	T4	T7
Tensile strength, MPa	354	400	430	436
Proof strength, MPa	250	330	265	347
Shear strength, MPa	255	-	-	257
Fatigue strength, MPa (a)	-	160	-	207
Elongation, % (b)	7	5	17	11.7
Hardness (c)	100HB	110HB	118HV	137HV
Poisson's ratio	0.33			
Modulus of elasticity, GPa	70			
Impact strength. Charpy V-notch, J	9.5			

(a) at 5×10^8 cycles; R.R. Moore rotating beam test (b) in 50mm or 2 in (c) 10 mm ball with 500 kgf load

but it was not until the middle of the last century that serious efforts were made to obtain quantitative information concerning dendrite refinement. A paper by Alexander and Rhines [39] in 1950 established on a quantitative basis the influence of composition and solidification rate upon some features of the dendrite. Since that time, there have been several published accounts that have described dendrite refinement and its relation to mechanical properties. [1,24,40-46] The interarm spacing characterizes the solidification morphology which constitutes the solute segregation pattern and, often, the formation of second phase in the interdendritic region and plays a larger role in the determination of as-cast mechanical properties which largely control the material. [1,24] Fine dendrite arm spacing has been shown to be desirable and often essential, to obtain high mechanical properties in cast aluminum alloys. [40-43] Similar results have been found for other cast alloys. [44-46] The major reason why the fine spacing is beneficial appears to be that improved homogenization can be achieved in heat treatment. [47-48]

The practical importance of dendrite arm spacing has stimulated considerable study during the second half of the last century on factors influencing the spacing. [28,29,49-53] Michael and Bever, [49] Reed, [50] Brown and Adams, [51] Horwarth and Mondolfo, [52] and Bardes and Flemings [28] have studied the effect of solidification time on dendrite arm spacing in aluminum-4.5% copper alloy. Reed, [50] and Brown and Adams [51] showed a linear relationship between the dendrite arm spacing and the square root of solidification time. Bardes and Flemings [28] showed a linear relationship between the dendrite arm spacing and solidification time exponent 0.39. Howarth and Mondolfo [52] fitted an empirical exponent of -0.25 to their plots of dendrite arm spacing and rate of solidification.
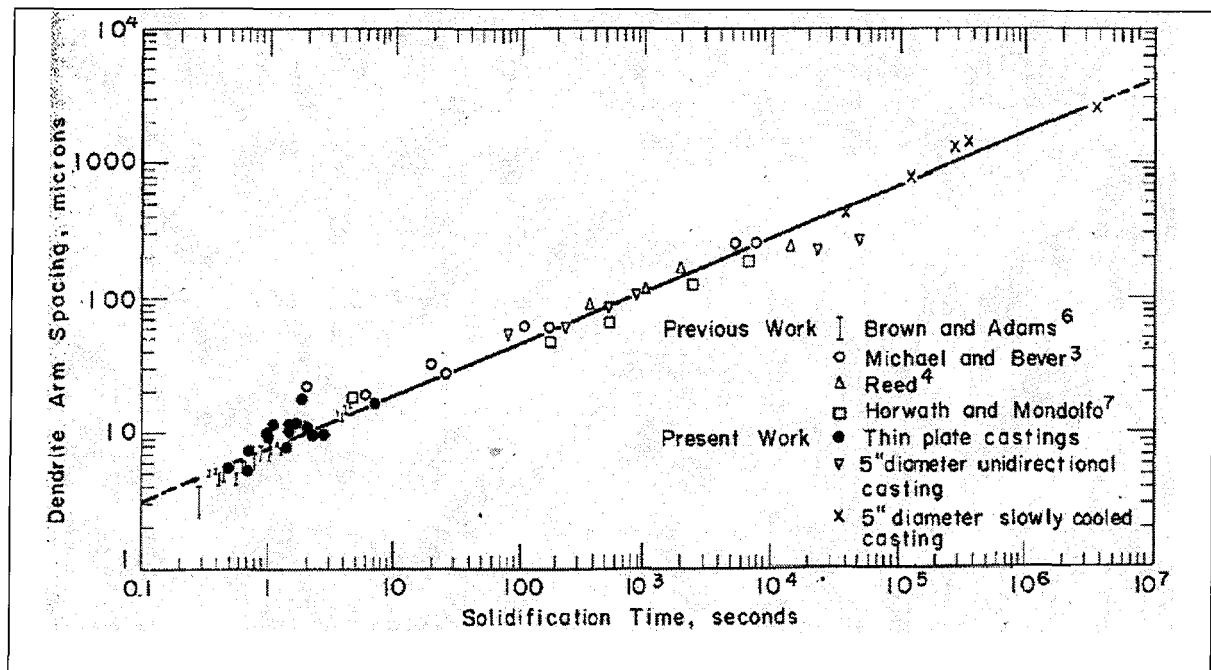
Figure 2. 1: Relationship between dendrite arm spacing and solidification time. [28]

Specimens examined by Reed, [50] and Bardes and Flemings [28] contained equiaxed grains. Some of the castings made by Michael and Bever [49] were columnar; others were equiaxed. Structures of other types of castings were columnar. The data from all these researchers plotted together by Bardes and Flemings [28] as shown in Fig. 2.1 lie on the single curve shown, independent of grain type or size. This provided evidence that dendrite arm spacing of an aluminum-copper alloy depends only on local solidification time (or local cooling rate) and not on factors such as grain size or structure. It was later supported by Kattamis et al. [29] and Rohatgi and Adams. [53] Furthermore, Kattamis et al. [29] proved false the mechanism previously suggested which assumed that all arms that form are stable throughout solidification. They showed that for Al-4.5%Cu alloy, the dendrite structure which forms at the start of solidification is highly unstable. Coarsening (disappearance of small dendrite arms and growth of larger dendrite arms) occurs rapidly both during
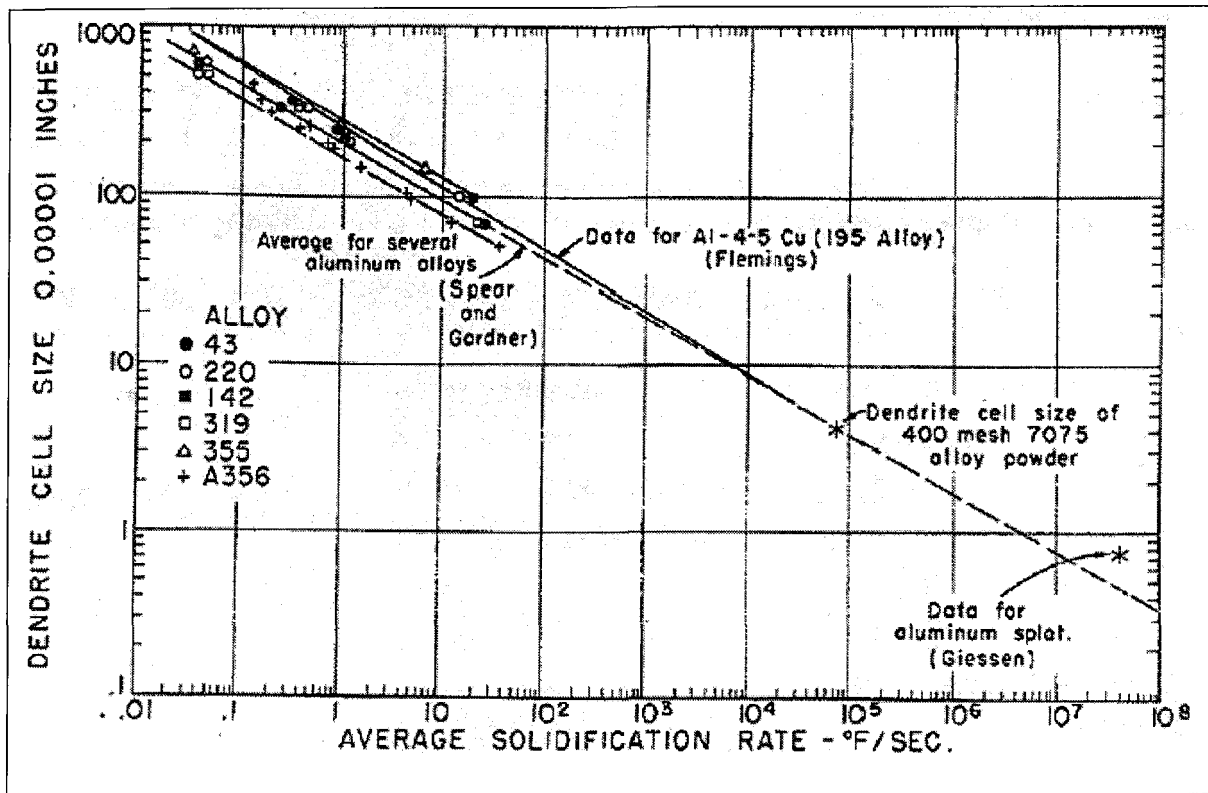
Figure 2. 2: The relationship between dendrite cell size and solidification rate for aluminum alloys. [28]

isothermal holding and during solidification. As a consequence, coarsening is of overriding importance in determining final dendrite arm spacing and coarsening time should be taken into consideration.

Several of the researchers mentioned above have examined the effect of variations in alloy content on dendrite arm spacing. [49,51,52,54] Alloy composition has generally been found to influence the spacing, although the effect is usually small compared with that of local solidification time. The relatively minor effect of changes in alloy analysis on dendrite arm spacing in aluminum alloys is particularly well illustrated in Fig. 2.2.

The microstructural feature of aluminum-copper alloys generally includes some "second phase" constituents that may consist of either pure alloying elements or

intermetallic-compound phases, and often exhibits some solidification defects such as porosity and hot tearing. These microstructural features which also affect the mechanical properties of the material are discussed in detail below.

2.2.1 Formation of intermetallics in Al-Cu alloys

When the content of an alloying element exceeds the solid-solubility limit, the alloying element produces "second phase" microstructural constituents that may consist of either the pure alloying element or an intermetallic-compound phase. Intermetallic phases are chemical compounds between two or more metals with crystal structures which differ from those of the constituent metals. These compounds in fact form (according to Hume-Rothery rules) between elements that differ in three attributes: crystal structure, atom size and electronegativity; valency also being an additional factor. Some of them such as copper based and magnesium based ones are beneficial due to their enhancement of aging, while some others such as iron-based ones are deleterious to mechanical properties due to their insolubility during heat treatment, their brittleness and incoherency with the aluminum matrix.

Copper is one of the most important alloying elements for aluminum, because of its appreciable solubility and strengthening effect. Many commercial alloys contain copper, either as the major addition or among the principal alloying elements, in concentrations of 1 to 10%. [55] Constituents formed in aluminum-copper alloys can be divided in two groups: in the soluble ones are the constituents containing one or more of copper, lithium,

magnesium, silicon, zinc; in the insoluble ones are the constituents containing at least one of the less insoluble iron, manganese, nickel, etc.[56,57]

The type of constituents formed depends not only on the amount of soluble elements available but also on their ratio. Available copper depends on the iron, manganese and nickel contents, as the copper combined with them is not available for strengthening. Copper forms $Al_6(CuFe)$ and Cu_2FeAl_7 with iron, $Al_6(CuFeMn)$ and $Cu_2Mn_3Al_{20}$ with manganese, Cu_4NiAl_7 and several not too well known compounds with nickel and iron.

In the Al-Cu-Fe system, the phase $Al_6(CuFe)$ (7%Cu, 24.6%Fe) which is also designated as $Al_{23}CuFe_4$ and $\alpha(FeCu)$ is a modification of the metastable phase Al_6Fe which becomes stable at 7-8%Cu and 22-25%Fe. This compound has an orthorhombic crystal structure of the Al_6Fe type with parameters a = 0.64343nm, b = 0.74604 nm, and c = 0.87769 nm. [58] The density of the phase is 3.45g /cm^3. [56] In Al-Cu-Fe-Mn system, the phase is formed from a continuous series of solid solutions of isomorphic phases Al_6Mn and $Al_6(FeCu)$, and designated as $(AlCu)_6(FeCuMn)$ with lattice parameters a = 0.7473nm, b = 0.6452nm, and c = 0.8794nm. [56] The Al_7FeCu_2 phase (36.9%Cu, 16.2%Fe) also designated as $\beta(FeCu)$ or N, has a broad range of homogeneity range of 29-39%Cu and 12-20%Fe. The structure of this phase belongs to the tetragonal crystal system with lattice parameters a = 0.6336nm and c = 1.4879nm. It has a density of 4.3/cm^3 [58] and a microhardness of 5.95 GPa at 20°C. [59] Depending on the alloy composition, these ternary phases can crystallize primarily or form by peritectic reactions. [57] The $Al_{20}Cu_2Mn_3$ (15.3%Cu, 19.8%Mn) phase also designated as T phase has a homogeneity range of

12.8-19%Cu and 19.8-24%Mn. It is orthorhombic with lattice parameters a = 2.41-2.411nm, b = 1.25-1.251nm, and c = 0.72-0.77nm. [56,57]

The amount of silicon available to some extent controls the copper compounds formed. Silicon above 1% favours the formation of Al_5FeSi over the iron-copper compounds, and $Al_{15}(CuFeMn)_3Si_2$ over the $(CuFeMn)Al_6$ and $Al_{20}Cu_2Mn_3$ compounds.

The phase Al_5FeSi (25.6% Fe, 12.8% Si) also known as $Al_9Fe_2Si_2$ exists in the homogeneity range 25-30% Fe and 12-15% Si. This phase has a monoclinic structure with the lattice parameters a = b = 0.612 nm, c = 4.148-4.150 nm, and β = 91°. [56,57,59] It has a density of 3.3-3.6 g/cm^3 and a microhardness of 11.47 GPa at 20°C. [59]

According to Mondolfo, [56] the solid solution of iron in the $Al_{15}(Fe,Mn)_3Si_2$ phase (0-31%Fe, 8%Si) has a cubic structure with the lattice parameter a = 1.25-1.265 nm depending on the iron content, and copper addition replaces mostly silicon. Its density and microhardness seems to have not been reported, but should be close to that of the $Al_{15}Mn_3Si_2$ phase which is respectively 3.55 g/cm^3 and 8.8 GPa at room temperature. [59] An approximate analysis of $Al_{15}(CuFeMn)_3Si_2$ is: Cu 5-7%, Fe 7-13%, Mn 4-10%, and Si 4-8%.[56] Similarly, but to a lesser extent, available silicon is affected by iron and manganese contents. With a Cu:Mg ratio below 2 and a Mg:Si ratio well above 1.7, the $CuMg_4Al_6$ compound is formed, especially if appreciable zinc is present. When Cu:Mg > 2 and Mg:Si > 1.7, $CuMgAl_2$ is formed. The compound $CuMgAl_2$ (48%Cu, 17%Mg), also designated S, is characterized by a narrow region of homogeneity; it has an orthorhombic crystal structure with lattice parameters a = 0.401nm, b = 0.925nm, and c = 0.715nm. Its density is 3.55g/ cm^3. [56,57] If the Mg:Si ratio is approximately 1.7, Mg_2Si and $CuAl_2$ are in

equilibrium. The Mg_2Si (63.2%Mg, 36.8%Si) phase has a cubic structure with lattice parameter a = 0.635-0.64nm. Its density is $1.88g/cm^3$. [56,57] The Al_2Cu phase also designated θ, has a tetragonal structure with lattice parameters a = 0.6063nm and c = 0.4872nm. This phase exists in a homogeneity range of 52.5-53.9%Cu which does not reach the stoichiometric concentration of copper (54.2%). Its density in binary alloys is $4.34g/cm^3$ [56,57] and its microhardness at 20°C is 5.3 GPa. [59] With the Mg:Si ratio 1 or less, $Cu_2Mg_8Si_6Al_5$ is formed, usually together with $CuAl_2$. The $Al_5Cu_2Mg_8Si_6$ (20.3%Cu, 31.1%Mg, 27%Si) phase also designated as Q phase has a hexagonal structure with lattice parameters a = 1.032nm and c = 0.405nm. [56,57,60] Magnesium is usually combined with silicon and copper. Only if appreciable amounts of lead, bismuth or tin are present can Mg_2Sn, Mg_2Pb, Mg_2Bi_3 form. [56] In none of the alloys within specified limits does magnesium combine with manganese or iron. [56] Silicon tends to combine first with magnesium as Mg_2Si; then it can combine with iron or manganese, or appear as Si. [56] The list of probable constituents is presented in Table 2.3.

Intermetallic phases can be formed in aluminum castings at high temperatures, before the aluminum dendrites are formed, concurrent with the solidification of the alloy, or they can form complex eutectic phases which solidify at temperatures as low as 480°C. [61,62] Diverse interpretations of predendritic formation of intermetallics in aluminum alloys have been suggested. According to Cao and Campbell, [63] it seems that Fe-rich phases may nucleate on the wetted sides of double oxide films, while the gap between the dry sides of oxide films constitutes the cracks commonly observed in the Fe-rich phases and aluminum matrix. Mondolfo [64] pointed out that the appearance of the large primary crystals of

α-Al$_{15}$(Fe,Mn)$_3$Si$_2$ in the microstructure is determined by the specific composition of the alloy, particularly the manganese and iron concentration, and the cooling rate. Increased cooling rates and lower manganese concentrations tend to depress the formation of the α-Al$_{15}$(Fe,Mn)$_3$Si$_2$ phase to lower temperature. At lower cooling rates and higher

Table 2. 3: Phases formed in aluminum-copper alloys [56]

Cu	Cu < 2% In solid soln.	Cu > 2% CuAl$_2$	Fe » Si Cu_2FeAl_7 or $(CuFe)Al_6$	Mg > ½ Si $CuMgAl_2$ or $CuMg_4Al_6$	Mn » Fe $Cu_2Mn_3Al_{20}$ or $(CuFeMn)Al_6$	Mg < Si $Cu_2Mg_8Si_6Al_5$ $(CuFeMn)_3Si_2Al_{15}$	Ni > 0.1% Cu_4NiAl_7 or $(CuNi)_2Al_3$ or $Cu_2(FeNi)Al_7$ or $(CuFeNi)Al_6$
Fe	Si > 2Mg Fe_2SiAl_8 or $FeSiAl_5$	Fe » Si Cu_2FeAl_7 or $(CuFe)Al_6$ or $FeAl_3$		Mn > 0.1% $(CuFeMn)Al_6$ or $(CuFeMn)_3Si_2Al_{15}$	Ni > 1% $FeNiAl_9$ or $(CuFeNi)Al_6$ or $(CuFeNi)_2Al_3$ or $Cu_2(FeNi)Al_7$		
Si	Si > Fe $FeSiAl_5$	Si < Fe, Mg > Si Mg_2Si	Mg ≈ Si $Cu_2Mg_8Si_6Al_5$	Mn > 0.1% $(CuFeMn)_3Si_2Al_{15}$	Si » Mg +Fe Si		
Mg	Mg < 0.2% In solid soln.	Mg > 0.6 Mg <1Mg Mg_2Si	Si ≈ Mg $Cu_2Mg_8Si_6Al_5$	Si « 0.6 Mg $CuMgAl_2$	Cu < Mg $CuMg_4Al_6$		
Mn	Mn < 0.2% In solid soln.	Fe > Si $(FeMn)Al_6$	Fe < Si $(CuFeMn)_3Si_2Al_{15}$	Fe.Si « Mn $Cu_2Mn_3Al_{20}$	Ni > 0.1% Mn_3NiAl_{16}		
Zn	Zn < 2% In solid soln.	Zn > 2% $Cu_5Zn_2Al_3$					
Ni	Cu » Fe Cu_4NiAl_7	Cu < 2Fe, Fe » Si $FeNiAl_9$ or $(CuFeNi)Al_6$ or $(CuFeNi)_2Al_3$ or $Cu_2(FeNi)Al_7$	Mn > 0.1% Mn_3NiAl_{16}				
Pb	Mg, Pb < 1% Pb	Bi < 0.1 Pb, Mg > 1.7 Si Mg_2Pb	Bi > 0.1 Pb $BiPb_3$				
Bi	Pb > 0.2 Bi $BiPb_3$	Pb < 0.2 Bi, Mg > 1.7 Si Bi_2Mg_3					
Sn	Mg < 1.7 Si Sn	Mg » 1.7 Si Mg_2Sn					
Cd	Cd (?) $TiAl_3$						
Ag	Ag < 0.3% In solid soln.	Ag > 0.3% Ag_2Al	Mg » 1.7 Si $(AgCuAl)_{49}Mg_{32}$ or AgMg (?)				

manganese concentrations, the α-Al_{15}(Fe,Mn)$_3$Si$_2$ phase may be able to form as a primary phase. Moustafa et al.[65] studied *the effect of solution heat treatment and additives on the microstructure of Al-Si A413.1 alloys*. They concluded that the size and distribution of α-Al_{15}(Fe,Mn)$_3$Si$_2$ phase during solidification is strongly related to the amount of strontium added to the alloy. In the unmodified alloy, α-Fe phase precipitates in the interdendritic regions, along with the eutectic silicon. However, with the addition of strontium, α-Fe phase precipitates prior to the formation of the α–Al dendritic network. They could not give any reason for such a dramatic change in the mechanism of precipitation of this phase, but mentioned the important fact that the solubility of this phase during solution heat treatment is almost nil. It should be noted that this primary precipitates seems to have not been reported for Al-Cu alloys.

Backerud et al.[66] studied the solidification characteristics of aluminum alloys. For A206.2 alloys which experimental and standard compositions are shown in Table 2.4, they reported the following reactions during solidification, and phases observed by microscopy/SEM/EDX as presented in Table 2.5 and Table 2.6, respectively. Their results are in good agreement with Mondolfo's predictions. [56] Typical microstructures obtained from their studies are also presented in Fig. 2.3.

Intermetallics can be characterized and affect properties of the alloy by their quantity, size, distribution, and morphology. The quantity is mainly controlled by the chemistry. For iron intermetallics, their amount is directly proportional to the iron content. [18,19] The size and distribution can be controlled by grain refining and precipitation temperature. The morphology can be controlled by chemical composition as mentioned earlier. Another

parameter that can affect morphology is heat treatment. This will be discussed in section 2.3.

Table 2. 4: Composition of A206.2 alloy used in experiments of Backerud et al. [66]

Alloy Composition	Elements							
	Si	Fe	Cu	Mn	Mg	Zn	Ti	Others
A206.2 Actual sample	0.05	0.03	4.36	0.26	0.30	0.02	0.40*	

* The sample supplied is outside specifications

Table 2. 5: Reactions during solidification of A206.2 suggested by Backerud et al. [66]

Reaction No.	Reactions	Suggested temperature, °C
1	Development of dendritic network	651-649
2	$Liq. \longrightarrow Al + (CuFeMn)Al_6$	649
3	$Liq. + (CuFeMn)Al_6 \longrightarrow Al + Cu_2Mn_3Al_{20}$	616
4	$Liq. \longrightarrow Al + CuAl_2 + Cu_2Mn_3Al_{20} + Cu_2FeAl_7$	537
5*	$Liq. \longrightarrow Al + CuAl_2 + Al_2MgCu + Mg_2Si$	500

* Reaction 5 can be observed at high cooling rate only

Table 2. 6: Phases observed by Backerud et al. [66] in A206.2 using Microscopy / SEM / EDX

No.	1	2	3	4	5	6		
Phase	α-Al	$Cu_2Mn_3Al_{20}$	Cu_2FeAl_7	$CuAl_2$	$(CuFeMn)Al_6$	Complex eutectic		
Characteristics	Dendrites	Square brown	Needles	Pink	Square brown			

Microstructure of sample from alloy A206.2.
Al_7FeCu_2 (brown needle), Al_2Cu (pink).
Cooling rate 0.3 °C/s;
X560.
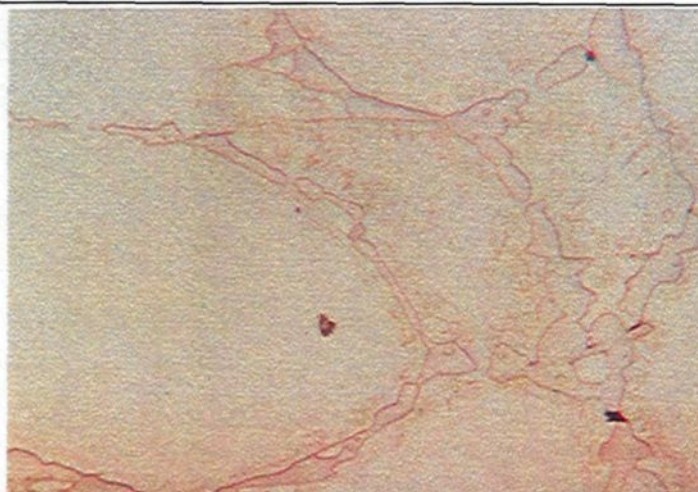
Microstructure of sample from alloy A206.2.
$Al_{20}Mn_3Cu_2$ (square brown).
Cooling rate 0.6 °C/s;
X1100.
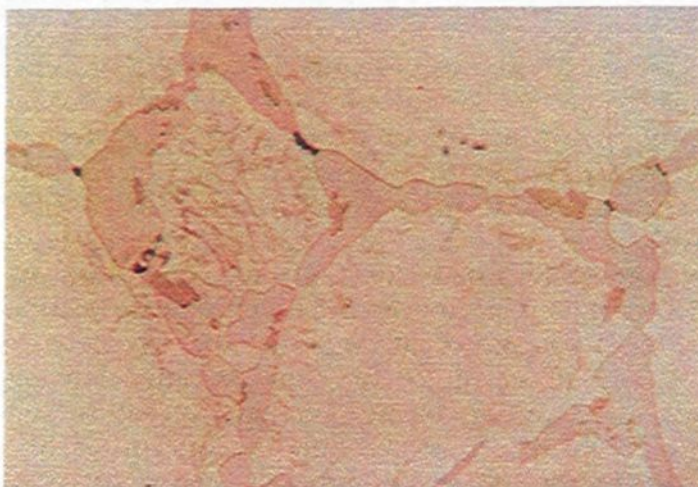
Microstructure of sample from alloy A206.2.
Cooling rate 4.5 °C/s;
X560.
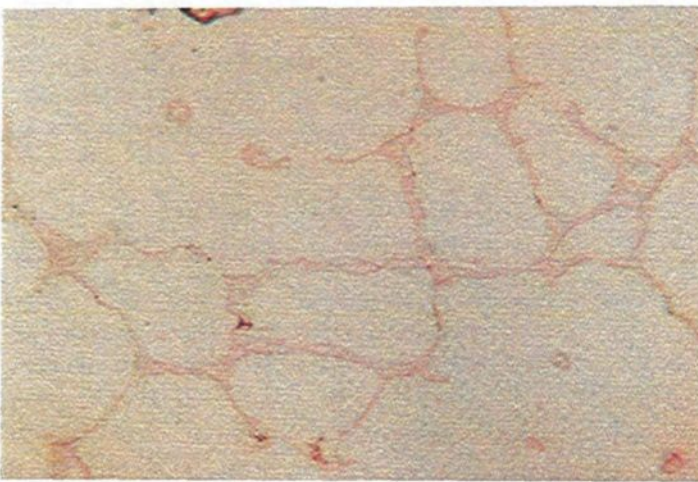
Figure 2. 3: Typical microstructures of A206 alloys at different cooling rates. [66]

2.2.2 Porosity in aluminum – copper alloys

In the metallurgical context, porosity refers to the presence of minute holes or cavities in a solid metal. It is one of the defects normally present in Al-Cu cast alloys. Porosity in a casting generally deteriorates its mechanical properties. It is particularly harmful to the ductility, fracture toughness, fatigue life, etc. [13,67-70] Extensive studies have been carried out to understand the origins and characteristics of porosity formation in cast alloys. [1,6,13,71-76] Results show that casting porosity is caused by a combination effect of shrinkage and dissolved gas. Shrinkage is created by the density difference between the liquid and solid states of the metal, as well as improper feeding. It is the primary source of porosity formation in aluminum castings. [77] In Al-Cu cast alloys, shrinkage porosity also occurs on a micro level as microshrinkage or microporosity, which is dispersed in the interdendritic solidification regions, typical of alloys with large solidification ranges. The evolution of dissolved gases (mainly hydrogen) is due to the difference in solubilities of these gases in the solid and liquid phases of the metal [178,79] as shown in Fig. 2.4. Pores may form either prior to, or during solidification. The former are spherical and relatively large, while the latter are small, of irregular shape, and attributed to shrinkage porosity. [72] The amount of porosity in a casting depends on several factors. In order of importance, they might be roughly listed as: solidification rate, gas content, pressure in the casting, metal cleanliness, modification and grain refining. [13] Solidification rate has an overriding influence. Castings that freeze quickly tolerate quite high contents of hydrogen gas. Slowly cooled castings, however, easily form significant amounts of porosity. Gas content is important, especially in such castings. Other things being equal, more gas gives more porosity. Pressure has a

significant effect on the formation of porosity. High pressure can be applied during solidification to reduce porosity. Metal cleanliness has a strong effect on porosity formation. Oxide films nucleate pores. In fact, when the metal is filtered to remove oxides, it is extremely difficult for porosity to form. Strontium modification increases both the size of pores and the amount of porosity. In practice, all these factors interact in a complicated way, to produce the porosity we find in castings. With mechanical degassing facilities and some typical fluxes, it is possible to minimize porosity content. In addition, grain refinement reduces both the amount of porosity and the size of pores.
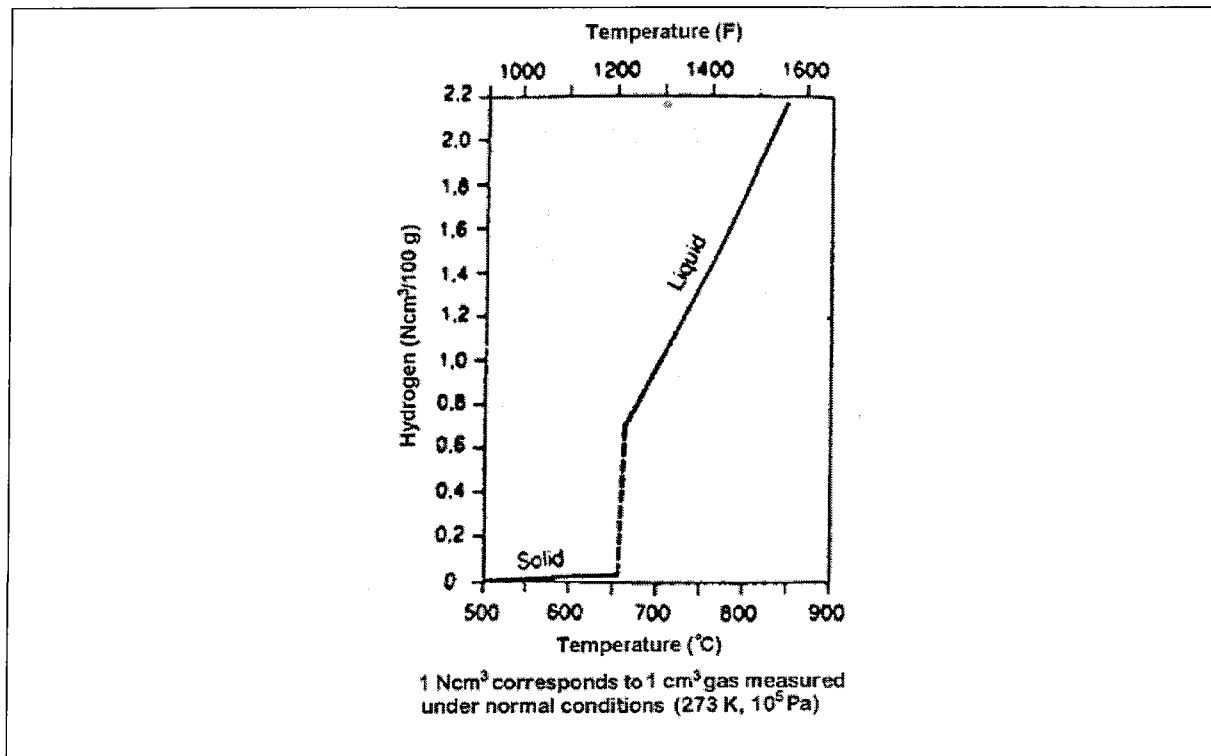
Figure 2. 4: Evolution with temperature of hydrogen solubility in pure aluminum. [78]

2.2.2.1 Effects of alloying elements on porosity formation

Copper is the major alloying element in Al-Cu alloys. In their studies on *micropoposity formation in Al-Cu-Si-Mg casting alloys*, Edwards et al.[80] found that adding copper significantly increases the amount of microporosity, due probably to the effect that copper has on solidification shrinkage and hydrogen gas pressure. Roy et al. [81] observed that copper in Al-Si alloys is present as Al_2Cu or in a complex form. The Al_2Cu phase particles could assist in pore formation in the absence of the needle-like β-Al_5FeSi intermetallic phase. However, they were not effective in the presence of the latter.

Magnesium acts as a hardening element in Al-Si-Cu alloys. Roy et al.[81] reported that its presence reduce percentage porosity without noticeable change in pore size or shape. They observed that the role of magnesium in reducing percentage porosity is more pronounced when the hydrogen content is higher. According to Edwards et al.[80], the effect of magnesium on microporosity formation in Al-Si-Cu casting alloys is not consistent. However, in most of the alloys, magnesium appears to decrease the porosity by amounts ranging from about 0.005% to 0.3%, and this effect is more evident at the riser end of the casting.

Silicon plays an important role in porosity formation. Iwahori et al. [82] studied the process of solidification in Al-Si alloy castings containing various levels of silicon. They found that with increasing silicon content, shrinkage porosity was more likely to occur, but could be controlled by increasing the cross-section area of the riser neck of the casting mould. Also, Chen and Engler [83,84] made a quantitative analysis of the effect of silicon concentration on porosity formation. They reported that silicon affects porosity formation

by changing the solidification mode. As silicon was added to pure aluminum, pore formation was increasingly favoured by the spongy dendritic solidification caused by the increase in silicon content. As the eutectic composition was approached, the tendency for porosity formation decreased, due to the freezing range and resultant lack of a dendritic structure.

2.2.3 Hot tearing of aluminum-copper alloys

Hot tearing is a common and serious defect that occurs during the solidification of liquid metals. This phenomenon, which is also referred to as hot cracking, hot shortness, super solidus cracking, and shrinkage brittleness is deleterious to mechanical properties of aluminum castings and has been the subject of previous investigations. Hot tearing involves the formation of a macroscopic tear in a solidifying casting as a result of stress built up in the solidified metal. This stress arises principally because of the volume contraction (usually 5-8%), associated with the liquid to solid phase change in solidifying metals, but it can be made worse by thermal contractions in the solid and/or by the constraints of the mould. Three approaches have been used towards generating information about hot tearing. These are experimental measurements of hot tearing, modeling of hot tearing, and generation of fundamental properties related to hot tearing such as strength of the mushy zone.

Early studies on hot tearing carried out between 1914 and 1936 clearly show the loss of ductility when an alloy is heated above its solidus temperature, and a liquid phase is

formed. [85-87] In 1946, Singer and Cottrell [88] conducted a more detailed study of the high-temperature tensile properties of Al-Si alloys. Their results are presented in Fig. 2.5 and Fig. 2.6. Figure 2.5 shows the strengths of ten different alloy compositions versus temperature. Each alloy shows a similar behaviour. There is a smooth decrease in tensile strength until the solidus temperature is reached. At this point, the strength drops much more rapidly, to a zero value at a temperature some 5-30 degrees above the solidus. Figure 2.6 shows a detailed view of the test results in the semi-solid region.

By comparing the results presented in Figure 2.5 and Figure 2.6 to the aluminum rich portion of the Al-Si phase diagram in Figure 2.7, it can be seen that reductions in strength and ductility occur at combinations of temperature and composition which place the material inside the region of two-phase (solid plus liquid) equilibrium. The bars drawn in this figure indicate the regions of brittle fracture, measured by Singer and Cottrell. [88] The sharp drop in strength observed in the semi-solid region was accompanied by an almost complete loss in ductility. From these results, one can see that the root cause of hot tearing was firmly established by early researchers.

Forest and Bercovici [89] also made hot tensile tests in several semi-solid commercial alloys, and Wisniewski [90] studied fracture of Al-Cu specimens containing 1-10% liquid. Both studies confirm the earlier results, and show that hot tearing is caused by a loss of strength and ductility, which has also been called liquid metal embrittlement, or a ductile/brittle transformation over the years. Based on the theory that the hot tearing temperature is higher than the solidus of an alloy, the temperature interval for hot tearing has become important and is considered to be significant for hot tearing. [91] This interval
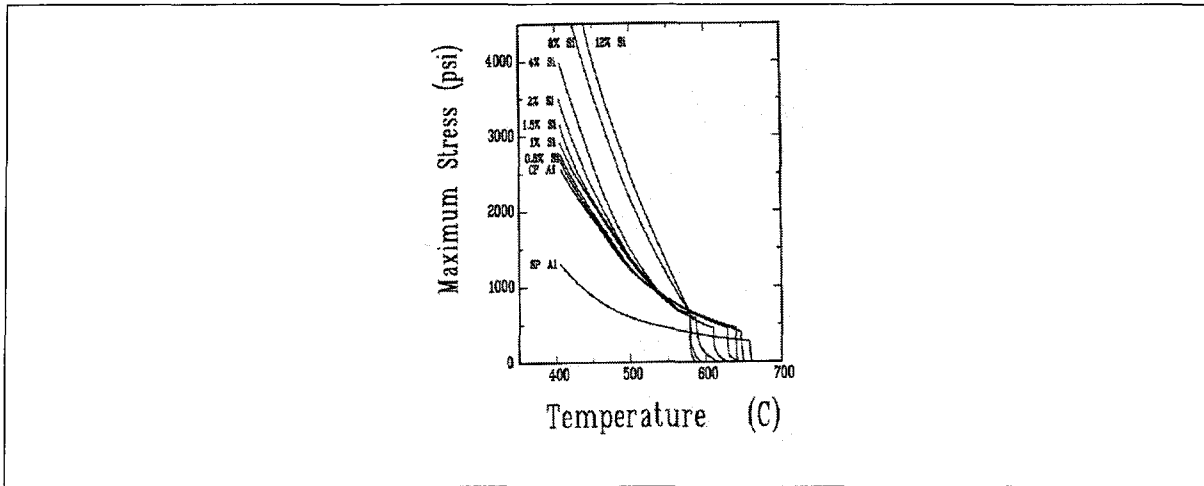
Figure 2. 5: Tensile strength of Al-Si alloys at temperatures in the vicinity of the solidus
(CP and SP are commercial and special pure aluminum). [88]
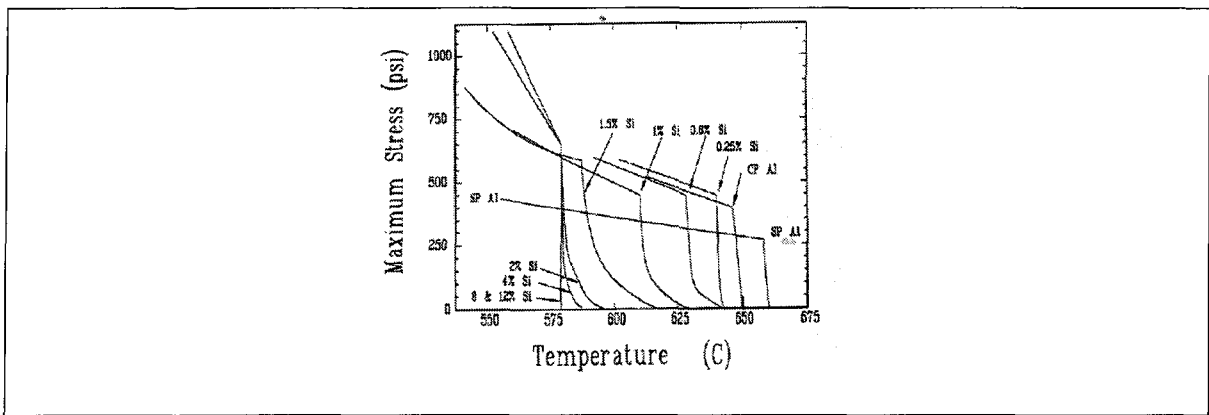
Figure 2. 6: Tensile strength of Al-Si alloys: detailed view of Fig. 2.14. [88]
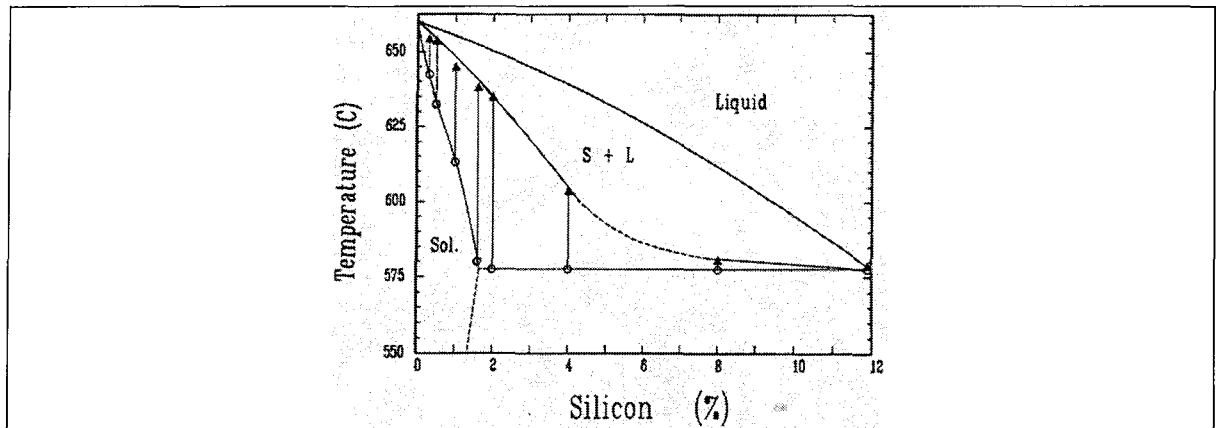
Figure 2. 7: Equilibrium phase diagram of the Al-Si rich portion of the Al-Si system
(bars indicate regions of semi-solid coherency). [88]

has been termed Hot Shortness Temperature Range, Brittleness Stage, or Critical Solidification Range (CSR). [91-93] It is regarded as the temperature range between the solidus and a temperature higher than, but close to, the solidus. [91] In this temperature range, many characteristics of the solidifying metal are different than for other stages of solidification. When an alloy solidifies through its freezing range, the α-Al dendrites will form a dendritic network. The temperature at which the solid crystals form this semi-continuous network is called the coherency temperature. The remaining liquid surrounds the solid dendrites as thin films. In the presence of interlocking dendrites, the feeding of the interdendritic regions and the accommodation of deformation of solid metal are impeded, giving rise to hot tears in the solidifying structure. At this stage, the relative movement of liquid and solid becomes increasingly difficult with increasing solid fraction. Two important phenomena are associated with an alloy cooling through the brittle range: one is 'stress accommodation' and the other is 'healing'. Both accommodation and healing can reduce the amount of hot tearing. Any factor that influences the extent of the brittle range may affect hot tearing susceptibility.

2.2.3.1 Effects of alloy composition

The general effect of composition has long been recognized. [87,88,94] The evidence obtained in these previous investigations indicates that the most important feature of the alloy constitution is the amount of eutectic. Hot tearing tendency is observed to be related to the amount of eutectic liquid present during the later stages of solidification. The presence of only a small amount of eutectic was observed to aggravate hot tearing

tendency. Early researchers suggested that maximum hot tearing occurs when there is less than two or three volume percent eutectic in the alloy. This composition corresponds to the case where thin films of liquid form around solidifying grains, thereby causing the hot shortness or embrittlement responsible for hot tearing. At composition giving more eutectic, hot tearing was believed not to occur, because the liquid films were large enough in volume that they served effectively as liquid channels, which feed any contraction. The limit of the brittle temperature range is a function of the constitution of the alloy. The alloys with a more narrow brittle temperature range show higher resistance to hot tearing. This has been confirmed in Al-Si, Al-Si-Cu and Al-Mg-Si alloys with and without grain refinement. [93] Castability of alloys with 4-6% Cu is very poor; the amount of eutectic, even in nonequilibrium conditions, is insufficient to feed the final shrinkage. Fluidity is also at the minimum and hot shortness at a maximum. [56] Smith *et al.* [95] studied *the influence of Mg, Mn, and Ag on hot tearing of Al-Cu binary alloy*. They found that Mn and Ag increase the hot tearing resistance. Similar effects have been reported for iron, nickel and chromium. [56] Magnesium on the other hand decreases it seriously. This has been attributed to its lengthening of the solidification range. Major and Sigworth [18] have shown that Ti below 0.1% composition improves 206 alloys behaviour with respect to hot tearing.

Results on investigations of hot tearing in aluminum alloys have been reported to be dependent on the type of test used and the casting employed. [3] Differences that occur have been mainly attributed to stress distribution during solidification and to the position of the riser. Warrington and McCartney [96] pointed out that in the ring test, a hoop stress develops perpendicular to the direction in which the solidification occurs; whereas, in a restrained

bar test, the stress is nearly parallel to the solidification front. This difference in stress distribution could seriously affect the experimental results, especially when columnar grains are present in the structure. [96]

2.2.3.2 Effects of dissolved gas and grain refinement

Few studies have been carried out on the effect of gas; but it has been reported that increased gas reduces the tendency towards hot tearing. [97,98] The effect of gas content has been studied using commercial alloy 424 and binary Al-Cu alloys which contain 4%Cu and 6%Cu. [98] Only the 424 alloy was found to have its hot tearing tendency to be evidently affected by the gas content in the melt. The explanation was that hydrogen rejected from solution during solidification sets up an internal pressure sufficient to force liquid eutectic into incipient tears to heal them. The gas bubbles that expand easily can also provide a volume change to compensate for solidification or contraction shrinkage, and reduce the development of stresses that could otherwise result in hot tearing. Some authors, [95-99] however, reported relative insensitivity to gas content. Smith et al.[95] study was carried out under various conditions as melted, degassed, degassed and filtered, degassed and filtered and grain refined. They found that filtering the undegassed melt improved the hot tearing resistance. But degassing, which also removes some inclusions present in the melt, did not change the rating. They concluded that the inclusions have a major effect on hot tearing compared with gas content, and that gas content may not have much effect on hot tearing in small castings if inclusions are not abundant.

Many researchers have studied grain refinement and most report that smaller grains have a beneficial effect on hot tearing. [97,100-103] One study reported that grain refinement has no significant effect. [104] On theoretical grounds, structures with smaller grain sizes can be expected to be more ductile and more resistant to hot tearing. It is well known that grain refinement delay the onset of the dendrite coherency point. [101,102,105,106] This means that the solidifying shell is better fed with liquid, and that it is solid or rigid during less of the solidification process. In many alloys, this means that the solidifying shell contracts less between the onset of dendrite coherency and final solidification, [102] so hot tearing could also be reduced by this mechanism.

2.3 Heat treatment of aluminum-copper alloys

The term heat treating in the aluminum industry is often used to describe the procedures and practices required to achieve maximum strength or hardness in a suitable alloy. Heat treatment modifies the inhomogeneity originating during casting and solidification by controlling diffusion processes and thereby set up a microstructural balance as regards phase segregation and solid solution. According to the required combination of properties therefore, the casting is subjected to one or more heat-treatment steps, alone or in combination, after removal from the mould. The normal sequence involves solution heat treating (SHT), rapid cooling (quenching) and precipitation hardening (aging). The more commonly heat treatments applied to aluminum castings are: [107,108]

- T4: Solution heat-treated, quenched and aged at room temperature (natural aging).

- T5: No solution heat treatment, artificially aged.

- T6: Solution heat-treated, quenched, and artificially aged (peak aging).

- T7: Solution heat-treated, quenched, and stabilized (overaging).

2.3.1 Solution heat treating

The purpose of solution heat treatment is to put the maximum practical amount of hardening solutes such as copper, magnesium, silicon, or zinc into solid solution in the aluminum matrix. Phase diagrams show that the solubility of these elements increases markedly with temperature, especially just below the eutectic melting temperature.

It is well known that the solidification structure of aluminum-copper hypoeutectic alloys exhibits a network of Al-CuAl$_2$ eutectic phase in the α-Al interdendritic regions. This eutectic phase accomplishes a state of homogeneity of the material by dissolving during solution heat treatment, together with some other copper-based and/or magnesium-based phases such as CuMgAl$_2$ and Mg$_2$Si when present. The degree of dissolution is highly dependent on the solidification history of the alloy; slowly-cooled alloys with coarser grains will require sufficient solution time to avoid incomplete dissolution which would contribute to the loss in mechanical properties. [109] Solution heat treating also converts the dendritic structure into a globular one, and promotes a slight coarsening of finer grains and increase in porosity. [109] Magnesium-bearing alloys may require somewhat longer times, since Mg$_2$Si dissolves at a slower rate than CuAl$_2$. [55] Step annealing to dissolve the soluble constituents below the eutectic temperature, followed by higher-temperature treatment to complete homogenization is recommended. Some of the

aluminum-copper casting alloys contain amounts of soluble elements that far exceed solid solubility limits. In these alloys, the phases formed by combination of the excess soluble elements with aluminum such as iron intermetallics will never be dissolved, although the shape of the undissolved particles may be changed by partial solution. [110] Fuchs and Roosz [111] proposed a nomograph for solution heat treatment of Al-Cu alloys (Fig. 2.8). The curves are drawn for a dendrite arm spacing (DAS) of 10 microns (μm), as a function of the solution heat treatment temperature which is given on the left hand scale. The right hand scale shows the solubility limit of copper at that temperature. An example of how to calculate the solution time is shown in the figure for an Al-2.5%Cu alloy, with a DAS of 50μm. For a solution treatment to be carried out at 465°C. A horizontal line is first draw on the figure for this temperature till it intersects the curve for 2.5% Cu, giving a solution time of about 15 minutes for a DAS of 10μm. Thereafter, one continues to the right on this line for a distance 'a', which is taken from the DAS scale at the top of the figure. This gives the solution time for a casting with a DAS of 50μm which is 5 hours in this case.

Solution treatments for 206 alloys are given in the AFS Handbook. [112] For 'rapidly solidified castings', the recommended treatment is given as:

- Hold 2 hours at (493-504°C)

- Increase gradually to (527-532°C) and hold for 8 hrs

- Quench into (66-100°C) water

The purpose of the two-step treatment is to dissolve components which may melt at the higher temperature. If the casting is heated too quickly, melting will occur at the grain

boundaries, and the mechanical properties (strength and elongation) will suffer. For 'slowly solidified' castings a three-step solution treatment is recommended:

- Hold 2 hours at (468-493°C)

- Hold 2 hours at (504-516°C)

- Increase to (527-532°C) and hold there 12 hrs

- Quench into (66-100°C) water
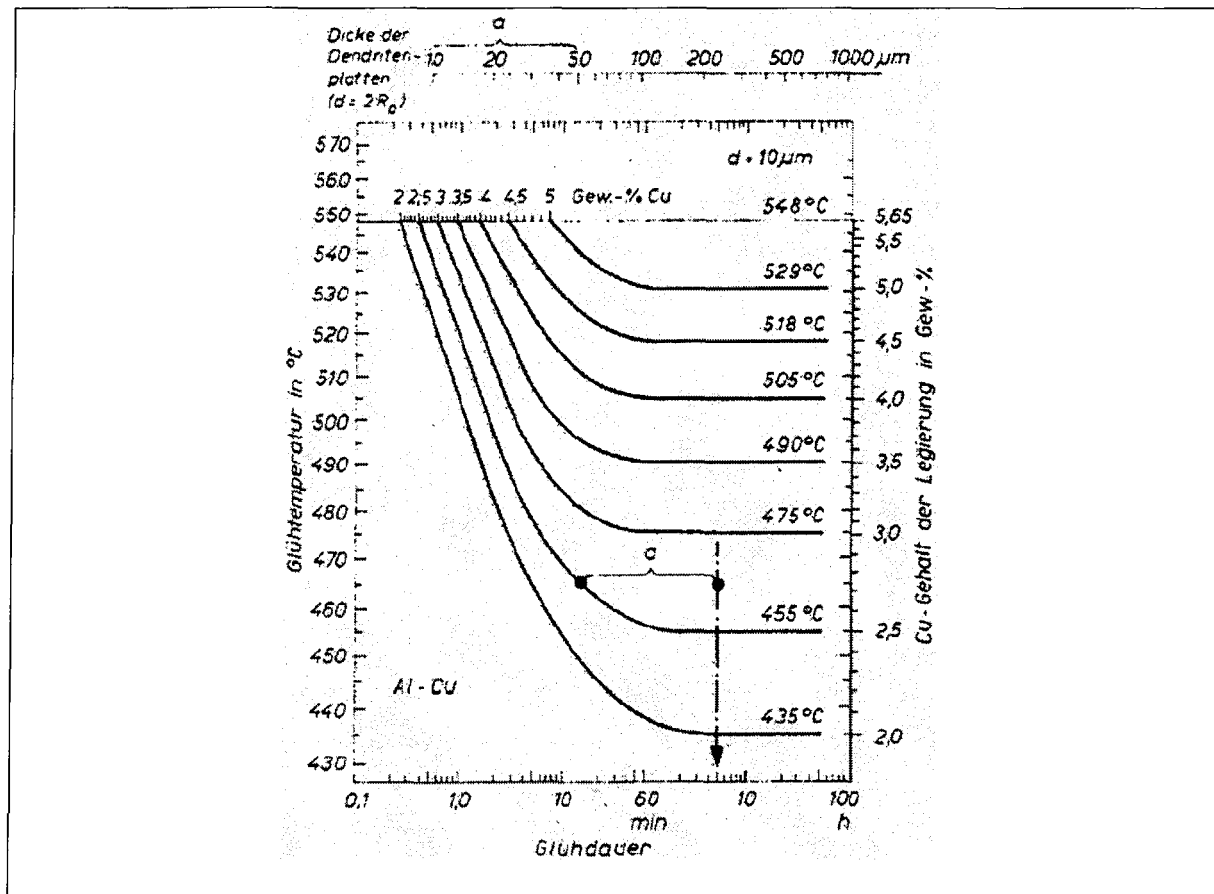
Figure 2. 8: Nomograph to Calculate Solution Times for Al-Cu Alloys. [111]

2.3.2 Quenching

Quenching is in many ways the most critical step in the sequence of heat treating operations. The objective of quenching is to preserve the solid solution formed at the solution heat treating temperature, by rapidly cooling to some lower temperature, usually near room temperature, and also, maintaining a certain minimum number of vacant lattice sites to assist in promoting the low temperature diffusion required for zone formation. [55,110,112-114] Quenching must be rapid enough to produce a supersaturated solution (SSS) at room temperature, and avoid precipitation in the intermediate temperature range. [55] The highest strengths attainable are those associated with the most rapid quenching rates. Resistances to corrosion and to stress-corrosion cracking are other characteristics that are generally improved by maximum rapidity of quenching. [56,110,]

The media used for quenching aluminum alloys include water, brine solution and polymer solution. [115-117] Most frequently, parts used to be quenched by immersion in cold water, however, distortion, cracking, and residual stress problems have been reported. [115,116,118,119] Although it is difficult to find published work on quenching sensitivity of aluminum-copper alloys, it has been reported that the water temperature affects the properties of the cast aluminum alloy A356 subjected to T6 heat treatment once the water exceeds 60-70°C, with tensile strength and yield strength being significantly more sensitive than ductility. [120]

2.3.3 Age hardening

Age-hardening has been recognized as one of the most important methods for strengthening aluminum alloys, which involves strengthening the alloys by coherent precipitates which are capable of being sheared by dislocations. [121] By controlling the aging time and temperature, a wide variety of mechanical properties may be obtained; tensile strengths can be increased, residual stresses can be reduced, and the microstructure can be stabilized. After solution treatment and quenching, the precipitation process can occur either at room temperature (natural aging) or may be accelerated by artificial aging at temperatures ranging from 90° to 260°C. It was indicated that aging must be accomplished below a metastable miscibility gap called the Guinier-Preston (GP) zone solvus line. [122] For 206 alloys, it is recommended to wait 12-24 hours after quenching before aging. [112]

The phenomenon of precipitation was originally discovered by Ardel in 1906. [123] He found that the hardness of aluminum alloys which contained magnesium, copper, and other trace elements increased with time at room temperature, which was later explained by precipitation hardening. Over the years, much research was carried out to understand natural and artificial aging kinetics and to study the effects of underaging, peak-aging, and overaging on hardness, [7] tensile strength, [7,109,124,125] elongation, [7] and fatigue behaviour of aluminum-copper alloys. [126] The generally accepted precipitation sequence in Al-Cu alloys is supersaturated solid solution, Guinier-Preston (GP) zones, θ'', θ', and finally the formation of the stable θ phase. [127,128] The first metastable phase to form is the fully coherent GP zone, so named after their discoverers.[129,130] These zones are clusters of copper atoms that are plate-like in shape, and form on the {100} planes of the aluminum matrix.

They consist of sheets of copper atoms up to 150Å in diameter and only one or two atom layers thick.[131] Immediately after quenching from the solutionizing temperature, the GP zones begin to nucleate at a very high rate, with the rate decreasing with elapsed time. The rapid formation of GP zones after quenching is attributed to the "quenching-in" of excess vacancies,[131,132] which facilitates the formation of the zones. The zones grow in such a manner as to minimize the rate of increase in strain energy of the precipitate and matrix.[133] The second intermediate phase θ'' (also referred to as GP II), is still coherent with the matrix, still resides on the {100} habit planes of the matrix, and is tetragonal in structure. This phase is a larger version of the GP zones and maintains the same chemical composition, hence the common reference to the phase as GP II. The maximum thickness of these platelets have been observed to be on the order of 100Å with a diameter of 1500Å.[134] The discrepancy in naming also arises from the fact that the phase has a definite tetragonal structure, which is argued to be more structured than a zone and as such should be termed a precipitate and have a distinct name. Byrne et al.[135] measured the separation between the centers of the zones to be less than 150Å for GP zones and less than 300Å for θ''. As the aging process continues, the final metastable precipitate to form is θ'. This precipitate is also tetragonal in structure but has a composition of $CuAl_2$. These precipitates are preferentially and heterogeneously nucleated on dislocations.[127,136,137] The preference to nucleate on dislocations is because of the low interface energy, high elastic-strain energy of the precipitates, and the benefit of nucleating on dislocations in lowering the elastic-strain energy.[138] The nucleation of θ' is independent of the GP zones and θ'' in that neither of these precipitates are necessary precursors to θ'. These precipitates are semi-coherent

with respect to the aluminum matrix as the broad faces of the precipitates are coherent with the matrix and the faces perpendicular to the habit plane are incoherent, with the misfit accommodated at the precipitate-matrix interface by dislocations that loop around the precipitates. After an extended period of aging, the broad faces of the θ' precipitates also begin to lose coherency and dislocations accommodate this misfit at the interface. The accommodation and coherency loss of θ' has been studied by a number of researchers. [139-147] In addition, the θ' precipitates also coarsen with increased aging due to the driving force of surface reduction area. The lengthening and thickening kinetics of the θ' plates have also been studied.[148-150] The final and equilibrium precipitate, θ, is body-centered tetragonal in crystal structure and is primarily incoherent with the matrix. Some coherency is left unless the precipitates are extremely large. The precipitates possess no single orientation relationship with the matrix and are no longer plate-like in shape. The θ precipitates can be nucleated directly from the supersaturated solution if the aging temperature is high enough (*i.e.*, >300°C) or even at lower temperatures if the kinetics and thermodynamic conditions in the material are favorable. However, at lower temperatures, if the general precipitation sequence is followed, the θ precipitates will generally nucleate at planar boundaries, such as grain boundaries and at the interface of θ' with the matrix.[127,151] In general, θ nucleates on high-angle grain boundaries (>9 deg.) because of its high surface energy, as the boundaries also have appreciable surface energy and can aid in lowering that of θ.[138] Laird and Aaronson [152] studied the formation of θ and observed the following three simultaneous reactions upon nucleation of θ: (1) θ consumes the θ' plate at which it nucleates, (2) regions of the matrix surrounding the θ precipitates simultaneously

transform to θ, and (3) θ' plates in the vicinity of growing θ precipitates are dissolved. With extensive aging, the final microstructure will contain only θ precipitates that will continue to coarsen and will eventually become ineffective barriers to dislocation motion as their interparticle spacing becomes larger than the dislocation slip length. [153]

The dislocation-precipitate interactions dictate the mechanical behaviour of aluminum-copper alloys. The presence of precipitates in the aluminum matrix affects not only the critical shear stress required to initiate slip, but also the hardening behaviour of the material. The degree to which these behaviours are affected depends upon the aging treatment used, which is directly responsible for the different precipitates.

The precipitation hardening that results from natural aging alone produces a useful temper (T4 type) that is characterized by a high ratio of tensile to yield strength, high fracture toughness, and high resistance to fatigue.[107] No discernable microstructural changes accompany the room-temperature aging, since the hardening effects are attributable solely to the formation of zone structures within the solid solution.[110] The relatively high supersaturation of atoms and vacancies retained by rapid quenching causes rapid formation of GP zones, and strength increases rapidly, attaining nearly maximum stable values in four to five days. The changes that occur on further natural aging are of relatively minor magnitude, and products are regarded as essentially stable after about one week. This is illustrated in Fig. 2.9 for 206 aluminum alloys. Precipitation heat-treatment following solution heat-treatment and quenching produces T6 and T7-type tempers. A characteristic feature of elevated-temperature aging effects on tensile properties is that the increased in yield strength is more than the increase in tensile strength. Also ductility, as

measured by percentage elongation, decreases. Thus, an alloy in the T6-tempered condition has higher strength but lower ductility than the same alloy in the T4-tempered condition. [110] Overaging decreases both the tensile and yield strengths, but ductility generally is not recovered in proportion to the reduction in strengths, so that combinations of these properties developed by overaging are considered inferior to those prevalent in the T6-tempered or underaged condition. Other factors, however, may greatly favour the use of a temper that produces overaging. In certain applications, for example, strength factors are outweighed as criteria selection by the resistance to stress corrosion cracking, which improves markedly with overaging, or by the greater dimensional stability for elevated-temperature service that is provided by overaging. [55,56,107,110] Precipitation heat treating temperatures used to produce overaging (T7-type tempers) generally are higher than those
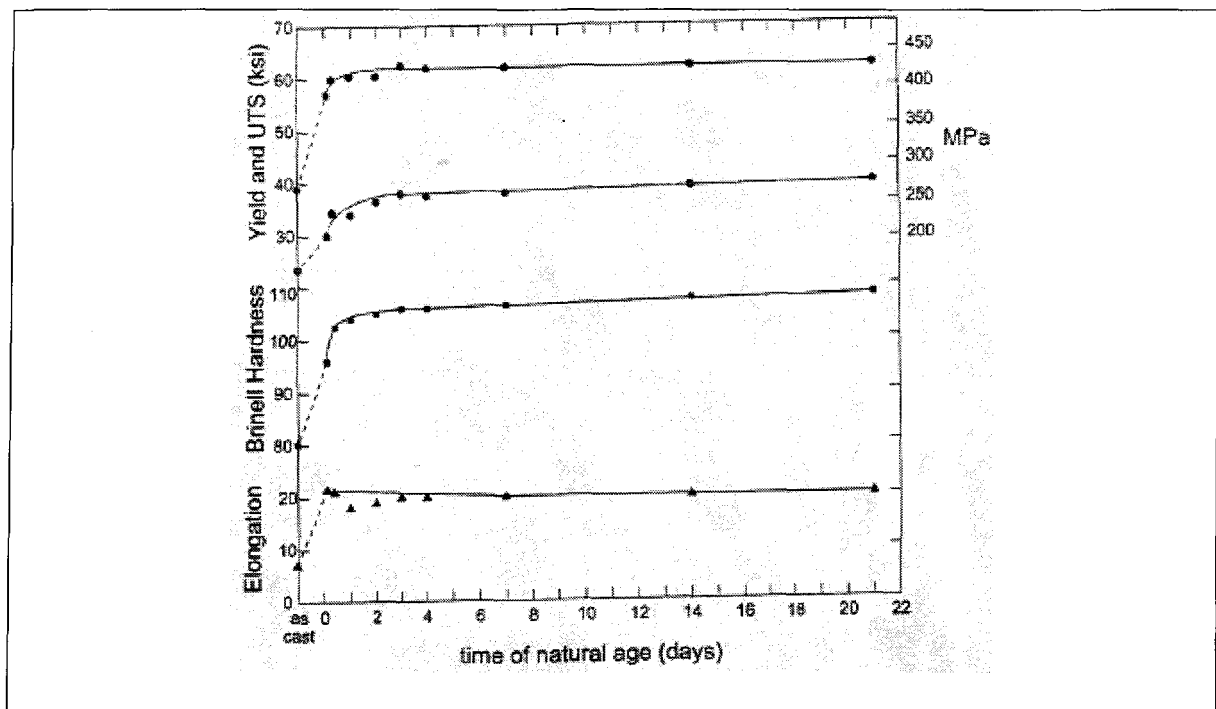
Figure 2. 9: Mechanical properties of 206 alloys during natural ageing. [7]

used to produce T6-type tempers in the same alloys. Best ductility and impact resistance are achieved by natural aging, which also produces good corrosion resistance. [56] The highest combination of strength and ductility is obtained by T6-type tempers, but this produces susceptibility to intergranular corrosion and stress corrosion cracking. High strength and hardness with good corrosion resistance are obtained with T7-type tempers. [56] In magnesium-free commercial alloys the age hardening is basically the same as in the pure aluminum-copper alloys, except that iron, manganese and silicon tend to reduce the hardening rate at the early stages, so that the commercial alloys show only limited hardening with natural aging.[56] In durals and aluminum-copper-nickel alloys the aging characteristics depend on the Mg:Si ratio. At high ratios, $CuMgAl_2$ produces substantial hardening by aging at room temperature. In alloys in which the ratio is close to 1.7, $CuAl_2$ and, to a more limited extent, Mg_2Si produce hardening; age hardening at room temperature is limited and artificial aging is necessary for best strength. At lower ratios, $Cu_2Mg_8Si_6Al_5$ together with $CuAl_2$ and, in the absence of magnesium, $CuAl_2$ alone are the hardening constituents, and these alloys, too, require artificial aging for best properties. [56]

For 206 alloys as a member of the Al-Cu family, the T6-temper should be avoided where stress-corrosion cracking could be a problem. [13,107] It has also been reported that T5 temper greatly reduces the tensile ductility and tensile strength, with no effect on the yield stress. [13] This is why the T5 temper is not employed commercially for this alloy. Consequently, T4 and T7 are recommended for aging. Temperatures and times for T7 are 185-190°C for 5 hours or 200°C for 4 hours. [107,112]

2.4 Effects of alloying elements on mechanical properties of aluminum-copper alloys

Mechanical properties describe the behaviour of a material subjected to mechanical forces, and are determined under conditions designed to simulate loading in service. Loads (forces) may be of many kinds (static, cyclic or dynamic), with different intensities and directions (tension, compression, torsion); accordingly, there are many tests designed with the specific aim of determining the maximum load bearing capacity of the material after which failure occurs. Mechanical properties of all materials are a function of temperature. Tests results are affected by the test method itself; therefore, tests must be conducted in conformance to standards. In many applications, the load is static, *i.e.*, constant and stationary, and several tests are conducted at such low speeds that the application of force can be regarded as static.[154] Commonly used testing includes tension testing, compression testing, torsion testing, bending tests, hardness tests, impact testing and fatigue testing. These tests are well documented in most Materials Engineering books and handbooks.

Aluminum-copper alloys are well known to be distinguished among other aluminum foundry alloys by excellent strength and toughness, which are obtained by natural or age-hardening. The best combination of strength and ductility is obtained when the copper content is close to the maximum solubility limit (5% Cu in commercial practice) and the material is heat treated so that the copper is distributed in the GP zones. Lower copper contents, unless compensated by magnesium, produce lower strength and better ductility. Copper higher than 5-6% somewhat increases the strength, but reduces the ductility substantially. Impact resistance, notch toughness and fatigue resistance are decreased by

the presence of a brittle network of eutectics (mostly Al-CuAl$_2$). Strength at high temperature and resistance to creep and wear, on the other hand, increase with increasing copper content.[56]

Silicon increases the strength in cast Al-Cu alloys, mainly by increasing the castability and thus the soundness of the castings, but with some loss of ductility and fatigue resistance, especially when it changes the iron-bearing compounds from Fe$_2$SiAl$_8$ or Cu$_2$FeAl$_7$ to FeSiAl$_5$.[56] In magnesium-bearing alloys silicon has some direct strengthening effect, but its main effect is indirect since the Mg:Si ratio controls the age hardening. Silicon reduces high-temperature strength and creep resistance, especially when they result from the magnesium content. Dreyer and Hansen [155] studied *the influence of Mg, Si, Mn, and Fe on the properties of the alloy Duralumin Cu 30*. From their results, it is readily seen that Si has virtually no effect on the room temperature aging process, or on the hardness of the alloy. It results in a slight decrease in ductility. Higher Si contents lower the yield stress by 5-10%, especially at low solution temperatures. The reason for this is not obvious, but it is probable that Mg$_2$Si formation robs the solid solution of dissolved Mg.

Magnesium increases the strength and hardness of Al-Cu alloys, especially in castings, with a decided decrease in ductility and impact resistance. It has been reported that in normal amounts (Mg < 2%), magnesium imparts room temperature aging and the amount and rate are controlled by the Mg:Si ratios: with high ratios the best strength and ductility are obtained by natural aging; with low ratios artificial aging is necessary for optimum properties.[56] Strength at high temperature and creep resistance are also improved by a high magnesium level, especially if the silicon content is low. [56] Entwistle *et al.* [156] studied *the*

effect of vacancy/impurity interaction on the rate of quench-age-hardening in Al-Cu alloys.
Their results shows that the presence of 0.3-0.4% Mg in Al-4%Cu alloys eliminates the
problem of quench sensitivity. It also strengthens the material, increasing the hardness (and
the yield strength) by 10-15%. It is most beneficial, therefore, to have Mg in Al-Cu casting
alloys. But, as shown in Figure 2.10, adding Mg lowers the solubility of Cu. It also lowers
the melting point of the eutectic phase, as mentioned earlier. Thus, large Mg additions
could be expected to worsen the hot-cracking sensitivity of the alloy. It may also make the
solution treatment more difficult, perhaps calling for a slower heat-up period, or a three-
step heat treatment cycle.

Iron has some beneficial strengthening effect, especially at high temperature and at
lower content (< 0.7%).[56] However these benefits are outweighed by the embrittling effect
of the iron-bearing compounds and the reduction of soluble copper that results from their
formation. In their studies, Dreyer and Hansen [155] reported that, Fe behaves similarly to Si.
Iron decreases the yield strength slightly, presumably by taking copper out of solution
through formation of the compound Cu_2FeAl_7. Also, Tseng et al. [19] studied *the effects of
iron content on microstructure and mechanical properties of A206 alloy.* They concluded
that samples heat-treated in the T7 condition exhibited a decrease in elongation and a linear
decrease in tensile strength with increasing iron content.

Manganese has been reported to have some strengthening effect, partly because of its
solubility, and partly because it reduces the embrittling effect of iron and reduces grain
growth.[56] But when the iron plus manganese is too high, the primary crystals reduce
ductility and especially fatigue resistance. [20,56] High-temperature strength is little affected
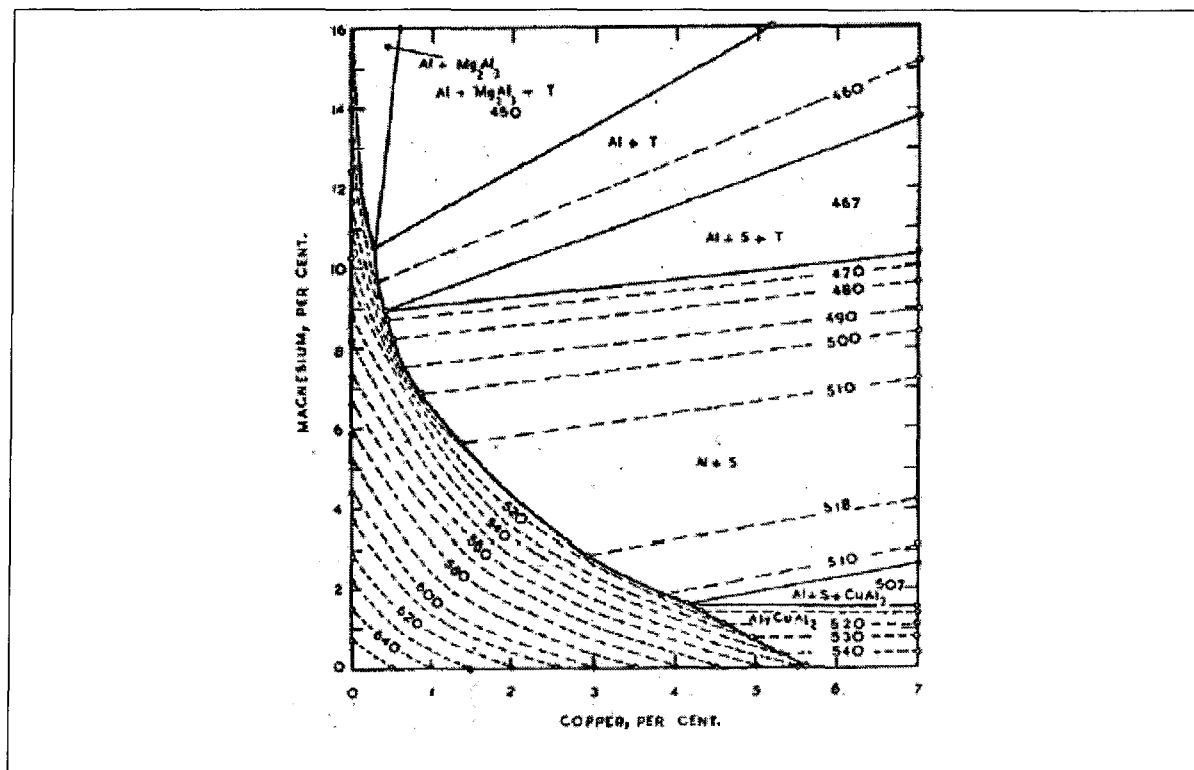
Figure 2. 10: Solidus and Solid Solubility of Cu and Mg in the Al-Cu-Mg System. [157]

by manganese; creep is reduced. Manganese affects the mechanical properties also because it has some influence on aging rates and tends to reduce stress corrosion susceptibility. [56] In the investigations of Dreyer and Hansen, [155] it was found that Mn strengthens the alloy, but does not otherwise change the room temperature aging process. In the same study, it was found at 480 and 500°C solution temperatures, and at Mn contents greater than about 0.5%, the elongation began to decrease. Consequently, the composition limits for AA206 (0.2-0.5% Mn) appear to be well advised.

Nickel has a strengthening effect similar to that of manganese, although more limited, because it only acts to reduce the embrittling effect of iron. Manganese and nickel together decrease the room-temperature properties because they combine to form aluminum-

manganese-nickel compounds and reduce the beneficial effects of each other. The effect of nickel is the increase in high-temperature strength, fatigue and creep resistance. In alloys that depend on copper for age hardening, nickel additions, by removing some of the copper in form of aluminum-copper-nickel compounds, may reduce strength.[56]

Titanium is added as a grain refiner and is very effective in reducing the grain size. If this results in a better dispersion of insoluble constituents, porosity and nonmetallic inclusions, a decided improvement in mechanical properties results. Also, it tends to reduce stress corrosion susceptibility.[56] But it has also been proved that Ti below 0.1% composition improves 206 alloy behaviour with respect to hot tearing.[7]

Zinc increases the strength but reduces ductility. At lower temperature and lower content the effect is not too pronounced. At higher temperatures zinc reduces the strength and creep resistance appreciably. [56]

Changes in the chemical composition and/or heat treatment aiming to improve strength or other properties can render the material too brittle for structural applications. It is thus important to assess simultaneously what effect on material ductility and strength any changes to the microstructure would have. Therefore, castings are evaluated using strength-ductility diagrams known as quality index charts. [158,159]

2.5 Quality Index of Aluminum-Copper alloys

Data from tension tests can be used to characterized hardness and fatigue behaviour of the material; therefore, properties are routinely checked via tensile testing, following ASTM Standard E8 specifications. [160]

2.5.1 Tensile testing

In tensile testing, a specimen is subjected to a continually increasing uniaxial tensile force while simultaneous observations are made of the elongation of the specimen. An engineering stress-strain curve is constructed from the load-elongation measurements. The process is illustrated in Fig. 2.11. The shape and magnitude of the curve for a metal will depend on its composition, heat treatment, strain rate, temperature, and state of stress imposed during the testing; the first two parameters have been successfully applied to B206 alloys within the allowable range of alloy elements and impurities.[20,161] Quantitative measurements obtained from a stress – strain curve that are of particular interest in the estimation of the quality of a material include tensile strength, yield strength or yield point, and elongation to fracture. The first two are strength parameters and the last one indicates ductility. The plot shown in Fig. 2.11(a) is divided into two distinct regions: (1) elastic deformation and (2) plastic deformation. Elastic deformation is a temporary deformation, which means the specimen can fully recover its initial state when the load is removed (Fig. 2.11b). In this region, the stress is linearly proportional to strain and Hooke's law is obeyed:

$$(P/e) = E = \text{constant} \qquad (2.1)$$

where P is the engineering strength,

  e is the engineering strain, and

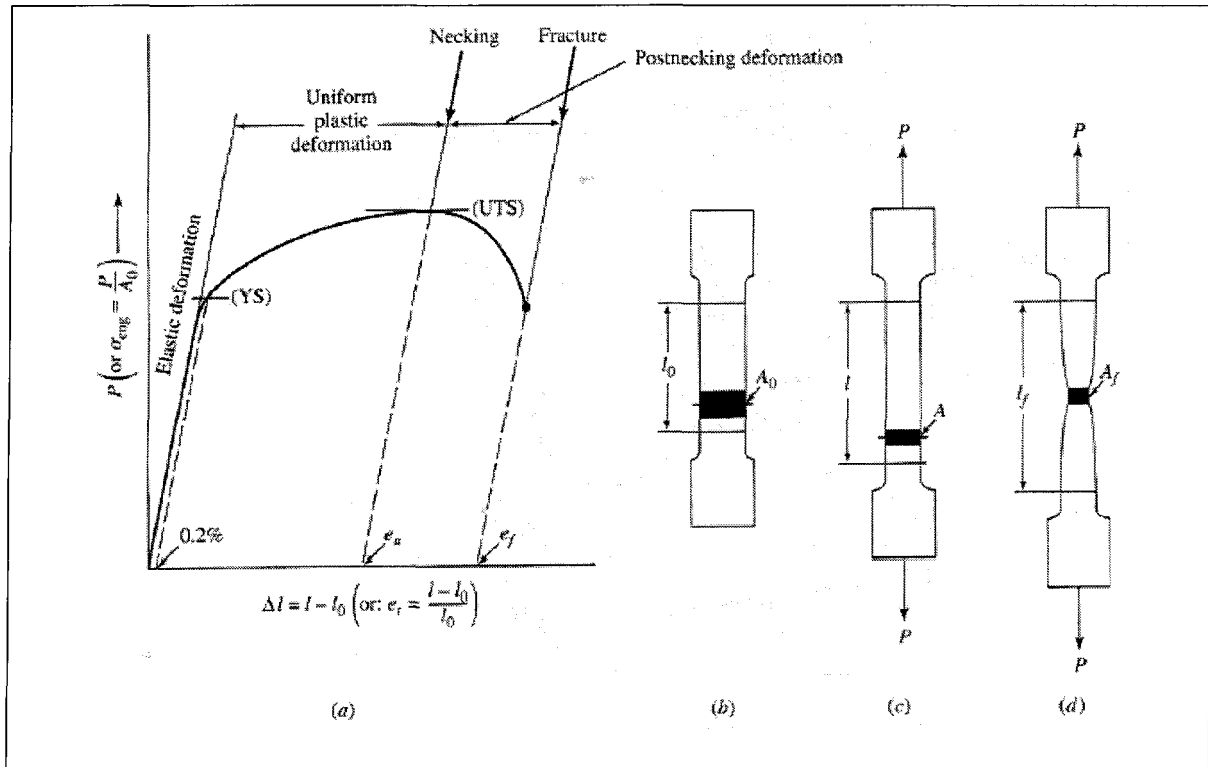 E is the modulus of elasticity or Young's modulus.

Figure 2. 11: (a) The force-displacement (or engineering stress-strain) curve obtained on tensile testing a ductile material reflects the sequence of events:
(b) a specimen of A_0 initial cross section first suffers elastic deformation, then
(c) deforms plastically more or less uniformly within the gage length and
(d) subsequently necks and finally fractures. [154]

The modulus of elasticity is a measure of the stiffness of the material. It is determined by the binding forces between atoms.[161] Since these forces can not be changed without changing the basic nature of the material, it follows that the modulus of elasticity is one of the most structure-insensitive of mechanical properties. It is only slightly affected by alloying additions and heat treatment.[161,162] The stress corresponding to the elastic limit, i.e., the stress after which permanent deformation occurs is called the yield stress (YS) and the corresponding strain is called the yield point strain (e_y). In several fcc metals, such as copper and aluminum, the yield point is not well defined. The operational definition of yield strength for such materials is given by the stress corresponding to a plastic strain of

0.2%. This value is known as the 0.2% offset yield strength or proof stress. When the load exceeds a value corresponding to the yield strength, the specimen undergoes gross plastic deformation. It is permanently deformed if the load is released to zero. The stress to produce continued plastic deformation increases with increasing plastic strain, *i.e.*, the metal strain hardens. The highest engineering stress reached during the test is called the ultimate tensile strength (UTS), or simply the tensile strength. The corresponding strain is called the uniform strain (e_u), because up to this point the strain is uniformly distributed throughout the gage section as shown in Fig. 2.11c. After this point, necking, defined as strain localization within a small region of the specimen, occurs (Fig. 2.11d). Subsequent to initiation of necking, strain accumulation is limited to the region of the neck and is non-uniform. The engineering strain at fracture, e_f, is usually reported as the percentage elongation at break (*i.e.*, $e_f \times 100$). This quantity is also referred to as the ductility of the sample. When reporting the percentage elongation of a material, it is customary to specify the initial gage length of the specimen, since the value e_f depends on the length-to-diameter ratio for the sample. The higher this ratio, the lower the engineering strain to fracture.[163] Percent reduction in area (%RA) is also commonly reported, and has the advantage of being independent of the length-to-diameter ratio. It is calculated as:

$$\%RA = ((A_0 - A_f)/A_0) \times 100 \qquad (2.2)$$

where A_0 is the original cross-sectional area and A_f is the final area of the necked region. Engineering stress and strain are based on original specimen dimensions and do not take into account the fact that sample dimensions change during a tensile test. The

corresponding quantities that reflect changing sample dimensions are known as true stress (σ) and true strain (ε).

$$\sigma = P\,(e + 1) \tag{2.3}$$

and $\varepsilon = \ln\,(e + 1)$ (2.4)

2.5.2 Casting quality

Casting quality is commonly defined based on the findings of the French scientists Drouzy, Jacob, and Richard.[158,159] These authors studied the effects of casting conditions, metal composition, and aging time and temperature on the mechanical properties of Al-Si-Mg (356 type) alloys. As they analyzed the aging process, they noticed that for a given 'quality' of casting, as determined by the freezing rate (DAS), porosity, and iron content, the T6 aging process produced tensile properties that followed a straight line on a certain type of plot. This result is shown in Figure 2.12 for an Al-7%Si-Mg alloy. The lines of constant "Q" are called the quality index, and are said to represent the quality of the alloy. They were found to depend on the soundness of the casting, i.e., on the solidification conditions, and less affected by the heat treatment of the alloy. Inversely, lines "E" of probable yield strength were found to depend on the degree of hardening, i.e. tempering treatment (magnesium content, tempering time and temperature) and less affected by the solidification conditions. In its most straightforward application, the Q-values allow for comparison between different alloys, or between batches of samples of the same alloy. Using this quality chart to plot the experimentally-determined tensile strength and tensile ductility for a particular alloy, the material of the best quality will be located near the upper

right-hand corner, an indication that the material has both high UTS and high ductility, $i.e$ its mechanical quality is high. The formula developed empirically by Drouzy, Jacob, and Richard [158,159] to calculate the quality index Q and the probable yield strength lines YS for aluminum casting alloys is:

$$Q = UTS + d \log (E_f) \tag{2.5}$$

$$YS = a*UTS - b*\log (E_f) + c \tag{2.6}$$

where Q and UTS are in MPa, and E_f ($\geq$ 1%) is the elongation to fracture in a tensile test. YS is the 0.2% offset yield strength. The constants a, b, c and d depend on the material. For the Al-7%Si-Mg alloys used in their studies, d = 150.

From Eq. (2.5), the quality index can be numerically defined as the tensile strength of a specimen which by a hypothetical heat treatment would strain by 1% at rupture. Drouzy, Jacob, and Richard [164] also found a correlation between yield strength and Brinell hardness which they proposed might be applied satisfactorily to all aluminum castings. This correlation is expressed as:

$$YS = 3 HB - 80 \quad \text{(YS in MPa, hardness in Brinell units)} \tag{2.7}$$

The original quality index chart was developed for alloy A356 and thus its use for other materials conveys the implicit assumption that the parameters involved, particularly the slope, d, of the iso-Q lines in Eq.(2.5), do not depend on the material. Drouzy et $al.$[158] included an explicit warning in this regard in their original publication, and in fact, it has been shown experimentally that the slope and position of the iso-Q lines in the quality index chart change with both the chemical composition and temper in some alloys.[165-167] Din et $al.$[165] pointed out that the quality index of Cu-containing casting alloys is greatly

affected by the temper. In contrast with the behaviour observed in alloy A356, for which the Q-value is largely independent of the aging as shown in Fig. 2.12, the Q-value for the copper-containing alloys followed a semicircular path as the alloy was first solution heat treated and progressively aged. This behaviour is illustrated in Fig. 2.13. The loss of quality with overaging was later ascribed by Caceres et al.[166] to the differences in precipitation hardening mechanisms occurring during each temper. Gauthier et al.[167] also observed a circular pattern in the strength-ductility relationship in Al-Si-Cu-Mg alloy 319.2 after aging at different temperatures. This observation suggests that the circular pattern in the quality index as the material is aged may be a characteristic of Cu-containing Al alloys.
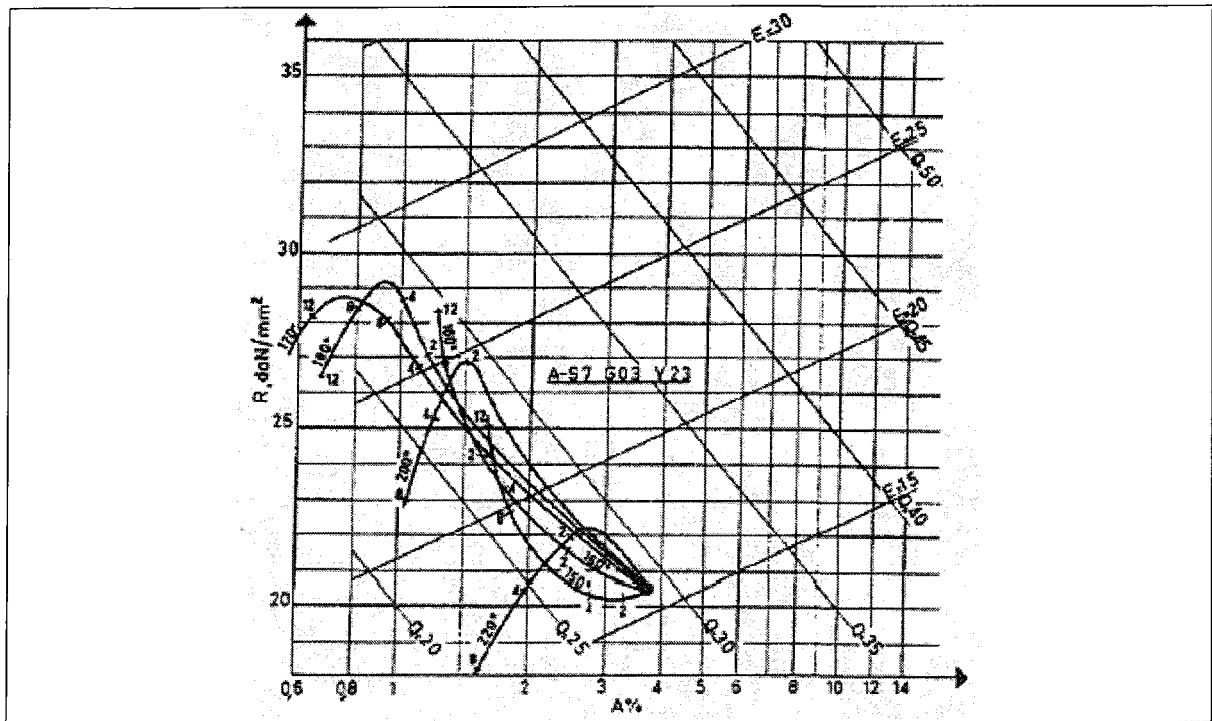

Figure 2. 12: Plot of mechanical properties and quality index of an Al-Si-Mg alloy.
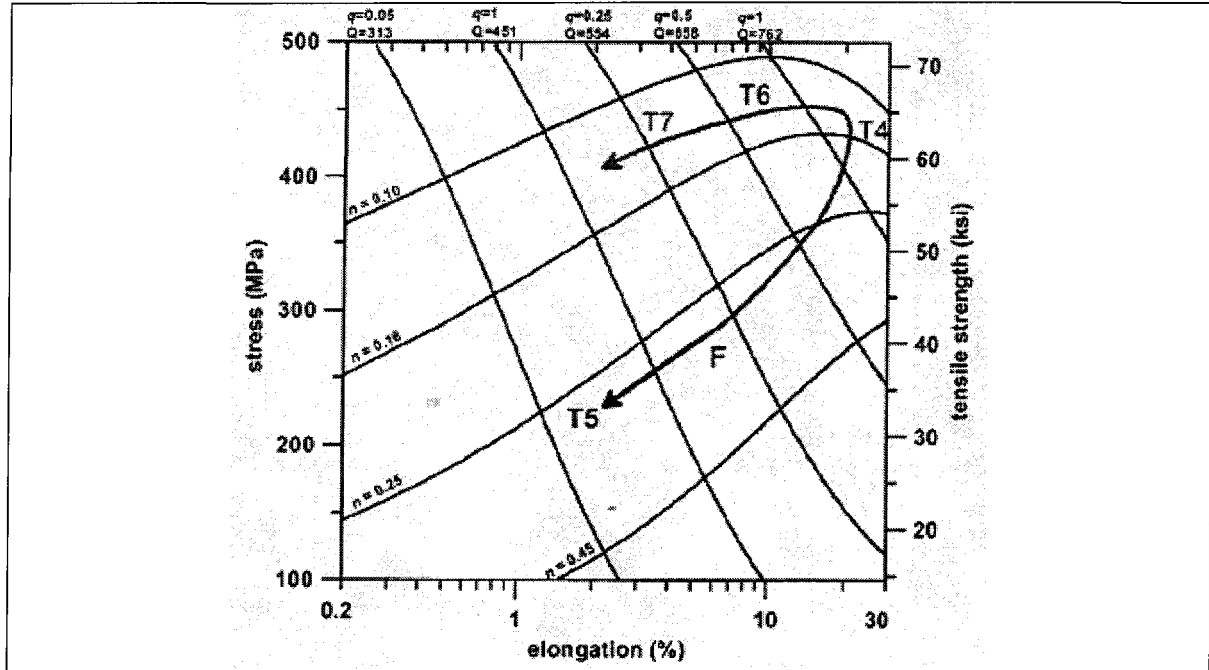(Aging times and temperatures are indicated on the curves). [159]

Figure 2. 13: Change in Q-index of B206 alloy. [13]

Caceres tried to use Eq.(2.5) but found that it did not work in other alloy systems.[168,169] He

then developed a theoretical framework for casting quality in each alloy system. He began

with the equation:

$$\sigma = K\varepsilon^n \tag{2.8}$$

which relates the true stress σ and true strain ε observed during a tensile test. K is the

strength coefficient and n is the strain hardening coefficient:

$$n = \frac{\varepsilon}{\sigma}\frac{d\sigma}{d\varepsilon} \tag{2.9}$$

Eq.(2.8) represents the flow curves quite well. A single value of K is used, and n is varied

to represent different heat treatments. In the casting having the highest ductility, tensile

failure involves necking. Necking will occur when the Considère criterion is met, or when

$$\frac{1}{\sigma}\frac{d\sigma}{d\varepsilon} = 1 \qquad\qquad (2.10)$$

Comparing Eqs.(2.9) and (2.10), it is obvious that necking will occur when $\varepsilon = n$. In other words, the strain hardening coefficient also determines the maximum uniform strain possible in the tensile sample.

The condition where $\varepsilon = n$ represents the maximum ductility, or the best quality possible, in a cast material. Samples failing earlier have a lower quality. Caceres consequently defined a relative quality factor q, by the relationship:

$$q = \frac{S_f}{n} \qquad\qquad (2.11)$$

where S_f is the nominal strain at which failure occurs in a particular alloy casting.

He further ignored the difference between nominal and true strain on the basis of the limited tensile ductility of casting alloys (usually less than 15%), and expressed the stress at any level of relative quality (q) by the equation:

$$P = K\, s^{s/q}\, e^{-s} \qquad\qquad (2.12)$$

where P represents the nominal stress.

Eq. (2.12) was used to generate the curves shown in Fig. 2.14, assuming K = 430 MPa.

The author also showed that the constant (d) on the right hand side of Eq.(2.5) is generally equal to about 0.4K, meaning that the maximum possible quality for a material (when q = 1) can be approximated by: [169]

$$Q = 1.12\, K \qquad\qquad (2.13)$$

According to this theory, the quality index in B206 alloy is given by the relationship:[20]
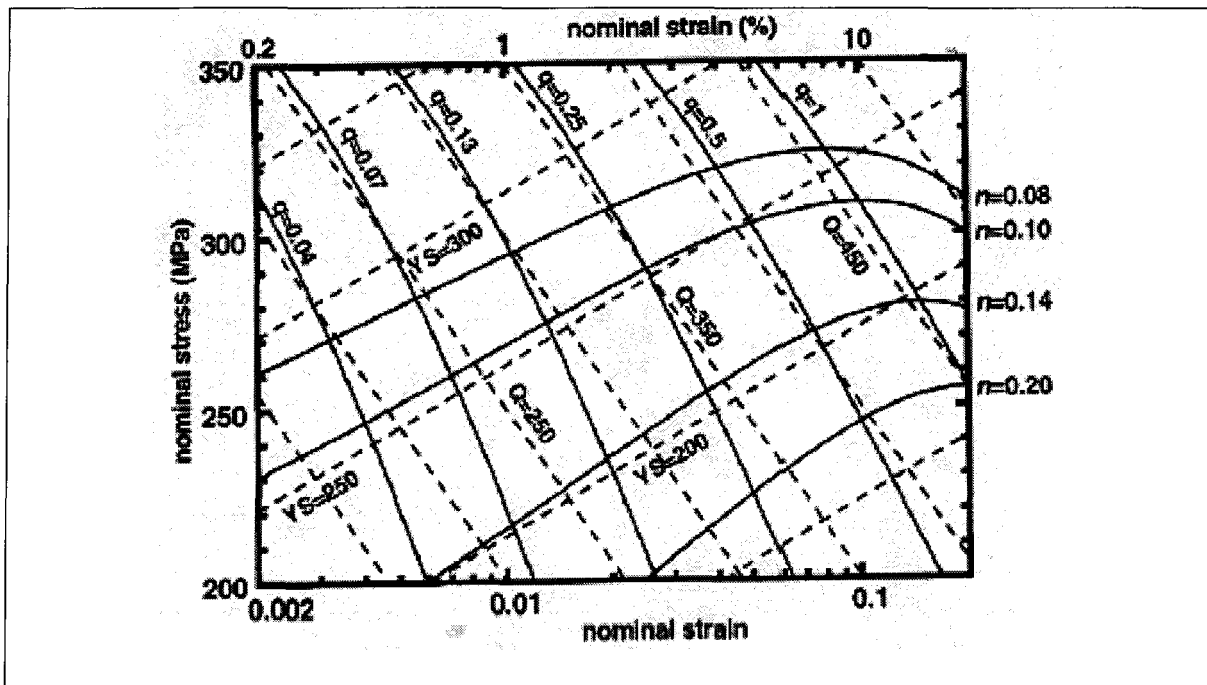
$$Q = UTS + 270 \log E_f \qquad\qquad (2.14)$$

Figure 2. 14: A quality index chart for alloy A356.
The dashed lines represent the quality index chart as determined by Drouzy *et al.*[158] The solid lines are flow curves (identified by n-value), and iso-q lines (identified by the q-value). [169]

The correlation between iso-q lines and iso-Q lines shown by Fig. 2.14 provides a straightforward physical meaning for the quality index in terms of the relative ductility parameter. This theoretical approach to quality is important, because it allows a casting user to establish unambiguously the absolute quality of a casting, and whether further improvements are possible. It is necessary only to measure the full true stress-true strain curve of a tensile specimen, so the constants K and n may be determined. If the elongation to fracture is approximately equal to n; which means that $q \approx 1$; or the quality index, $Q \approx 1.12$ K, then it would not be possible to obtain better results for the alloy used. On the other hand, if $q < 1$ and $Q < 1.12$ K, it is possible to obtain higher mechanical properties in the casting.

CHAPTER 3
STUDY ON SOLIDIFICATION BEHAVIOUR

CHAPTER 3
STUDY ON SOLIDIFICATION BEHAVIOUR

3.0 Aim

The aim of this study was to determine the combined effect of both addition of iron and silicon on the formation of intermetallic phases in B206 aluminum-copper alloys; their size, distribution, morphology and quantity, as all these parameters determine the mechanical properties of the alloy.

3.1 Experimental procedures

The base alloy was a B206 ingot produced by Rio Tinto Alcan and its chemical composition is shown in Table 3.1. Different levels of Fe/Si ratios and two cooling rates (low and high) were used. A drawback of having a high manganese content is the increment in both hardness and quantity of intermetallic particles for a given iron content, in such a way that its positive effect on the modification of the Fe-intermetallic morphology to increase the resistance to crack propagation is offset by the increased brittleness and volume of the α-Fe particles.[170] Since our goal was to maximize the iron content, manganese was kept constant and at the lowest acceptable, that is about 0.2%. Two different levels of copper were used to assess the importance of copper content. Compositions were modified using aluminum1020 and commercial Al-50%Si and Al-25%Fe master alloys. Chemical analyses carried out with an optical spectrometer are presented in Table 3.2.

Table 3. 1: B206 Alloy Composition (wt%)

Cu	Si	Fe	Mn	Mg	Ti	Zn	Ni	Al
4.98	0.05	0.07	0.39	0.21	0.01	0.01	0.02	balance

Table 3. 2: Alloy codes and chemistry

Alloy Code*	% of Alloying elements (wt%)					
	Cu (%)	Fe (%)	Si (%)	Mn (%)	Mg (%)	Ti (%)
U1206(A)	4.03	0.12	0.06	0.23	0.24	0.02
U1710(A)	4.16	**0.17**	**0.10**	0.23	0.25	0.02
U2410(A)	4.12	**0.24**	0.10	0.23	0.24	0.02
U2320(A)	3.92	0.23	**0.20**	0.23	0.25	0.02
U3420(A)	4.06	**0.34**	0.20	0.23	0.26	0.02
U2430(A)	3.99	0.24	**0.30**	0.23	0.25	0.02
B1106(A)	4.59	0.11	0.06	0.23	0.25	0.02
B1710(A)	4.57	**0.17**	**0.10**	0.23	0.25	0.02
B2710(A)	4.64	**0.27**	0.10	0.23	0.25	0.02
B2420(A)	4.31	0.24	**0.20**	0.23	0.26	0.02
B2919(A)	4.70	**0.29**	0.19	0.23	0.25	0.02
B3128(A)	4.28	0.31	**0.28**	0.23	0.25	0.02
B2328(A)	4.70	**0.23**	0.28	0.23	0.26	0.02

*- Uxxxx designate alloys with copper content under B206 range

-Bxxxx designate alloys with copper content within B206 range

- The first two xx digits represent 100% of Fe

- The last two xx digits represent 100% of Si

- A is used when the sample was air cooled

Compositions in bold shows the change in composition from upper and lower designations

3.1.1 Melt treatment and casting

About 1.4 kg of material was melted in a salamander crucible by means of an electrical

resistance furnace and the temperature of the melt was maintained at about 730 ± 5 °C. At

this temperature, it is probable that most precipitates were dissolved. The melt was alloyed with sufficient Al-5Ti-1B grain refiner added in rod form to give final Boron content of about 20 ppm. Stirring was carried out before the first casting, and thereafter after each four castings. Prior to casting, a specimen was prepared for chemical analysis. The steel crucible used for sample casting was preheated first in a separate furnace to about 450 °C, and later by immersion in the melt for about two minutes. In this way, no nucleation could occur in the sample before the system was in thermal balance. The filled crucible was then placed on an alumina plate laid at the bottom of a copper cylindrical cup which could accommodate a pressurized air cooling system. Two k-type thermocouples were then dipped into the melt in the sampling crucible, one at the center and the other close to the wall, while the temperature evolution was recorded with a computerized recording system at the frequency of ten readings per second. The 0.5 mm diameter thermocouple tips were located 20 mm above the bottom of the crucible. Eight samples were produced per batch. A schematic representation of the casting crucible (in view) and the casting and data recording set up is shown in Fig. 3.1 and Fig. 3.2 respectively. Solidification was allowed under free atmosphere and under 40 Psi pressurized air. These conditions could provide cooling rates of about 1°C/sec and 4°C/sec respectively, calculated from the portion of the cooling curve prior nucleation of primary aluminum dendrites. Two cooling curves were recorded for each condition to ensure consistency of the results. The holding time was kept under 90 min. Preliminary experiments showed that the decrease in grain refinement during this time is negligible.

3.1.2 Thermal Analysis and Microscopy

Cooling curves were analyzed to determine precipitation temperatures, growth periods, solidification ranges and times, and dendrite coherency points. As most of the alloys of this system do not freeze under equilibrium conditions and are used after heat treatment, differential scanning calorimetry (DSC) was carried out at the heating rate of 1°C/min on a DSC 7 PERKIN ELMER power compensator calorimeter (Fig. 3.3) to determine near equilibrium dissolution temperatures of phases and optimize heat treatment conditions.

Samples of 10-20mg were taken from the center of the castings used for thermal analysis. The phases were associated to the dissolution temperature by heating the sample to about ten degrees above the DSC peak temperature, holding for about 20 minutes to allow for dissolution or local burning, and then quenching. The sample was later polished and the phases corresponding to the peak temperature identified. One-quarter sections of the as-cast samples measuring approximately 25mm x 15mm were cut parallel to the thermocouples, mounted in bakelite resin with carbon filler using a Struers Labopress-3 Mounting Press (force of 30 KN; heating time of 4 min, cooling time of 2 min), polished using a Struers Tegrapol-31 Grinder-Polisher to obtain the desired surface finish, and then etched with 0.5% HF solution to reveal the microstructure. Details of the grinding and polishing procedures are provided in Table 3.3. At each stage of the procedure, the coolant which was used also acted as a lubricant and ensured constant cleaning of the polishing cloth and the specimens simultaneously. Between the different stages, the samples were cleaned with water. Six samples were polished at a time. Optical microscopy, scanning electron microscopy (SEM), electron microprobe (EPMA) and image analysis was used to

examine the microstructure. Clemex image analyzer in conjunction with the optical microscope (Olympus) was used to characterize the amount of intermetallic compounds, their size, distribution, and morphology. These equipments used for microstructure characterization are presented in Fig. 3.4 and Fig. 3.5.
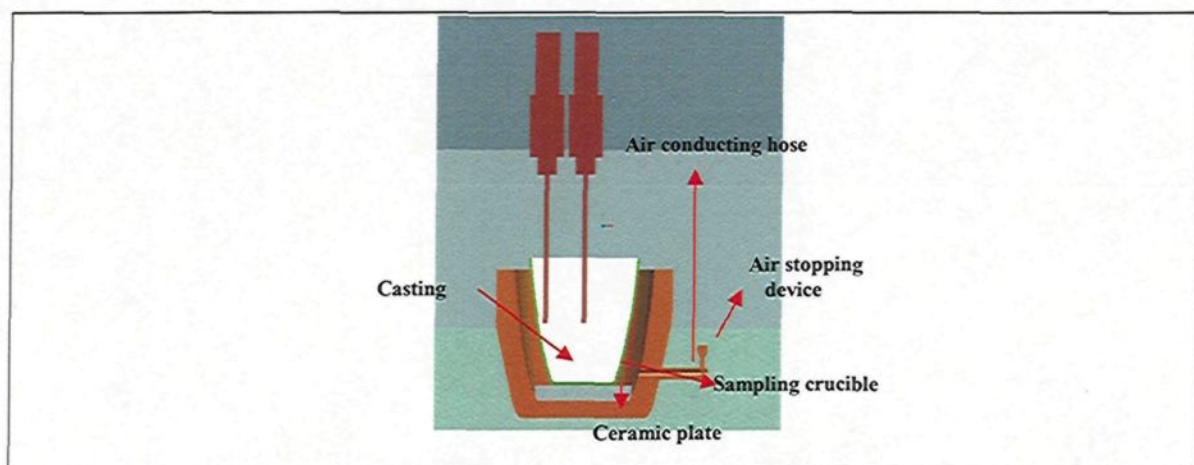

Figure 3. 1: Sampling steel crucible (in the copper cup)
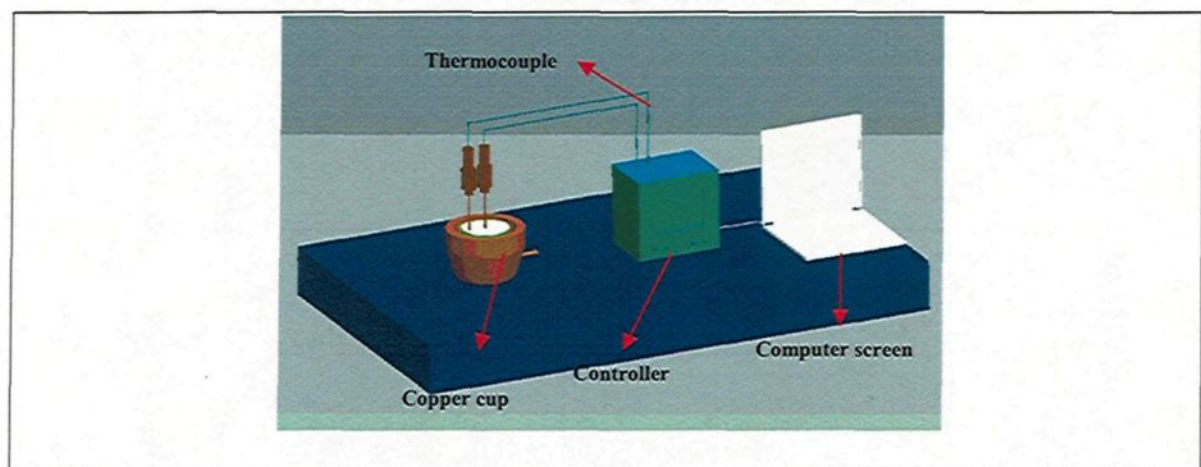Thickness 1mm; Height 42mm; Upper diameter 44mm; Bottom diameter 25mm.

Figure 3. 2: Casting and data recording setup.

Figure 3.3: DSC 7 PERKIN ELMER power compensator calorimeter.
(*courtesy CURAL labs*)

Table 3.3: Grinding and polishing procedures for metallographic samples

Stage	Abrasive	Particle size (μm)	Coolant	Force (N)	Time (Sec)	Speed (rpm)
1	SiC (220)	63	Running Water	150	90	300
2	Diamond	9	DP lubricant (Blue)	180	360	150
3	Diamond	3	DP lubricant (Blue)	150	450	150
4	Colloidal Silica	0.5	-	90	30	150
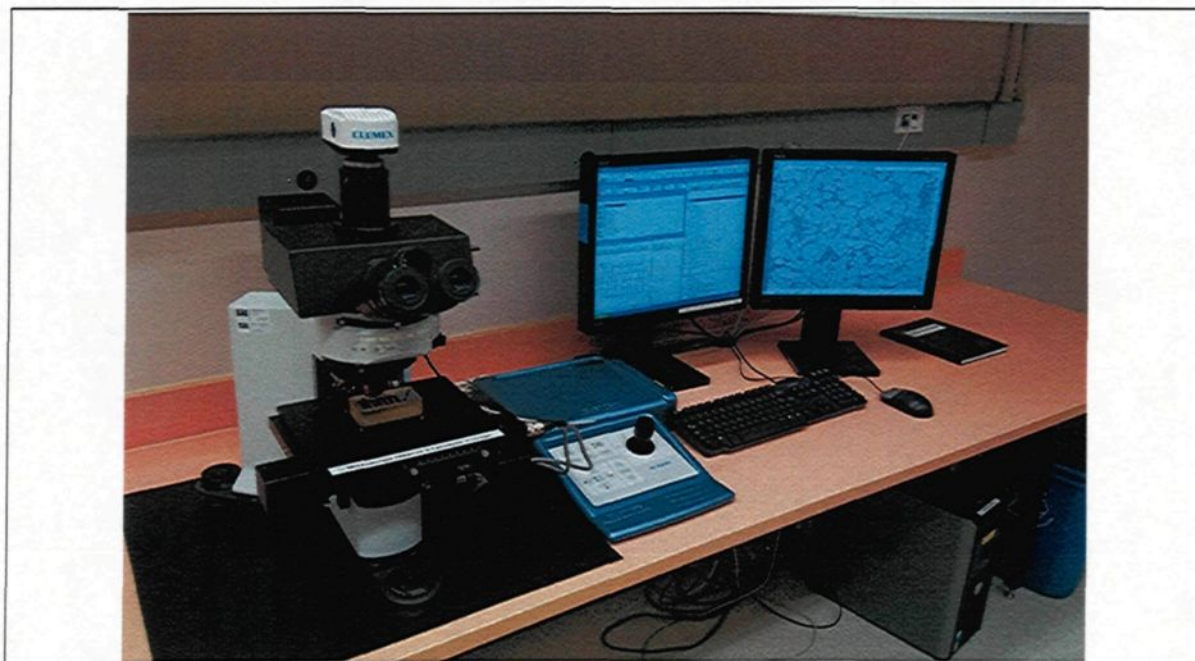
Figure 3. 4: Clemex image analyzer coupled with the optical microscope (Olympus).
(*courtesy NRC-CTA labs*)

Figure 3. 5: SEM Hitachi FEGSEM SU-70.
(*courtesy NRC-CTA labs*)

3.2 Results

Cooling curves obtained for the various B206 alloy compositions at low and high cooling rates and their derivatives are shown in Figs. 3.6 to 3.9. They were compiled for comparison purposes. It is evident from these curves that the copper content has no qualitative effect on precipitation reactions, but slightly affects their non-equilibrium precipitation temperature. Consequently, further analysis on solidification will refer only to B alloys. Individual analyses of these curves presented in Appendix A and shown in Fig. 3.10a and 3.10b for alloy B1106 and B1106A, respectively, clearly identify four main precipitation reactions, indicated on the low cooling rate curve. Table 3.4 presents a summary of solidification data. The start of solidification was taken as the point where the derivative wall temperature curve suddenly deviates from the slowly increasing base level. This could vary from 650°C at low silicon content to 644°C at high silicon content. The growth period was taken as the time interval between the beginnings of two reactions. The growth period is important in that it gives an idea of the size of the particle precipitated as it increases with the growing period. The dendrite coherency point was defined, following Backerud et al., [66] as the point where the difference in temperature between the wall and the centre is at a minimum. It indicates the temperature at which a skeleton network of dendrites is formed, and the remaining solidification below this point takes place in the interdendritic areas. It is an important characteristic of as-cast alloys because it marks the transition from mass to interdendritic feeding during solidification. [2,66,106] Casting defects such as macrosegregation, shrinkage porosity, and hot tearing develop below the dendrite
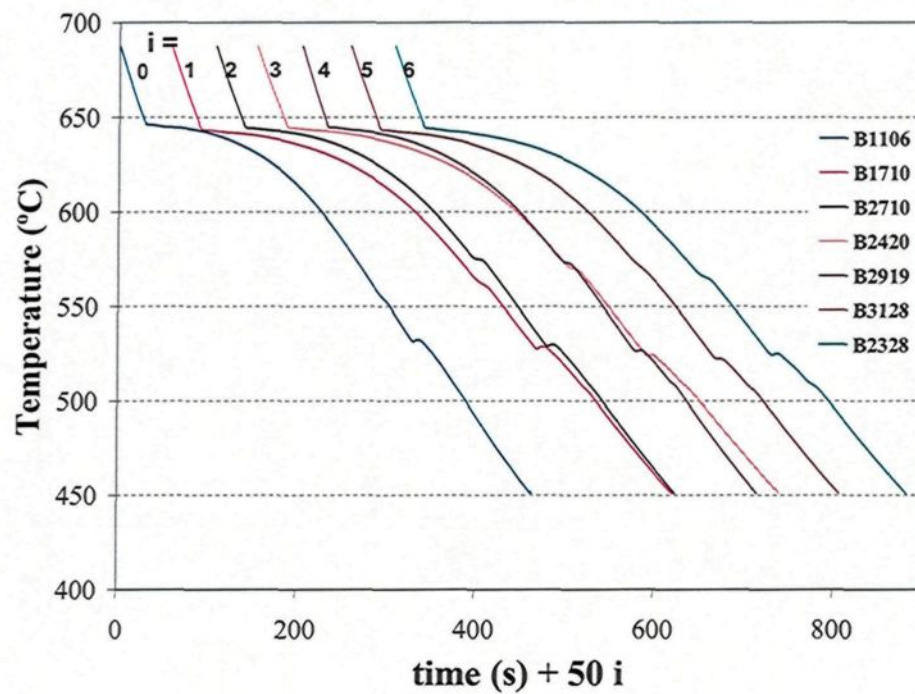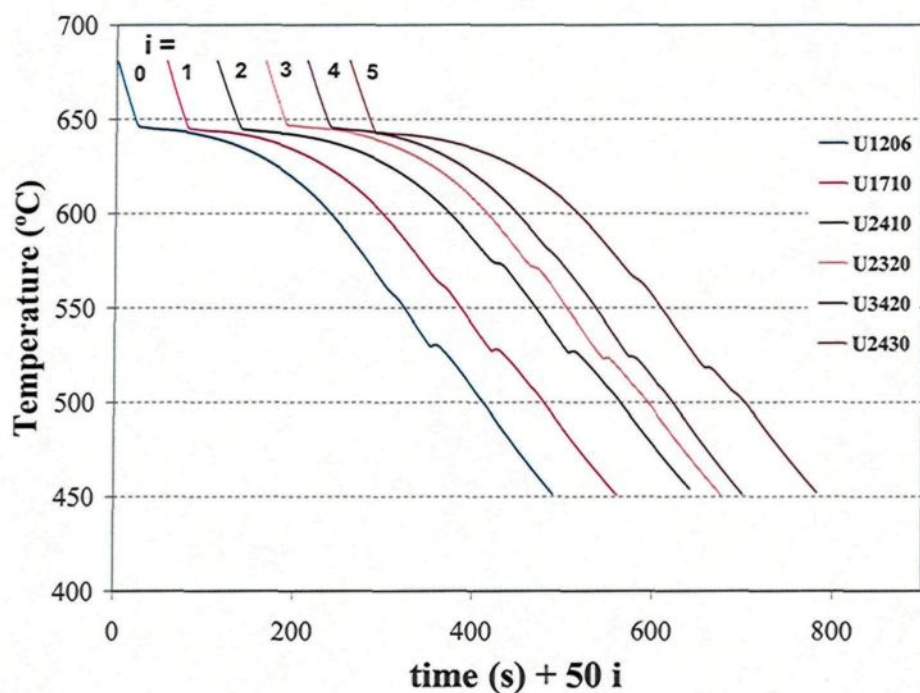
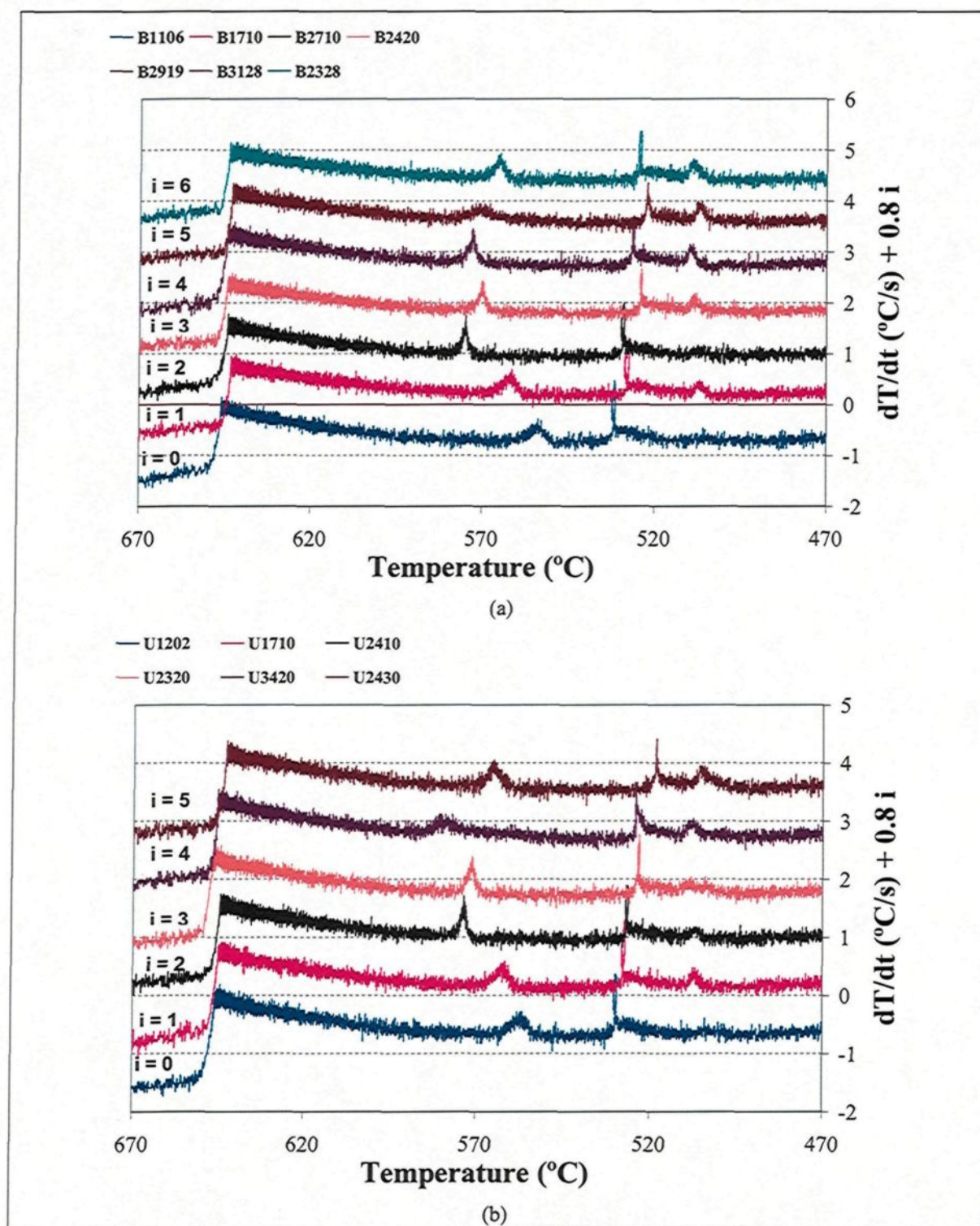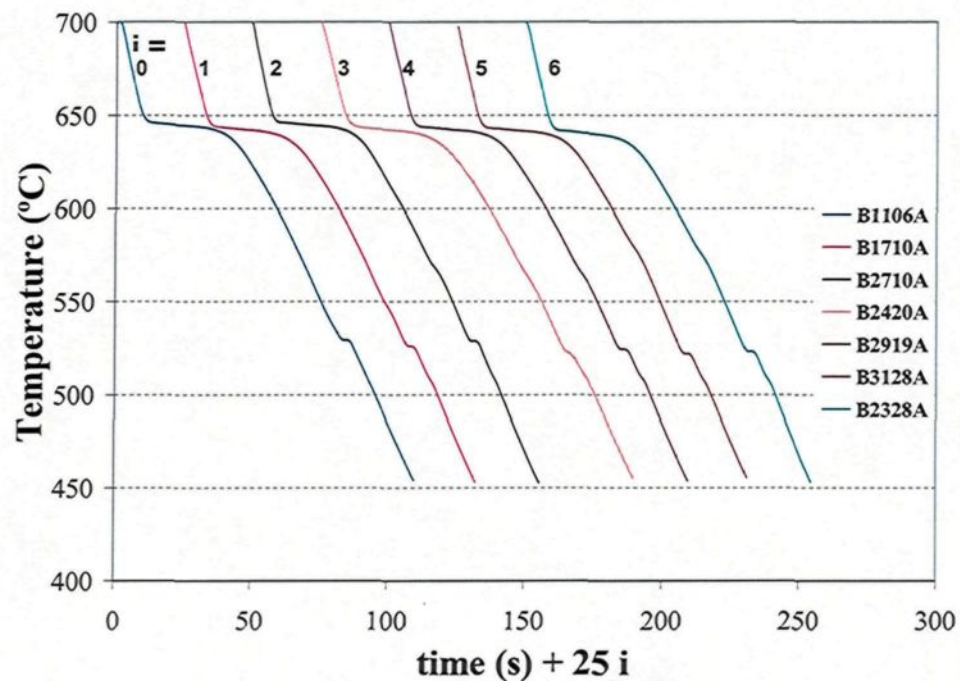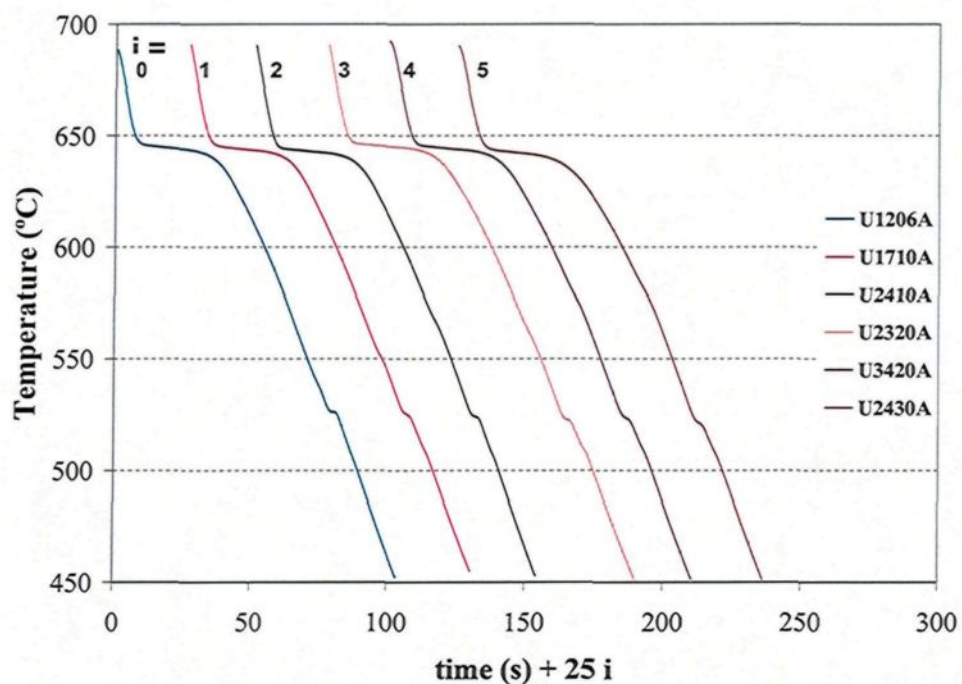Figure 3.6: Cooling curves of various B206 alloys obtained at low cooling rate.

Figure 3.7: First derivative curves corresponding to the cooling curves of Fig. 3.6.

Figure 3.8: Cooling curves of various B206 alloys obtained at high cooling rate.
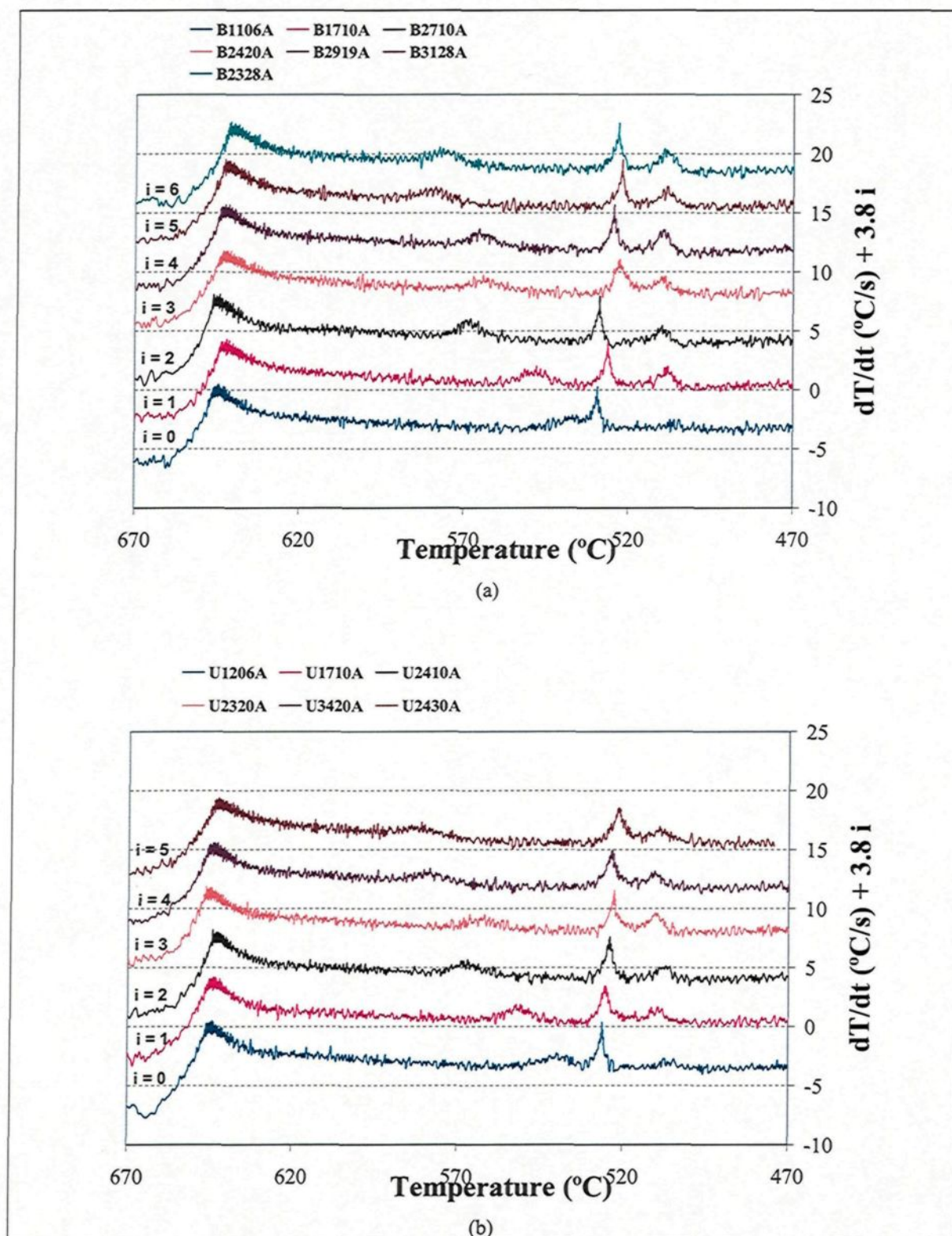
72

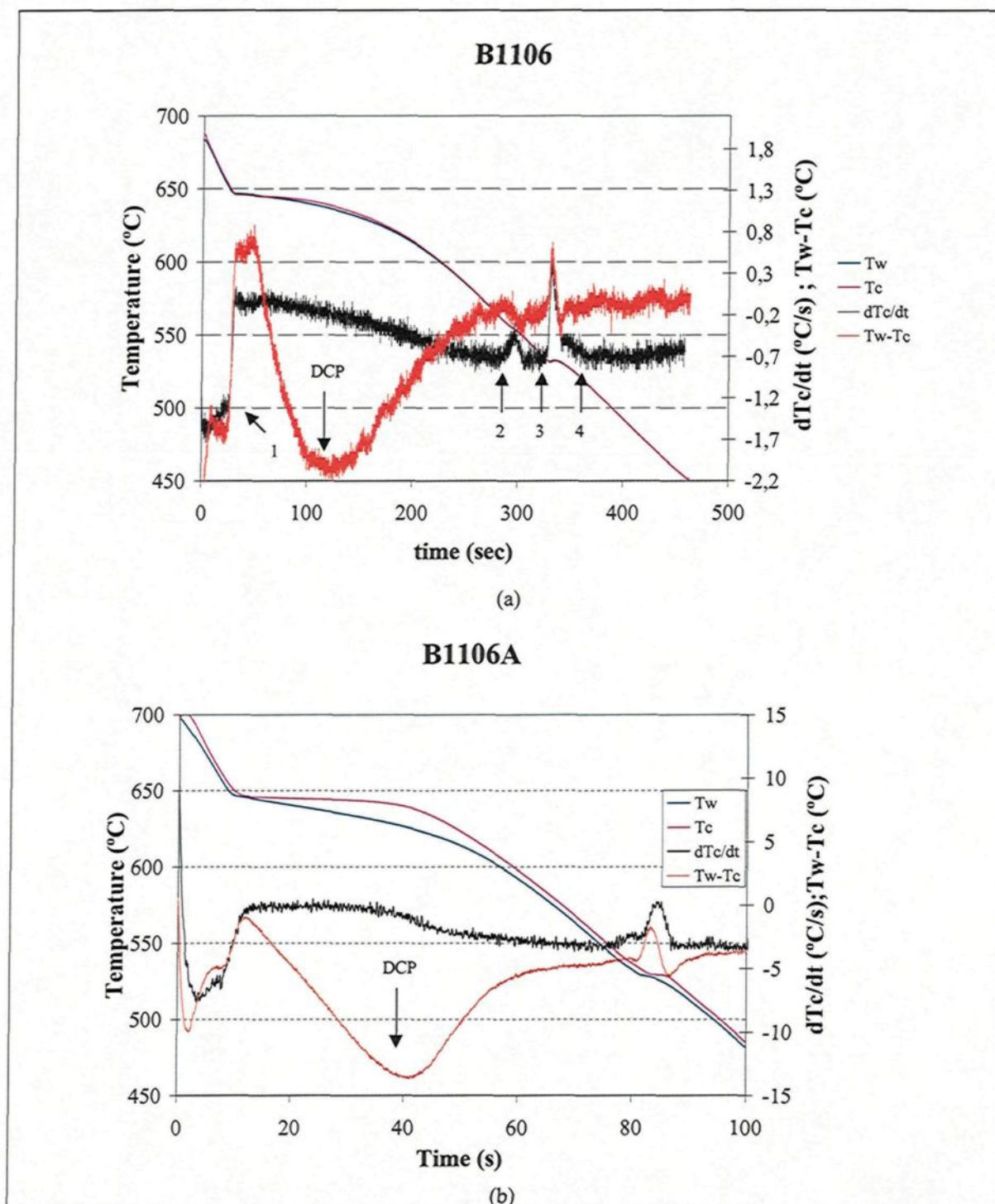Figure 3.9: First derivative curves corresponding to the cooling curves of Fig. 3.8.

Figure 3.10: Cooling curves obtained for B1106 alloy at the wall and the center of the casting; the first derivative curve (black) is shown at the center; Evolution of the difference in temperature between the wall and the center is shown by the orange curve.

Table 3. 4: Summary of solidification data for B206 alloys

a) Low cooling rate

Alloy Code	Reactions				S.R*	S.T*	SDAS*	DCP *
	Precipitation range T (°C) / Growth Period (seconds)							
	1	2	3	4	ΔT (°C)	t_{sol} (sec)	(μm)	°C /fs/t(sec)
B1106	647-646	560-556 / 42	532-531 / 50	507-505/7	142	371	90	639/0.35/95
B1710	645-644	567-562 / 67	530-528 / 48	508-507/1	138	431	95	638/0.36/95
B2710	645-644	576-575 / 81	529-528 / 41	508-506/3	139	388	85	640/0.29/76
B2420	646-645	572-570 / 80	525-524 / 36	510-509/6	137	421	110	639/0.35/92
B2919	646-645	575-573 / 81	527-526 / 38	511-509/7	137	397	97	639/0.30/91
B3128	644-643	575-572 / 91	523-522 / 37	508-507/4	137	435	110	637/0.37/99
B2328	645-644	567-566 / 76	525-524 / 40	511-509/3	136	419	111	636/0.37/110

a) High cooling rate

Alloy Code	Reactions				S.R*	S.T*	SDAS*	DCP *
	P Precipitation range T (°C) / Growth Period (seconds)							
	1	2	3	4	ΔT (°C)	t_{sol} (s)	(μm)	°C /fs/t(sec)
B1106A	650-646	545-537 / 3	531-529 / 10	505-504/1	146	87	54	639/0.35/31
B1710A	647-644	557-550 / 9	528-526 / 8	511-508/2	139	83	56	637/0.40/32
B2710A	650-647	575-569 / 15	532-529 / 8	515-511/2	139	84	49	639/0.32/30
B2420A	648-643	571-566 / 14	525-522 / 6	512-509/2	139	87	62	636/0.42/30
B2919A	647-644	570-565 / 16	526-524 / 7	512-509/2	138	87	55	637/0.34/31
B3128A	647-643	586-580 / 20	524-522 / 7	511-508/2	139	87	61	637/0.37/31
B2328A	646-642	581-576 / 18	526-523 / 7	512-508/3	138	82	65	634/0.43/30

*S.R: Solidification range; S.T: Total solidification time; SDAS: Secondary dendrite arm spacing; DCP: Dendrite coherency point

coherency point. [106] A good understanding of how solidification is influenced at this point is important in tailoring new commercial alloys. Knowledge of fraction solid at the dendrite coherency point (DCP) provides important information in predicting the quality of the casting. This was obtained from consistent results of simulation with Thermo-Calc and Visual measurement softwares.

Table 3.5 lists the composition of phases obtained by energy dispersive spectroscopy (EDS) and suggested phases. EDS measurement is semi-quantitative. The phases were therefore suggested based on the homogeneity range of constituent elements.

Table 3.6 presents their volume fractions as measured by optical microscopy. Two hundreds fields of 28525.75 μm^2 surface area each were analyzed per measurement at magnification 500x. The sample was traversed in a regular and systematic manner along the solidification path; $i.e.$ from the wall to the centre. In quantitative stereology, the measured area fraction of a phase is equal to the volume fraction under the assumption that the morphology is equiaxed. [171] Consequently, the measured area fractions of these intermetallic compound particles were transferred to volume fractions.

A typical microstructure of alloy B1106 is shown in Figure 3.11. It consists essentially of a network of Al_2Cu or θ phase, with needle-like β(FeCu) phase Al_7FeCu_2 present at the grain boundaries of the aluminum matrix, together with some Mg,Si phase particles. The microstructures of alloys B1710 and B2710 presented in Appendix B are similar to that of alloy B1106. In addition to the phases found in alloy B1106, negligible amount (less than 0.01%, Table 3.6) of iron which precipitated as the α-Fe phase, some $Al_{20}Mn_3Cu_2$ phase particles and very little $Al_5Mg_8Si_6Cu_2$ phase particles were also found in the microstructure of alloy B2420 (Fig. 3.12). The microstructures of alloys B2919 and B2328 presented in Appendix B are similar to that of alloy B2420. Even at low cooling rate, about 33% of the iron precipitated as the α-Fe phase in alloy B3128 (Table 3.6, Figure 3.13a), and $Al_5Mg_8Si_6Cu_2$ phase was clearly observed nucleating and growing from Al_2Cu phase particles (Figure 3.13b). At high cooling rate, the precipitation of α-Fe at the expense of

the β(FeCu) phase Al_7FeCu_2 is more effective and nucleation of $Al_5Mg_8Si_6Cu_2$ is suppressed. About 70% and 54% of iron precipitated as the α-Fe phase in alloys B2420A and B2919A, respectively (Table 3.6).

A typical microstructure of alloy B2919A is presented in Fig. 3.14. In alloys B3128A and B2328A, almost all iron precipitated as the α-Fe phase (Table 3.6). A typical microstructure of alloy B3128A is presented in Fig. 3.15. At high cooling rate, some β(FeCu) phase particles are fragmented in alloys B1106A, B1710A, and B2710A, taking script-like morphology. Their characterization (Fig. 3.16) showed negligible silicon content and no effect on stoichiometry.

DSC curves are presented in Figures 3.17 and 3.18 and the resultant peak dissolution temperatures are listed in Table 3.7. They were compiled for comparison purposes. The similarity of the curves of U and B alloys both for slowly cooled and rapidly cooled samples confirms the fact that copper does not affect precipitation reactions on a qualitative basis. Consequently, further analysis will refer only to B alloys. Three peaks were observed at all compositions and cooling rates, at around 650°, 597°, and 540°C. A fourth peak was observed around 514°C for alloys B2420, B2919, B3128, and B2328, while a minor fifth peak was observed mainly in alloys B3128A and B2328A between 622° and 635°C.

Table 3. 5: Phases found in microstructures of various B206 alloys
a) Low cooling rate

Chemical Compositions (Wt%) *							Suggested phase	Appearance
B1106	B1710	B2710	B2420	B2919	B3128	B2328		
43.08Al 55.47Cu	45.5Al 51.4Cu	44.88Al 51.82Cu	43.73Al 52.14Cu	44.1Al 51.92Cu	43.96Al 52.53Cu	45.23Al 51.27Cu	Al_2Cu (θ)	Pink
64.73Al 29.87Cu 7.83Fe 1.68Mn	59.17Al 32.17Cu 9.84Fe 1.59Mn	58.37Al 28.25Cu 10.12Fe 1.14Mn	48.82Al, 34.35Cu 12.27Fe 1.47Mn	54.25Al 33.62Cu 10.41Fe 1.09Mn	57.00Al 29.65Cu 10.94Fe 1.70Mn	50.53Al 33.67Cu 11.51Fe 1.37Mn	$Al_7(Fe,Mn)Cu_2$ $\beta(FeCu)$	Gray, needle
35.35Al 10.17Mg 11.75Cu 10.25Si 13.49O	57.91Al 7.44Mg 6.3Cu 10.05Si 8.1O	80.51Al 1.46Mg 9.47Cu 2.75Si 5.17O	53.5Al 10.53Mg 1.6Cu 21.23Si 13.05O	36.62Al 5.18Mg 20.21Cu 11.91Si 17.88O	54.59Al 7.46Mg 26.09Cu 6.83Si 2.01O	59.41Al 7.04Mg 25.6Cu 6.04Si 5.47O	Mg_2Si / SiO_x	Black
-	-	-	-	-	43.18Al 19Cu 20.25Mg 17.62 Si	-	$Al_5Mg_8Si_6Cu_2$	Light gray, dendritic
-	-	-	67.8Al 13.8Cu 18.4Mn	-	-	-	$Al_{20}Mn_3Cu_2$	Gray, square
-	-	-	56.25Al 11.32Cu 18.78Fe 5.8Mn 4.63Si	54.82Al 13.73Cu 18.86Fe 5.5Mn 3.8Si	56.5Al 9.75Cu 18.87Fe 5.66Mn 5.92Si	55.1Al 10.75Cu 19.17Fe 5.05Mn 6.12Si	$(Al,Cu)_{15}(Fe,Mn)_3Si_2$ $(\alpha\text{-Fe})$	Gray, script

b) High cooling rate

Chemical Compositions (Wt%) *							Suggested Phase	Appearance
B1106A	B1710A	B2710A	B2420A	B2919A	B3128A	B2328A		
45.49Al 51.88Cu	43.86Al 52.23Cu	44.33Al 52.11Cu	42.83Al 52.15Cu	43.31Al 53.44Cu	45Al 51Cu	45.86Al 51Cu	Al_2Cu (θ)	Pink
53.89Al, 36.07Cu 8.9Fe 1.14Mn	52.22Al 36.12Cu 9.24Fe 1.61Mn	50Al 35.25Cu 10.6Fe 1.11Mn	52.61Al, 27.91Cu 13.4Fe 1.69Mn	56.15Al 33.86Cu 7.82Fe 1.27Mn	-	-	$Al_7(Fe,Mn)Cu_2$ $\beta(FeCu)$	Gray, needle
50.08Al 4.77Mg 10.72Cu 8.35Si 11.77O	67.91Al 5.34Mg 6.3Cu 6.05Si 7.81O	59.52Al 7.34Mg 12.81Cu 8.37Si 9.8O	68.72Al 2.28Mg 16.05Cu 5Si 7.39O	60.81Al 9.42Mg 9.09Cu 9.42Si 8.31O	67.9Al 4.54Mg 4.57Cu 7.76Si 10.13O	60.6Al 4.25Mg 19.57Cu 6.34Si 8.72O	Mg_2Si / SiO_x	Black
-	-	-	54.8Al 4.82Cu 19.95Fe 11.04Mn 4.88Si	55Al 12.6Cu 20.34Fe 4.76Mn 4.75Si	56.83Al 9.77Cu 21.42Fe 4.42Mn 3.68Si	55.78Al 10.4Cu 22.68Fe 3.7Mn 4.97Si	$(Al,Cu)_{15}(Fe,Mn)_3Si_2$ $(\alpha\text{-Fe})$	Gray, script

*Only elements with at least 1% weight were considered. The compositions were normalized.

Table 3. 6: Volume fraction of the phases observed in various B206 alloys

a) Low cooling rate

Alloys				Volume fraction (%)			
Code	%Fe	%Si	Fe/Si	Al₂Cu	Al₇(Fe,Mn)Cu₂ / Al₂₀Mn₃Cu₂	(Al,Cu)₁₅(Fe,Mn)₃Si₂	Mg,Si,O
B1106	0.11	0.06	**1.85**	4.04	0.76	0	0.085
B1710	0.17	0.10	**1.70**	4.08	0.97	0	0.087
B2710	0.27	0.10	**2.70**	3.73	1.35	0	0.05
B2420	0.24	0.20	**1.20**	3.90	1.16	<0.01	0.15
B2919	0.29	0.19	**1.53**	3.90	1.33	<0.01	0.11
B3128	0.31	0.28	**1.10**	4.06	0.90	0.45	0.17
B2328	0.23	0.28	**0.82**	4.01	1.22	<0.01	0.18

b) High cooling rate

Alloys				Volume fraction (%)			
Code	%Fe	%Si	Si/Fe	Al₂Cu	Al₇(Fe,Mn)Cu₂/ Al₂₀Mn₃Cu₂	(Al,Cu)₁₅(Fe,Mn)₃Si₂	Mg,Si,O
B1106A	0.11	0.06	**1.85**	4.15	0.88	0	0.06
B1710A	0.17	0.10	**1.70**	4.18	1.15	0	0.17
B2710A	0.27	0.10	**2.70**	3.95	1.45	0	0.12
B2420A	0.24	0.20	**1.20**	4.69	0.37	0.87	0.18
B2919A	0.29	0.19	**1.53**	4.48	0.66	0.78	0.19
B3128A	0.31	0.28	**1.10**	4.79	<0.01	1.48	0.14
B2328A	0.23	0.28	**0.82**	4.74	<0.1	1.33	0.17
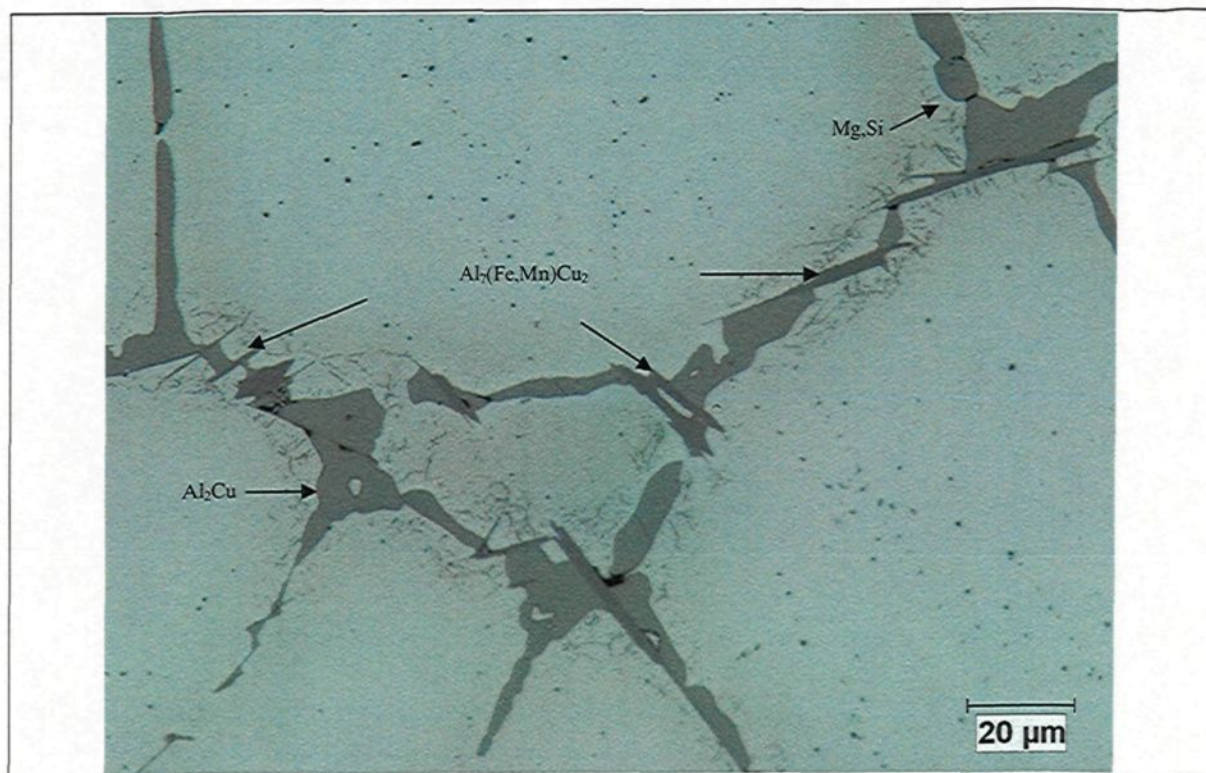
Figure 3 11: Typical microstructure of alloy B1106.
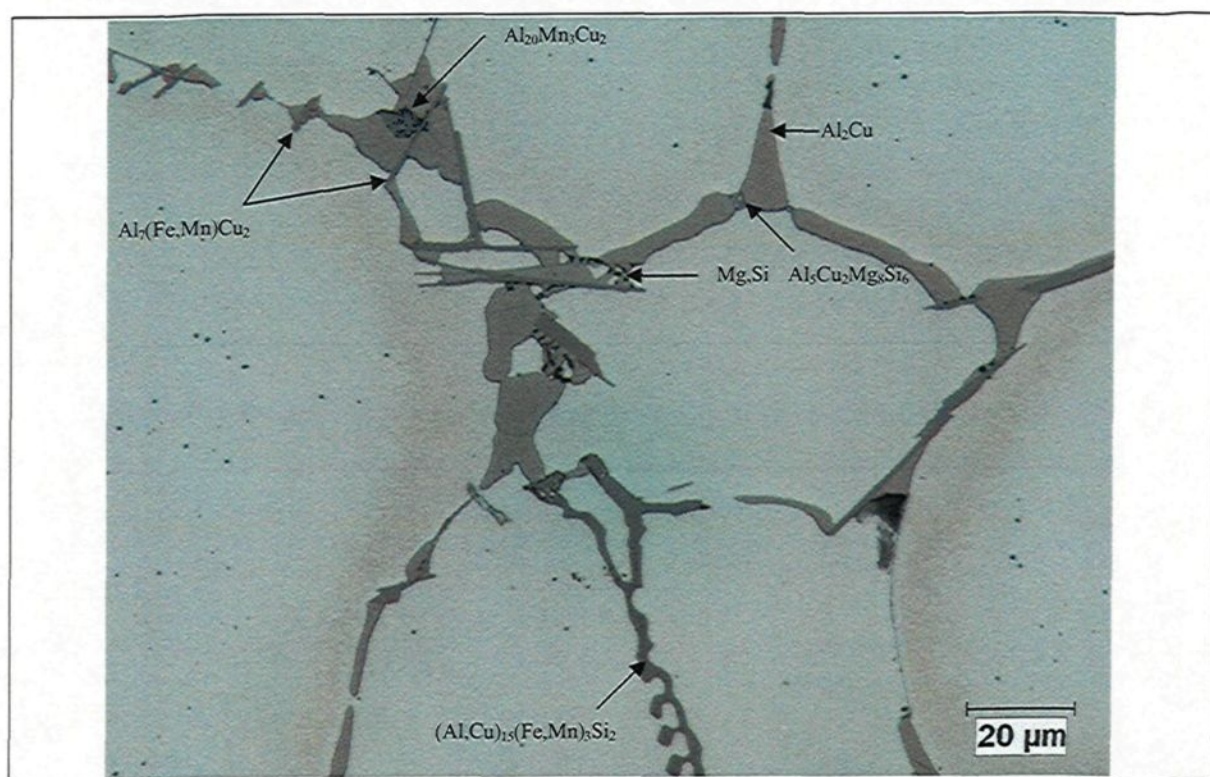
Figure 3 12: Typical microstructure of alloy B2420.
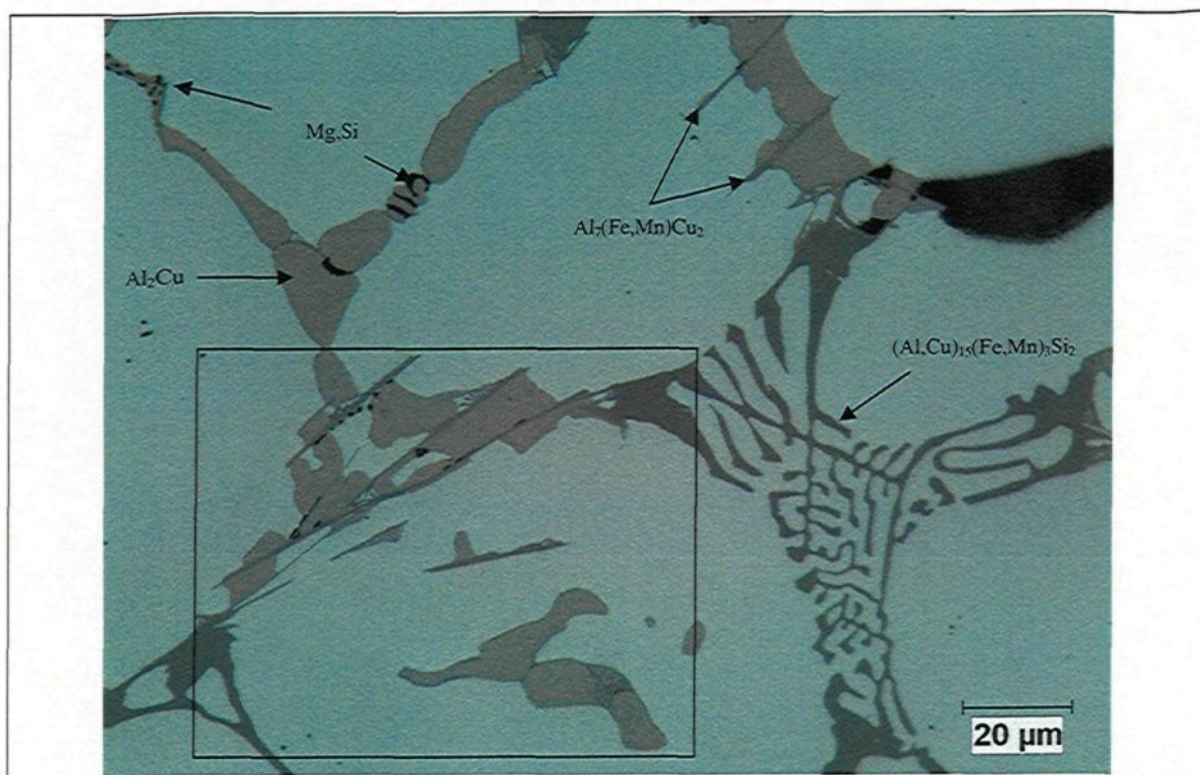
Figure 3. 13a: Typical microstructure of alloy B3128.
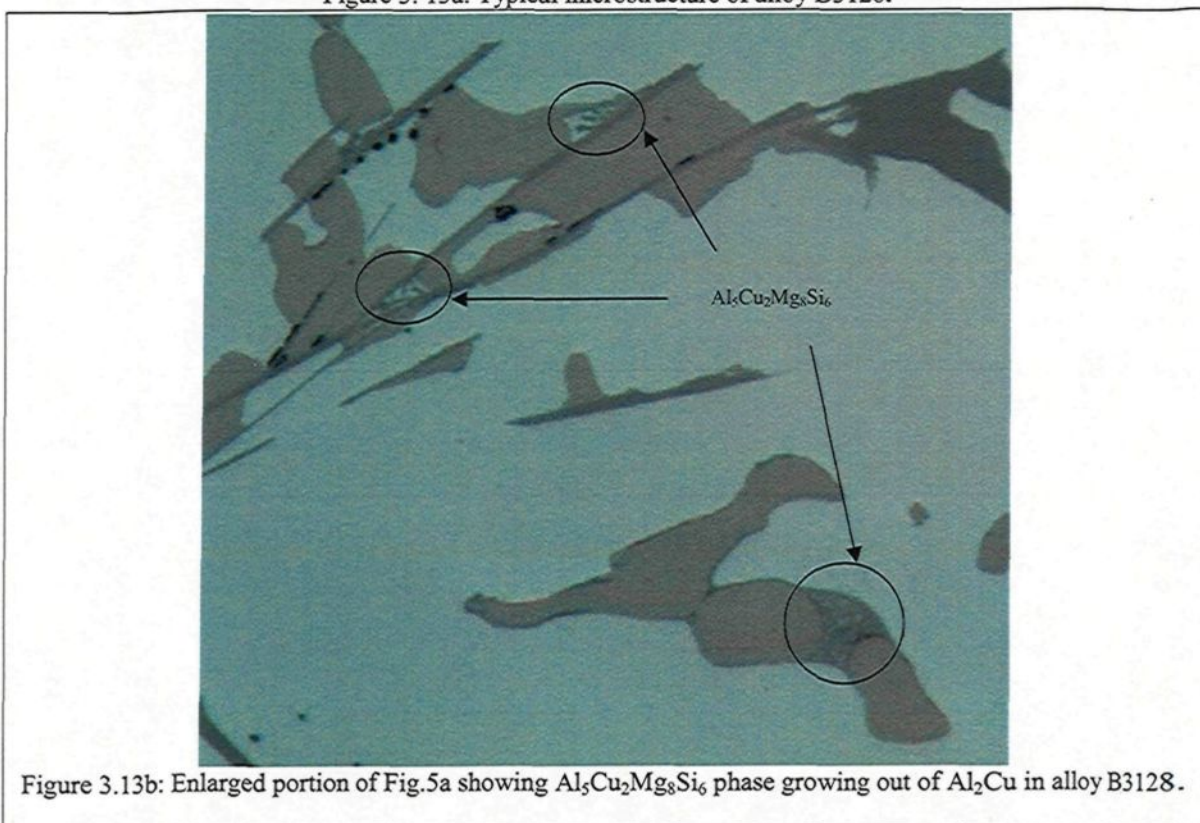
Figure 3.13b: Enlarged portion of Fig.5a showing Al$_5$Cu$_2$Mg$_8$Si$_6$ phase growing out of Al$_2$Cu in alloy B3128.
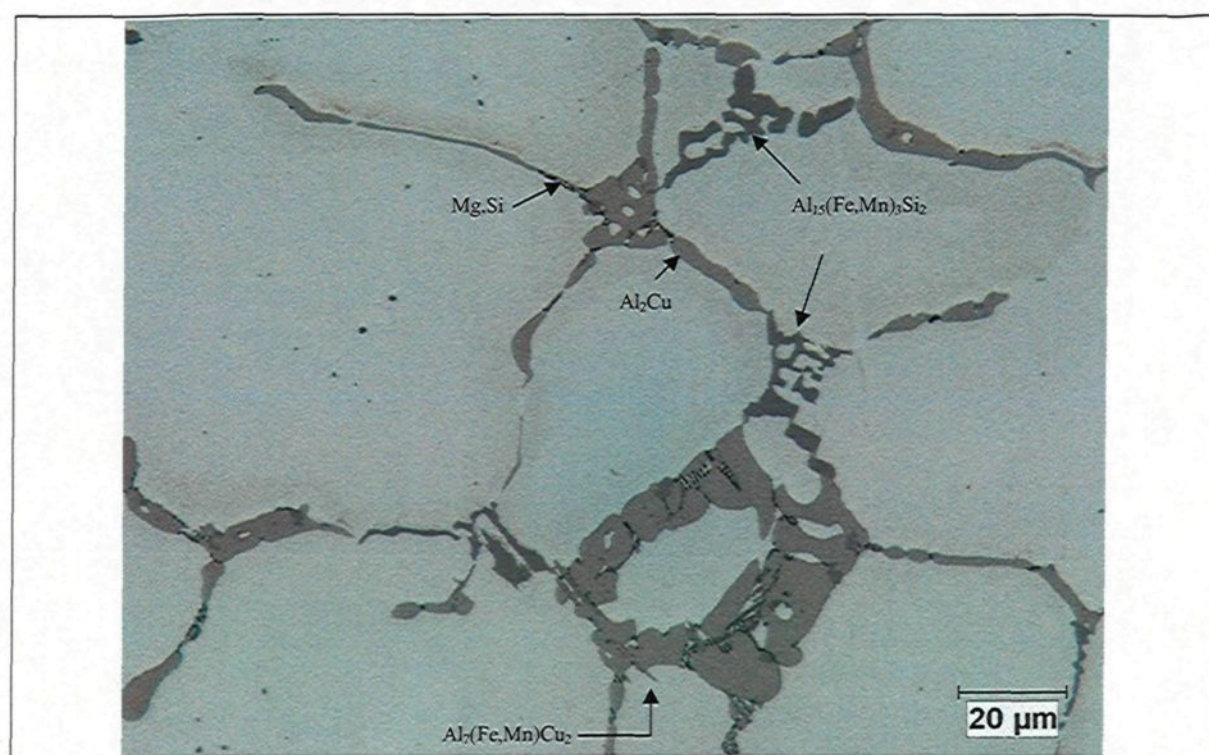
Figure 3. 14: Typical microstructure of alloy B2919A.
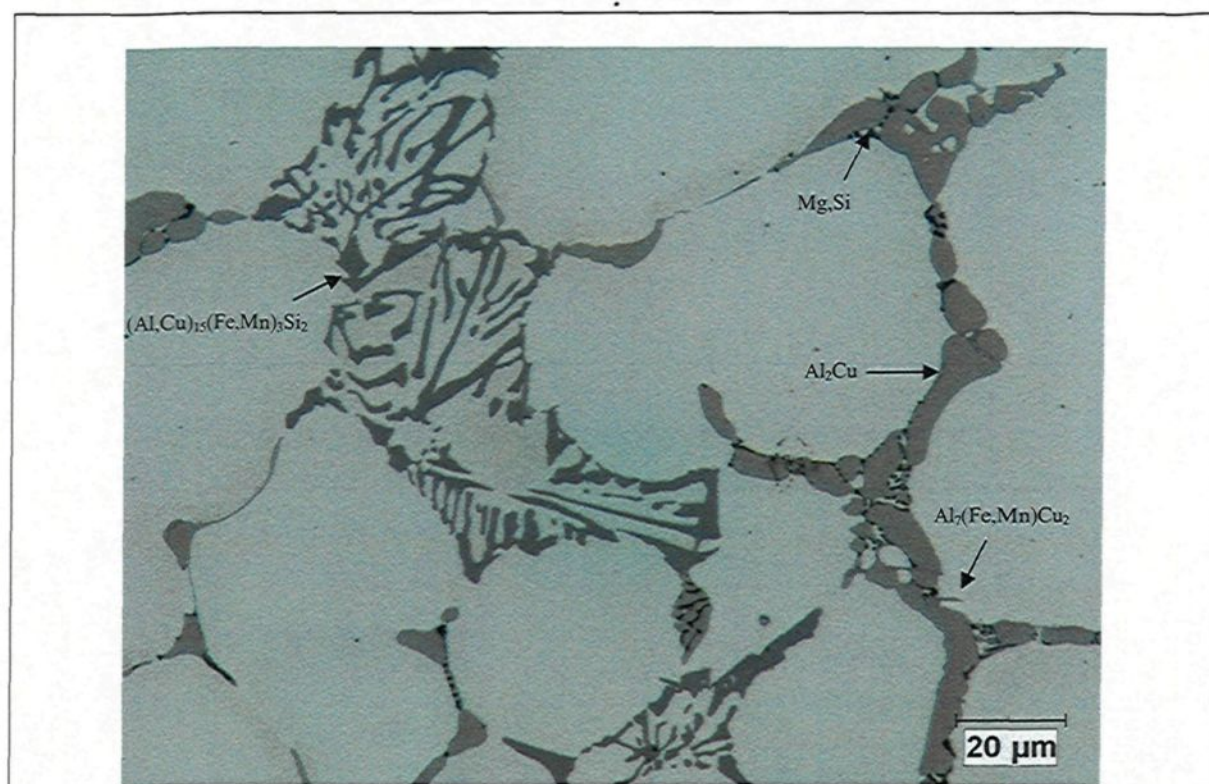
Figure 3. 15: Typical microstructure of alloy B3128A.
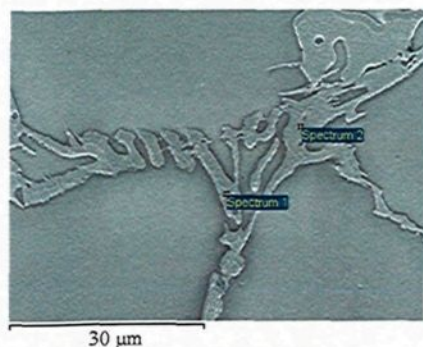
	In stats.	Al	Si	Fe	Cu
Spectrum 1	Yes	41.98	0.00	26.75	31.26
Spectrum 2	Yes	40.54	0.57	24.43	34.46

30 μm

Figure 3. 16: Fragmented β(FeCu) phase during solidification of alloy B2710 at high cooling rate. (compositions in weight %)

(a)

(b)
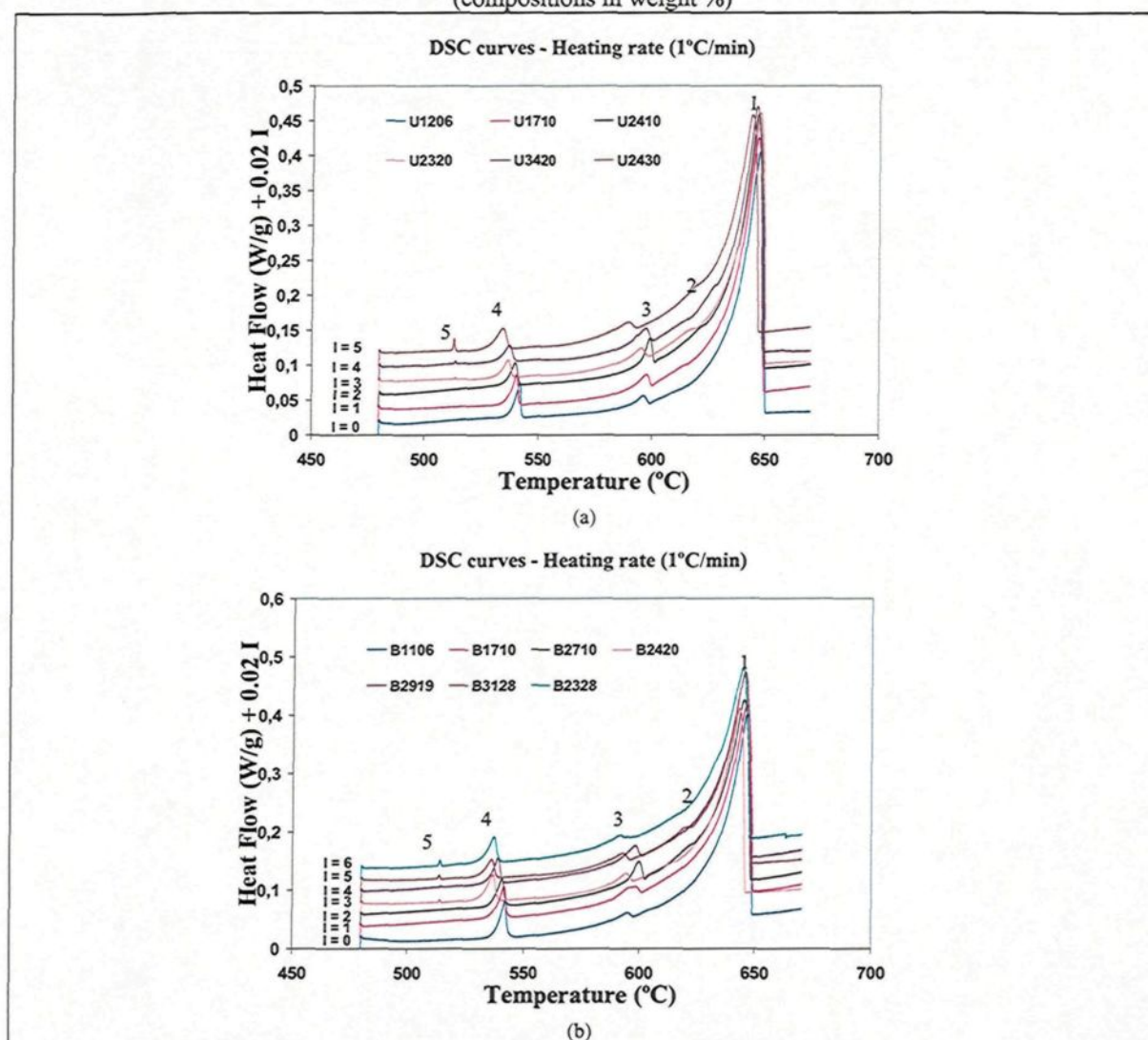
Figure 3. 17: DSC curves of various B206 alloys obtained under low cooling rate conditions.
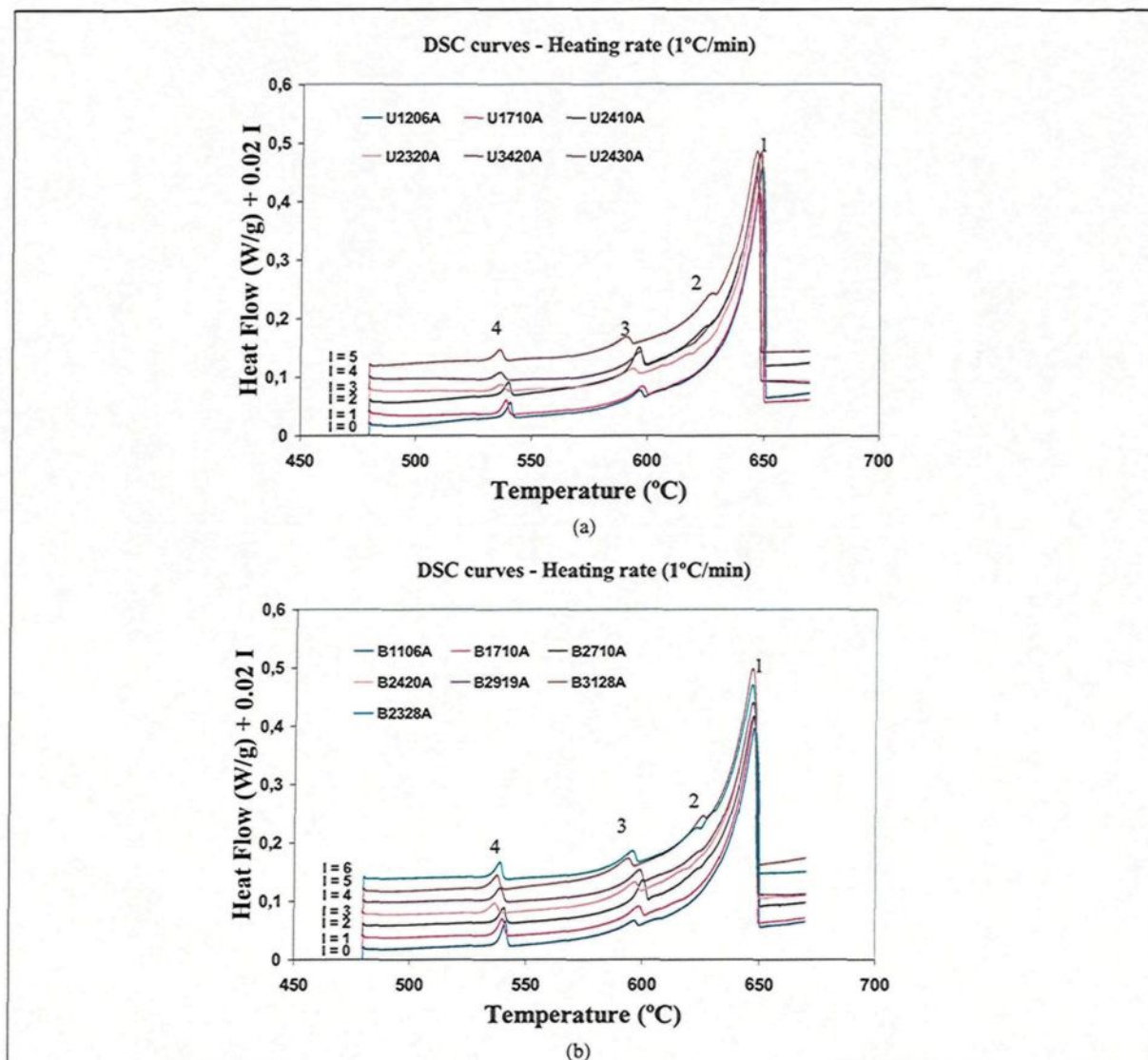
Figure 3. 18: DSC curves of various B206 alloys obtained under high cooling rate conditions.

Table 3. 7: Peak dissolution temperatures of various B206 alloys
a) Low cooling rate

Alloy Code	Peak Dissolution Temperature (degree Celsius)				
	1	**2**	**3**	**4**	**5**
B1106A	646.6	-	595.0	542.0	-
B1710A	646.5	-	595.5	541.6	-
B2710A	645.2	-	599.9	540.8	-
B2420A	643.3	-	594.0	536.9	513.8
B2919A	645.4	-	598.0	539.0	514.0
B3128A	645.5	622	592.8	536.4	513.6
B2328A	645.0	634	592.0	537.5	514.0

b) High cooling rate

Alloy Code	Peak Dissolution Temperature (degree Celsius)				
	1	**2**	**3**	**4**	**5**
B1106A	647.7	-	596.7	541.5	-
B1710A	647.3	-	598.4	540.3	-
B2710A	647.0	-	600.0	540.7	-
B2420A	646.7	-	596.7	536.7	-
B2919A	646.6	-	598.7	539.0	-
B3128A	646.0	627	593.5	537.7	-
B2328A	646.4	631	595.9	538.9	-

3.3 Discussion of the results

3.3.1 Solidification

High iron and silicon content lead us into a complex Al-Cu-Fe-Mn-Mg-Si system for which thermodynamic computational tools can be helpful to understand the solidification path. A computational algorithm calculating the solidification path in multiphase systems and using the mobility of each element to calculate the effect of back diffusion was developed by Larouche. [172] This scheme was used in this study with the software Thermo-

Calc. [173] Thermodynamic variables were computed with the database TTAL6 [174] and the mobility of elements were retrieved from the MOBAL1 database. [175] The simulations were first conducted by considering all possible phases of the database and assuming local equilibrium conditions at the liquid - solid interface. The scheme predicted the formation of the (Cu,Mn,Fe)(Al,Mg)$_6$ phase (called Al$_6$Mn) in all cases, but this phase was not observed in our samples. Backerud *et al.* [66] reported that the (CuMnFe)Al$_6$ phase precipitates at 549° C, *i.e.* immediately after the formation of primary aluminum dendrites in B206 alloys. Our cooling curves however, did not show any evidence of phase formation at this stage of the solidification process. Although some minor deflections are observed at the end of formation of the primary aluminum dendrites on the first derivative curves (Fig. 3.10a), it is really difficult to say if these deflections result from phase formation or from a thermal equilibrium process. According to global equilibrium calculations, this intermetallic phase is supposed to appear between 595°C and 614°C, depending on the alloy, and to disappear at around 580°C in a peritectic reaction. In addition, some minor peaks (peaks 2, Table 3.6) appear on the DSC curves at 622-634°C and 627-631°C for alloys B3128 and B2328 for samples cooled at the low rate and high rate, respectively. These peaks may result from the dissolution of partially transformed (CuMnFe)Al$_6$ phases (although they could not be identified in the microstructure) or their formation on heating. The ranges of precipitation temperature of (CuMnFe)Al$_6$ as predicted by calculations and those observed on the DSC curves are very wide compare to the differences in the end precipitation temperature (max of 3°C at low cooling rate and 5°C at high cooling rate) of the primary aluminum dendrites in these alloys (Table 3.4).

Based on these observations we believe that this phase is formed somewhere after the primary aluminum dendritic reaction and at a temperature above 610°C.

Likewise, the Scheil model, which does not consider any reaction of a solid phase, the scheme used in this work was not developed to consider the reaction of a specific solid phase with the liquid, although it can assume a sub-system larger than the liquid phase to calculate interfacial reactions. In order to simplify the calculations, we decided to reject phase Al_6Mn as a potential phase in the solidification path, which is the equivalent of saying that phase Al_6Mn did not nucleate in our samples. Considering that up to 1wt% of this phase should have formed before the peritectic reaction, one sould have obtained a clear peak in the cooling curves, but the latter did not show any evidence of secondary phase formation at this stage of the solidification process. The same thing was done for the $(Al,Si)_3(Fe,Cu,Mn)$ phase (called Al_3Fe) since this phase was not observed in any specimen. The simulations were thus carried out rejecting phases Al_6Mn and Al_3Fe. Calculations were made with the compositions given in Table 3.2, using secondary dendrite arm spacings and solidification times given in Table 3.4. The cooling rate in each case was taken as the solidification range divided by the solidification time. The same calculations were carried out for the higher cooling rate and will not be presented here because of their similarity with those presented for the lower cooling rate. It is worthwhile to mention, however, that the volume fractions of secondary phases obtained for the higher cooling rate were larger than those obtained for the lower cooling rate by 5 to 11% and the temperatures of precipitation did not differ from one to another by more than 1 K. The results of the simulations will be presented by first considering the formation of phases

β(FeCu) and α(MnFe), which may have a strong detrimental impact on the mechanical properties of the alloy.

Figure 3.19 presents the calculated volume fractions of α(MnFe) and β(FeCu) phases versus their temperature of precipitation for the alloys solidified at the lower cooling rate. A comparison between the results shows that the measured volume fractions of β(FeCu) are larger than the calculated values by a factor comprised between 1.0 and 1.9. For α(MnFe), the measured values are almost zero in all cases except for alloy B3128 where the measured value is 0.45%. The calculated volume fractions for this phase are all below 0.2% except for alloy B3128 which is 0.25%. The higher content of α(MnFe) phase in
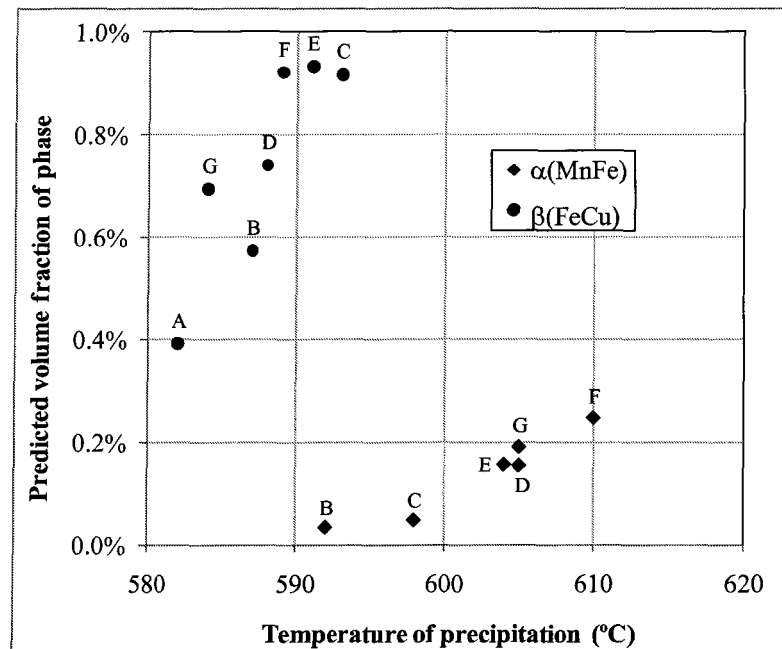
Figure 3. 19: Calculated volume fractions for alloys B1106 to B2328 solidified at the lower cooling rate.

alloy B3128 at low cooling rate was thus correctly predicted. For these two intermetallic phases, the measured volume fractions involved are always below 1.4%, so one could not expect to obtain a much better agreement for such low amounts of phase.

The measured volume fractions of the eutectic phase θ were larger than the calculated values by a factor ranging between 1.3 and 1.5. For instance, the maximum volume fraction of θ phase obtained experimentally was 4.08% in alloy B1710, while the calculated volume fraction for this alloy was 2.79%. The maximum calculated volume fraction of θ phase was 3.2% and was obtained in alloy B2328. The amounts of eutectic phase were thus satisfactorily predicted, considering the inherent difficulty of measuring volume fractions of secondary phases.

The measured and calculated liquidus were very close, differing by less than ± 1K. The onset temperatures of reaction 4, which corresponds to the experimental solidus, are in good agreement with the calculated onset temperatures of the following quaternary eutectic reactions:

Alloys B1106, B1710, B2710:

$$L \rightarrow Al + Al_2(AlCu) + Al_7Cu_2Fe + Mg_2Si \tag{3.1}$$

Alloys B2420, B2919, B3128 and B2328:

$$L \rightarrow Al + Al_2(AlCu) + Al_7Cu_2Fe + Al_5Cu_2Mg_8Si_6 \tag{3.2}$$
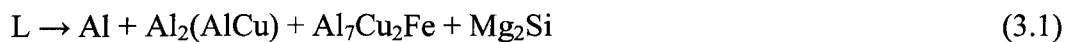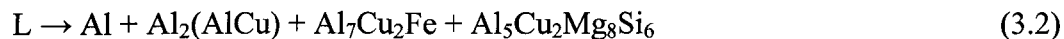
Indeed, the calculated temperatures were higher than the measured temperatures by 2 to 4 K, the largest error occurring for alloy B3128. The calculated mass fraction evolutions of the most important secondary phases are presented in Figure 3.20 for one of the

compositions studied (alloy B2420). The onset temperature of reaction 4 is highlighted on this figure by the vertical line at 513°C. At this temperature, a sudden and significant increase of θ phase occurred, which was just intense enough to cause a measurable deviation in the cooling rates. The theoretical true solidus of this alloy is 504°C and occurs after the formation of Mg_2Si starting at 510°C. This reaction could not be seen explicitly on the cooling curves because of the low mass fractions involved. Reactions 2 and 3 of Table 3.4 correspond respectively to the formation of $\beta(FeCu)$ and θ phases. The measured and calculated temperatures of precipitation of these two phases are significantly different, the calculated temperatures being 14 to 22 K higher for the $\beta(FeCu)$, and 7 to 9 K higher for the θ phase. These differences could not be reduced significantly by changing the
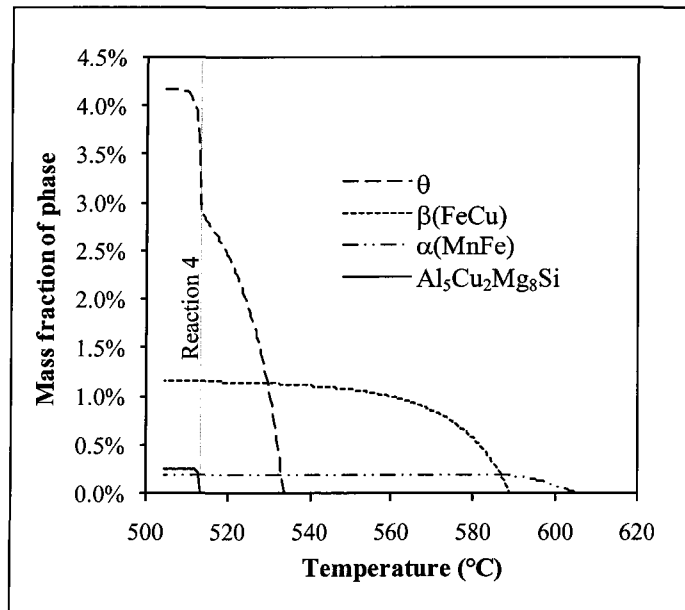
Figure 3. 20: Calculated mass fraction evolutions of 4 secondary phases observed in alloy B2420.

compositions inside the margins of error or by modifying the equilibrium conditions prevailing at the interface, as was done previously for AA6111. [172] Since the experimental temperatures are lower than the calculated ones, it is reasonable to think that these two phases experienced undercooling. The absence of a peak at around 600°C in the cooling curves in all alloys investigated at both low and high cooling rates, probably indicates that the amounts of α(MnFe) as well as Al_6Mn were not large enough to provoke a measurable deviation in the cooling rate. It is possible, however, that undercooling may have delayed the formation of α(MnFe) up to the point where the following reaction occurred:

$$L \rightarrow Al + Al_7Cu_2(Fe,Mn) + Al_{20}Cu_2Mn_3 + Al_{32}(Cu,Fe,Mn)_8(Al,Si)_4Si_2 \qquad (3.3)$$
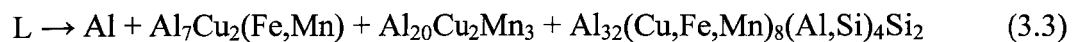
Notice that the phase $Al_{20}Cu_2Mn_3$ was not predicted by our simulations, except for alloy B1106 where a negligible amount (0.006%) was calculated. Inversely, this phase was not observed in the microstructure of alloy B1106 and was observed in only very small amounts in alloys B2420, B2919, B3128 and B2328. Mondolfo [56] predicted the formation of $Al_{20}Cu_2Mn_3$ in the (Al-Cu-Fe-Mn-Si) alloys system through reaction (3.4) without mentioning the temperature at which it occurs. Also he mentioned that no data was available on the distribution of phases involved and their fields of existence in the solid state.

$$L + (CuMnFe)Al_6 \longrightarrow Al + Cu_2FeAl_7 + Cu_2Mn_3Al_{20} + (Al)_{15}(CuFeMn)_3Si_2 \qquad (3.4)$$
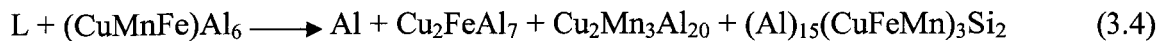
In Al-Cu alloys, Mg-containing phases generally form during eutectic or post-eutectic reactions. It is thus fairly reasonable to believe that the early stage of solidification is

controlled by the Al-Cu-Fe-Mn-Si system and reaction (3.4) could have taken place, considering the closeness of the reaction products in Mondolfo's equation and those in equation (3.3) predicted by calculations. If α(MnFe) phase was not observed in significant quantities at low cooling rate, much larger amounts were observed at the higher cooling rate for alloys B2420, B2919, B3128 and B2328 as indicated in Table 3.4b. Very small amounts of β(FeCu) phase were obtained for alloys B3128 and B2328 at the higher cooling rate and surely this explains why these specimens contained more than 1.3% of α(MnFe). The model has not predicted such low amounts of β(FeCu) and volume fractions of α(MnFe) above 0.3% for these two alloys. In fact, one has to reject phase β(FeCu) in our calculations to obtain amounts of phase approaching those measured for these cases.

One particularity in the cooling curves obtained for alloys B3128 and B2328 at high cooling rate is the onset temperatures of reaction 2, which were 10 K higher than for any of the other alloys. Since the α(MnFe) phase had much larger volume fractions than the β(FeCu) phase in these cases, the peak of reaction 2 observed in the corresponding cooling curves would indicate the start of the formation of α(MnFe). Adding a driving force to the nucleation of α(MnFe) phase in the model to simulate undercooling did not reduce the calculated volume fraction of β(FeCu). Modifying the sub-system at the solid-liquid interface also did not permit to obtain volume fractions of α(MnFe) larger than β(FeCu).

Since growth kinetics phenomena other than back-diffusion were not modeled in the computational scheme, we decided to conduct DICTRA [176] simulations to see if limited diffusion in the liquid could explain the onset temperature of the α(MnFe) phase. Even by reducing the mass diffusivity of the heavier elements by 10, the temperature of nucleation

of the α(MnFe) in alloy B3128 did not change significantly. Notice that α(MnFe) started to form in these simulations when the volume fraction of the primary phase reached 73%, so the size of the remaining liquid was just in the order of 8 μm, promoting a good mixing.
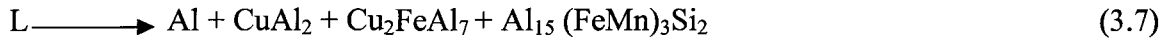
Before going further in the discussion, we will summarize the findings. With the silicon content equal to or less than 0.1%, *i.e.* for alloys B1106, B1710, and B2710, iron precipitated as β(FeCu) phase under both cooling rates employed. With increasing silicon content, α(MnFe) started to precipitate. The rate of precipitation of α(MnFe) at the expense of the β(FeCu) phase increased with the cooling rate and at around 0.3% Si and high cooling rate, almost all iron precipitated as α(MnFe). The reactions described by Equations 3.3 and 3.4 indicate that 3 intermetallic phases compete together when they grow simultaneously at the expense of the liquid phase. The phase $Cu_2Mn_3Al_{20}$ was rarely formed in the microstructure. This scarcity may be explained by two reasons. First, manganese has a great affinity with α(MnFe) and Mondolfo [56] reported that if the silicon composition in the liquid is greater than 1% in Al-Cu alloys, α(MnFe) will form over $Cu_2Mn_3Al_{20}$ compounds. It is therefore likely that at the temperature where this reaction occurred, the enriched melt contained sufficient silicon to promote the precipitation of α(MnFe). This melt enrichment in silicon may also explain the higher precipitation of phase Q in this alloy. The second reason is related to the crystal structure of the phases. Most intermetallic phases grow by stepwise nucleation on specific crystallographic planes. There are, of course, differences in the growth rate of different intermetallic crystals. The phase α(MnFe) has a cubic structure and will nucleate and grow more easily and more quickly than the tetragonal β(FeCu) phase and the orthorhombic $Cu_2Mn_3Al_{20}$ phase. The

first one should therefore dominate at high cooling rate, provided that the chemical composition allows the formation of this phase. Based on Mondolfo's assumption for the promotion of α-(Fe,Mn) phases, one should have expected more α-(Mn,Fe) phases in the B2328 alloy than in B3128 alloy. But the reverse was found. We do not have a clear explanation for this. May be the formation of the α-(Mn,Fe) phases does not depend solely on the percentage of silicon in the liquid metal, but also on the iron level and the ratio of Fe/Si, with a ratio closer to one being more favourable. Also, in aluminum alloys, silicon has been reported to have a growth restriction factor of 5.74 that is about twice that of iron which is 2.86. [177] This restriction factor may have played a role in the growth of the α-(Mn,Fe) phase, delaying the growth with more silicon present, which resulted in lower fraction of α-(Mn,Fe) phase in the B2328 alloy. Manganese is known to stabilize α(MnFe) but in this case, the effect of cooling rate on stabilization of α(MnFe) phase is the dominating factor due to the lower manganese content of the alloy. In the case of the β(FeCu) phase, the precipitates have a thin platelet morphology, which indicates that the rate of transformation of this phase is essentially governed by the mobility of the large facets. This certainly contributes in minimizing the volume fraction of that phase when the cooling rate is high so that iron atoms have the possibility of being captured by another intermetallic phase with faster growth kinetics.

In the eutectic region, the θ phase precipitates together with either α(MnFe) or β(FeCu) or both according to the following reaction:

$$L \rightarrow Al + Al_2(AlCu) + Al_7Cu_2(Fe,Mn) + Al_{32}(Cu,Fe,Mn)_8(Al,Si)_4Si_2 \qquad (3.5)$$

In this alloys system, Mondolfo [56] and Belov [57] also predicted the precipitation of θ phase together with either $\alpha(MnFe)$ or $\beta(FeCu)$ or both according to the following reactions:

$$L \longrightarrow Al + CuAl_2 + Cu_2FeAl_7 \tag{3.6}$$

$$L \longrightarrow Al + CuAl_2 + Cu_2FeAl_7 + Al_{15}(FeMn)_3Si_2 \tag{3.7}$$

$$L \longrightarrow Al + CuAl_2 + Al_{15}(FeMn)_3Si_2 \tag{3.8}$$
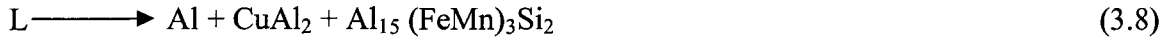
Notice that at this stage of solidification, the growth rates of $\alpha(MnFe)$ and $\beta(FeCu)$ are very small, as can be seen from Figure 3.20 below the eutectic temperature ($533C°$). Indeed, the large portion of $\alpha(MnFe)$ or $\beta(FeCu)$ phases is forming at temperatures above the eutectic point, as confirmed from Figure 3.21, where both iron phases are present after soaking and quenching a sample of alloy B2328 at 560°C.

In the final stage of solidification (post-eutectic), the θ phase precipitates together with Mg_2Si and $\beta(FeCu)$ through the reaction given by Eq. (3.1) for all alloys at high cooling rate, and for alloys B1106, B1710, and B2710 at low cooling rate. For alloys B2420, B2919, B3128 and B2328, $Al_5Cu_2Mg_8Si_6$ precipitated at low cooling rate through the reaction given by Eq. (3.2). The precipitation of $Al_5Cu_2Mg_8Si_6$ became significant at 0.3%Si (alloys B3128 and B2328). The phases Mg_2Si and pure silicon were found agglomerated in many places with other phases containing oxygen, probably silicon oxides (Table 3.5). These agglomerated phases were labeled (Mg,Si) in Figures 3.11 to 3.15, irrespective of the fact that they had oxygen or not. X-ray spectroscopy revealed that (Mg,Si) zones contain a level of oxygen comprised between 1 and 22 wt%. It thus became difficult to identify the phases unambiguously. After investigation, it was found that oxygen was brought in by Al-Si master alloy as shown by the presence of oxygen in the
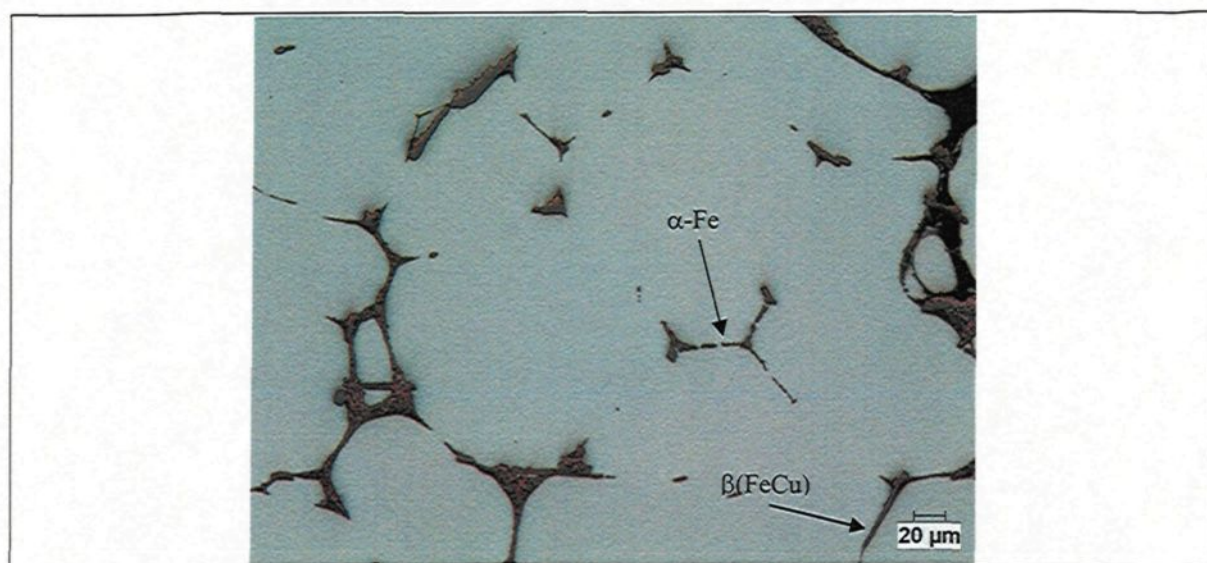
Figure 3. 21: Microstructure of B2328 alloy after soaking and quenching at 560 °C.
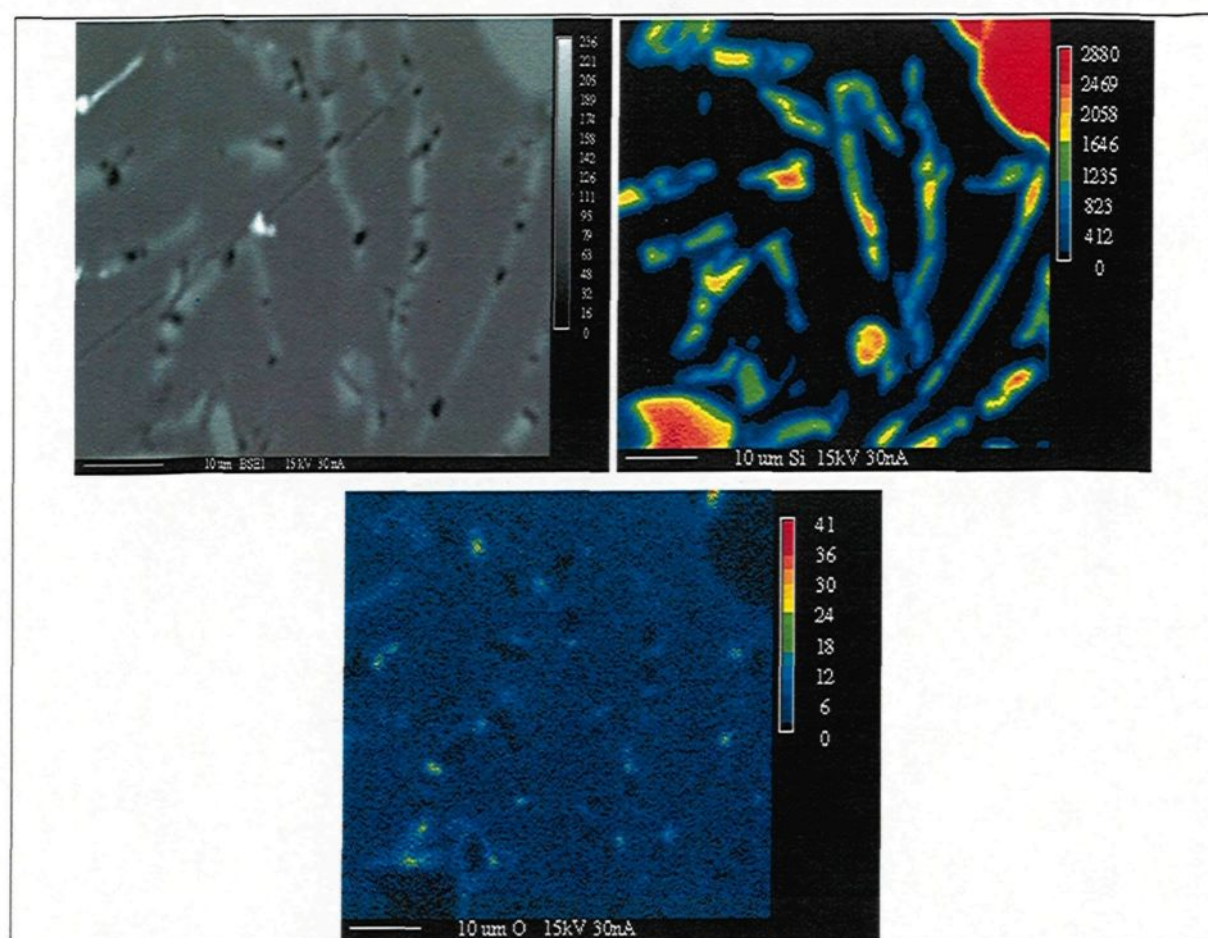
Figure 3. 22: AlSi master alloy, Backscaterred image and mapping for silicon and oxygen.

WDS mapping of the master alloy (Figure 3.22). Fortunately, most of the silicon was not combined with the oxygen; but it is clear that the effective silicon content was a little bit below the concentration given in Table 2. From this observation, it was concluded that commercial master alloys should always be investigated carefully before use.

Increasing silicon from 0.06% to 0.1% decreases the solidification range by 4°C and 7°C at low and high cooling rate respectively, but further increase has little effect. At the same time, the pre-eutectic precipitation temperature of iron phases increases substantially (Table 3.4). This early precipitation may be explained by increased consumption of silicon by these phases, as shown by the WDS mapping of iron and silicon for alloys B1106, B1710 and B3128 in Figures 3.23, 3.24 and 3.25, respectively.

Dendrite arms spacing shows lowest value for alloy B2710 and highest value for alloy B2328 (Table 3.4). This is related to the growth restriction factor effect of iron and silicon which are 2.86 and 5.74, respectively. [177] The Fe/Si ratio is at the maximum in alloy B2710 and minimum in alloy B2328. Therefore, the iron factor will be dominant in alloy B2710, while the silicon factor will be dominant in alloy B2328. The restriction being lower in alloy B2710, dendrites grow faster and at the coherency point, the fraction solid is lower compare to that of alloy B2328 as shown in Table 3.4. Phases containing iron were found to increase in proportion to the nominal iron content. At the same time, the volume fraction of Al_2Cu was found to increase with increasing silicon content and cooling rate (Table 3.6). This is because silicon reacts with iron and thus frees copper, which consumption by Al_7FeCu_2 phase decreases. At high cooling rate when silicon is increased to 0.2% and above, it partly contributes to free copper through the formation of α-(Fe,Mn),
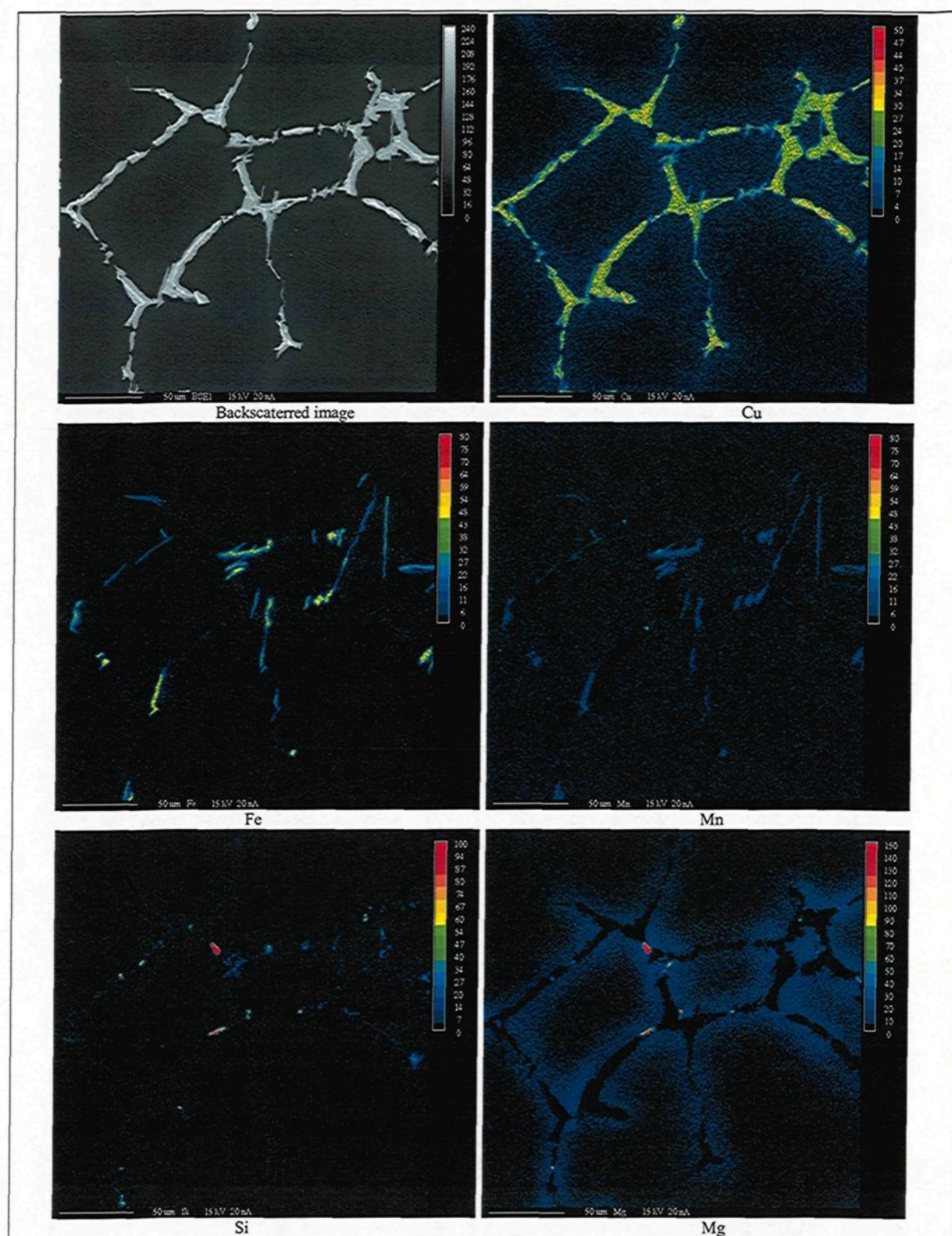
Figure 3. 23: Alloy B1106, Backscaterred image and mapping for different elements.
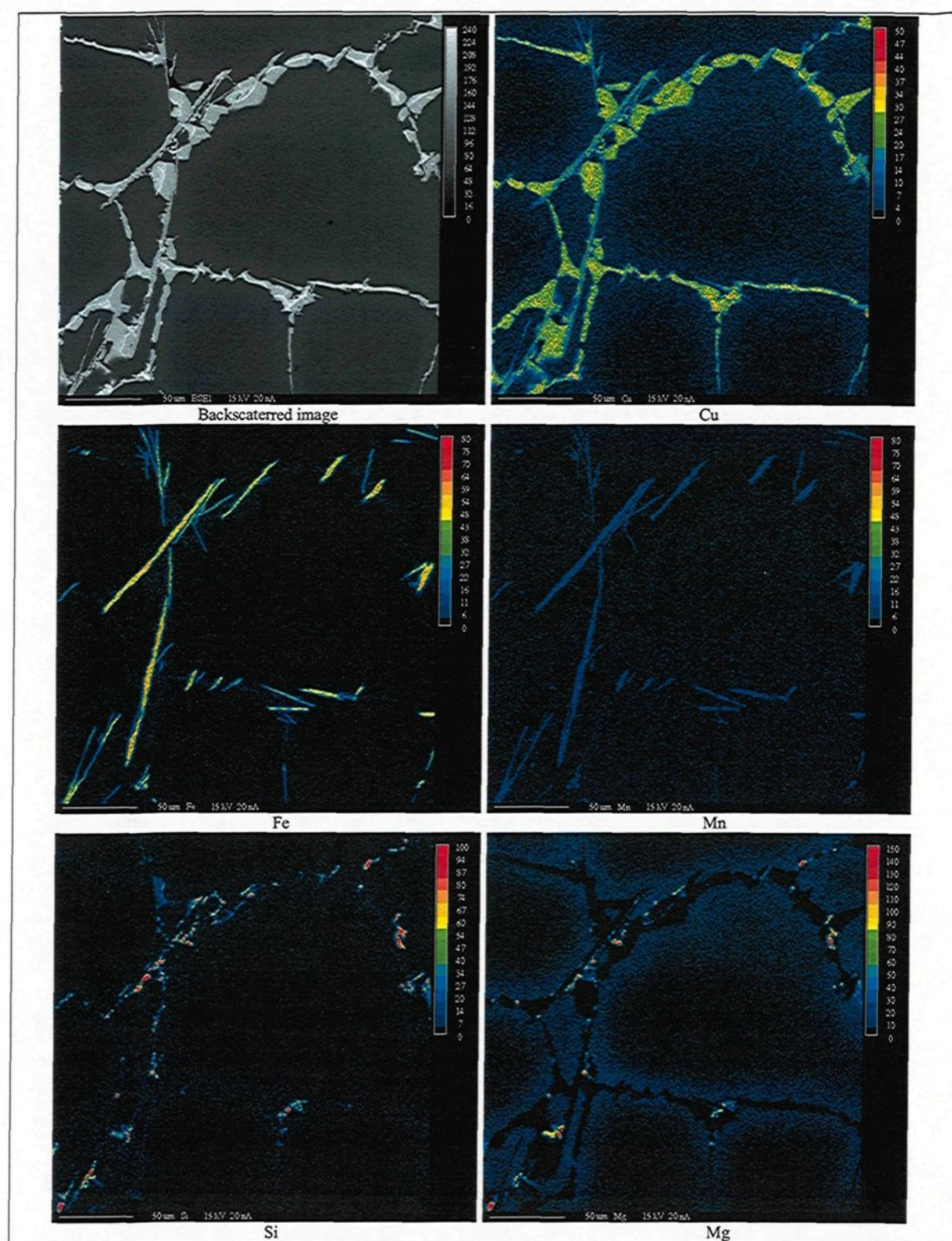
Figure 3. 24: Alloy B1710, Backscaterred image and mapping for different elements.
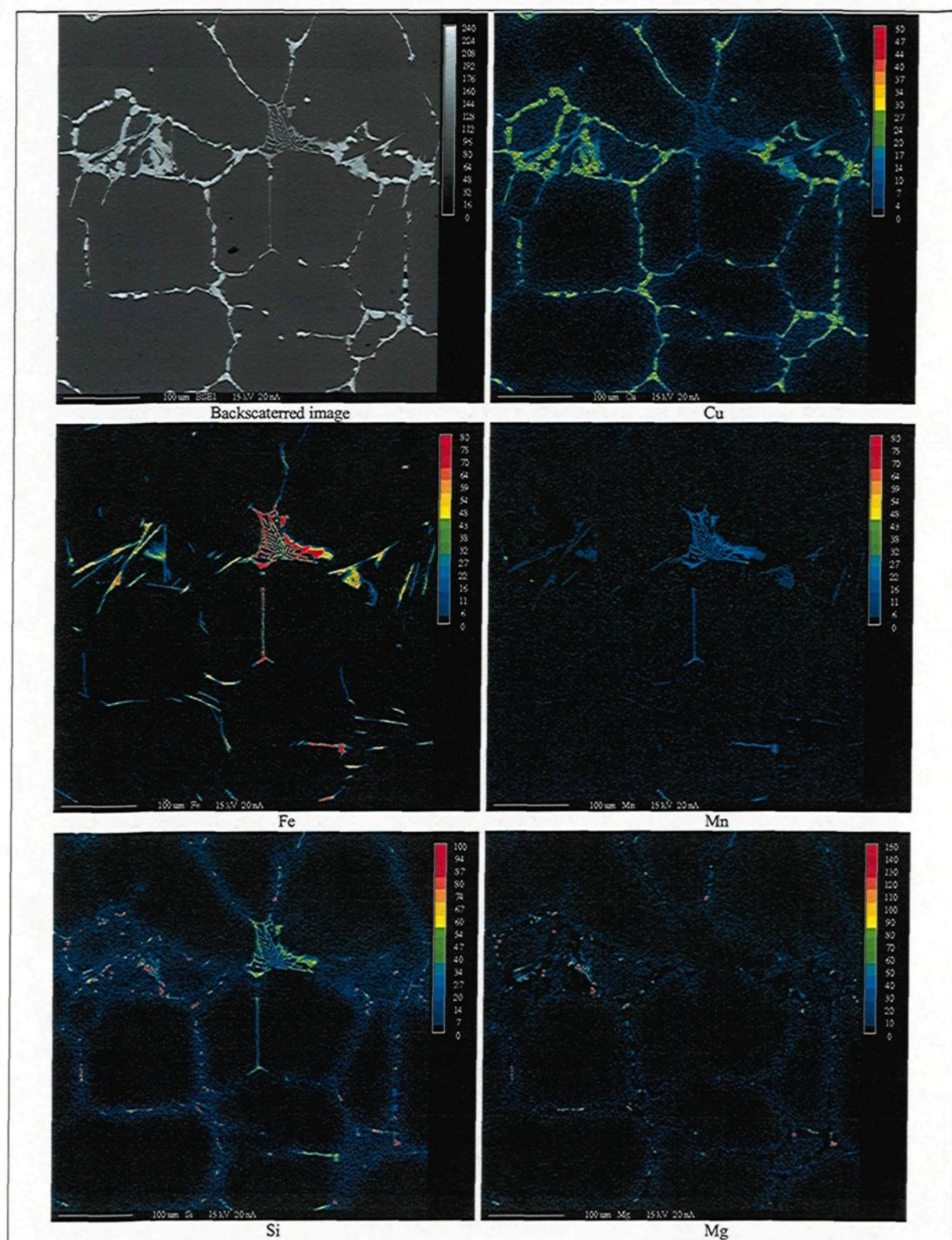
Figure 3. 25: Alloy B3128, Backscaterred image and mapping for different elements.
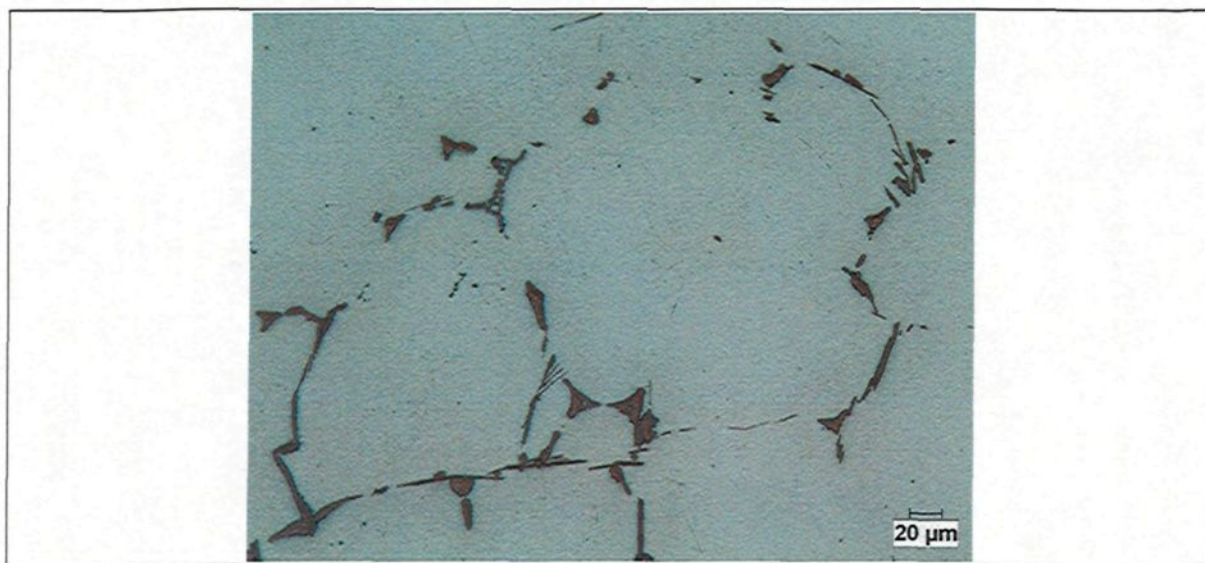
Figure 3. 26: Microstructure of alloy B2328 after soaking and quenching at 520 ºC.

and partly favours the precipitation of the (Mg,Si) phase, as shown in Fig.3.23-3.25, where the quantity of magnesium dissolved in the matrix decreases with increasing silicon. If silicon has to be used at such high percentage, it will probably be interesting to also increase magnesium for strengthening purposes.

3.3.2 DSC

The peak temperatures obtained during the heating of samples in the DSC were in good agreement with the onset temperatures calculated with the multiphase back diffusion scheme. The liquidus temperatures differ by less than 1.6 K, except for alloy D at low cooling rate, which shows a distinct behaviour, as can be seen in Figure 3.17. Near the solidus (around 513ºC), the temperatures of the quaternary eutectic (reaction 4; Eq. 3.1 and 3.2) differ also by less than 1.6 K. Notice, however, that the peaks were found only for

alloys D, E, F, and G previously cooled at the lower rate. The absence of peaks around 513°C results from the dissolution of the Mg_2Si and silicon phases during the heating process, as this can be deduced from Figure 3.26 where these phases are difficult to find after soaking and quenching at 520°C. Notice also that incipient melting did not occur in this sample. It seems that a heating rate of 1 K/min was slow enough to allow sufficient time for diffusion and dissolution. For the samples cooled at the higher rate, no peak was observed in any of them. Dissolution was complete in these samples due to the small size of the particles. The presence of residual phases in low cooling rate solidified samples containing at least 0.2%Si, and which amount increases with silicon, reveals the presence of either grown (Mg,Si) phase particles which have no sufficient time to diffuse, or $Al_5Cu_2Mg_8Si_6$ phase particles which were remained insoluble during solution treatment of Al-Si (A413.1) alloy at 500°C for times up to 24h. [65] For alloys with up to 0.2%Si, this phase is more likely to dissolve during a three step heat treatment. But when silicon is increased to about 0.3%, especially with a Fe/Si ratio less than one (alloy B2328), the volume fraction becomes important and the possibility of incipient melting during heat treatment becomes a serious threat. The agreement obtained between the calculated precipitation temperatures of β(FeCu) and θ phases and the corresponding DSC peak temperatures is better than the agreement obtained between the former and the thermal analysis results. For the precipitation of the β(FeCu) phase, the temperatures differ between 3.8 and 13.7 K, and for the precipitation of the θ phase, they differ between 3 and 6.9 K. The DSC peak temperatures for these two transformations are all above the calculated onset temperatures. Some of these discrepancies can be explained by the

chemical compositions of the DSC samples, which may be different from the nominal compositions of the alloy because of the macrosegregation occurring during the solidification of the thermal analysis samples. One has to recall also that a slow reheating process is not a perfect inverse solidification path, as demonstrated by the dissolution of the low melting phases. Some minor peaks (peaks 2) appear on the DSC curves at between 622° and 634°C for alloys B3128 and B2328 shown in Fig. 3.17 and Fig. 3.18. These peaks may result from the formation and dissolution of (CuMnFe)Al$_6$ phases (although they could not be identified in the microstructure). The calculated precipitation temperature of (CuMnFe)Al$_6$ at equilibrium by Thermo-Calc with the TTAL6 database and those observed on DSC curves differ by a gap comprised between 5.2 and 20.3 K. Some of the DSC experiments were repeated and the cooling curves obtained showed variable temperatures of precipitation, supporting the idea that the main source of deviation lay in the variations in the composition of the DSC samples. Some of the DSC experiments gave temperatures of precipitation in very good agreement with the multiphase back diffusion scheme, giving us the confidence that the thermodynamic database is not an issue regarding the accuracy of the model.

3.4 Summary

The solidification path of 206 type aluminium alloy was investigated to see the influence of minor additions of iron and silicon when different cooling conditions are applied. It was found that the content of iron intermetallics β(FeCu) and α(MnFe) are

largely dependant upon the cooling rate. Important undercoolings for the precipitation of these phases were observed at a moderately low cooling rate (1 K/s before liquidus) for all compositions investigated and a very few β(FeCu) platelets were obtained at a high cooling rate (4 K/s before liquidus) when the Si content was 0.3wt% and the Fe content did not exceed 0.3wt%. In order to precipitate iron as α(MnFe) phase, a minimum of 0.2%Si was required, with a Fe/Si ratio of one being preferred, the optimum ratio being 0.3wt%Fe/0.3wt%Si. High cooling rate was essential to prevent the formation of the β(FeCu) phase and this is likely caused by the low mobility of the large facets of the β(FeCu) platelets. The limit of 0.3wt% Fe when the alloy contains 0.3wt% Si is therefore conditional to castings undergoing rapid solidification. The phases Al_6Mn and Al_3Fe were not observed in the specimens and this is probably due to the difficulty of these phases to nucleate from the melt. A multiphase back diffusion model would have predicted the formation of phase Al_6Mn in the seven compositions investigated of the alloys and very few Al_3Fe in some of them. The inaccuracy of the database used and the limited diffusion of the elements in the liquid were not considered to be the cause of the discrepancies between the calculated and measured temperature of precipitations of the iron intermetallics. Undercooling is very likely the main cause to explain the differences. The solidification of these alloys may be divided in three main regions: dendritic (including postdendritic and pre-eutectic), eutectic, and post-eutectic. Table 3.8 summarizes the possible reactions based on the present observations and simulation results, as well as data reported by Mondolfo [56], Belov et al. [57] and Backerud et al. [66] in the literature.

Table 3. 8: Possible reactions during solidification of various B206 alloys

		Reactions	Suggested Temp (°C)
Dendritic [T_L - T_E]	1	L ⟶ α-Al Formation of aluminum dendrite	650-647
	2	L ⟶ Al + (CuMnFe)Al$_6$ (Postdendritic)	> 610
	3 a	(Pre-eutectic) L + (CuMnFe)Al$_6$ ⟶ Al + Cu$_2$(Fe,Mn)Al$_7$ + Cu$_2$Mn$_3$Al$_{20}$ + (Al,Cu)$_{15}$ (FeMn)$_3$Si$_2$	602-594
	3 b	*L→Al+Al$_7$Cu$_2$(Fe,Mn)+Al$_{20}$Cu$_2$Mn$_3$ + Al$_{32}$(Cu,Fe,Mn)$_8$(Al,Si)$_4$Si$_2$*	*592-610*
Eutectic [~ T_E]	4 a	L ⟶ Al + CuAl$_2$ + Cu$_2$(Fe,Mn)Al$_7$	544-542 (545-533)*
	4 b	L ⟶ Al + CuAl$_2$ + Cu$_2$(Fe,Mn)Al$_7$ + (Al,Cu)$_{15}$ (FeMn)$_3$Si$_2$	541-539 (546-533)*
	4 c	L ⟶ Al + CuAl$_2$ + (Al,Cu)$_{15}$ (FeMn)$_3$Si$_2$	540-539 (547-533)*
	4 d	*L→Al+Al$_2$(AlCu) + Al$_7$Cu$_2$(Fe,Mn) + Al$_{32}$(Cu,Fe,Mn)$_8$(Al,Si)$_4$Si$_2$*	*531-539*
Post-eutectic [T < T_E]	5 a	L ⟶ Al + CuAl$_2$ + Mg$_2$Si + Cu$_2$(Fe,Mn)Al$_7$	515 *508 -513*
	5 b	L ⟶ Al + CuAl$_2$ + Mg$_2$Si + Al$_5$Cu$_2$Mg$_8$Si$_6$ + Cu$_2$(Fe,Mn)Al$_7$	515 (~ 515)*

Suggested temperatures are taken from DSC experiments and the marked temperatures (*) from Mondolfo [56] and Belov et al. [57]. Reactions in italic are predictions from simulations. The terms T_L and T_E refer to the liquidus temperature for the formation of aluminum dendrites and the Al-CuAl$_2$ eutectic temperature in the present experiments.

CHAPTER 4
STUDY ON HOT TEARING BEHAVIOUR

CHAPTER 4
STUDY ON HOT TEARING BEHAVIOUR

4.0 Aim

Hot tearing is an inherent defect in aluminium-copper alloys and is deleterious to mechanical properties of the material. The aim of this study was to understand how it can be influenced by additions of both iron and silicon in B206 aluminum alloys.

4.1 Experimental procedures

4.1.1 Materials

The base alloy was a B206 ingot produced by Rio Tinto Alcan and its chemical composition is shown in Table 4.1. In keeping with the results obtained from the solidification studies, only B alloys (defined in section 3.1) were considered. Compositions were modified using aluminum1020 and commercial master alloys (Al-50%Si, Al-25%Fe, Al-25%Mn, Al-50%Mg, and Al-50%Cu). Chemical analyses of the various compositions prepared were carried out using an optical spectrometer, and are presented in Table 4.2.

A Constrained Rod Casting (CRC) mould was used in this part of the study. It is a permanent mould made of cast iron (Figure 4.1). The mould cavity is capable of producing four 12.7mm diameter cylindrical constrained rods with nominal lengths of 50.8mm (bar A), 88.9mm (bar B), 127mm (bar C), and 165.1mm (bar D). The bars are constrained at one end by a sprue and at the other end by a spherical riser (feeder) of 19.05mm diameter.

The cylindrical rods are separated from each other by a distance of 38.1mm center to center. The melt is fed to the rods through a 177.8mm long sprue. To reduce experimental uncertainties, the mould was heated to 200°C and the mould cavity was cleaned and coated with graphite prior to each series of tests.

4.1.2 Melt treatment and casting

The as-received B206 ingots were cut into smaller pieces, cleaned, dried and melted in charges of 52 kg each to prepare the required alloys. The melting process was carried out in a SiC crucible of 55 kg capacity, using an electrical resistance furnace. The inner surface

Table 4. 1: B206 Alloy Composition (wt%)

Cu	Si	Fe	Mn	Mg	Ti	Zn	Ni	Al
4.60	0.10*	0.06	0.40	0.25	< 0.01	0.00	< 0.01	balance

* Si was out of specification

Table 4. 2: Alloy codes and chemistry

Alloy Code	wt% of Alloying elements					
	Cu (%)	Fe (%)	Si (%)	Mn (%)	Mg (%)	Ti (%)
B1213	4.68	0.12	0.13	0.24	0.32	0.02
B2312	4.70	**0.23**	0.12	0.24	0.30	0.01
B3511	4.54	**0.35**	0.11	0.25	0.30	0.01
B3223	4.74	0.32	**0.23**	0.24	0.29	0.03
B3134	4.73	0.31	**0.34**	0.24	0.32	0.04
B2121	4.72	**0.21**	**0.21**	0.24	0.29	0.02
B2332	4.95	0.23	**0.32**	0.27	0.35	0.01
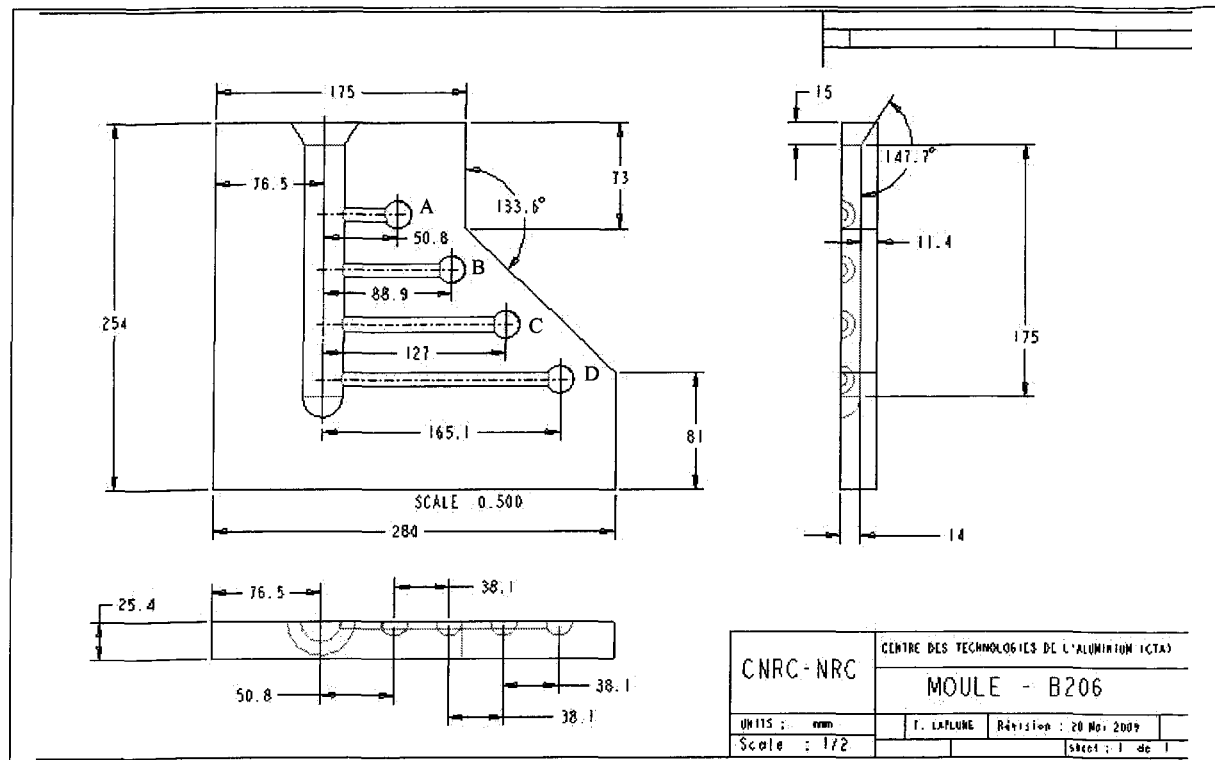
Figure 4. 1: Schematic diagram of the constrained Rod Casting (CRC) Mould.

of the crucible was coated with a layer of refractory coating to avoid melt crass-contamination. The melting temperature was maintained at 750 ± 5°C. All alloys were grain-refined by adding Ti as Al-5%Ti-1%B in rod form. All melts were degassed using pure, dry argon injected into the melt for 20 minutes by means of a rotating graphite degassing impeller, at 150 rpm rotation, to ensure homogeneous mixing of the additives. After degassing, the melt was kept under argon protective atmosphere to avoid oxidation. Actual casting took place by pouring the degassed melt in the CRC mould preheated at 450°C. During the experiments, mould temperature was monitored with a thermocouple, which was embedded into the body of the mould. The castings were removed from the mould after complete solidification of the top of the sprue. For each alloy, a sampling for

chemical analysis was carried out during the first and the last pourings to obtain the corresponding mean alloy melt composition. Four castings were produced per alloy. The first casting was used to stabilize the mould, and the three others which presented the same casting characteristics were considered for hot tearing indexation.

4.1.3 Hot tearing indexation

Cracks were inspected visually and under a microscope. They were classified according to the degree of severity into four categories as surface crack, light crack, severe crack, and complete crack. Hot tear severities are described below and corresponding photographs are presented in Figure 4.2.

- **a-** Surface Crack: a crack located on the surface and which extends over a maximum of half the circumference of the bar.

- **b-** Light Crack: a surface crack that extends over the entire circumference of the bar.

- **c-** Severe Crack: a crack that extends over the entire circumference of the bar and in depth.

- **d-** Complete Crack: a complete or almost complete separation of the bar.

Hot tear sensitivity of the alloys were quantified using an index called Hot Tearing Sensitivity (HTS) index. To obtain this index, first, each category of crack severity was assigned a numerical value (C) given in Table 4.3. Then, bars of different lengths were each given a different numerical value as listed in Table 4.4. The numerical values of the bars were given based on the fact that the probability of cracking increases as the length of the bar increases. It is indeed well known that longer bars are more prone to hot tearing
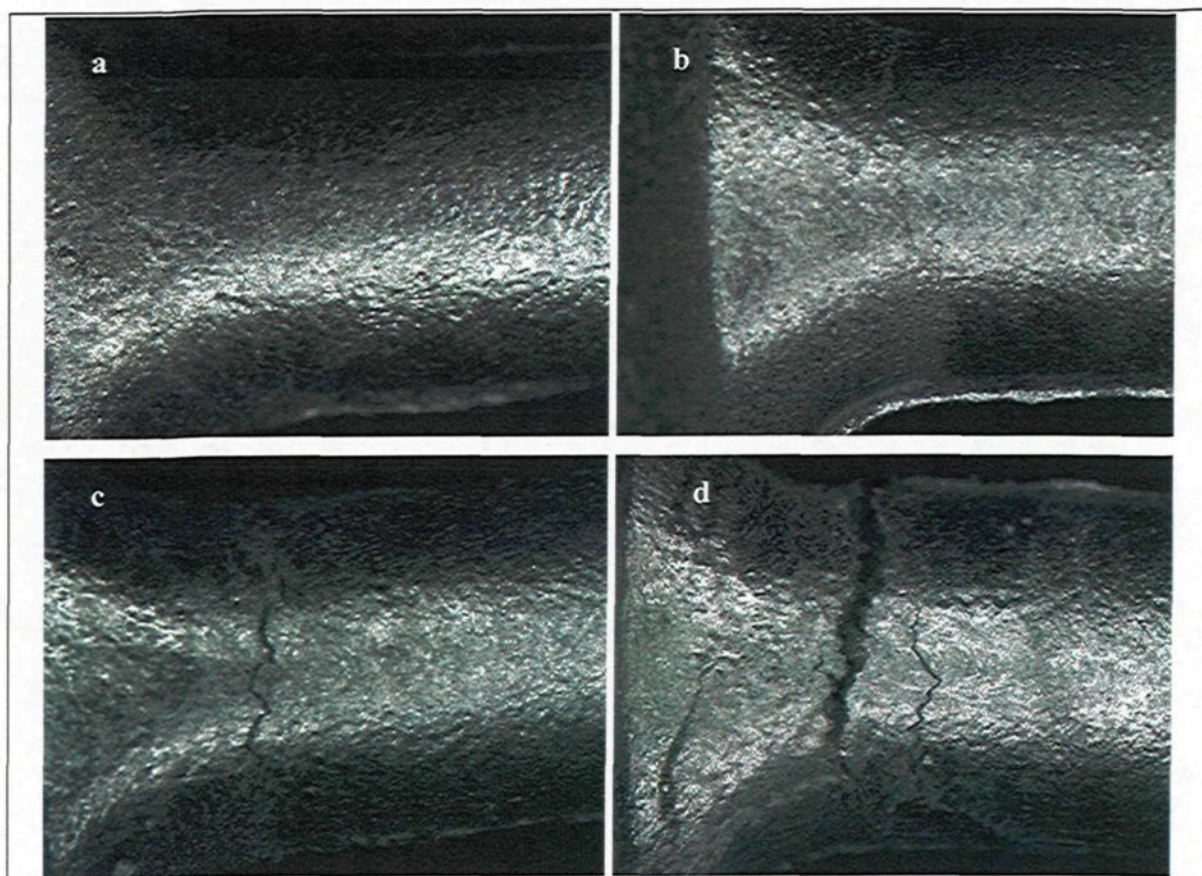
Figure 4. 2: Photos of typical hot tearing with different levels of severity:
(a) Surface crack, (b) Light crack,(c) Severe crack and (d) Complete crack.

Table 4. 3: Cracks categories and hot tearing numerical values (C)

Categories	Numerical Value (C)
Not Cracked	0
Surface Crack	1
Light Crack	2
Severe Crack	3
Complete Crack	4

Table 4. 4: Bars and associated numerical values (L)

Bar (length, in)	Numerical Value (L)
A (2.0)	1/2
B (3.5)	1/3.5
C (5.0)	1/5
D (6.5)	1/6.5

than shorter ones. The value of HTS for a sample is given by:

$$HTS = \sum_{i=A}^{D}(C_i.L_i)$$ (4.1)

Where C_i and L_i are, respectively the assigned numerical values for respectively the severity of crack and the length of the bar i =A, B, C or D.

The best alloy will have an HTS = 0, while the worst will have an HTS = 4.56

After indexation, samples were prepared from these bars for tear surface analysis and microstructural characterization of the corresponding alloys.

4.1.4 Sample preparation and characterization

Constrained-rod castings of the alloys are shown in Figure 4.3. It can be seen that the locations of cracks are similar from alloy to alloy. In order to study the constituents and structure of the alloys for hot tearing characterization, the specimens were taken as close as possible to the hot-tear location as shown in Fig.4.4. Samples for tear surface analysis were segments of completely broken bars containing hot tears that were removed usually at the junctions of the bars and the sprue (Fig 4.2d, Fig 4.4). For uncompletely broken bars, breaking was completed to expose the tear surface before removal of the segment. During the whole process, the hot tear surfaces were protected from any damage and contamination. Fractographic examinations were conducted using a SEM equipped with EDS and WDS facilities (see section 3.1.2.) operating at an acceleration voltage of 20 kV, a filament current of 48μA, and a working distance of around 15 mm. After SEM examination, the broken pieces were carefully brought back together at the tear interface,
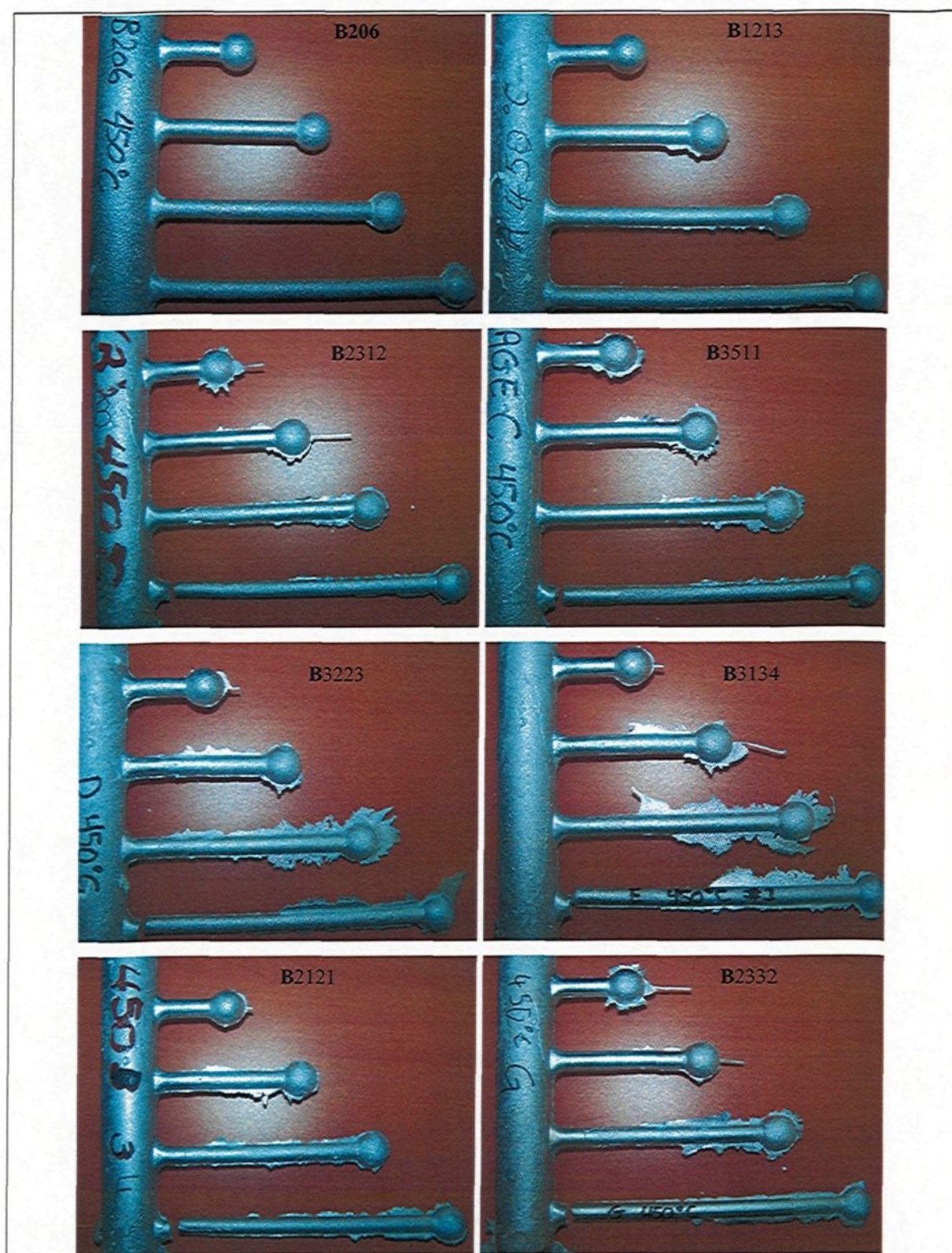
Figure 4. 3: Photos of typical CRC castings of the different alloys studied.
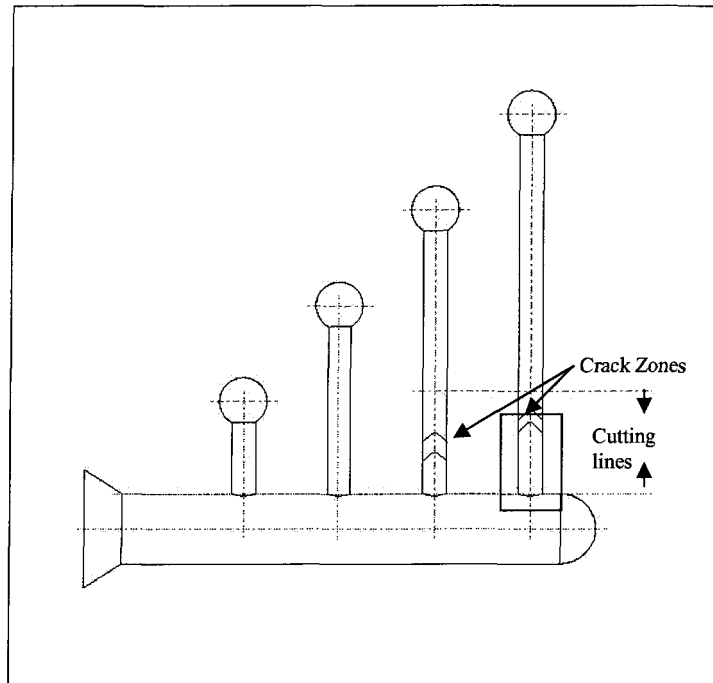
Figure 4. 4: Section of the casting area used for preparing specimens for tear surface analysis and microstructural characterization.

mounted in bakelite resin and polished following the procedures described in section 3.1.2. The polished samples were then examined to identify and to analyze the morphology and distribution of second phase constituents around the tear surface and the grain size using the optical microscopy facilities described in section 3.1.2.

4.2 Results and discussion

4.2.1 Hot tearing sensitivity

The HTS values obtained for the different alloys are given in Table 4.5 and these values are plotted against the Fe to Si ratio in Figure 4.5. The results show that the susceptibility to hot tearing is highly influenced by the iron to silicon ratio and the nominal concentration

of the single elements. The best resistance is obtained with both a ratio close to one and low concentrations of iron and silicon. The resistance decreases as this ratio differs from one. The higher the ratio, the worse the resistance to hot tearing, especially at a ratio of about two and above. It is worth mentioning that the experimental results obtained in this investigation were reproducible, which demonstrates the ability of the CRC mould to reveal the hot tearing susceptibility of these alloys.

Table 4. 5: HTS of different alloys

Alloy Code	Bar A		Bar B		Bar C		Bar D		HTS
	C	L	C	L	C	L	C	L	
B206	0	1/2	0	1/3.5	0	1/5	2	1/6.5	0.31
B1213	0	1/2	0	1/3.5	1	1/5	3	1/6.5	0.66
B2312	0	1/2	0	1/3.5	2	1/5	4	1/6.5	1.02
B3511	0	1/2	0	1/3.5	3	1/5	4	1/6.5	1.22
B3223	0	1/2	0	1/3.5	0	1/5	4	1/6.5	0.62
B3134	0	1/2	0	1/3.5	0	1/5	4	1/6.5	0.62
B2121	0	1/2	0	1/3.5	0	1/5	4	1/6.5	0.62
B2332	0	1/2	0	1/3.5	0	1/5	4	1/6.5	0.62
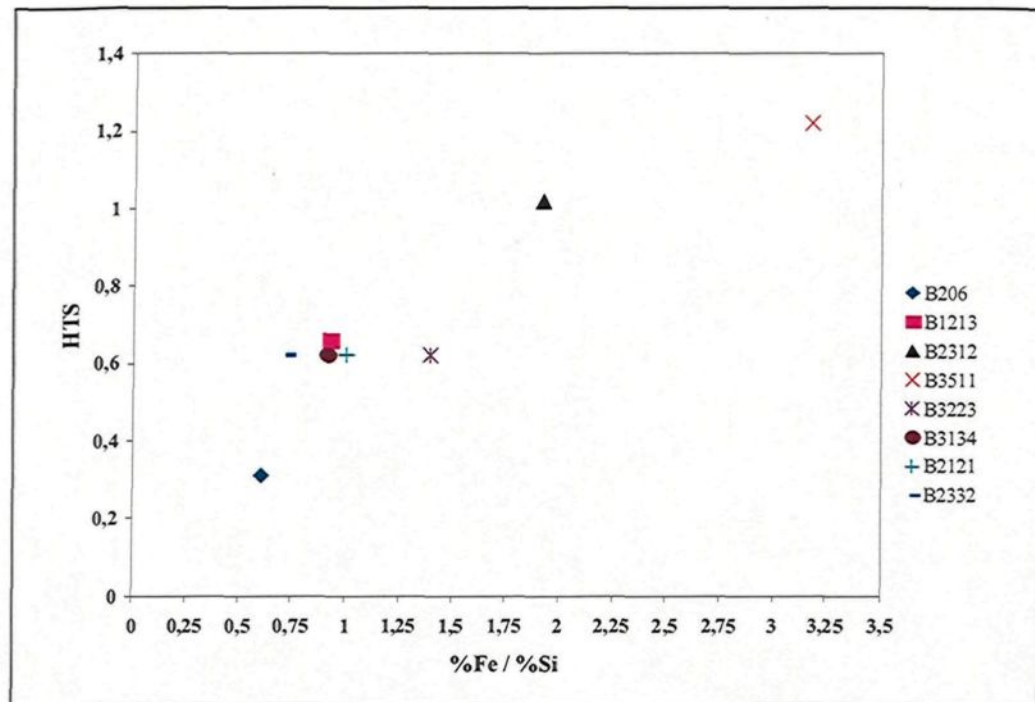
Figure 4. 5: HTS as a function of iron to silicon ratio.

4.2.2 Hot tear surface analysis

The objective was to analyze and determine the hot-tear features and to relate the fractography of the tear surface to the probable causes and mechanisms of hot tearing. Hot tear surfaces may reveal the sequence of events preceding the failure, allowing to correlate the fracture surface characteristics of the alloys to their solidification characteristics.

The fracture surface analysis was carried out on completely broken bars of the alloys B2312, B3511, B3223, B3134, B2121, B2332, and on the partially broken bar of the alloy B1213. The macroscopic photographs of the hot tear surfaces of these alloys are shown in Appendix C. Usually, stereo microscopes provide a good contrast that easily differentiates the fracture surfaces of different alloys. But these photographs do not show clear evidence of differences in the fracture surfaces of these alloys. Tear surfaces were, therefore, observed under SEM and the microstructure around the tear observed under an optical microscope.

Pictures taken near the surface and at the center of the partially broken bar of alloy B1213 are presented in Figures 4.6a & 4.6b respectively. The tear zones include iron-intermetallics platelets, globular θ phase particles and frozen liquid on primary aluminum dendrites. Pictures of completely broken bars of alloys B2312, B3511, B2121, B3223, B3134 and B2332 are presented in Appendix D and include some or all the constituents present in the B1213 alloy sample. During solidification studies, it was found that iron-intermetallics phases precipitates mainly at the pre-eutectic stage of the solidification process, while θ phases mainly precipitated during eutectic and post-eutectic reactions. The presence of eutectic phases on the tear surfaces of alloys B1213, B2312, B2121, B3134

and B2332 suggest that tearing occurred before solidification was complete, but at a temperature lower than the onset temperature of the eutectic reaction (< 540°C). The similarity in shape (globular) of θ phase particles and their small sizes results from eutectic precipitation and insufficient time to growth due to rapid solidification. At this point, the dendrite coherency point had been reached and dendrite separation was necessary for tearing to occur. On the other hand, globular θ phases are completely absent on the tear surfaces of alloys B3511 and B3223 (Figure 4.7). The tear surfaces of these alloys include essentially iron-intermetallics platelets and frozen liquid on primary aluminum dendrites and at grains boundaries. Electron dispersive spectrometry of the frozen liquid as presented in Figure 4.8 for alloy B3511 shows a composition close to that of the θ phase. The small size of the iron platelets suggest that tear possibly occurred during the early stages of the pre-eutectic precipitation (~590°C). One should also notice the difference in concentration and size of globular θ phases near the surface and towards the center of alloy B1213. Near the surface the concentration of θ precipitates is low and their size is small, while at the center the concentration is high and their size is significantly larger. In this case, the bar was not completely cracked and the difference in observations between the center and the periphery of the cracked surface likely results from the different local intergranular separation experienced in each zone.
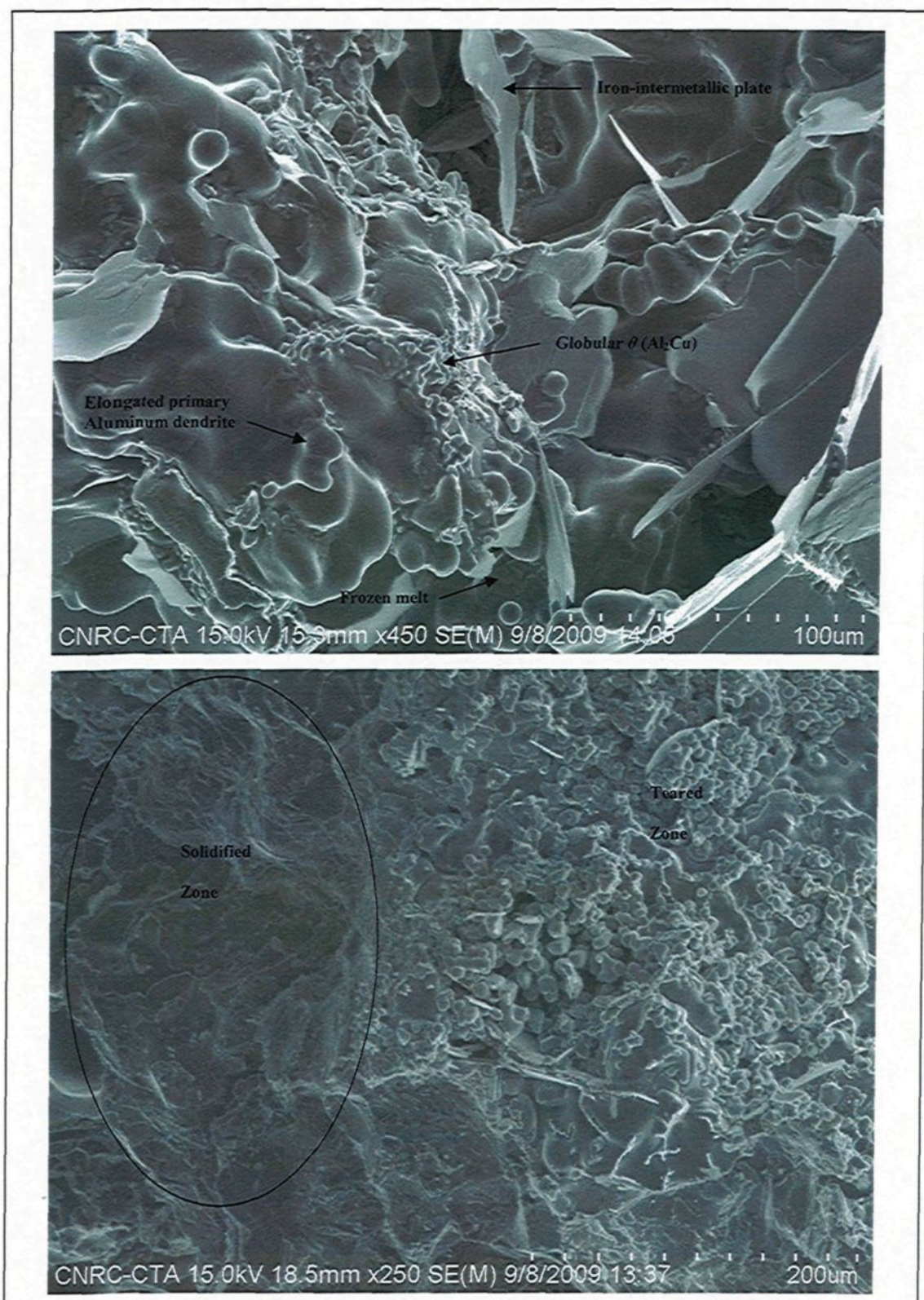
Figure 4. 6: SEM photos of partially broken bar of alloy B1213 (a) near the surface (tear zone) (b) center.
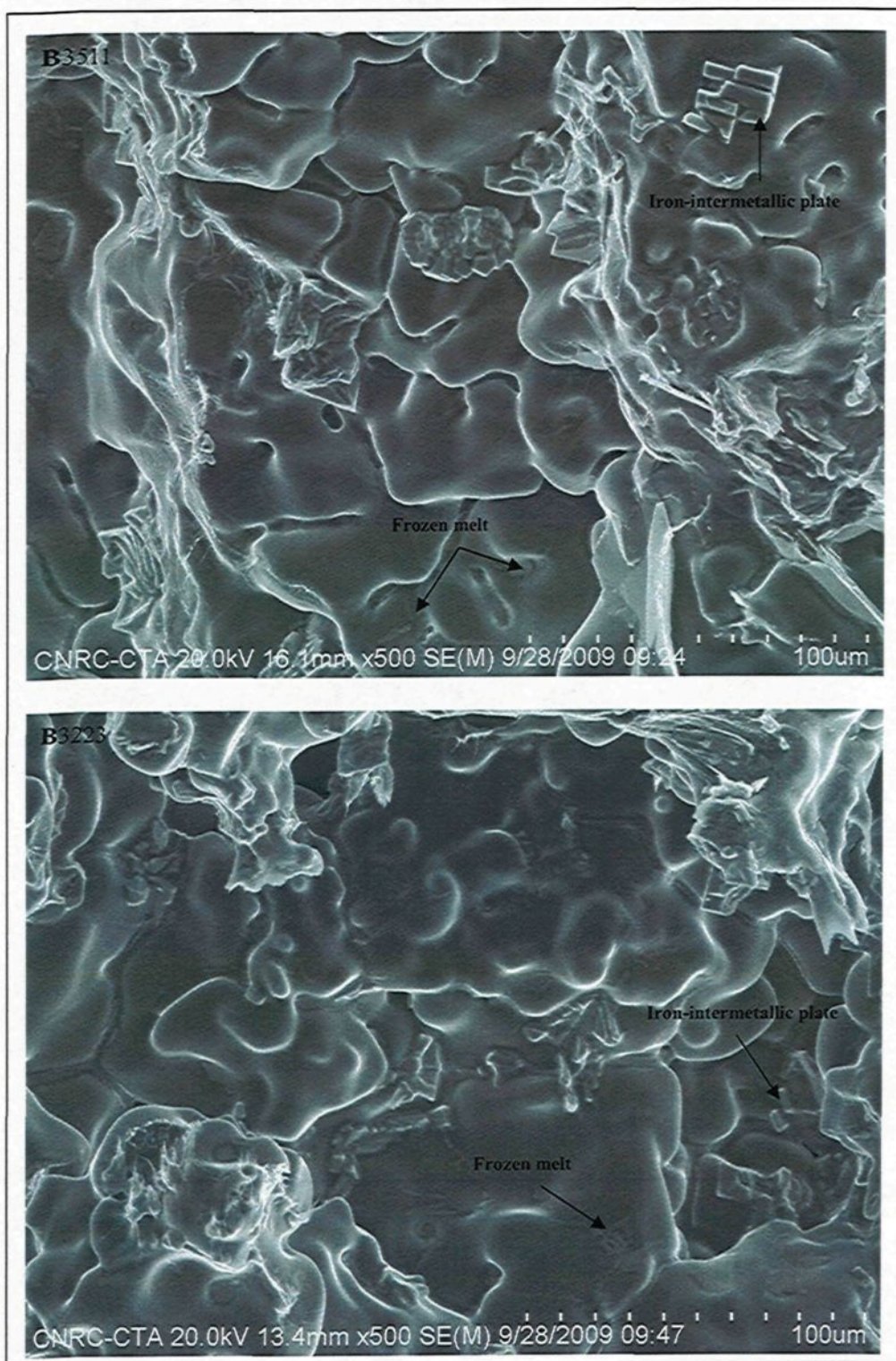
Figure 4. 7: SEM photos of completely broken bars of alloys B3511 and B3223.

Element	Weight%	Atomic%
O K	2.90	6.34
Mg K	1.29	1.86
Al K	52.02	67.49
Si K	0.21	0.27
Fe K	0.44	0.27
Cu K	43.14	23.76
Totals	100.00	
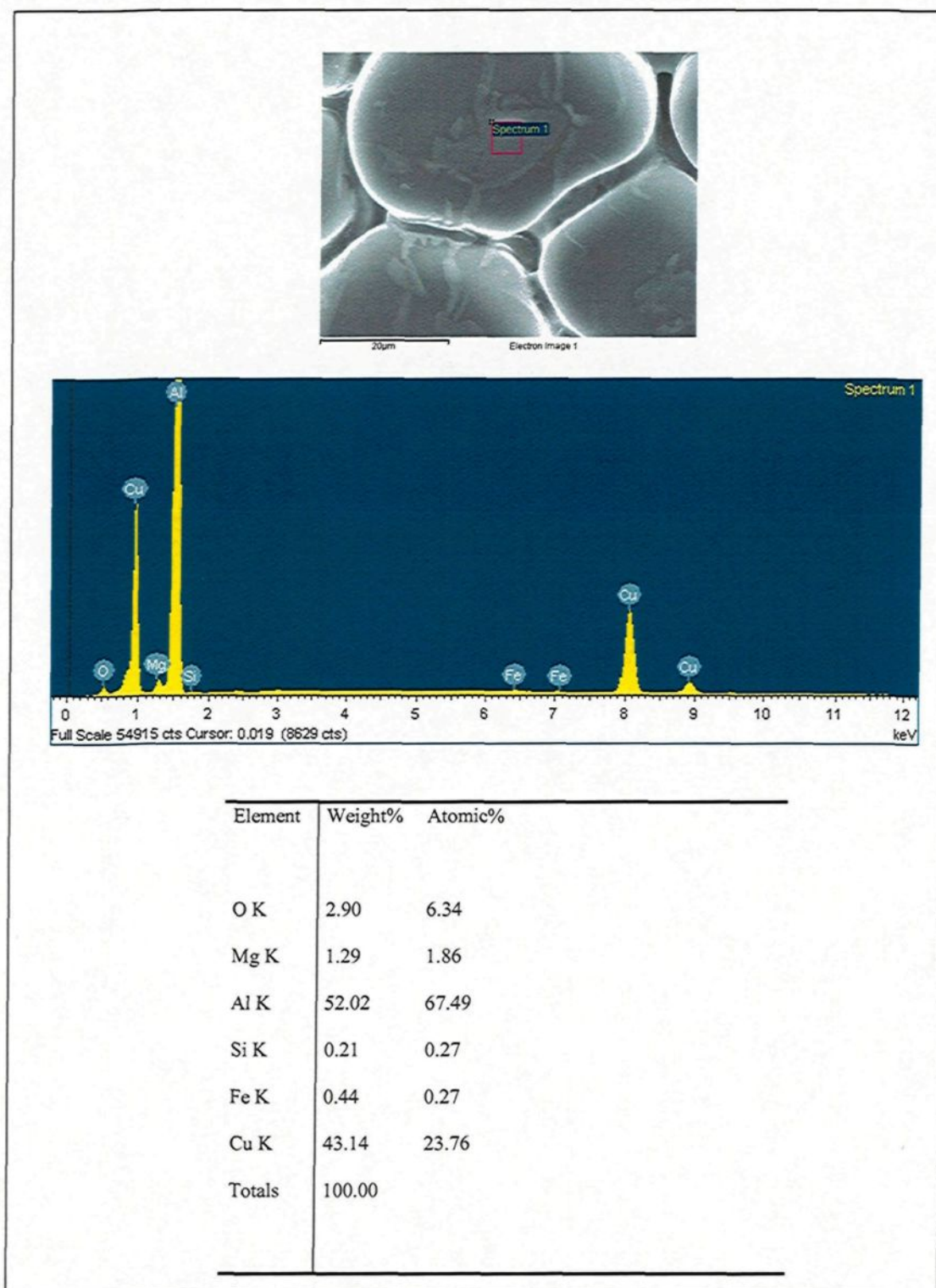
Figure 4. 8: Energy Dispersive Spectrometry of frozen liquid in alloy B3511.

Figure 4.9 shows the crack morphology and the microstructure obtained for a second identical casting of alloy B1213, the first one being used for surface examination. Secondary phases are found agglomerated along the plane perpendicular to the axis of principal tensile stresses. Also, large porosities are present in this region. Usually, solidification of castings starts by the formation of a solid shell at the interface of the melt and the mould. At this time, the center of the casting is still liquid. Freezing continues by inward growth of the skin. At the junctions of the bars and sprue, the shell zone is submitted to a higher stress because of stress concentration. The corresponding strains may be thermal, elastic or plastic. Thermal strain may be associated with volume contraction resulting from the liquid-solid phase change in metals or to the coefficient of thermal expansion. Elastic and plastic strains are linked to the mould restriction of the metal to contract freely. If the strength of the metal shell cannot accommodate these strains, surface tears may occur at the junctions. One should also remember that in the CRC mould used in this study, the bars are constrained at one end by a sprue and at the other end by a spherical riser (feeder). These constraints from the sprue and the spherical riser create at the junction a concentration of tensile stresses nearly parallel to the solidification front (Fig .4.4). [96] The resultant tensile stress is first relaxed by grain boundary sliding, which allows the liquid phase to form intergranular films with their thickness increasing in the direction of the principal tensile stress, and decreasing in other directions. These liquid films have their interface oriented perpendicularly to the direction of tensile stresses (Fig. 4.9b). The stability and quantity of these films will delay or inhibit dendrite interconnection, leading to the formation of large iron-intermetallics and solidification

porosities observed along the tear regions. These porosities, often called microporosities, are created by insufficient feeding from the liquid network connecting them.
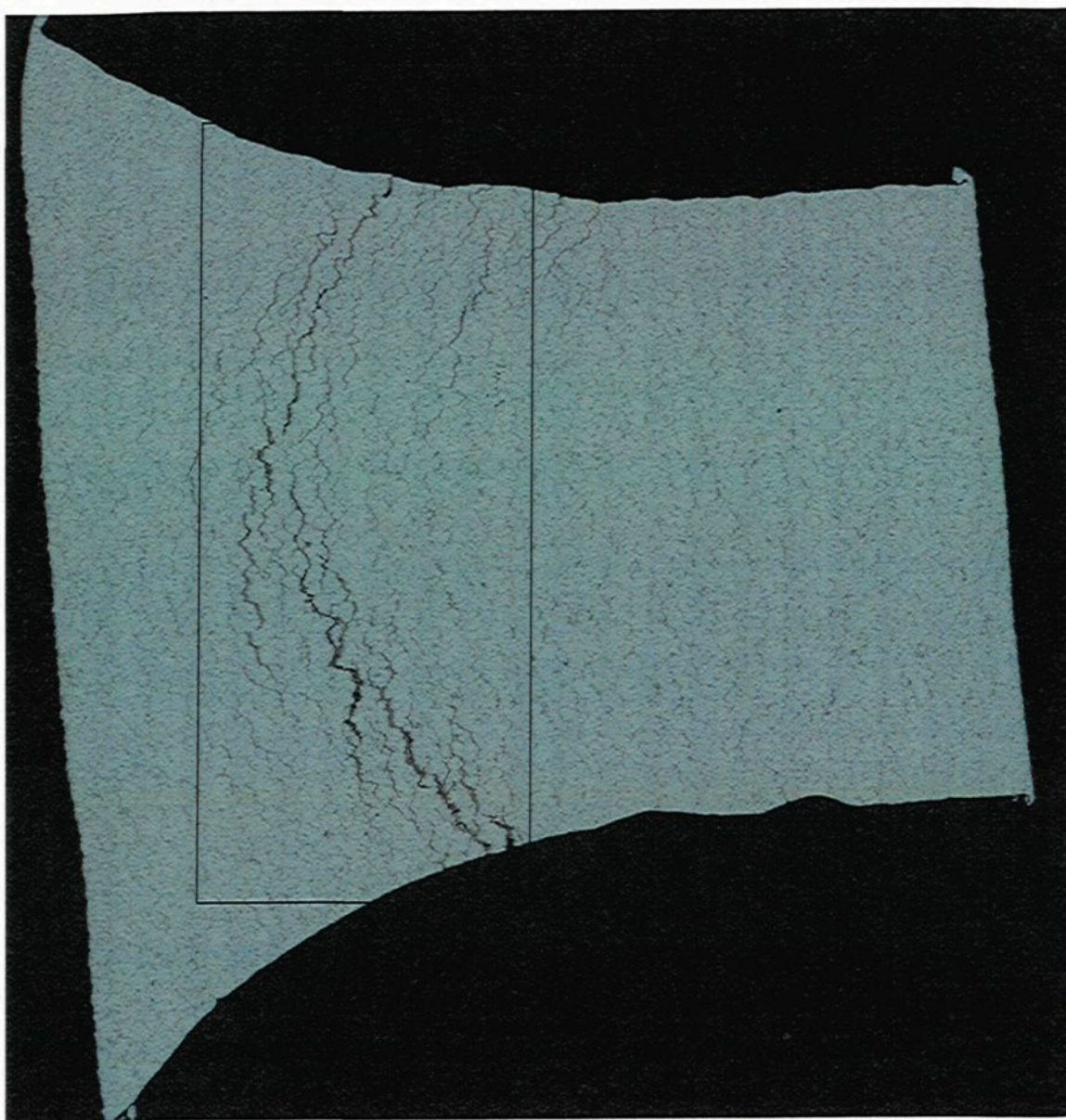
Figure 4. 9a: Microstructure of alloy B1213 at the junction of the sprue and bar D showing the agglomeration of secondary phases and large porosities along the tear plane (mosaique building).

Figure 4.9b: Enlarged portion of Fig 4.9a.
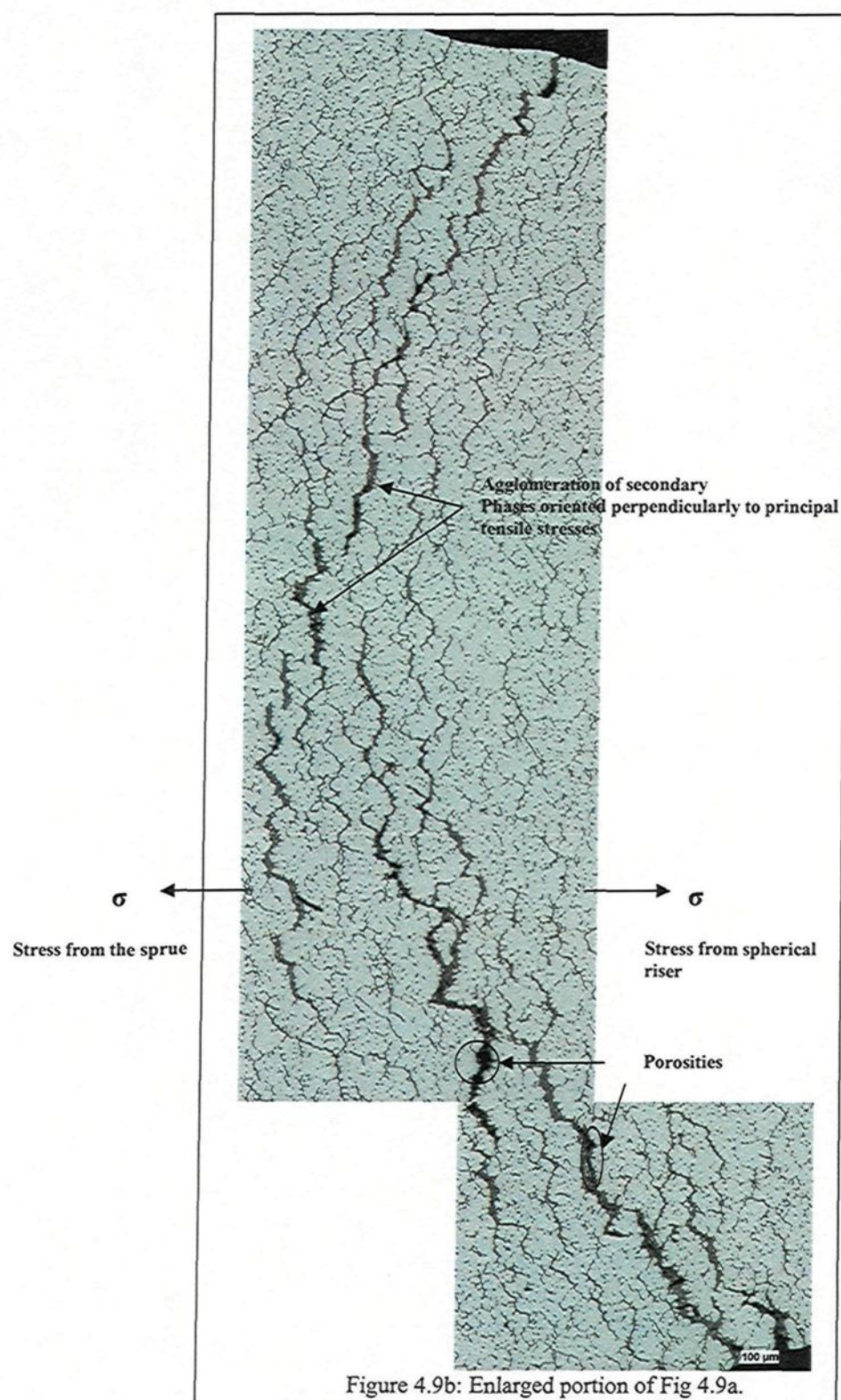
Indeed, from a metallurgical point of view, resistance to hot tearing of metals and alloys has long been proportionally associated to the amount of liquid present at the eutectic temperature and their solidification ranges.[87,88,93,94] Therefore, the fraction liquid evolution during solidification of these alloys were calculated from the model developed by Larouche, [172] which was introduced in section 3.3. The average cooling rates were evaluated by dividing the solidification interval with the solidification time, the latter being estimated from dendrite arm spacing (DAS) measurements conducted on alloy B206. The following relationship was used (Eq. 4.2).

$$DAS = A \cdot V_c^{-n}$$ (4.2)

where A and n are empirical parameters and V_c is the cooling rate (K/s).

Eskin et al. [181] determined for the binary alloy Al-4.3%Cu that A and n were respectively 76.1 and 0.40 with DAS given in μm. The composition of this alloy was near the composition of alloy B206 used in this investigation, so the values given above for A and n were used. Based on the DAS measured on alloy B206, a cooling rate of 341 K/min and a characteristic solidification time of 25.1 s were estimated for specimens cast in the CRC mould. These parameters were used for all compositions considering that cooling conditions were the same for all and that the difference of compositions had only marginal effects on thermophysical properties. The calculated fraction liquid at the last stage of solidification is presented in Fig. 4.10 for the different alloys. One can see that at the eutectic temperature, less than 10% liquid remains for all these alloys, placing them in the vulnerable range (10-1% liquid). This vulnerability range was suggested by Clyne and Davies, [178,179] and has been successfully applied by Campbell and Clyne [180] and Forest and

Bercovici [89] to experimental results with a high degree of reliability. Since we assumed cooling rate to be constant, the differences in temperature at 10% liquid and 1% liquid or temperature ranges (ΔT) of alloys in the vulnerable range can be substituted to the time spent in this range. By plotting the vulnerable temperature range ΔT of these alloys against the Fe/Si ratio (Fig. 4.11), it is evident that the time spent in this vulnerable range is really influenced by the Fe/Si ratio. As this ratio gets closer to one, the time is reduced. The higher is this ratio, the longer is the time spent, especially at a ratio of about two and above. It is interesting to notice the similarities between Figures 4.5 and 4.11. Of course the vulnerable range theory provides an accurate scientific base to the physical determination of the hot tearing sensitivity of alloys. It simply implies that the Fe/Si ratio determines the resistance of the alloy to hot tearing by controlling the amount of eutectic liquid and the time spent in the vulnerable regime. This is logical with the fact that creep is the main deformation mechanism in hot tearing, which is largely activated by grain boundary sliding. This mechanism has a damaging effect beginning as soon as a stress is applied. If the stress is not relaxed, the damage cumulates with time until rupture occurs. The time spent in the vulnerable range seems therefore to be a good criterion to compare the hot tearing susceptibility of alloys. Still, comparing Fig. 4.5 and Fig. 4.11, one may notice that alloy B2328 shows less resistance to hot tearing than that predicted theoritically. This could be explained by another factor very important to consider; *i.e* the grain size. Figure 4.12 shows the microstructure obtained in the vicinity of the cracks. Alloys B1213, B3223, B2121 and B3134 have fine grains compare to that of alloys B206, B2312, B3511 and B2332. Alloys
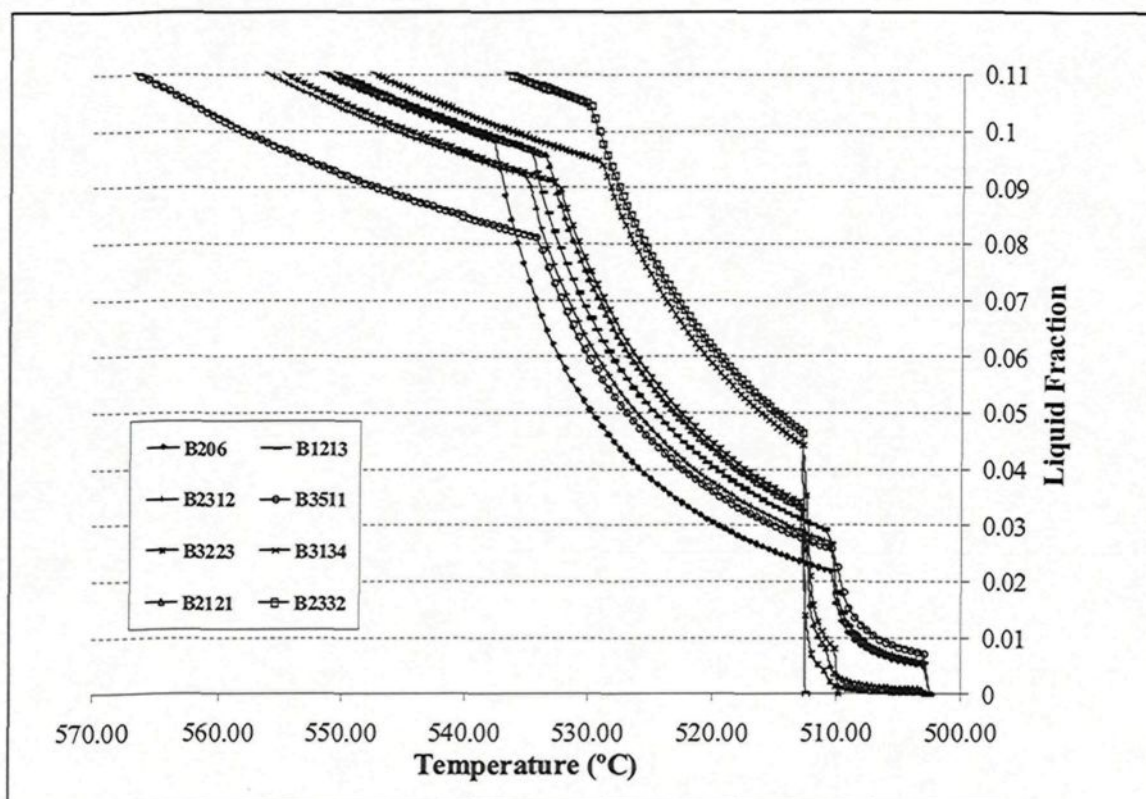
Figure 4. 10: Evolution of the liquid fraction as a function of temperature.
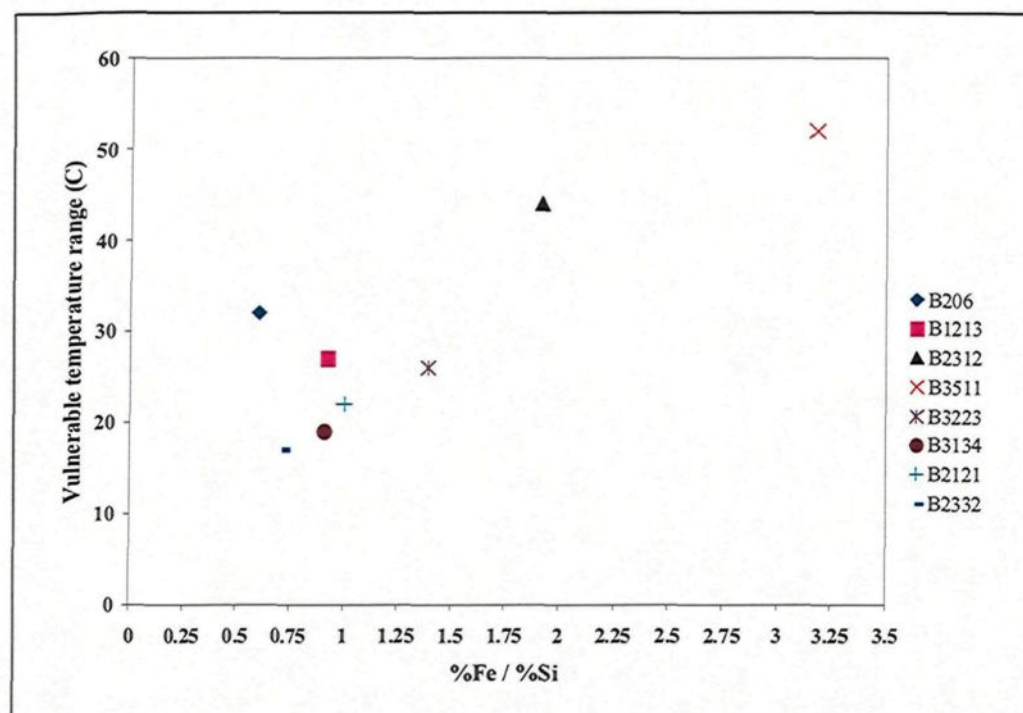
Figure 4. 11: Vulnerable temperature range as a function of Fe/Si ratio.
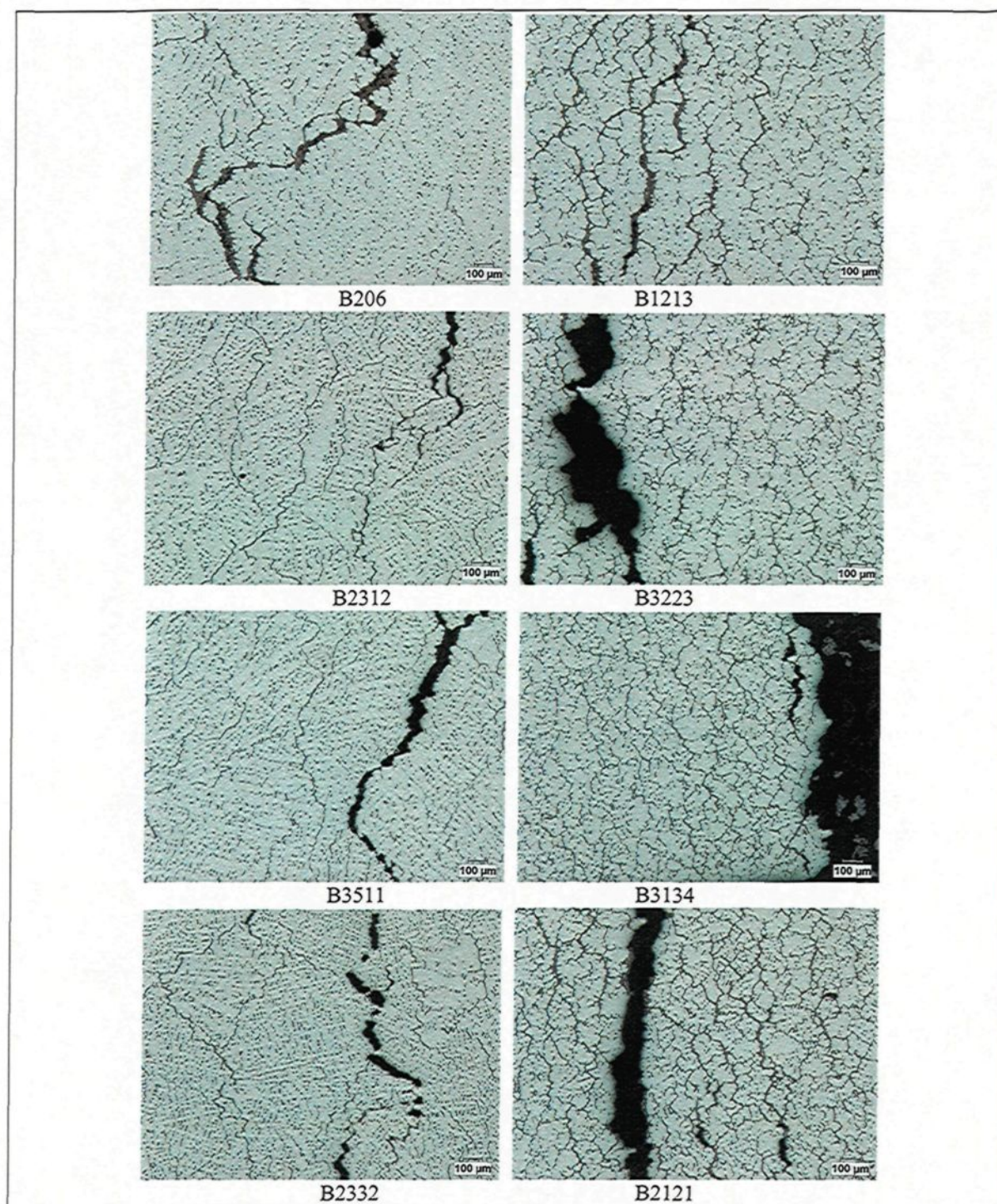
Figure 4. 12: Coarse grains (left) and fine grains (right) microstructure of various alloys.

with coarse grains have a maximum titanium content of 0.01%, while alloys with fine grains have titanium contents between 0.02 and 0.04% (Tables 4.1 and 4.2). The grain coarseness of alloys B206, B2312, B3511 and B2332 results from their very low level of titanium content (0.01%, Tables 4.1 and 4.2), which leads to poor refining. This probably contributed to increasing their hot tearing sensitivity (HTS), especially for alloys containing higher levels of Fe. The large grain size obtained in alloy B2332 very likely promoted a resistance lower than expected considering its relatively low Fe/Si ratio. Alloys B2312 and B3511 had poor resistance to hot tearing due certainly to the combined effects of a high Fe/Si ratio and a large grain size. Plotting HTS against the Fe/Si ratio for these two groups of alloys in Fig. 4.13a and b shows that with better refining, hot tearing resistance is almost unaffected by the Fe/Si ratio, while with poor refining, sensitivity to hot tearing increase linearly with the Fe/Si ratio. This linearity can be described by Eq. (4.3) with a confidence of 88%.

HTS = 0.3158 (Fe/Si) + 0.2859 (4.3)

The titanium content in these alloys should therefore be always kept between 0.02 and 0.05% for effective refinement and subsequent decrease in the risk of hot tearing. One has to recall that a maximum of 0.05% titanium content was specified for B206 alloys in the literature, in order to improve their resistance to hot tearing. [18]
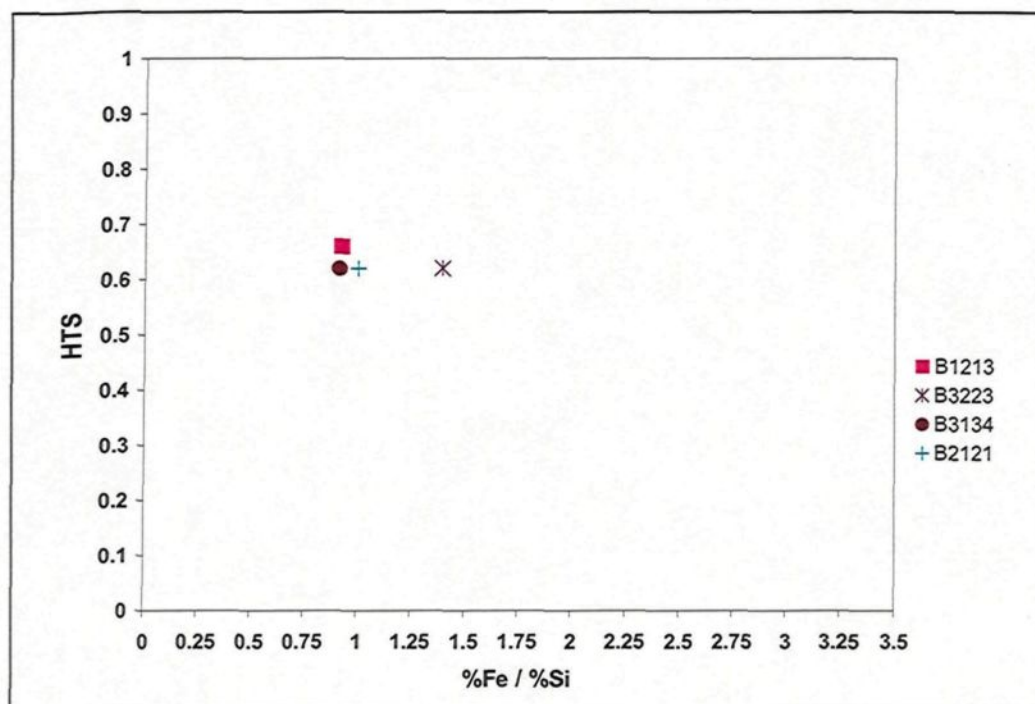
Figure 4. 13a: Hot tearing sensitivity at various Fe/Si ratios for alloys containing 0.02-0.04% Ti.
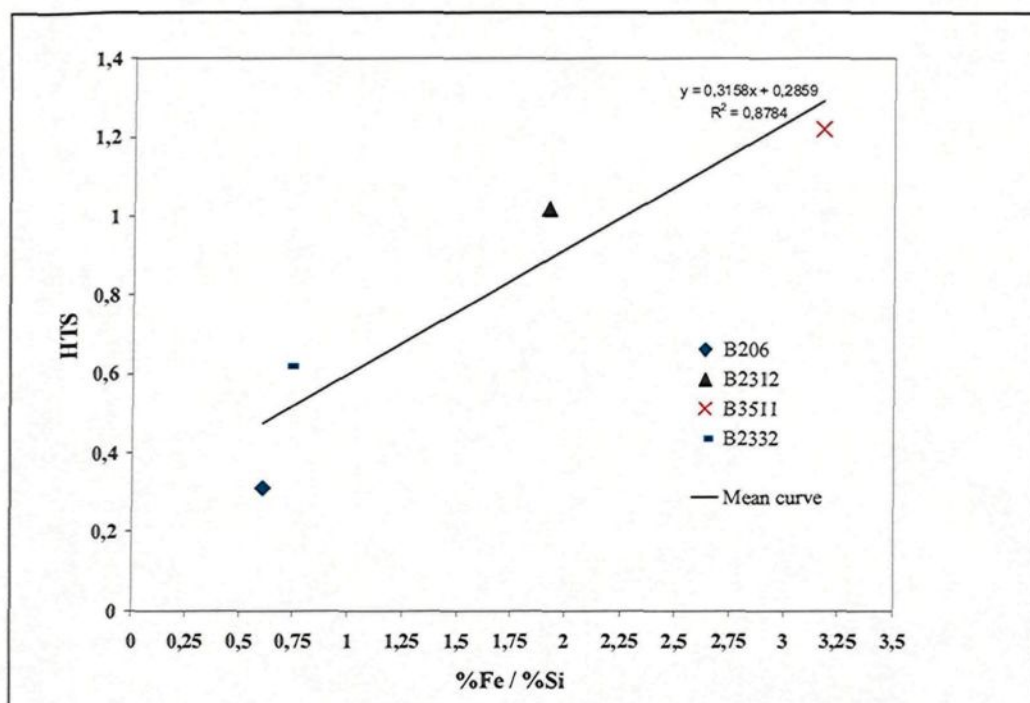
Figure 4.13b: Hot tearing sensitivity at various Fe/Si ratios for alloys containing 0.01% Ti or less.

4.3 Summary

The hot tearing behaviour of 206 type aluminium alloy was investigated to see the influence of minor additions of iron and silicon. The results show that the susceptibility to hot tearing is highly influenced by the iron-to-silicon ratio and the nominal concentration of the single elements. This influence is exerted through the determination of the amount of liquid at the eutectic temperature and the times spent in the vulnerable regime. The best resistance is obtained with both a Fe/Si ratio close to one and low concentrations of iron and silicon. The resistance decreases as this ratio distances itself from one. The higher this ratio, the worse the resistance to hot tearing, especially at a ratio of about two and above. It is probable that proper refining with titanium in the range of 0.02-0.05% inhibit the effect of the Fe/Si ratio on the resistance to hot tearing. These results are in agreement with the concept that hot tearing is affected by the distribution of the liquid phase and stresses within the casting. Since rupture is in general initiated at the weakest point of the microstructure, it seems logical that a microstructure promoting the distribution of the liquid phase into fine intergranular liquid films will provide a better hot tearing resistance, especially in situations where the stress is not applied over a long period of time.

CHAPTER 5
STUDY ON MECHANICAL PROPERTIES

CHAPTER 5
STUDY ON MECHANICAL PROPERTIES

5.0 Aim

The aim of this study was to determine the combined effects of both additions of iron and silicon as well as heat treatment on the tensile, hardness and impact properties of B206 alloys.

5.1 Experimental procedures

5.1.1 Materials, melt treatment and casting

Alloys used in this study were the same as those used during hot tearing studies and their chemical compositions are presented in Tables 4.1 and 4.2. For each alloy, the same melt preparation and treatment procedures as those described in section 4.1.2 were employed. The degassed melt was carefully poured into an ASTM B-108 permanent mould to obtain castings for tensile testing, and into a mild steel impact test mould to obtain samples for impact testing. Both moulds were preheated to 450°C and the pouring temperature was 750 ± 5°C. Fig. 5.1(a) shows the ASTM B-108 type permanent mould used for preparing the tensile test castings, while Fig. 5.1(b) shows the actual casting obtained. As can be seen, each casting provides two tensile test bars, as shown in Fig. 5.1(c). The mould used to prepare the impact test bars is shown in Fig. 5.2(a) and Fig. 5.2(b) shows the actual casting obtained. Each casting provides ten impact bars which

are cut from the casting, and then machined to the required ASTM specifications for conducting Charpy impact tests thereafter. The machined specimens are then given different heat treatments.

(a)

(b)

(c)

Figure 5. 1: (a) ASTM B-108 Permanent Mould; (b) Actual Casting; (c) Tensile test specimens.
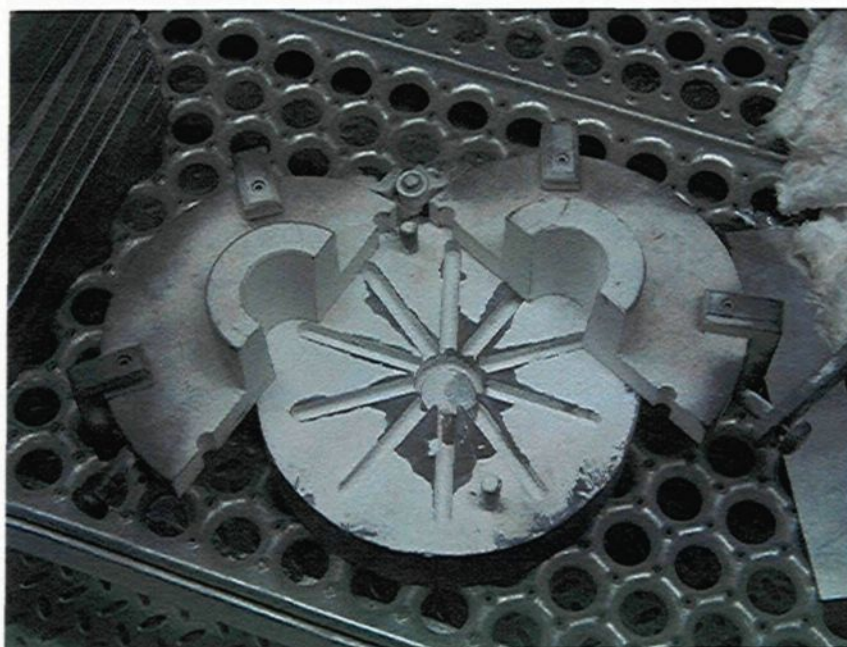
(a)
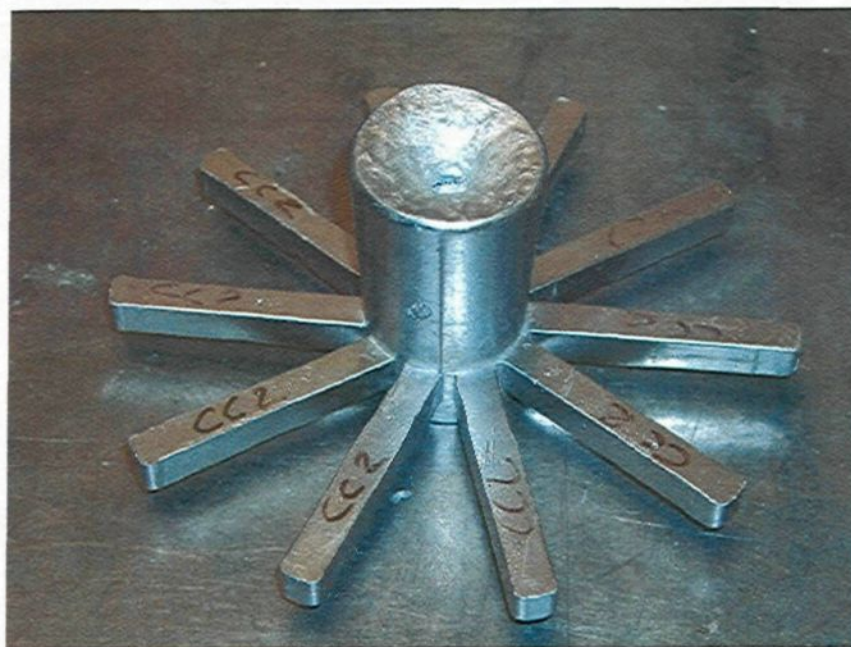
(b)

Figure 5. 2: (a) Permanent mould used to produce impact test bars; (b) Actual Casting.

5.1.2 Heat treatment

Two sets of heat treatment were conducted. The first set which concerned all alloys followed the standard procedures prescribed for 206 alloys, i.e:

For naturally aged samples (T4)

- Ramp from room temperature to 480 °C in 2 hours;

- Continue ramping from 480 °C to 503 °C in ½ hour;

- Hold at 503 °C for 2 hours;

- Ramp from 503 °C to 527 °C in ½ hour;

- Hold at 527 °C for 8 hours;

- Quench into 66 °C water;

Wait 21 days before mechanical testing.

For artificially aged samples (T7)

- Conduct solution treatment as outlined in the T4 schedule above;

- After the 66 °C water quench hold 24 hours at room temperature;

- Age 4 hours at 200 °C;

- Cool to room temperature in still air.

In addition to the standard 8 hours, holding times of 4 hours and 16 hours at 527 °C were also used for all alloys.

The second set, conducted only on B2121 and B3134 alloys, used holding times of 2 hours, 3 hours, 5 hours and 6 hours at 527 °C, followed by natural aging only.

A summary of the heat treatment procedures is provided in Table 5.1. The solution and aging heat-treatments were carried out in a forced-air Blue M Electric Furnace equipped

with a programmable temperature controller (± 2°C). The aging delay was less than 5 minutes and the quenching time was always less than 10 seconds. For each individual heat treatment, five test bars were used. These procedures were followed for the heat treatment of the tensile and impact test samples.

Table 5. 1: Summary of the heat treatment procedures used

Alloys Code	Solution Heat Treatment (SHT) and quenching	T4 Temper (21 days)	T7 Temper	
			Temp (°C)	Time (hrs)
All	1- SHT (503 °C for 2 hrs) 2- SHT (527 °C for 4hrs;8hrs;16hrs) 3- Water quenching (66 °C)	yes	200	4
B2121 B3134	1- SHT (503 °C for 2 hrs) 2- SHT (527 °C/2hrs;3hrs;5hrs;6hrs) 3- Water quenching (66 °C)	yes	No	

5.1.3 Mechanical testing

The mechanical properties examined in this study were the tensile, microhardness and impact properties. A description of the castings prepared for tensile and impact tests and the actual samples sectioned from the respective castings have been provided in subsection 5.1.1. Samples for microhardness analysis were prepared from fractured tensile specimens.

5.1.3.1 Tensile testing

Tensile test bars produced using the ASTM B-108 mould are shown in Figure 5.1 (c). Each bar has a gauge length of 50 mm and a cross-sectional diameter of 12.8 (±0.07mm). The bars were not perfectly cylindrical and the values used represent the mean of the largest and smallest measured diameter values. These light variations in diameter probably

result from imperfect alignment of the mould during casting. For each individual heat treatment, at least 5 test bars were used.

The as-cast and heat-treated test bars were pulled to fracture at room temperature with a crosshead velocity of 0.5 mm/min using a 100 KN capacity electromechanical MTS Testing machine (model RT/100), as shown in Fig. 5.3. A strain gauge extensometer was attached to the test bar to measure elongation as the load was applied. The yield strength (YS) was calculated according to the standard 0.2% offset strain, and the elongation to fracture was calculated as the percent elongation (%El) over the 50 mm gauge length. The ultimate tensile strength (UTS) and the Young's modulus were also obtained from the data acquisition system of the MTS machine. This machine was calibrated each time before any testing was carried out. The average %El, YS or UTS values obtained from the five samples tested per alloy were considered as the value representing that specified condition.

Figure 5. 3: Electromechanical MTS Testing machine with data-acquisition system.

5.1.3.2 Impact testing

Each impact mould casting provided ten impact test bars. The samples were sectioned from the casting, and machined according to the dimensions shown in Figure 5.4. The impact tests were performed on unnotched samples. A computer-aided instrumented SATEC SI-1 Universal Impact Testing Machine (SATEC Systems Inc., Model SI-1D3) was used to carry out the impact tests, as shown in Fig. 5.5. This machine is equipped with bolt-on weights in addition to the pendulum. The pendulum is capable of being latched in two separate modes, known as "high latch" and "low latch," providing a total of four operating capacities, namely, a capacity of 25 ft-lbs (33.9 J) on low latch and 60 ft-lbs (81.35 J) on high latch without the bolt-on weights attached, and a capacity of 50 ft-lbs (67.8 J) on low latch and 120 ft-lbs (162.7 J) on high latch with the additional weights attached. A data acquisition system connected to the impact machine monitored the dynamic behaviour of the test specimen and measured the load and energy values as a function of time. The total absorbed energy (E_t) during impact testing was determined, together with a number of specific parameters such as crack initiation and crack propagation energies, total time, and the maximum load required to break the specimens. The load-deflection curves and energies absorbed were obtained using a Dynatup IPM/PC Impact Testing System. The average values of the energies obtained from the five samples tested for each alloy condition were taken as the representative values for that particular condition.
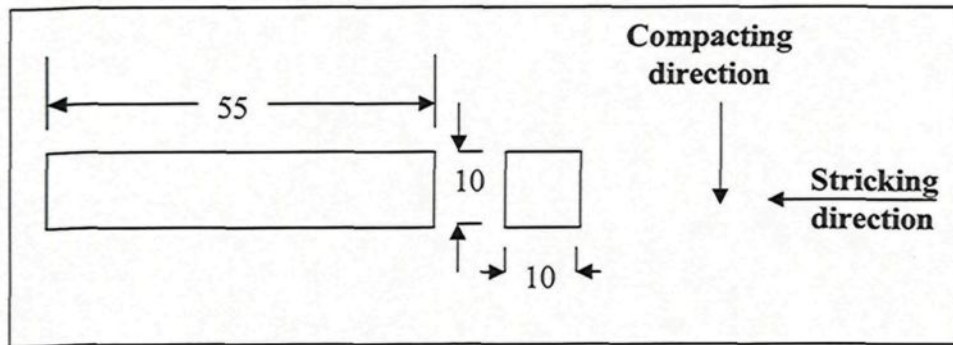
Figure 5. 4: Charpy unnotched impact specimen
(all dimensions in mm).
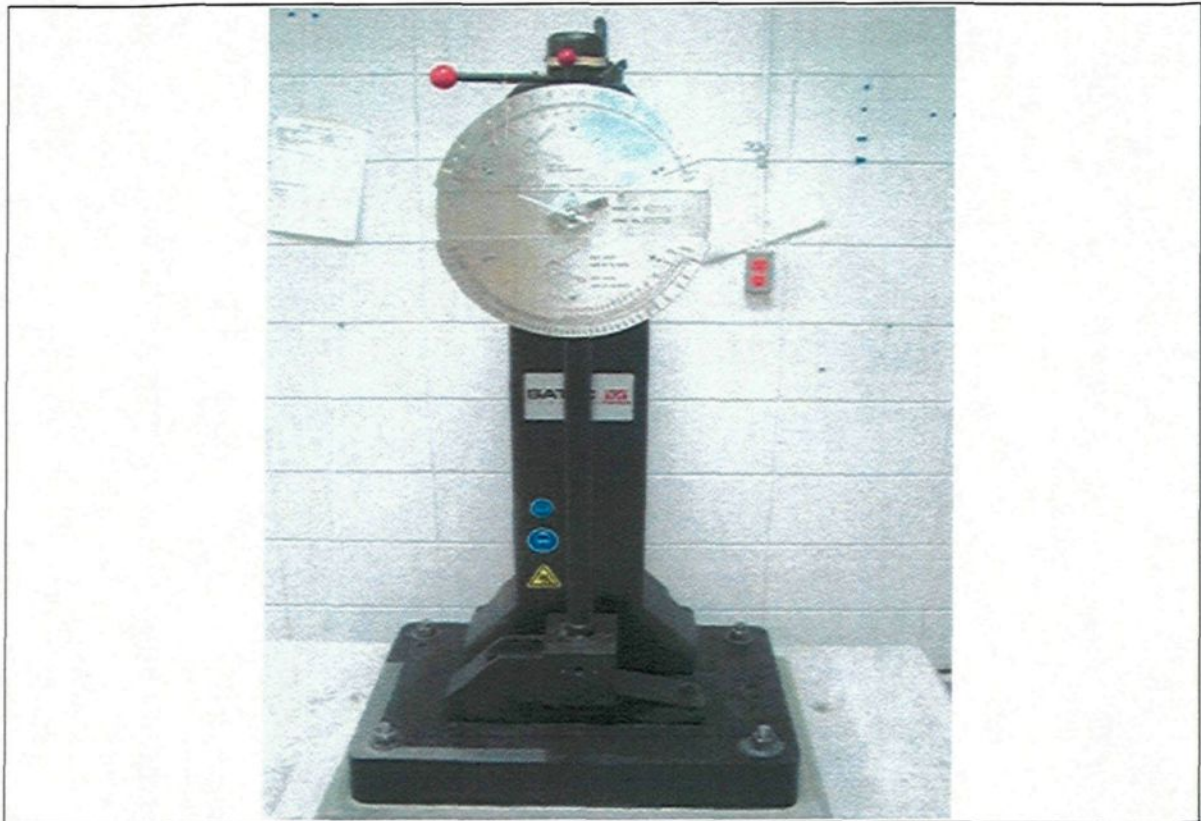
Figure 5. 5: A computer-aided instrumented SATEC SI-1 universal impact testing machine
with a Dynatup IPM/PC impact testing system for data acquisition.
(*Courtesy TAMLA labs*)

5.1.3.3 Microhardness testing

Microhardness tests were performed on polished samples used for metallographic characterization. These samples were cut from fractured tensile specimens as shown in Figure 5.6. Actual tests were carried out using a Clemex computer-controlled hardness tester of 10-1000 gramme-force (gf) capacity which could execute Vickers (HV) and Knoop hardness tests in compliance with ASTM E-384 standards (Fig.5.7). HV method was used in this analysis. The measurement principles include continuous monitoring of the force and the depth of the indentation which allows the determination of hardness and materials properties. A schematic representation of the Vickers probe and its indentation (Figure 5.8) depicts the indenter on the left, illustrating the angles of the pyramidal form of the probe. On the right is the depth 'h' of the indentation. The illustration at the bottom depicts the indentation diagonal length 'D'. The software used calculates the Vickers hardness using the following formula:

$$HV = 1854.4 \, P/D^2$$

where: P is the test load (gf), and D is the average diagonal length (μm).
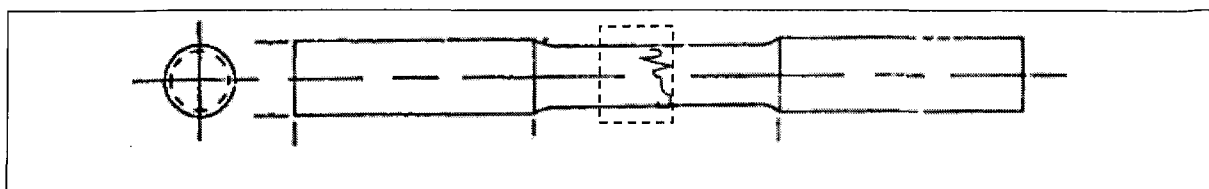
Figure 5. 6: Schematic representation of a fractured tensile specimen showing how samples were selected for metallographic characterization and microhardness testing.
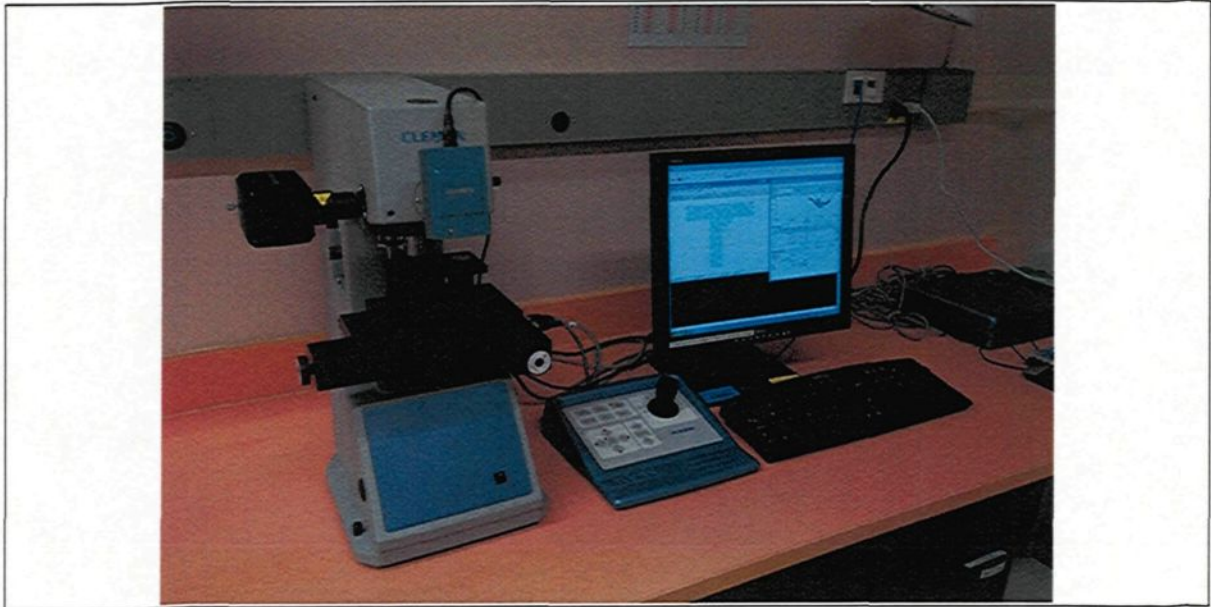
Figure 5. 7: Clemex Microhardness Tester.
(*Courtesy NRC-CTA labs*)
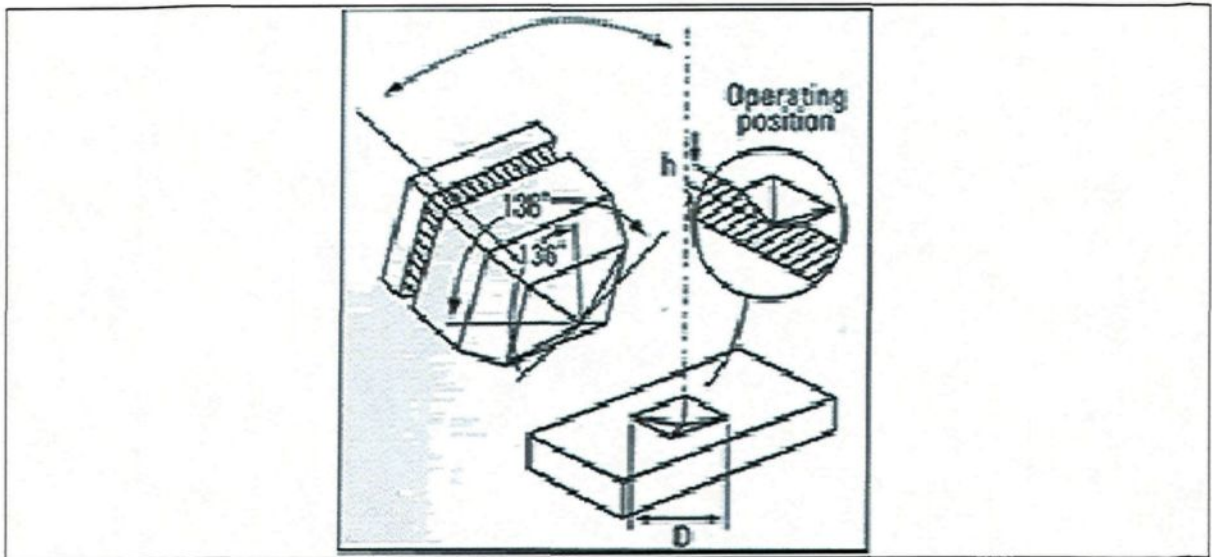
Figure 5. 8: Schematic presentation of Vickers probe and its indentation. [182]
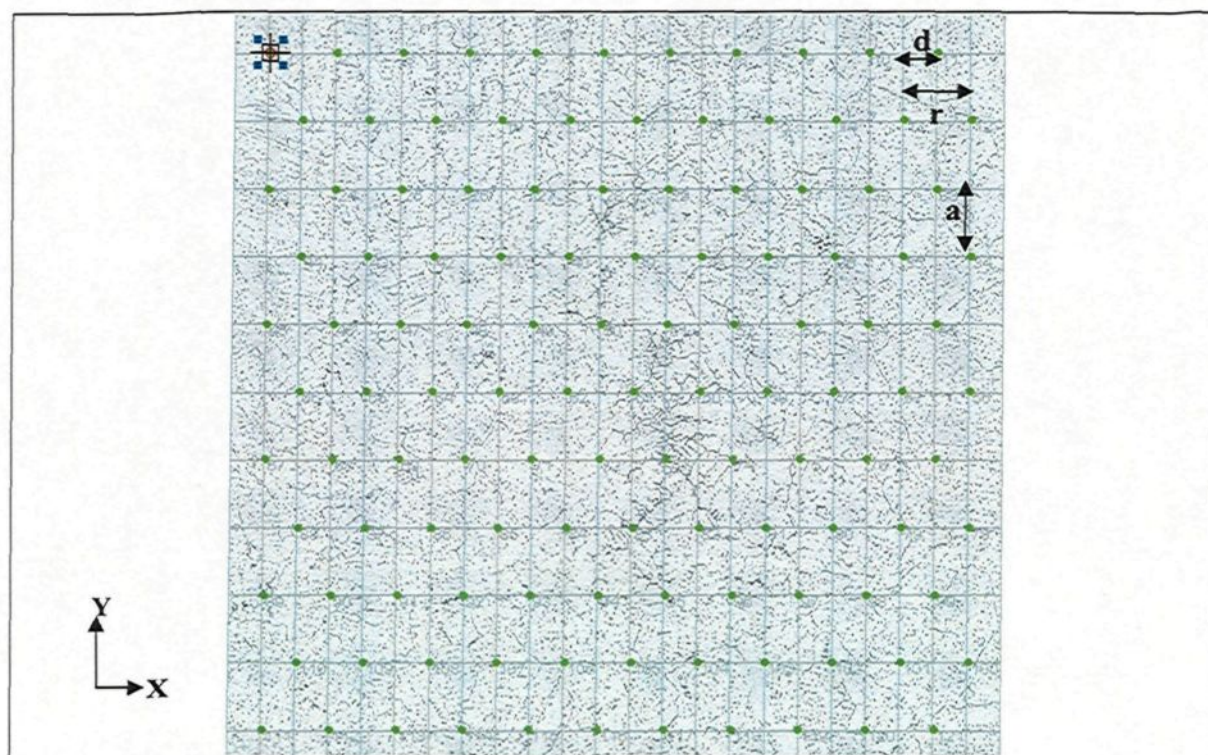
Figure 5. 9: Indentation pattern on a background mosaique image of B206 alloy.
(from this study)

Diagonals can be measured automatically or semi-automatically. The load force used was 500gf with a dwell time of 15 seconds and the lens magnification 400 X. The indentation mode used was the automatic zigzag path which enables the indentations to be made with a small point-to-point separation along the horizontal x-axis without contravening the 2.5D rule. The border distance 'r' between two points in the x-direction was 500μm. The point distance 'd' was 250μm. The line distance 'a' in the y-direction was 500μm. One hundred and twenty one (121) indentations were made on a square surface of 25 mm^2 at the center of the specimen. This is illustrated in Figure 5.9. The average of the hardness values obtained from these indentations for each alloy condition was taken as the representative values for that particular condition.

5.1.4 Metallography and microstructure characterization

Samples for metallographic observations were cut from selected fractured tensile specimens as shown in Fig. 5.6. The selected specimen for each condition was the one whose mechanical properties were the nearest to the mean value. These samples were later mounted in resin and polished, following the procedures presented in section 3.1. Quantitative evaluation of the microstructure was carried out using the optical microscope and the Clemex image analyser system. All these equipments have been discussed in section 3.1. Quantitative characterization of the microstructure included measurements of secondary dendrite arm spacing, area percentage porosity and size. Porosity measurements were carried out on 35 fields of 694160 μm^2 each at magnification 100X at the center of the specimen.

5.2 Results and discussion

5.2.1 Tensile properties

Tensile curves and resulting data are presented in Appendix F for various alloys in different heat treatment conditions. Curves are plotted for true values of stress and strain while data given in the tables are engineering values. The variations in UTS, yield strength and percentage elongation at fracture with iron to silicon ratios and heat treatment conditions are presented in Figures 5.10 to 5.15. From these figures, it is evident that the best combinations of strength and elongation are obtained with Fe/Si ratios close to one. These observations are in perfect agreement with the results obtained from the solidification and hot tearing studies. At artificial aging, i.e, in T7 temper (Figure 5.10-

5.12), alloys with a Fe/Si ratio close to one (Alloys B1213, B2121 and B3134) are found lining near the upper right-hand corner in the direction of iso-Q (see Figs. 2.12-2.14). At the same time, alloys B1213, B2312 and B3511 are lining in the direction of probable constant yield strength (The significance of directions of iso-Q and probable constant yield strength lines has been provided in section 2.5.2). This implies that the soundness of the casting improves as the Fe/Si ratio gets closer to one. As the ratio gets farther from one, the quality decreases, with a more pronounced effect when the iron content is about 0.3%. This decrease in both strength and elongation of T7-tempered 206-type alloys with increase in iron content had also been observed by Tseng *et al.*[19] At natural aging, *i.e,* in T4 temper (Figs. 5.13 to 5.15), all the alloys are found lining in the direction of constant yield strength. Although alloys B1213, B2121 and B3134 are still found concentrated at the upper right corner, *i.e,* showing better combinations of strength and ductility, the slight differences in their quality is more explicit. These variations in quality with heat treatment of copper-containing aluminum castings have also been reported by some authors. [165-167] Since our objective is to optimize the iron content in B206 alloy, further analysis will be restricted only to alloys with high iron content that present better properties, *i.e,* alloys B2121 and B3134. Comparing Figures 5.13, 5.14, and 5.15, it is clear that the best combinations of strength and ductility for alloys B2121 and B3134 in the T4 temper are obtained with a solution heat treatment time of 4 hours. In T7 temper (Fig. 5.10, 5.11 and 5.12), the variation in properties with solution heat treatment time is not very significant. Solution heat treatment time was therefore optimized as 4 hours for naturally aged samples.
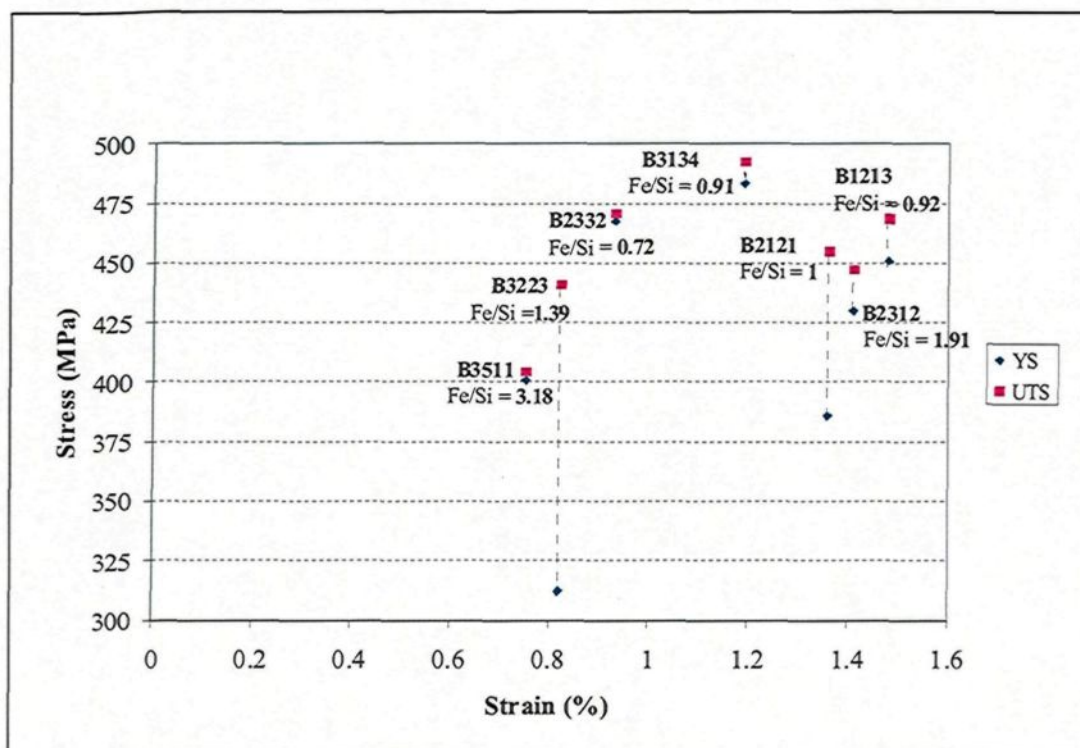
Figure 5. 10: Stress-Strain relationship at different Fe/Si ratios - T7 temper (SHT- 4hrs; Aging- 4hrs at 200°C).
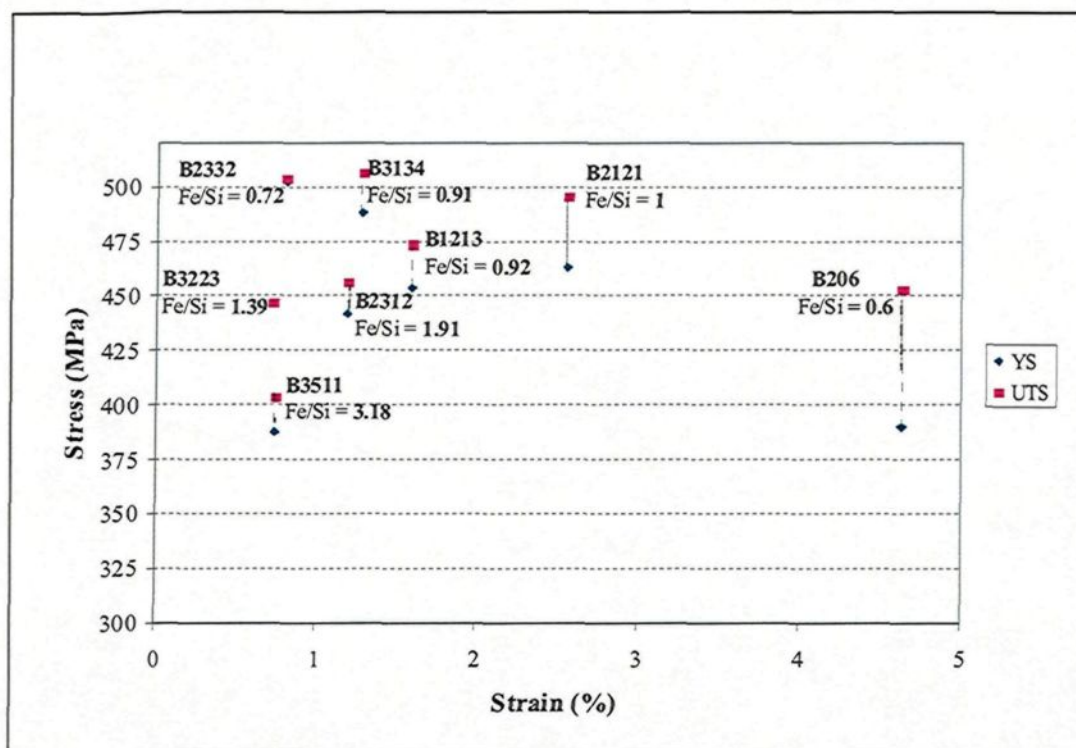
Figure 5. 11: Stress-Strain relationship at different Fe/Si ratios - T7 temper (SHT- 8hrs; Aging- 4hrs at 200°C).
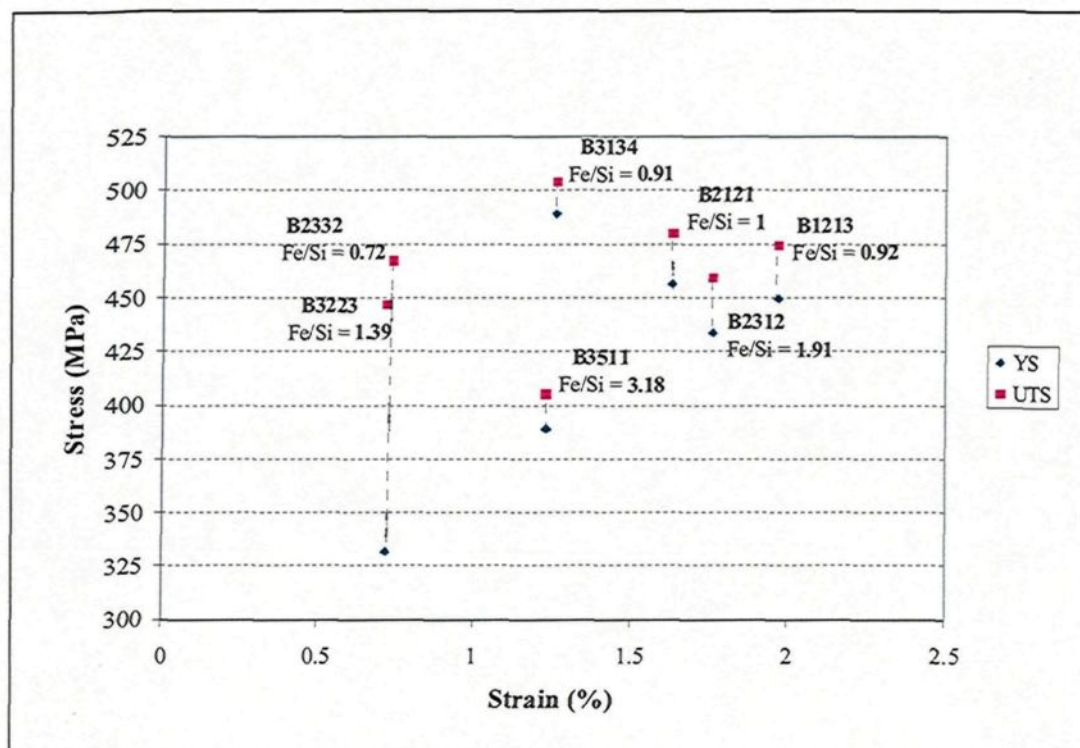
Figure 5. 12: Stress-Strain relationship at different Fe/Si ratio - T7 temper (SHT-16hrs; Aging- 4hrs at 200°C)
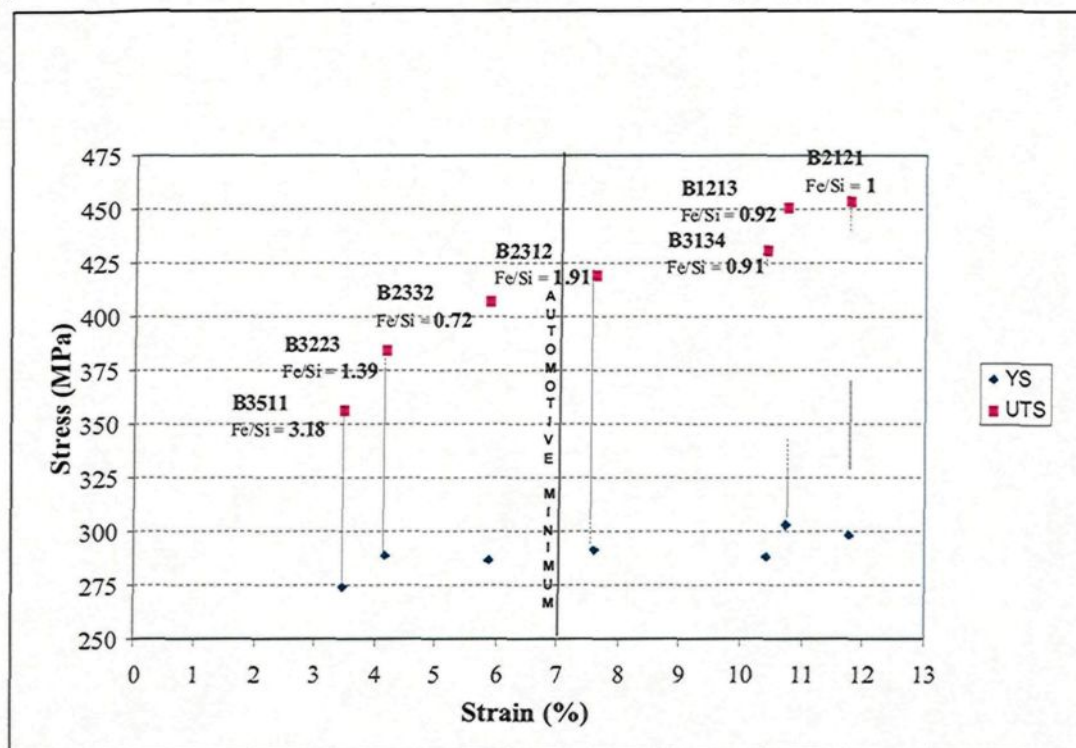
Figure 5. 13: Stress-Strain relationships at different Fe/Si ratios – T4 temper (SHT - 4hrs).
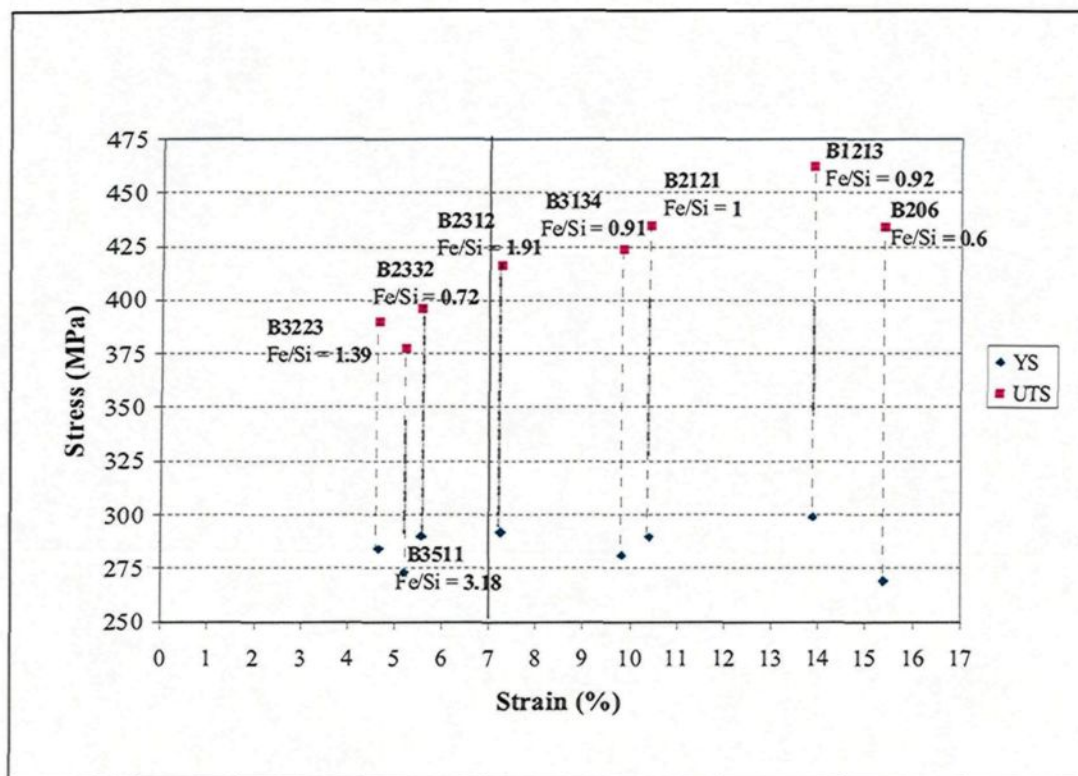
Figure 5. 14: Stress-Strain relationships at different Fe/Si ratios – T4 temper (SHT - 8hrs).
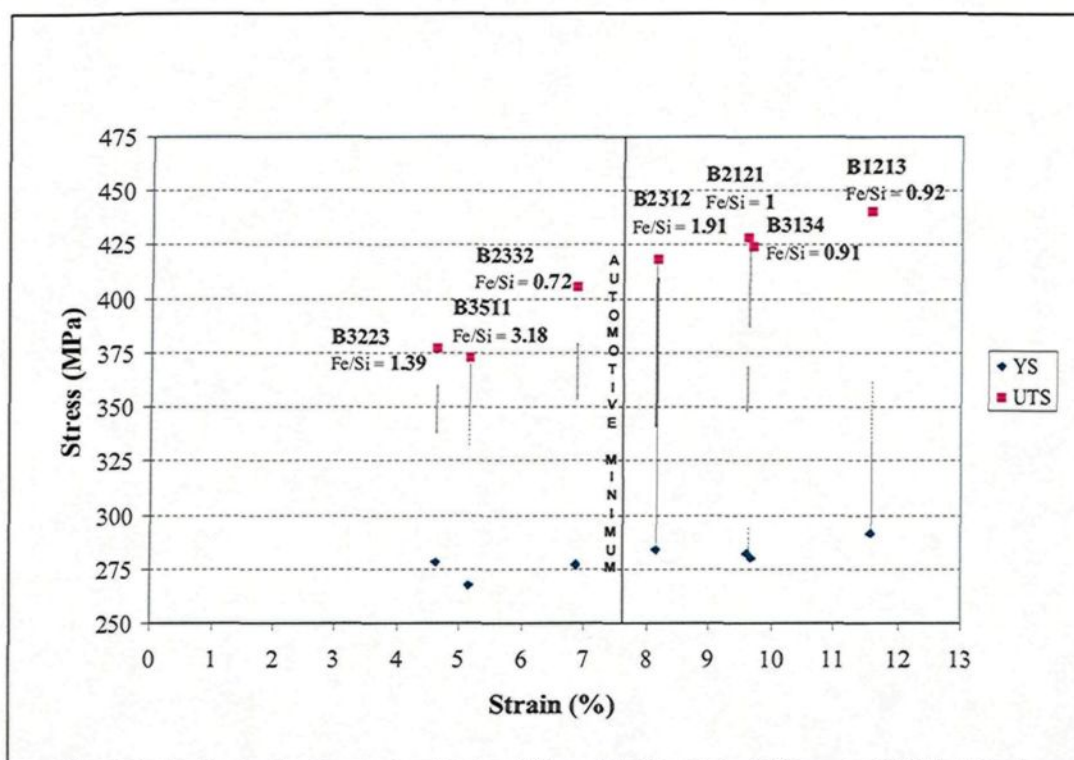
Figure 5. 15: Stress-Strain relationships at different Fe/Si ratio. – T4 temper (SHT - 16hrs).

Figure 5.16 present the stress-strain relationship for naturally aged alloys B2121 and B3134. Specimens were solution heat treated for 2, 3, 4, 5, and 6 hours. In comparison, data for B206 alloy for the standard heat treatment time of 8 hours is also presented. It is once more evident that the best solution heat treatment time for alloys B2121 and B3134 is 4 hours. In this condition, alloys B2121 and B3134 shows improved strength compared to B206 alloy. The increase in yield strength and UTS for B2121 alloy is 29MPa and 20MPa, respectively. For alloy B3134, the increase in yield strength is lower, just about 19MPa, while the UTS remains almost unchanged. On the other hand, the ductility of B2121 and B3134 alloys are lower than that of B206 alloy. Notwithstanding this decrease in ductility, B2121 and B3134 alloys still stand above the minimum requirements for both the aerospace and the automotive industries, which are 3-5%, and 7%, respectively.[18,21]
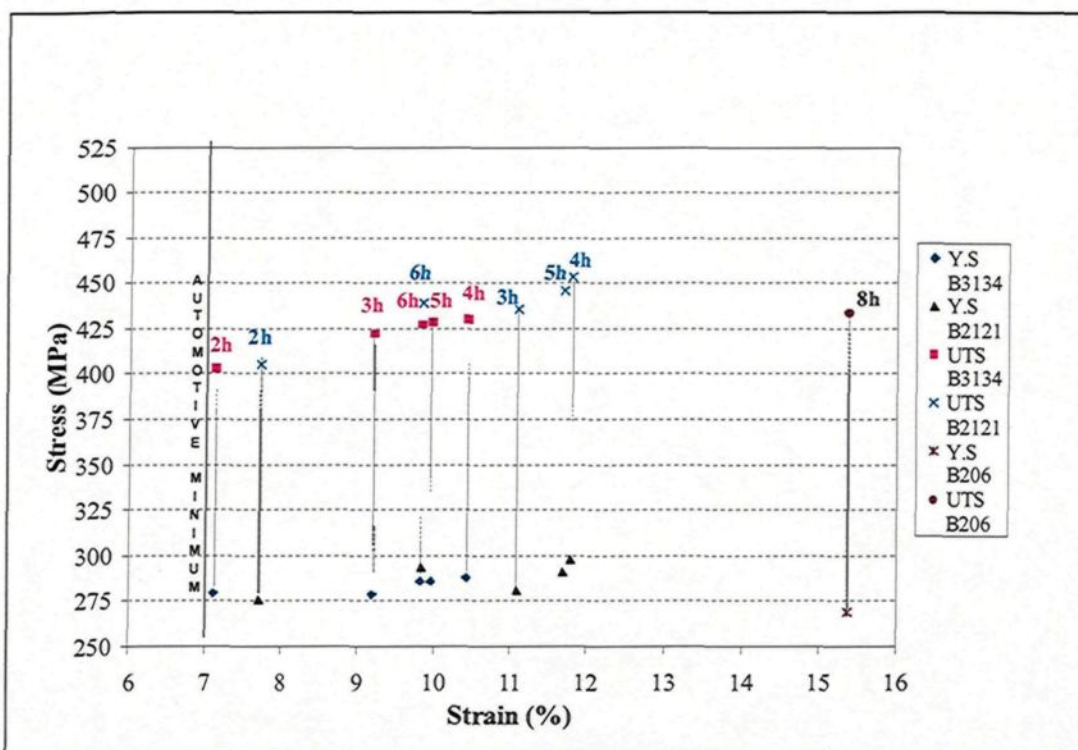
Figure 5. 16: Stress-Strain relationships at different SHT times for alloys B2121 and B3134 – T4 temper.

As previously mentioned, the simultaneous effect of heat treatment on material ductility and strength is best evaluated by the quality index of the material. Quality indices of different alloys were therefore calculated and are presented in Table 5.2. In the calculation of the quality index of B206 alloy, values of 270 and 301 were obtained for the constant d for the artificially aged and naturally aged alloys, respectively. The 270 value is the same as that calculated by Sigworth and Major. [20] In their work, these authors calculated the quality index of B206 alloy in T4 and T7 tempers, using d = 270 for both conditions. For the T7 temper, they obtained a quality index of about 650 MPa with an elongation of about 4.30%. This is very close to the 640 MPa with 4.63% elongation obtained in our calculations. For the T4 temper their quality index was about 775 MPa with an elongation of about 17%. This is also very close to the 800 MPa with an elongation of about 16% obtained in our calculations, considering the fact that they used a value of 270 for d compared to 301 used in our calculations. In addition, the maximum elongations possible in our B206 alloy are calculated to be 11.5% for artificial aging. This is in agreement with the 11.7% value recommended by ASTM for A206 alloys (see Table 2.2). Based on the similarities between our calculated values for B206 alloys and those reported by other authors, our methodology appears to be reliable. Also, Table 5.2 shows for three solution heat treatment times (4, 8, and 16 hours) that the values of d in T4 and T7 conditions are significantly different, higher values being obtained in the former case. The use of a single value for evaluation of the quality index in both conditions may therefore leads to significant errors. Figures 5.17 and 5.18 present the plot of calculated quality index values of experimental castings and their projected maximum values against solution heat

treatment times. For natural aging (Figure 5.17), variation of the quality index with solution heat treatment time for alloy B2121 and alloy B3134 may be similar or completely inversed depending on the solution heat treatment time interval. From two hours to six hours solution heat treatment time, both alloys show a similar behaviour. Their quality index increases, reach a maximum at four hours and then decreases. This decrease may be drastic, as in alloy B2121, or smooth, as in alloy B3134. From six hours to sixteen hours solution heat treatment times, the quality index of these alloys move in opposite directions. For alloy B3134, the quality index continues to decrease up to eight hours solution heat treatment time and then rises slightly. For alloy B2121, the quality index rises up to eight hours solution heat treatment time and then decreases. Variation of maximum projections of the quality index shows the same trend. Similar variations are observed for artificial aging (Figure 5.18), especially at maximum projections, taking into consideration that data at five and six hours solution heat treatment is missing. This is normal as the increase in strength is solely attributed to the formation of θ hardening precipitates.

Table 5. 2: Quality Index (Q) and Relative Quality Index (q) of alloys B206, B2121 and B3134 obtained at various aging conditions

Alloy Code	Temper	SHT (hrs)	Aging T(°C)	Aging t (hr)	K	n	R² (%)	d	q	Q (MPa)	Max strain (%)	Max Q (MPa)
B206	T7	8	200	4	677	0.11	99.58	270	0.42	640	11.5	758
	T4	8	25	504	737	0.21	99.21	301	0.76	800	21.2	825
B2121	T7	4	200	4	664	0.080	99.90	266	0.33	594	8.00	744
	T7	8	200	4	681	0.077	99.87	272	0.50	668	7.70	763
	T7	16	200	4	675	0.083	99.85	270	0.23	553	8.30	756
	T4	2	25	504	740	0.188	99.42	296	0.57	744	18.8	829
	T4	3	25	504	747	0.190	99.29	299	0.56	750	19.0	836
	T4	4	25	504	764	0.191	99.20	307	0.71	810	19.1	855
	T4	5	25	504	745	0.184	99.30	298	0.63	766	18.4	834
	T4	6	25	504	743	0.183	99.30	297	0.56	744	18.3	832
	T4	8	25	504	766	0.194	99.19	287	0.68	801	19.4	858
	T4	16	25	504	709	0.186	99.04	284	0.53	704	18.6	794
B3134	T7	4	200	4	685	0.067	98.06	274	0.22	549	6.70	767
	T7	8	200	4	634	0.048	99.19	254	0.32	557	4.80	710
	T7	16	200	4	691	0.069	98.77	276	0.20	544	6.90	608
	T4	2	25	504	681	0.169	99.75	272	0.42	638	16.9	763
	T4	3	25	504	708	0.177	99.53	283	0.55	705	17.7	793
	T4	4	25	504	734	0.185	99.39	293	0.66	760	18.5	822
	T4	5	25	504	726	0.183	99.56	290	0.65	749	18.3	813
	T4	6	25	504	725	0.183	99.46	290	0.63	744	18.3	812
	T4	8	25	504	718	0.184	99.42	287	0.59	727	18.4	804
	T4	16	25	504	733	0.191	99.23	293	0.58	748	19.1	821

In the above table, the labels in the columns refer to the following:

SHT: solution heat treatment time.

Aging T, t: aging temperature, time.

K and **n** are obtained from the true stress – true strain curve. They represent the strength constant and strain hardening coefficient calculated from equation 2.8.

R² represent the coefficient of determination or degree of confidence in the estimation of K and n from the log true stress – log true strain regression curve.

d represents the constant on the right hand side of Eq. 2.5 and is equal to about 0.4K.

q is the relative quality factor calculated from equation 2.11.

Q is the quality index of the alloy and is calculated from equation 2.5.

Max strain was calculated using equation 2.11 and assuming q = 1 at maximum ductility. [169]

Max Q is calculated from equation 2.13.
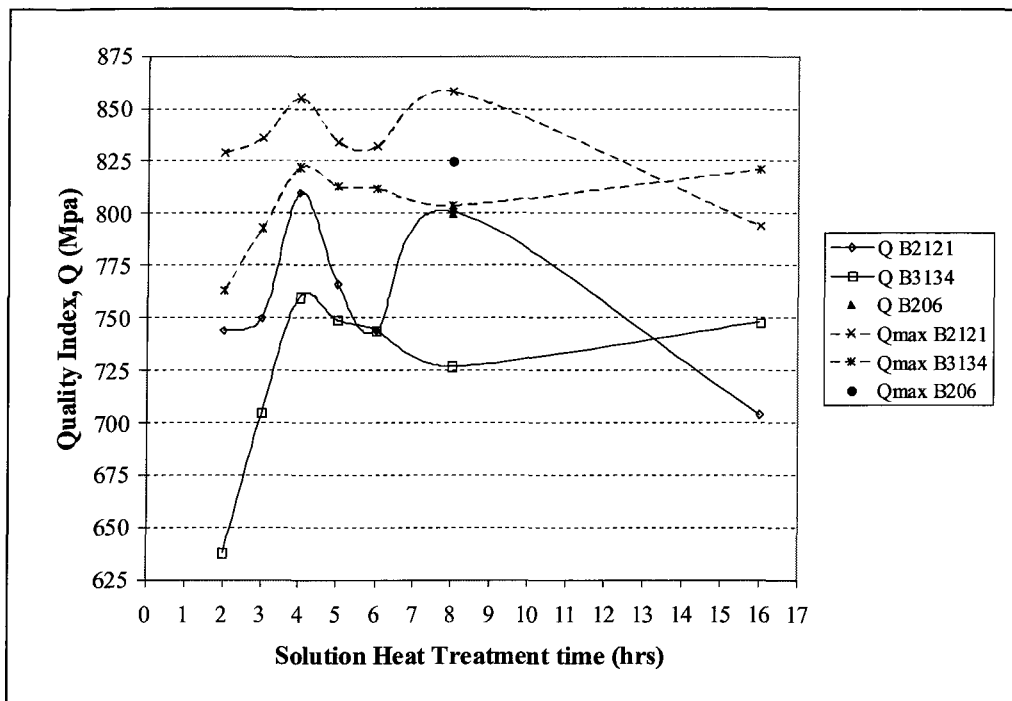
Figure 5. 17: Quality index and projected maximum at different solution heat treatment times for alloys B2121 and B3134. Data for B206 is given only at 8 hours – T4 temper.
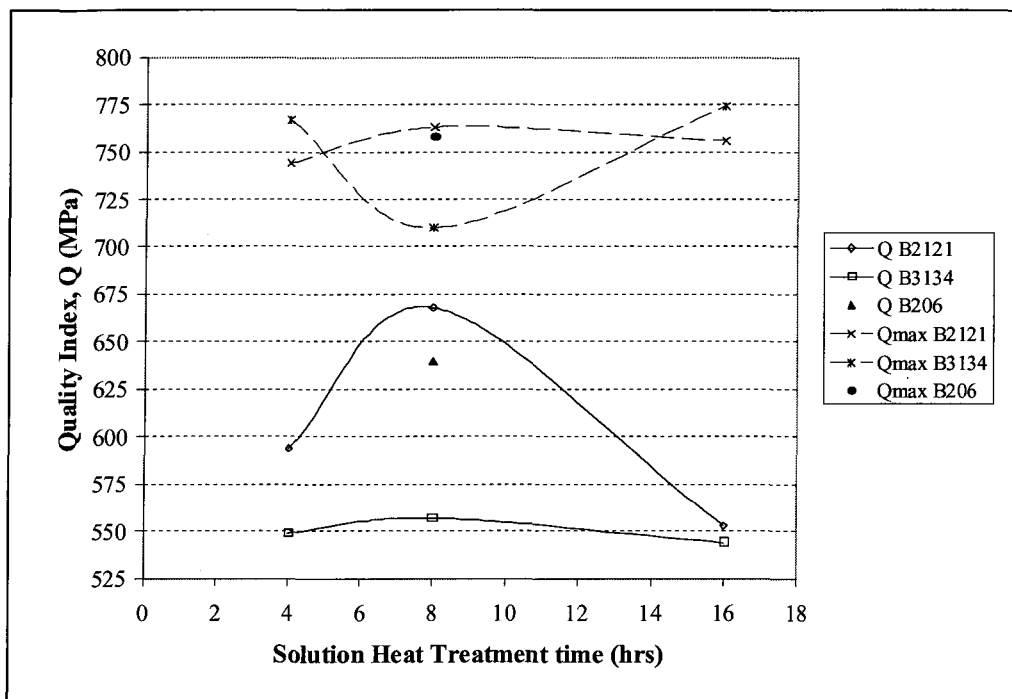
Figure 5. 18: Quality index and projected maximum at 4, 8, and 16 hours solution heat treatment times for alloys B2121 and B3134. Data for B206 alloy is given only at 8 hours – T7 temper.

The variation in quality index with solution heat treatment time may be explained from the microstructural point of view. The evolution of the microstructure with solution heat treatment time and natural aging are presented in Figures 5.19 and 5.20 for alloy B2121 and B3134 respectively. All the micrographs were taken from the centre of the specimens selected from the fractured portion of the gauge region of the test bars, shown in Figure 5.6. The main microstructural constituents in the B2121 alloy are Al_2Cu, $\beta(FeCu)$ and $\alpha(FeMn)$ phases. Very little (Mg_2Si) phase particles were observed since they almost completely dissolved during solution heat treatment. In alloy B3134, the $\beta(FeCu)$ phase was difficult to locate but some tiny particles could be fobserved after solution heat treatment of the material, as shown in Fig. 5.20(c). These tiny phase particles probably precipitated at the end of solidification and indicate some probable microsegregation during solidification of B3134 alloy. The mechanism of solidification of these alloys has been discussed in Chapter 3.

The tensile behaviour of the materials seem to result from a competitive prevalence of four phenomena; namely, in order of importance, Al_2Cu phase dissolution, dendrite coarsening, $\beta(FeCu)$ to $\alpha(FeMn)$ phase transformation, and porosity evolution. Dendrite coarsening and porosity evolution were quantitatively evaluated while Al_2Cu phase dissolution and $\beta(FeCu)$ to $\alpha(FeMn)$ phase transformation were qualitatively evaluated through microhardness measurements. The reason being that dissolution of foreign particles increases the hardness of the matrix. Results are summarized in Table 5.3. The evolution of yield strength, ultimate tensile strength, quality index, percentage elongation, secondary dendrite arm spacing, and hardness are plotted against the solution heat

treatment time in Figures 5.21 and 5.22 for alloys B2121 and B3134, respectively. Area fraction and mean pore size evaluated in terms of perimeter are plotted against solution heat treatment time in Figures 5.23 and 5.24 for alloys B2121 and B3134, respectively. Let us first analyze what happens up to 4 hours solution heat treatment time where maximum quality is observed. For both alloys, it can be seen that within this period, dendrite coarsening occurs at maximum rate within the first two hours. At the same time, an increase in porosity area fraction and pore size is observed. One could have therefore expected the quality of the material to drop, but an increase in elongation and strength is observed. This improvement in quality results from dissolution of the Al_2Cu phase followed by the increase in hardness. Looking at the microstructures, one may suggest that 2 hours is the optimum solution time. Although most of the θ phase disappeared within this period, it is interesting to see the increase in both hardness and quality of the material on proceeding from 2 to 4 hours solution time. This increase is more pronounced in B2121 alloy. Maximum dissolution of θ phase therefore occurs within 4 hours solution time and outweighs the dendrite coarsening and porosity evolution. Also, it was reported that θ phase could assist in pore formation. [81] The increase in porosity during this period may therefore be just apparent, already present porosities becoming more visible with dissolution of θ phase. After the 4 hours maximum dissolution time, porosity generally decreases and dendrite coarsening continues. Both elongation and strength, and hence the quality of the materials, decrease. Dendrite coarsening seems to be the controlling factor. For alloy B2121, an increase in quality is observed at 8 hours solution time. Although still lower than that of 4 hours solution time, this increase is likely due to a $\beta(FeCu)$ to $\alpha(FeMn)$

phase transformation as more α(FeMn) phase particles can be observed in the microstructure after 8 and 16 hours of solution heat treatment (Fig. 5.19 (g) and (h)). In addition, the hardness value at 8 hours is comparable to that of B3134 alloys in which iron phases are almost completely precipitated as the α(FeMn) phase. From the present experimental results and calculated maximum projected values of strain and quality index, it would be no problem using natural aging (T4) with a better casting practice, to obtain the minimum of 7% elongation required by the automotive industry by doubling or tripling the present limit of 0.1%Fe in these alloys. This will lead to a potential loss in ductility in the order of 2.5%, but a global gain in alloy quality in the order of 1.3% at 0.2% Fe and 0.2% Si (alloy B2121), while at 0.3% Fe and 0.3% Si (alloy B3134) a global loss in quality in the order of 2.6% would be expected. For artificial aging (T7) conditions, it will be very difficult, if not impossible, to reach the 7% elongation at 0.2%Fe and 0.2%Si, while at 0.3%Fe and 0.3%Si it is quite impossible (see Table 5.2).
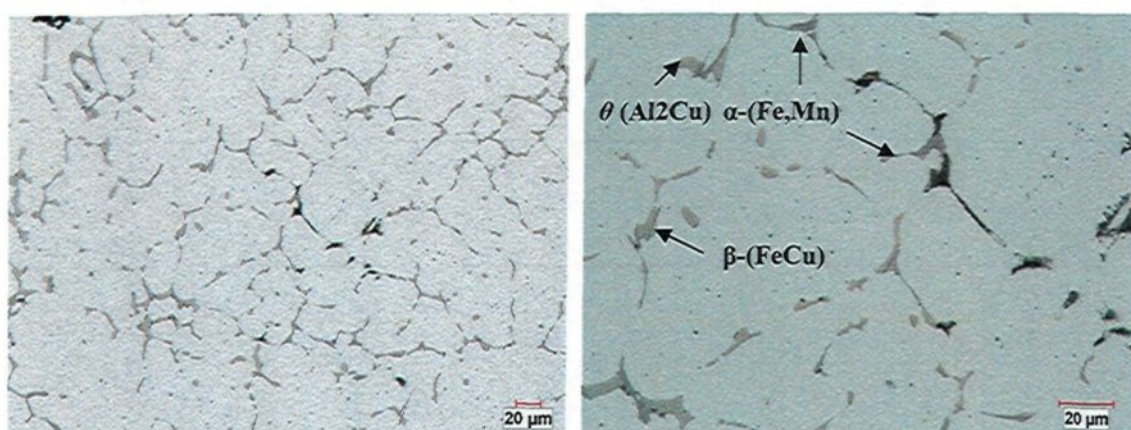
(a) B2121- As cast

Continued
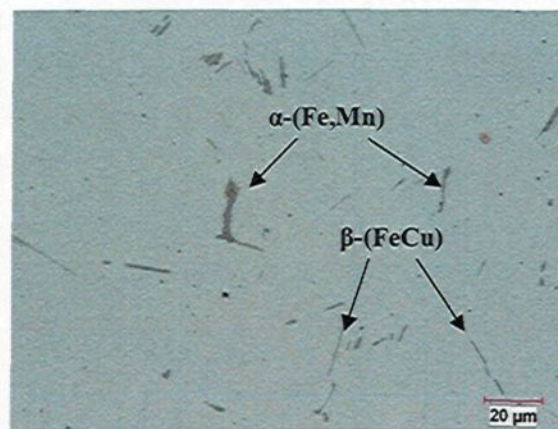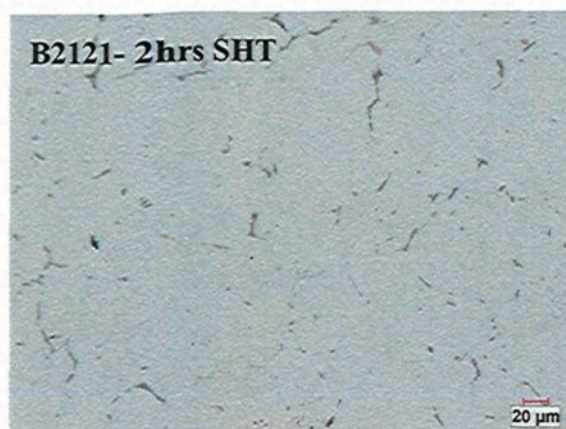
(b) B2121- 2 hrs SHT
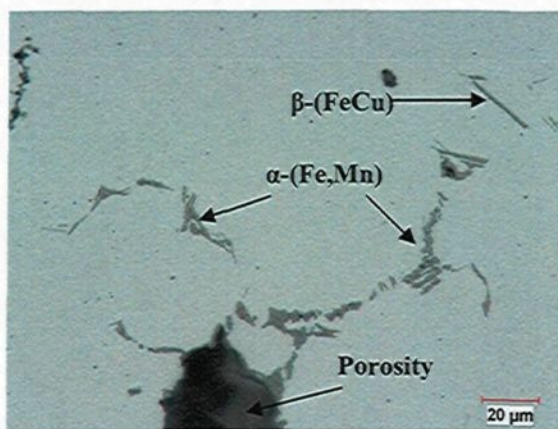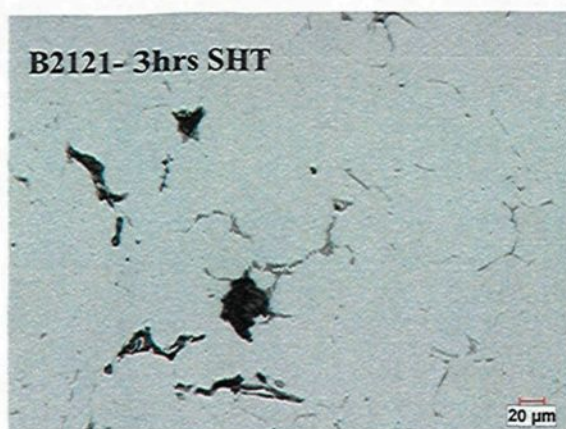
(c) B2121- 3 hrs SHT
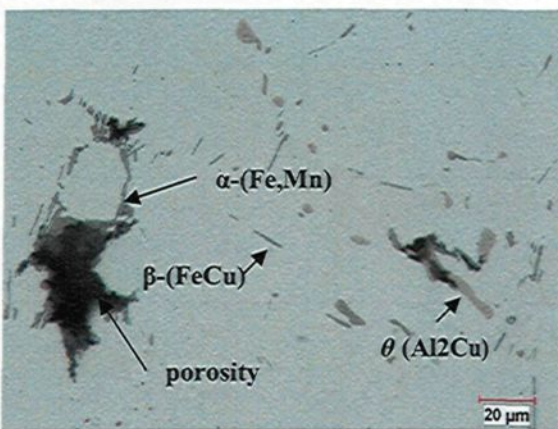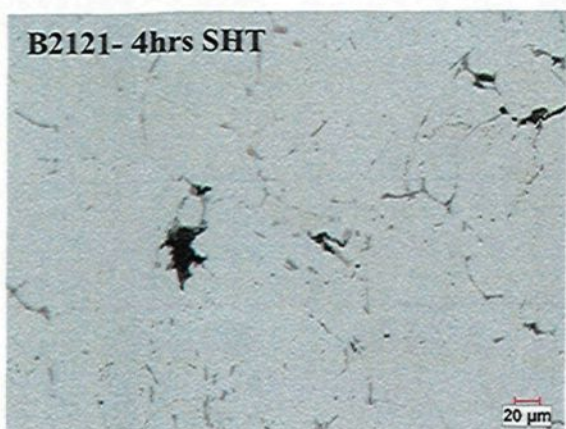
(d) B2121- 4 hrs SHT

Continued
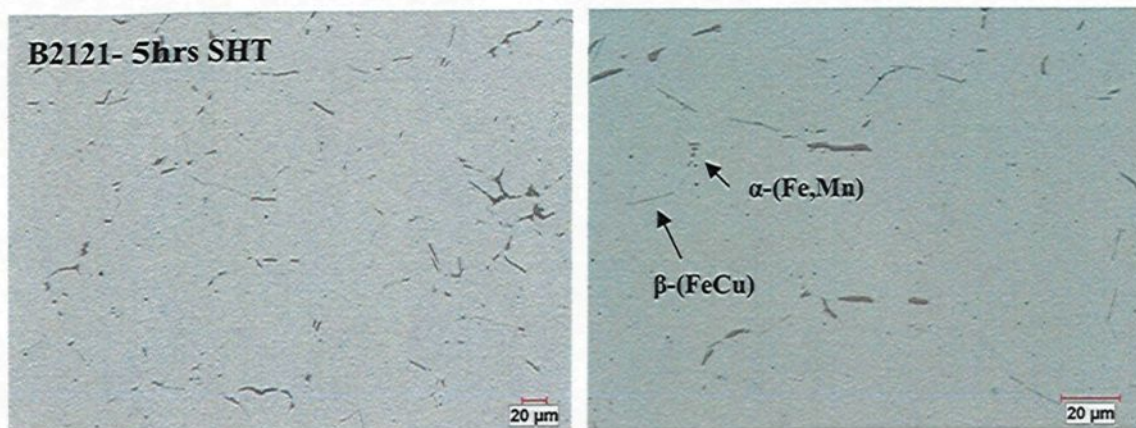
(e) B2121- 5 hrs SHT
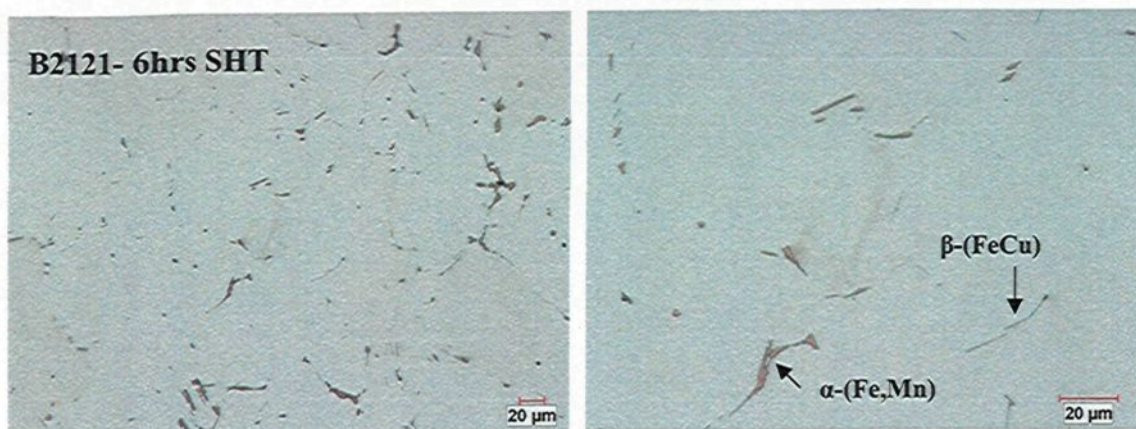
(f) B2121- 6 hrs SHT
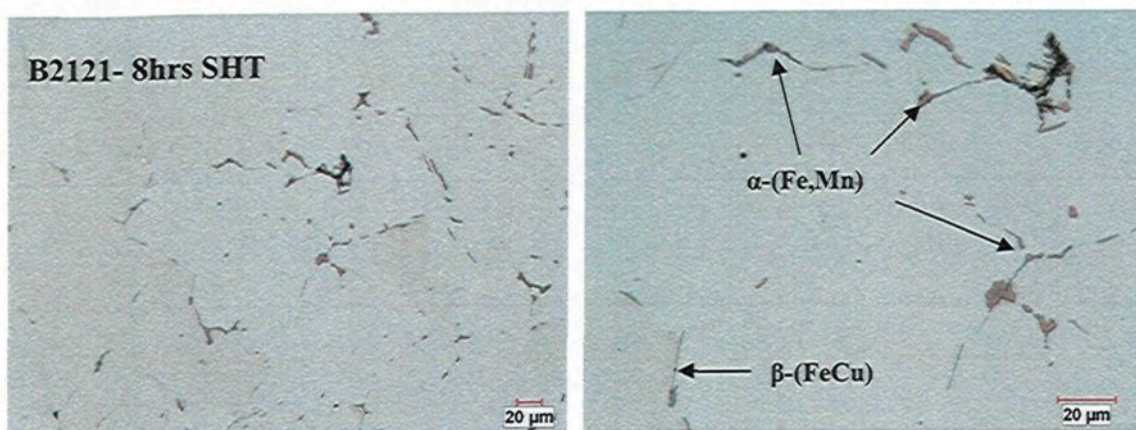
(g) B2121- 8 hrs SHT

Continued
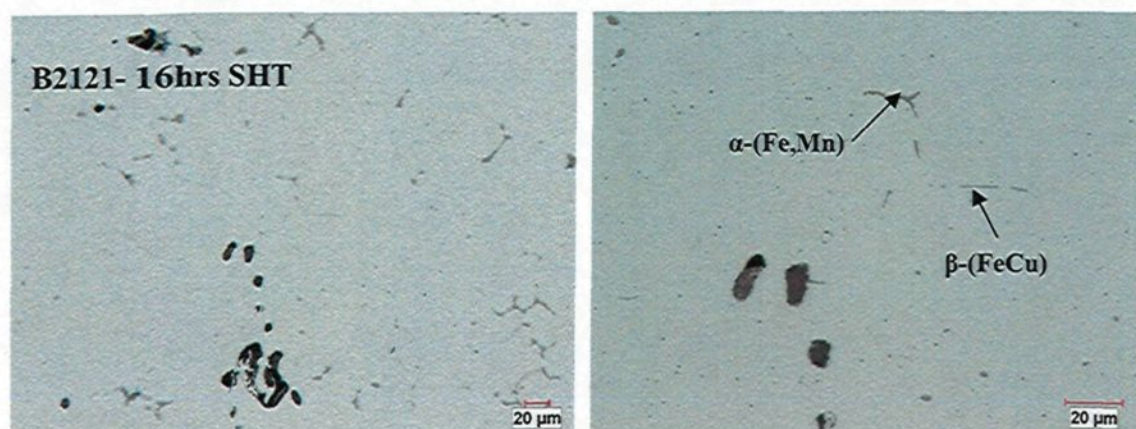
(h) B2121- 16 hrs SHT

Figure 5. 19: Microstructure evolution of alloy B2121 with solution heat treatment time. Each condition is presented at low magnification at the left and higher magnification by the right.
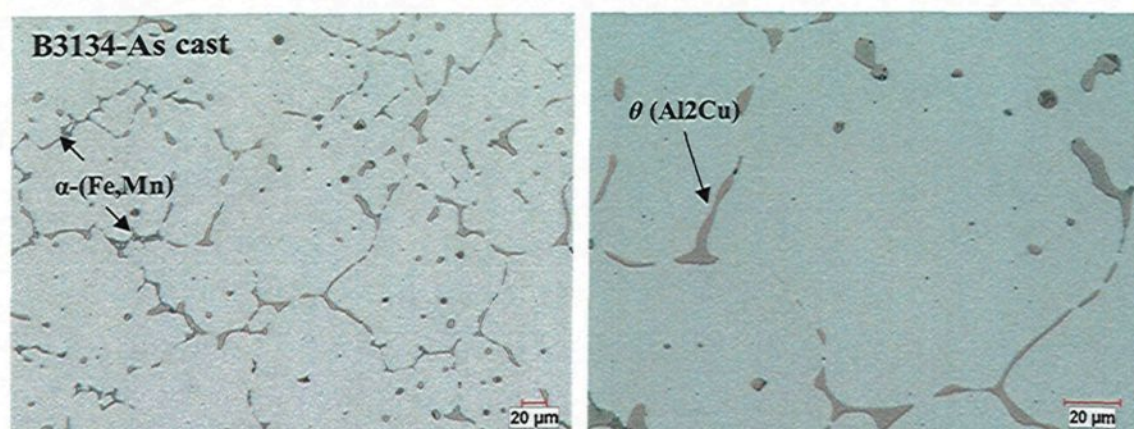
(a) B3134- As cast
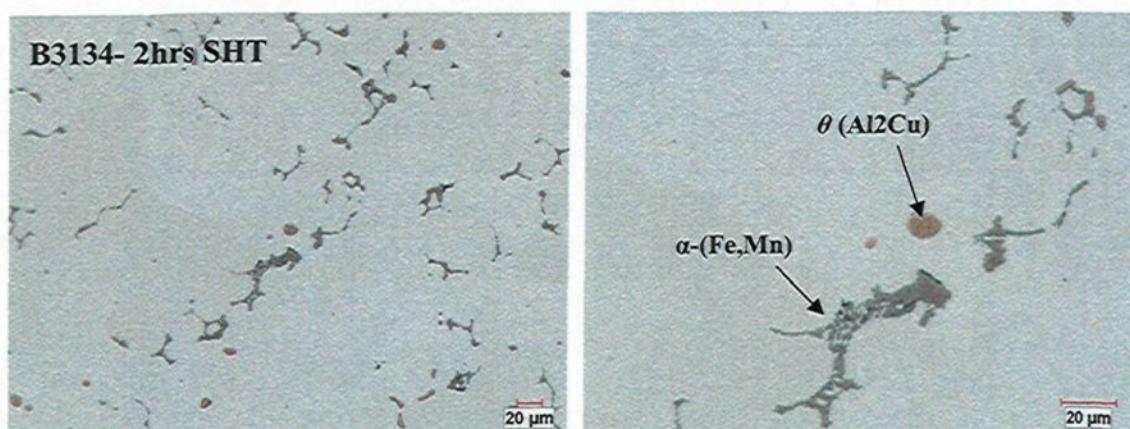
(b) B3134- 2 hrs SHT

Continued
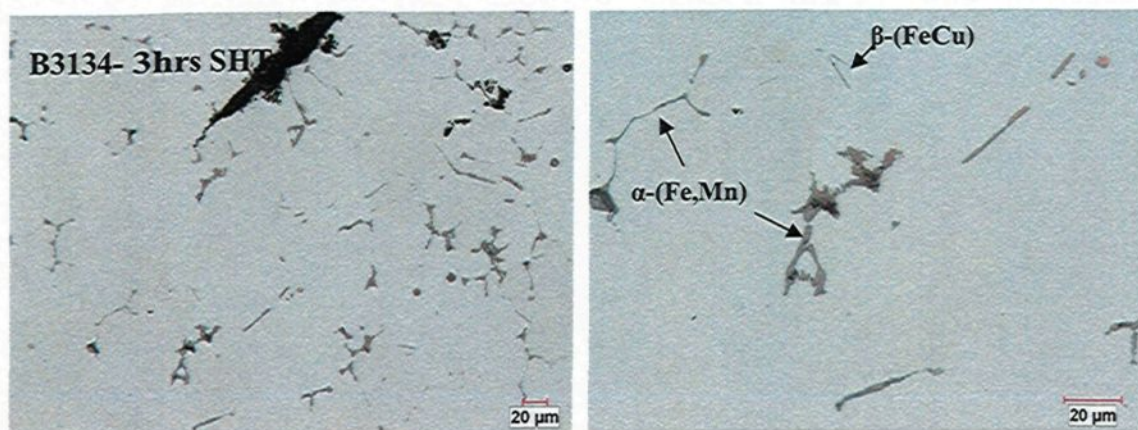
(c) B3134- 3 hrs SHT
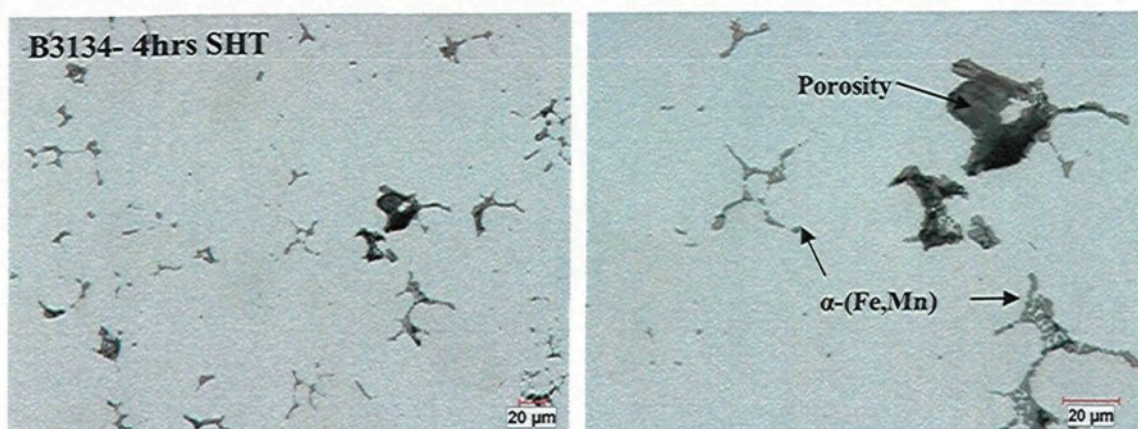
(d) B3134- 4 hrs SHT
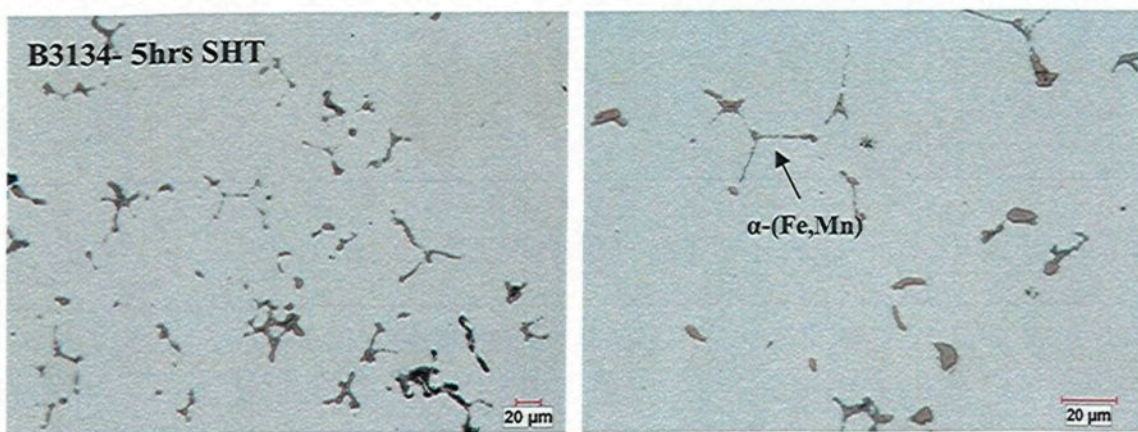
(e) B3134- 5 hrs SHT

Continued
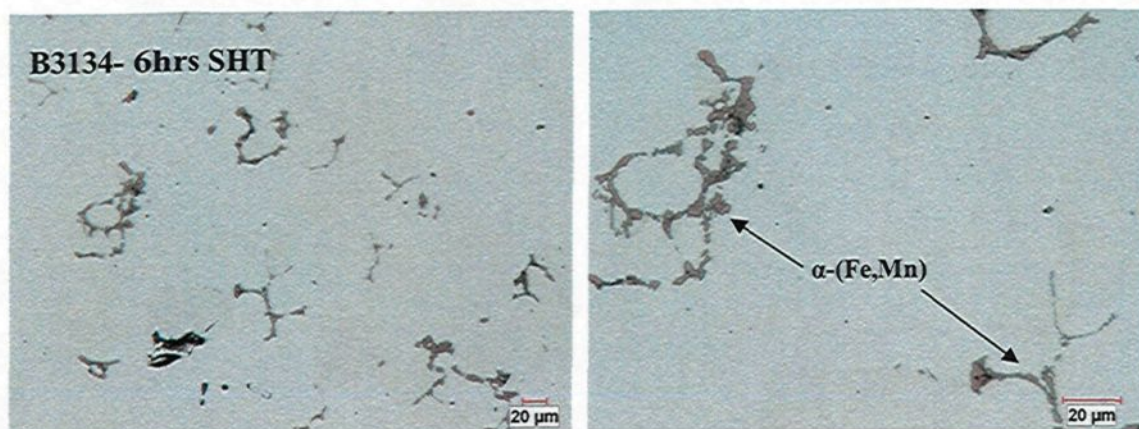
(f) B3134- 6 hrs SHT
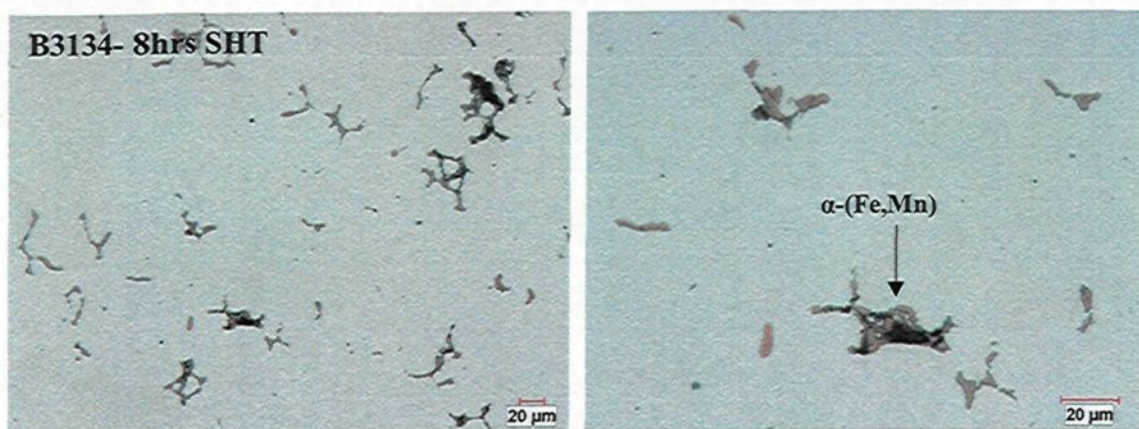
(g) B3134- 8 hrs SHT
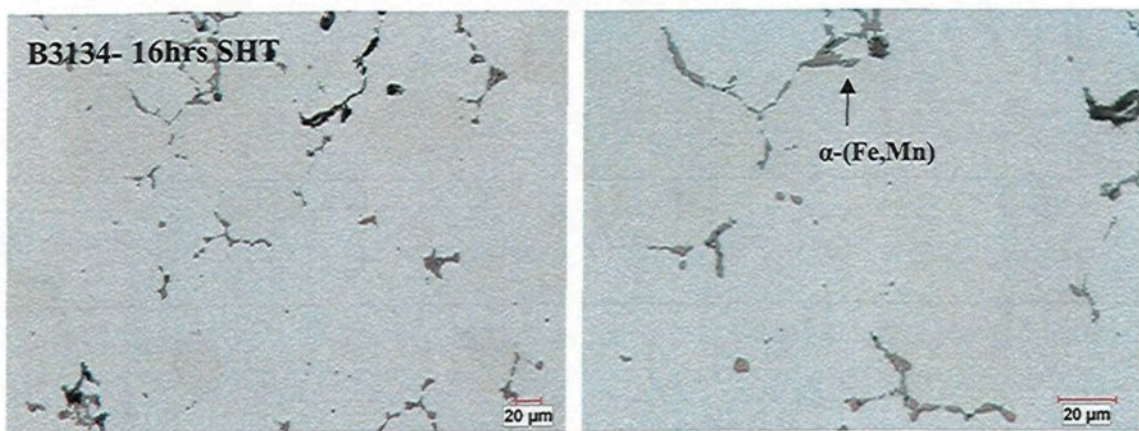
(h) B3134- 16 hrs SHT

Figure 5. 20: Microstructure evolution of alloy B3134 with solution heat treatment time. Each condition is presented at low magnification on the left and higher magnification on the right.

Table 5. 3: Secondary dendrite arm spacing (SDAS), porosity and hardness evolution with solution heat treatment time for alloys B206, B2121 and B3134

Alloy	SHT (hrs)	SDAS (μm)	Porosity				Hardness, (HV) (SD)
			Area %	Pore Size (perimeter, μm)			
				Min	Avg (SD)	Max	
B206	0	59	0.12	190	624 (359)	1809	092.0 (±8)
	8	63	0.45	56	799	4648	122.0 (±8)
B2121	0	41	0.10	15	322 (418)	2066	086.5 (±9)
	2	50	0.16	44	431 (378)	1895	119.3 (±8)
	3	51	0.32	79	849 (653)	2874	119.9 (±5)
	4	51	0.45	80	1102 (808)	3910	126.3 (±7)
	5	58	0.10	17	316 (512)	2831	118.1 (±5)
	6	58	0.22	0	517 (806)	3897	119.3 (±8)
	8	58	0.33	48	758 (581)	2189	126.7 (±5)
	16	60	0.34	43	904 (860)	2889	118.4 (±12)
B3134	0	44	0.12	61	372 (248)	971	087.8 (±8)
	2	57	0.23	232	851 (534)	2614	120.4 (±8)
	3	59	0.66	334	1947 (1241)	6629	123.8 (±10)
	4	64	0.52	332	1614 (751)	4067	125.9 (±10)
	5	65	0.45	499	1431 (572)	2631	124.1 (±7)
	6	65	0.55	1027	1865 (542)	3123	123.4 (±9)
	8	68	0.53	344	1589 (940)	4002	124.0 (±8)
	16	76	0.32	276	934 (572)	2777	124.3 (±9)
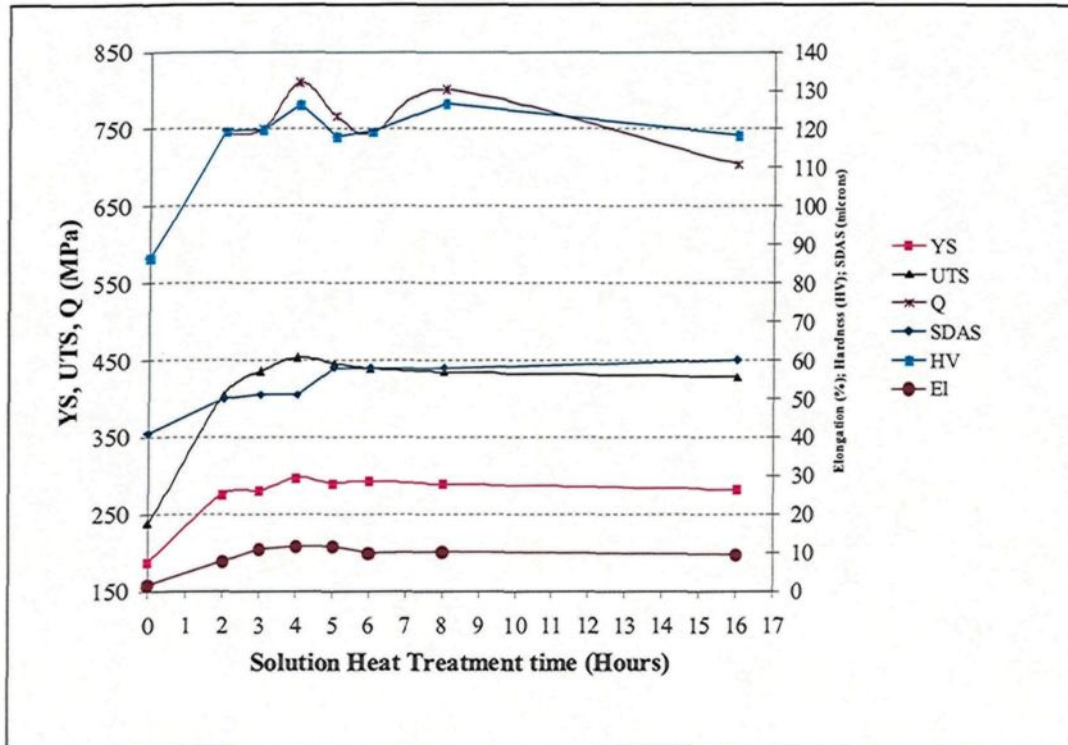
Figure 5. 21: Evolution of YS, UTS, Q, SDAS, Elongation and Hardness with solution heat treatment time for alloy B2121 after natural aging.
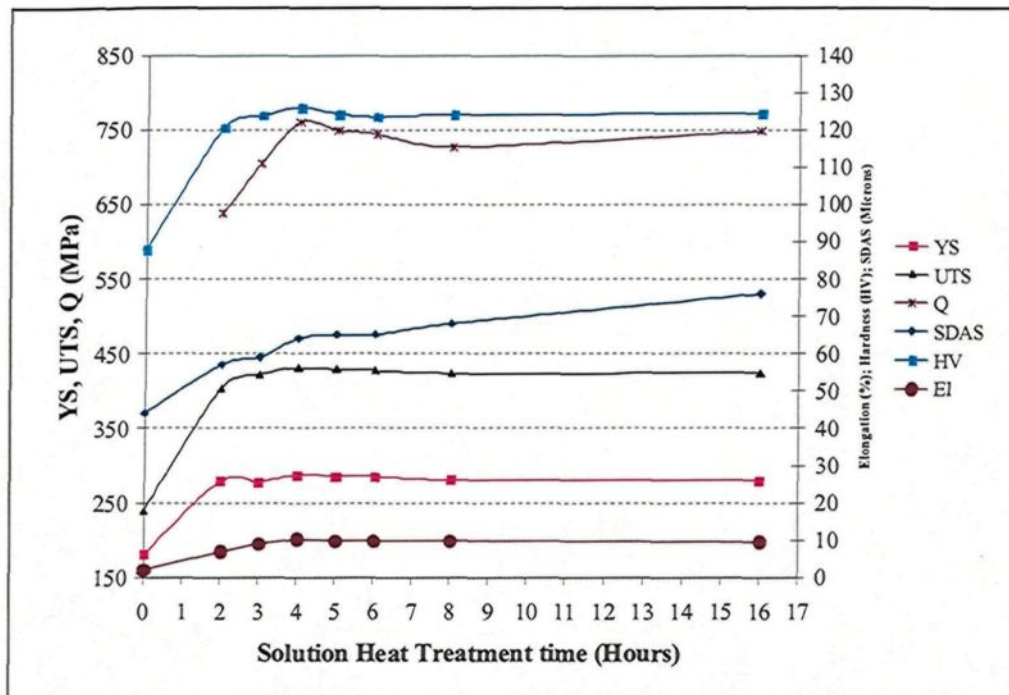
Figure 5. 22: Evolution of YS, UTS, Q, SDAS, Elongation and Hardness with solution heat treatment time for alloy B3134 after natural aging.
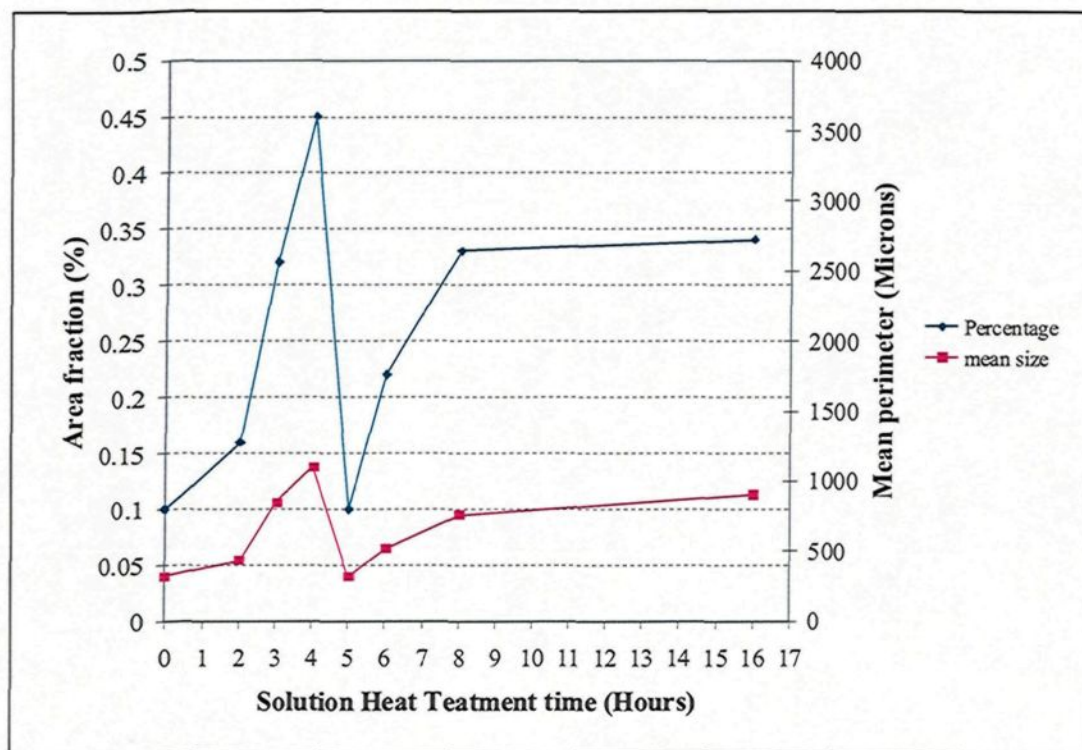
Figure 5. 23: Porosity evolution with solution heat treatment time for alloy B2121.
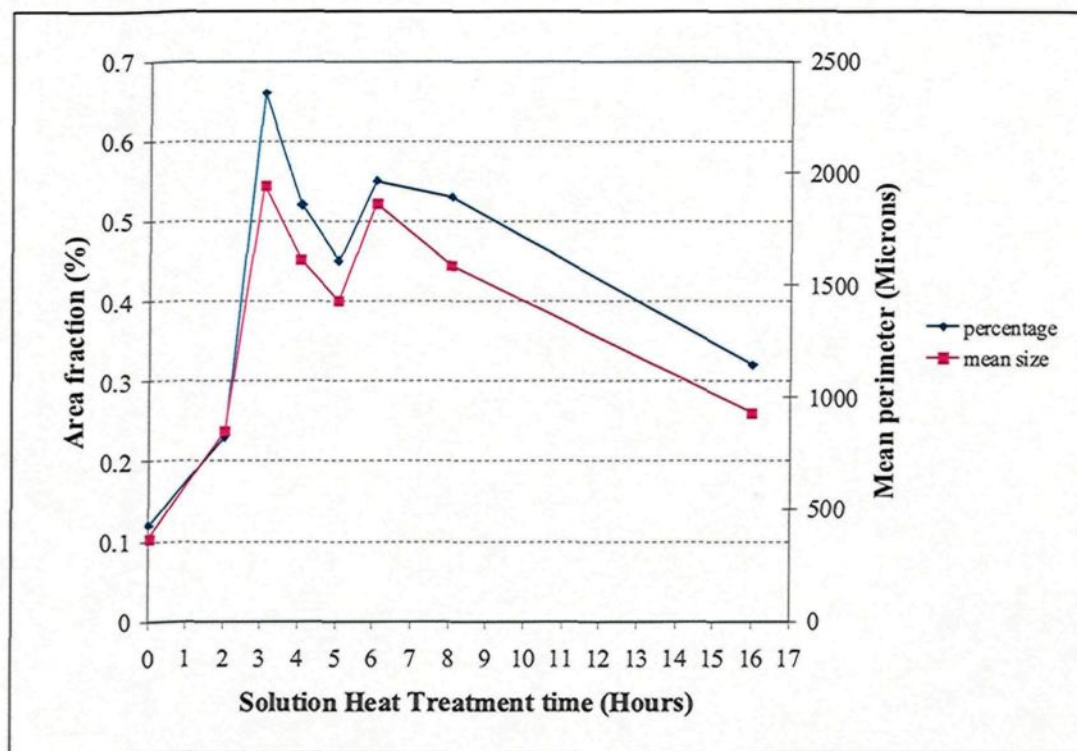
Figure 5. 24: Porosity evolution with solution heat treatment time for alloy B3134.

5.2.2 Impact properties

Although tensile testing is the most commonly used method for quantifying the mechanical properties of aluminum alloys, impact strength is also of importance in certain applications and can provide an informative estimation of the ductility of an aluminum alloy. The energy recorded by the Charpy test generally correlates with the area under the total stress-strain curve in tensile testing. Testing the materials in the same heat treated condition for impact toughness was therefore dedicated as a confirmation method of the results obtained during tensile tests. For comparison purposes, it was decided not to notch the impact bars in order to emphasize the effects of the microstructure. We will restrain our study to natural aging (T4) conditions, as it was demonstrated that it will be very difficult to obtain required ductility for automotive applications under artificial aging (T7) conditions. However, behaviour after natural aging can be applied to artificial aging as well, as the evolution of the tensile properties of alloys with different iron to silicon ratios shows the same trend in the two heat treatment conditions. Results from tensile tests shows that the best combinations of stress and strain are obtained with 4 hours solution heat treatment for both alloys B2121 and B3134 (Fig. 5.15). Impact data will therefore be analyzed only for samples solution heat treated for 4 hours and 8 hours, and the relationship between impact energy and tensile ductility discussed, for these conditions.

The instrumented impact testing equipment measures the fracture response of the specimen in terms of absorbed fracture energy. This absorbed energy may be read directly on the dial of the pendulum machine as in the traditional test, or else calculated from the curves obtained on the oscilloscope in the case of an instrumented test. When the system is

well calibrated, the calculated total absorbed energy (E_t) value will match the dial energy. This match up was verified for each sample, thus only the results obtained from the curves themselves will be considered here. The instrumented impact test results recorded the evolution of the applied load and energy absorbed during fracture as a function of time. These curves are presented in Figure 5.25 and resulting data are summarized in Table 5.4. Selected curves are those that better represent the average properties in each heat treatment condition. The shape of the load-time curve is an indication of the deformation and fracture history of the impacted test sample. These curves show some similarities with those obtained during tensile tests and can therefore be used to mark the deformation stages. The total absorbed energy, E_t, the crack initiation energy, E_i, the maximum load, total time, and time to maximum load were all determined from the curves, whereas the crack propagation, Ep, and average crack speed were obtained by means of calculation. The results represent the average values and their standard deviation. The impact strength or total absorbed energy is seen to be better for alloys B2121 and B3134 solution heat treated for 4 hours but still below that of B206 alloy. This is in agreement with results from tensile tests but it does not provide much information on the details of the fracture behaviour of a material, hence the interest of dividing the energy into two parts: crack initiation energy (E_i) and crack propagation energy (Ep). In real terms, any brittle, high strength material will manifest high crack initiation energy, E_i, and low crack propagation energy, E_p. Conversely, a low strength ductile material will have low E_i and high E_p. Therefore, even though the Charpy energy for two materials may be the same, their fracture behaviour may be quite different.
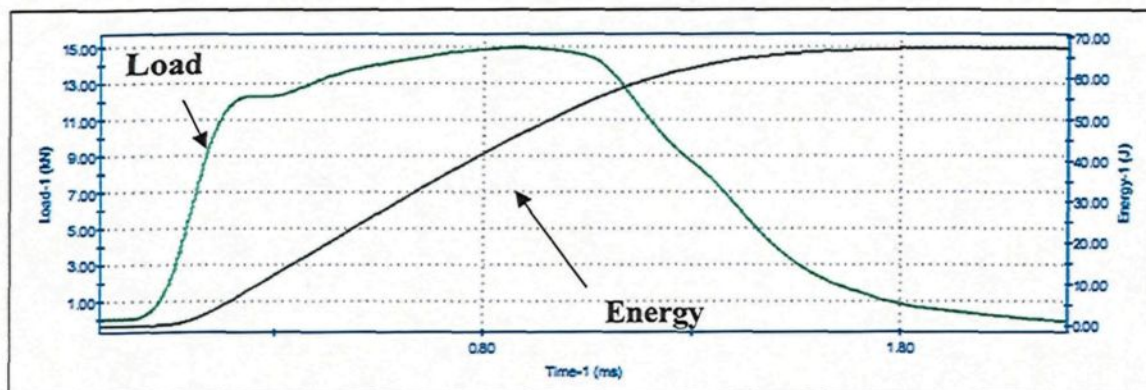
(a) B206-T4: SHT, 8 hrs.
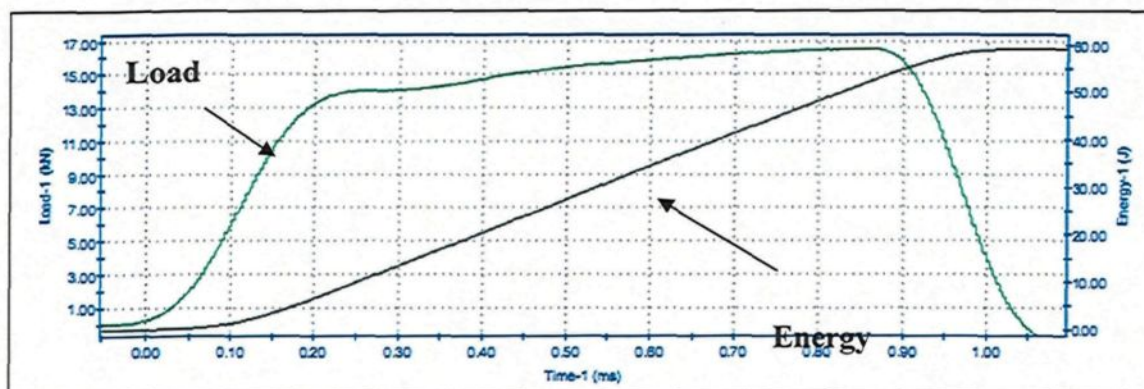
(b) B2121-T4: SHT, 4 hrs
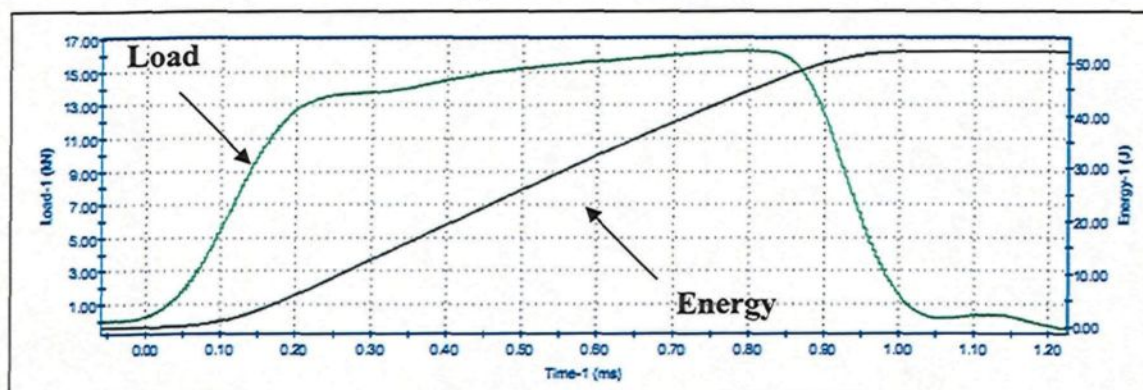
(c) B2121-T4: SHT, 8 hrs.
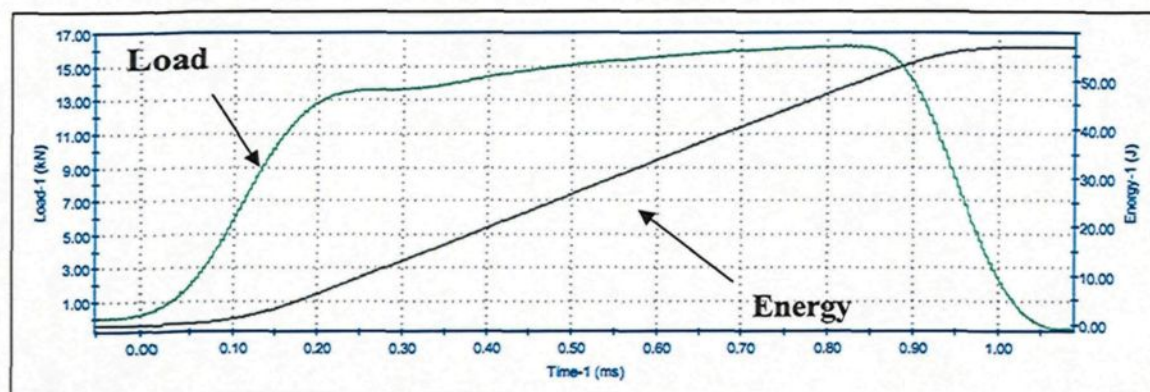
(d) B3134-T4: SHT, 4 hrs.
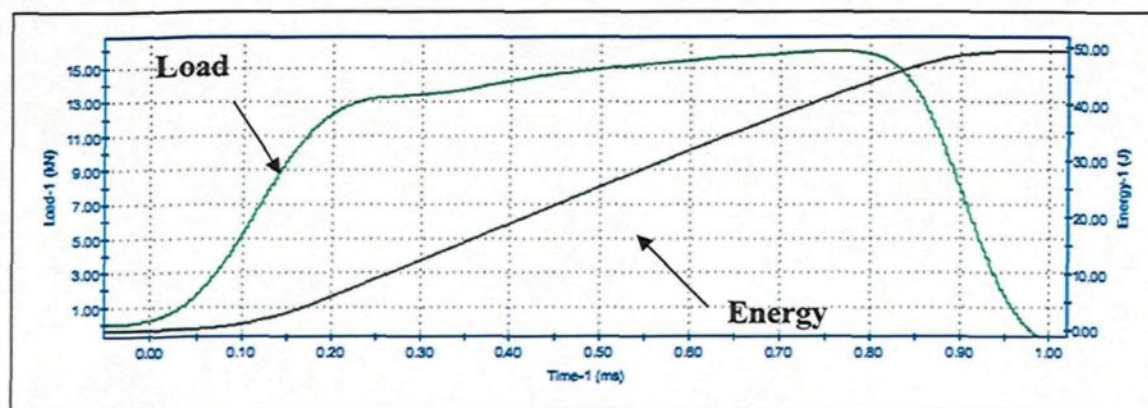
(e) B3134-T4: SHT, 8 hrs.

Figure 5. 25: Load – Time and Energy – Time curves for:
(a) Alloy B206 – 8 hrs SHT (b) Alloy B2121 – 4 hrs SHT
(c) Alloy B2121 – 8 hrs SHT (d) Alloy B3134 – 4 hrs SHT
(e) Alloy B3134 – 8 hrs SHT

Table 5. 4: Effect of Fe/Si ratio and solution heat treatment time on impact properties

Alloy code	SHT time	Total absorbed energy E_t (J)	Crack initiation energy E_i (J)	Crack propagation energy E_p (J)	Maximum Load (KN)	Total time (ms)	Time to maximum load (ms)	Average crack speed (mm/ms)
B206	8	68.75±3.31	52.37±7.06	16.38±4.72	15.17±0.30	2.63±0.78	1.02±0.15	04.98±2.14
B2121	4	56.38±6.08	48.37±6.08	08.01±0.66	16.44±0.13	1.01±0.10	0.81±0.10	10.38±1.15
	8	52.00±12.5	44.54±11.5	07.45±1.38	16.08±0.43	1.11±0.34	0.81±0.21	10.56±2.79
B3134	4	52.10±12.5	43.41±11.8	08.69±1.42	15.88±0.51	0.99±0.24	0.74±0.17	11.32±2.65
	8	45.15±11.3	37.78±11.9	07.36±0.94	15.33±0.95	0.92±0.19	0.70±0.19	12.02±3.17

The first part of the curve, where the load varies linearly with time, corresponds to the elastic deformation up to the yield load; it should be noted that the yielding load is in decreasing order higher in B2121 than B3134 and B206 alloys. This observation is in agreement with the results from the tensile tests. After yielding, plastic or permanent deformation occurs, where the damage is generally distributed over a relatively large volume of alloy so that a decrease of the load is not observed. This zone, where the load may increase up to a maximum, is wider for B2121 and B3134 alloys solution heat treated for 4 hours than it is for those solution treated for 8 hours. In other words, it takes a longer time for a crack to be initiated and to begin to propagate as demonstrated by the crack initiation energies in Table 5.4. In accordance with tensile properties, this zone is wider for B206 alloy. Finally, there is a sharp decrease in load after the ultimate point (corresponding to the maximum load) is reached, which is associated with the catastrophic cracking leading to failure. The propagation energy here is again higher for B2121 and B3134 alloys solution heat treated for 4 hours but still about half of that needed to propagate cracks in B206 alloys, leading to a crack propagation speed twice slower in the latter. In comparison to B206 alloy, the decrease in the impact strength of B2121 and B3134 alloys solution heat treated for 4 hours are 18% and 24%, respectively. However, it is interesting to see that the decrease in crack initiation energy which should be of prime consideration in design is much lower, 7% and 17% respectively, meaning that about 66% and 30% of the lost in impact strength of B2121 alloy and B3134 alloy respectively occurs during the crack propagation stage. This is well illustrated in Figure 5.26. Data from previous studies [183] for A319 and A356 alloys currently used in the automobile industry

and which were tested in the same conditions are included in the figure for comparison purposes. It is obvious that properties of B2121 and B3134 alloys although lower than that of B206 alloy in the present experimental conditions, are still far better than that of A319 and A356. The 18% and 24% decrease in impact strength are somehow proportional to the 23% and 32% reduction in ductility observed in tensile tests, considering the fact that solidification conditions of the prepared samples were different, with a likely more uniform structure in the smaller impact samples. Impact and tensile data therefore show some good correlations and confirm 4 hours solution heat treatment as the optimum time. This is illustrated in Figure 5.27 where total energy, crack initiation energy and crack propagation energy are plotted against elongation. In all the cases, the correlations are quite good, as seen from the R^2 values. Each of the energy components can therefore be used to describe the ductility of the material with an advantage to the initiation energy, but total energy remains the perfect tool.
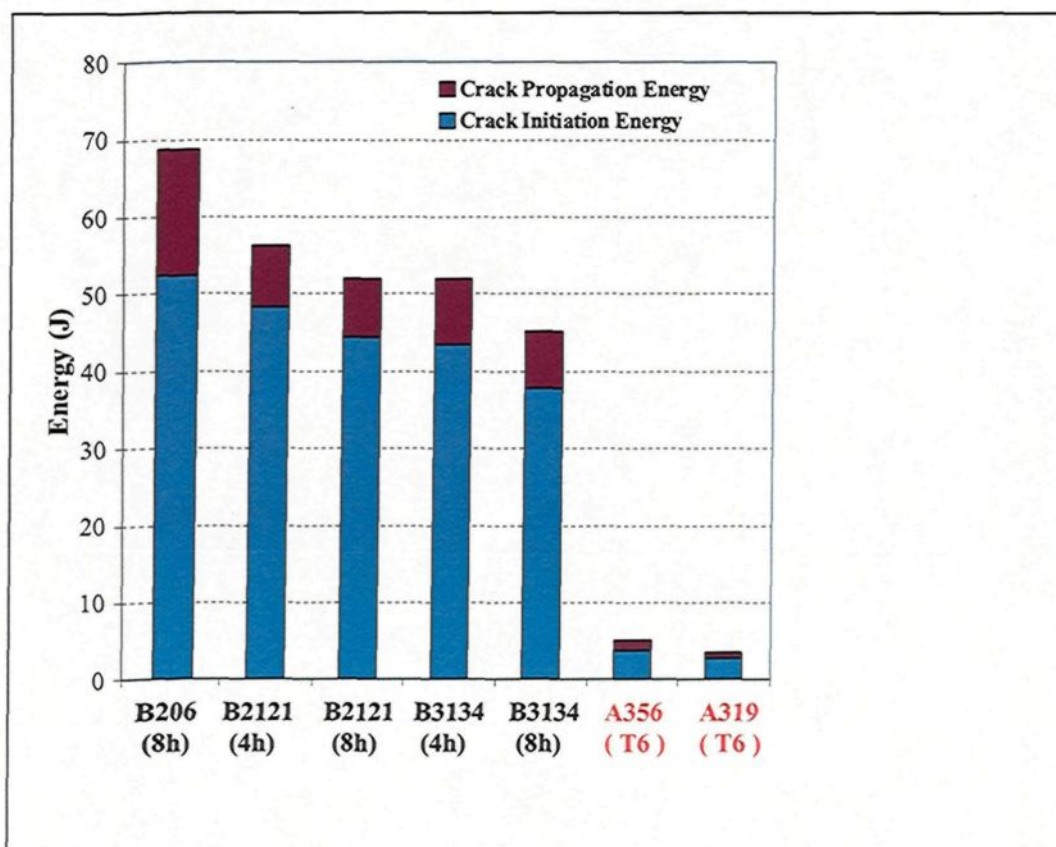
Figure 5. 26: Impact energy components involved in the fracture of the samples subjected to various SHT times.
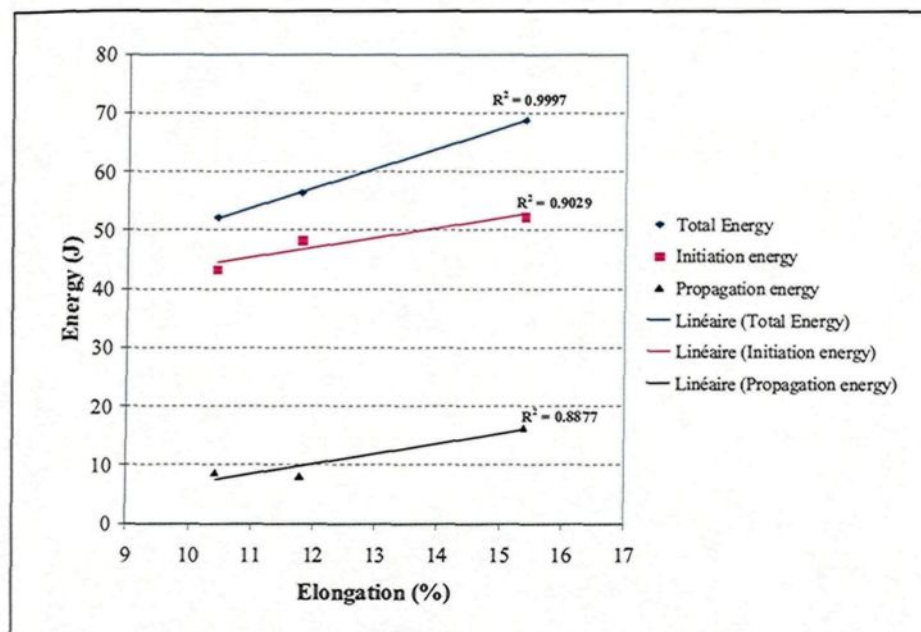
Figure 5. 27: Correlation between impact energy and ductility of B206, B2121 and B3134 alloys
B206 SHT for 8 hrs ; B2121 and B3134 SHT for 4 hrs.

5.3 Summary

Mechanical properties were investigated to determine the combined effects of both additions of iron and silicon as well as heat treatment on tensile, hardness and impact properties of B206 alloys.

The results show that properties are highly influenced by the iron-to-silicon ratio and the nominal concentrations of the individual elements. The best properties were obtained with both a ratio close to one and low concentrations of iron and silicon, in agreement with the results obtained during solidification and hot tearing studies. Two main parameters were found to determine the properties of heat treated sample, namely, solubility of the Al_2Cu phase and dendrite coarsening. Maximum solubility of Al_2Cu phase was observed at four hours solution heat treatment time. During this period, the properties of the alloys increase and reach a maximum. With further solution time, the properties as well as the quality index of the material decrease. This decrease in quality above four hours solution heat treatment time is attributed to dendrite coarsening which seems to be the controlling factor after maximum solubility of the θ phase is reached. Four hours is therefore considered as the optimal solution heat treatment time for B2121 and B3134 alloys.

Porosity is known to affect the ductility of the material but in this case no noticeable effect of its evolution could be observed within the optimum period of four hours solution heat treatment time. Ductility of the material seems therefore to mostly depend on the porosity characteristics of the material in the as-cast condition. Present experimental results show it will not be problem, under natural aging (T4) conditions to obtain the minimum of 7% elongation required by the automotive industry by doubling or tripling the present limit

of 0.1%Fe in these alloys, while increasing the strength. From calculated maximum values of strain, the loss compared to B206 alloy also naturally aged may be narrowed to 2.5% with good casting practice. Under artificial aging (T7) conditions, it will be very difficult if not impossible to reach the 7% elongation at 0.2%Fe and 0.2%Si, while at 0.3%Fe and 0.3%Si it will be quite impossible. Impact energy correlates well with tensile ductility. The results shows that most of the decrease in total absorbed energy of B2121 and B3134 alloys in comparison to B206 alloy is related to the crack propagation energy.

CHAPTER 6
CONCLUSION
AND
RECOMMENDATIONS

CHAPTER 6
CONCLUSION AND RECOMMENDATIONS

6.1 Conclusion

The main objective of this research project was to optimize the iron content in aluminum type B206 alloys without major loss in mechanical properties in order to make the alloy cost competitive. This was fulfilled by neutralization of iron by silicon through studies on the effects of additions of both these elements on solidification, hot tearing and mechanical properties of B206 alloys. A summary of findings from these three aspects of the study have been presented in sections 3.3, 4.3, and 5.3 respectively. From these detailed summaries, a general conclusion may be drawn as follows.

The results of this investigation show that if the iron to silicon ratio is kept close to one, it is possible to double or even triple the present 0.1% maximum iron allowable in aluminum type B206 alloy, resulting in improved strength, and still meeting the ductility requirements of the automobile and aerospace industries. Furthermore, 4 hours was identified as the optimum solution heat treatment time, *i.e* half the time of 8 hours presently used for B206 alloy. Reducing the solution time by 50% will lower the cost of production and thereby increase the competitiveness of the alloy. In addition, these properties are obtained under natural aging conditions thereby removing problems

associated with stress corrosion cracking. Even though these alloys show lower ductility than the base B206 alloy in the present experimental conditions, they still stand far above currently used A356 and A319 alloys and therefore need to be considered. There is still some room for improvement, however, as shown by maximum projections of strain and quality index, as well as sources of worry like the 100% increase in crack propagation speed compared to B206 alloy. These points have to be clarified before any adaptation of the results to foundry practice and commercial exploitation can be made. These clarifications are left as recommendations for future work.

6.2 Suggestions for future work

Recommendations for further research therefore may be:

1- A study on grain refining and melt treatment in order to increase the quality of the casting.

2- A study on fatigue properties of these alloys in order to determine their usefulness for critical applications. Machinability characteristics could also be of interest.

3- Fractography studies on tensile and impact samples in order to examine the fracture features and to relate them to the causes and basic mechanisms of fracture.

Appendix A
Cooling curves and derivatives at various Fe/Si ratios and cooling rates

B1106
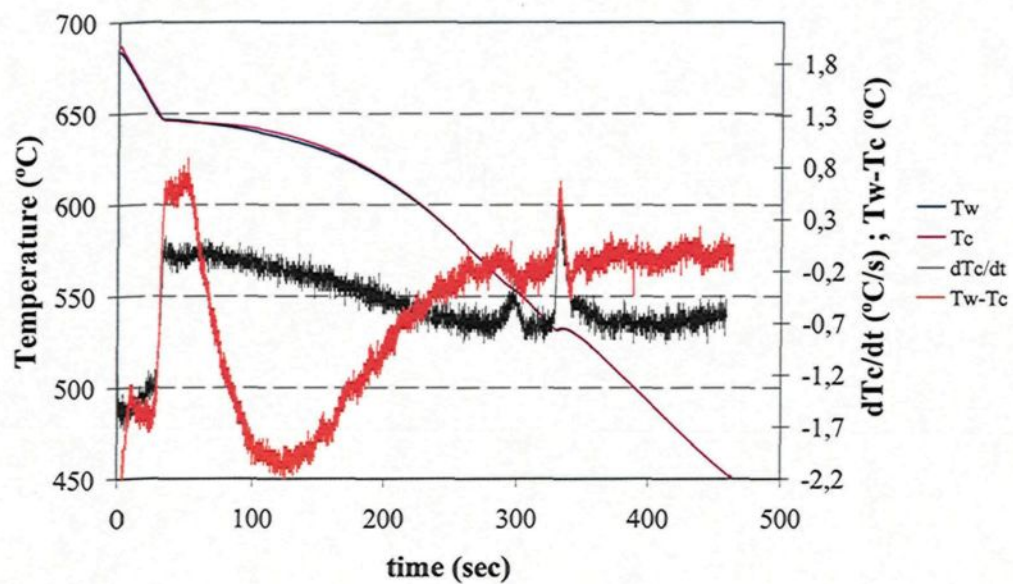
B1106A
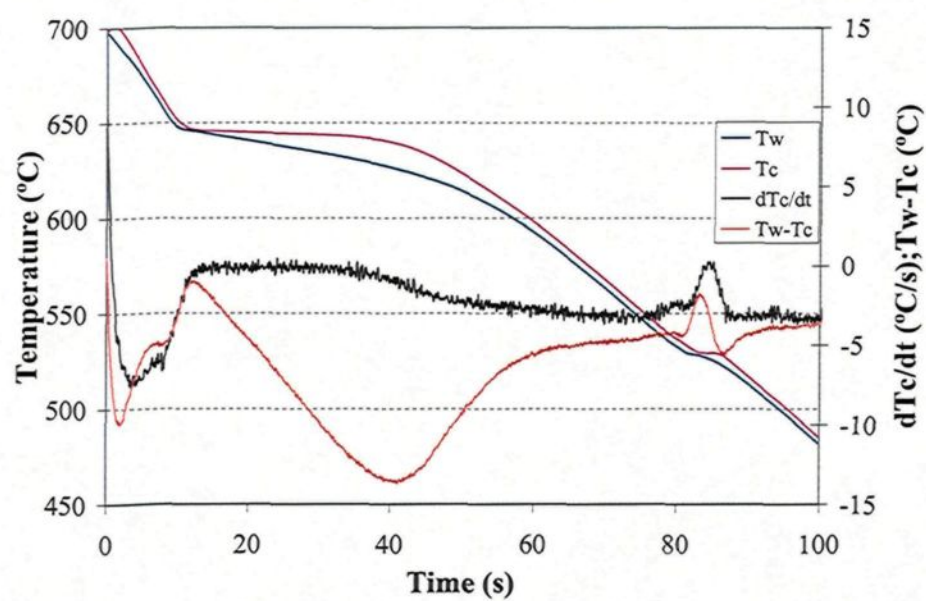
B1710
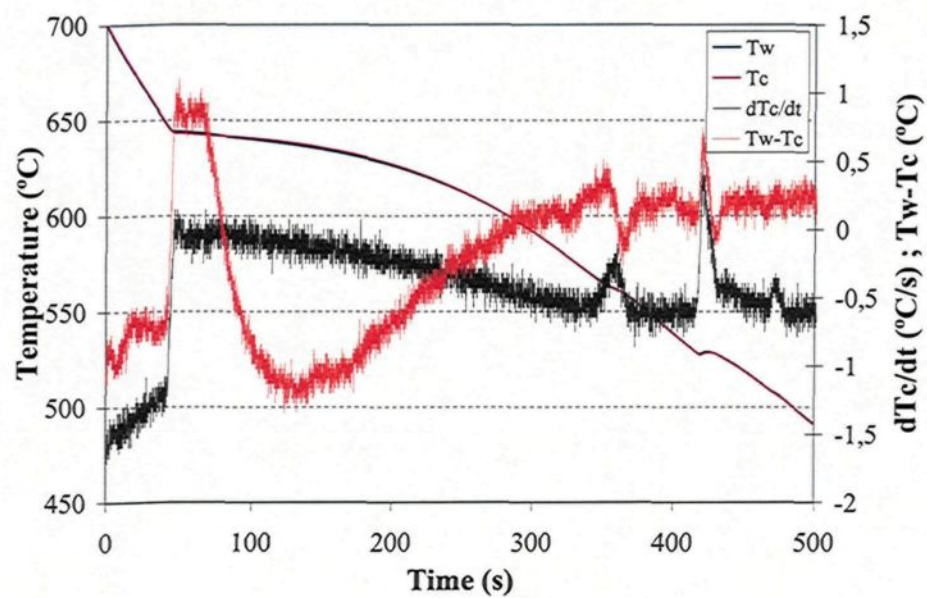
B1710A
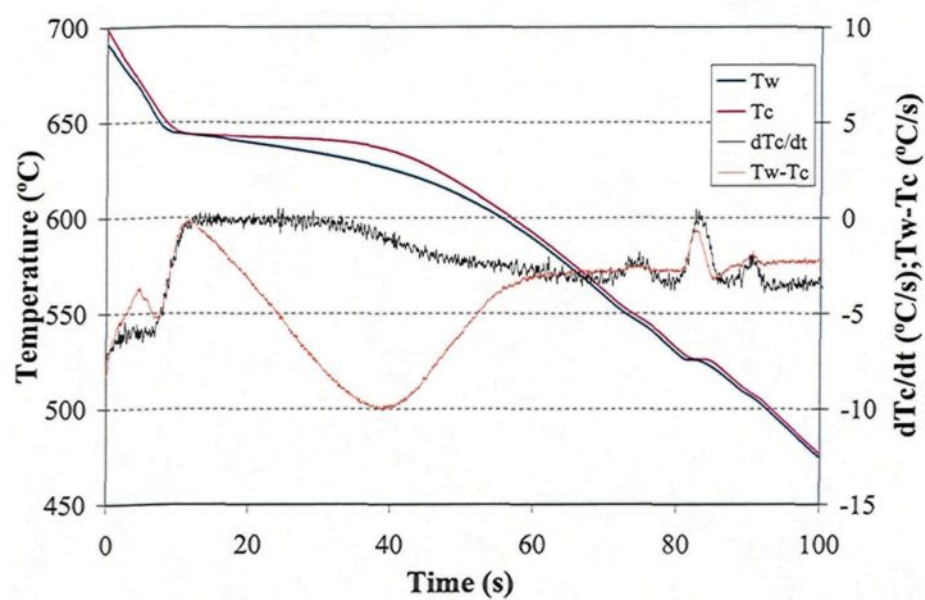
B2710
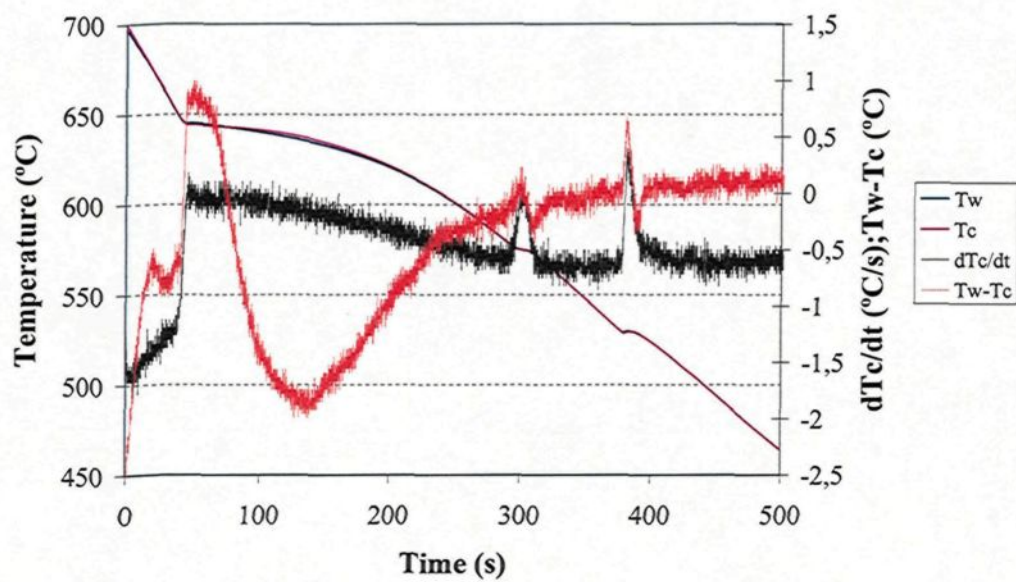
B2710A
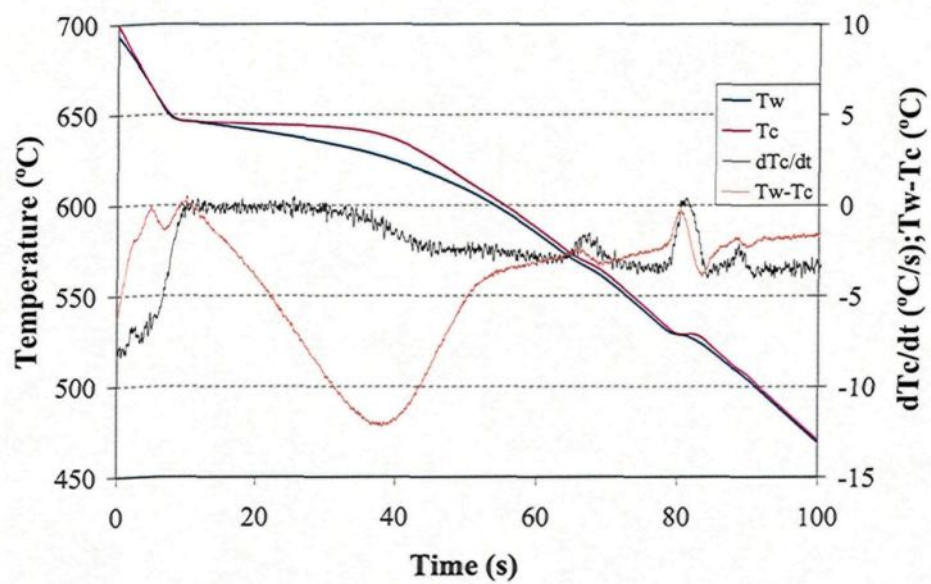
B2420
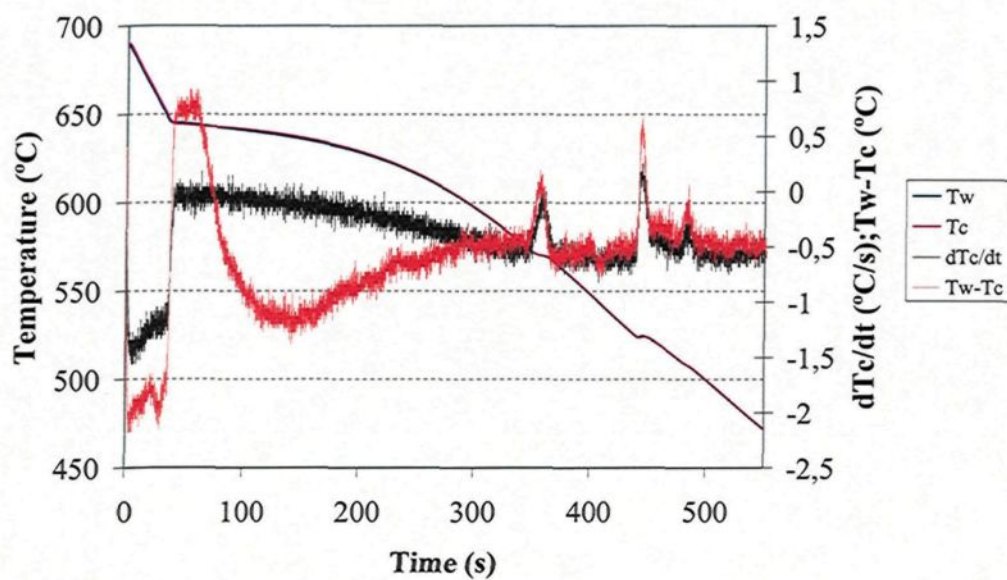
B2420A
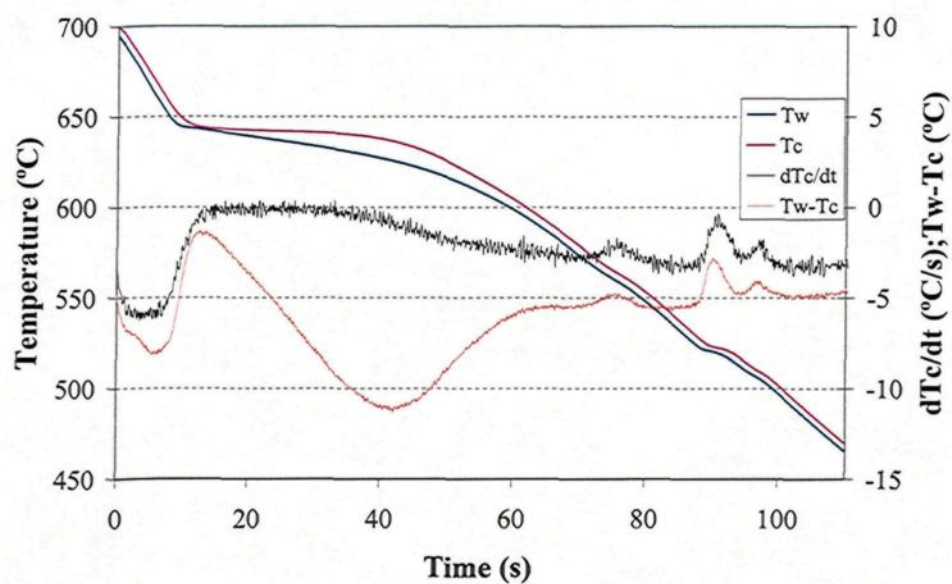
B2919
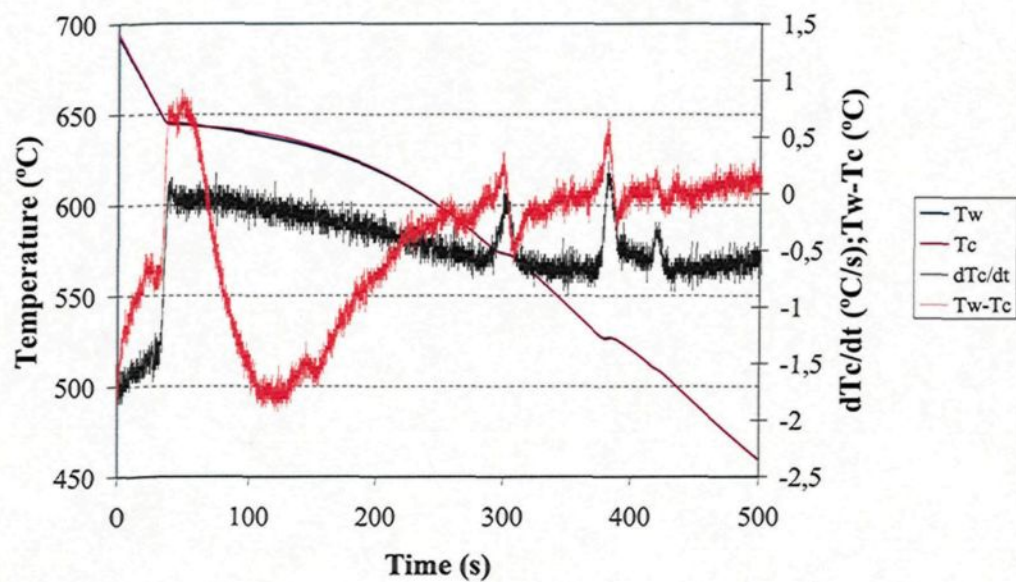
B2919A
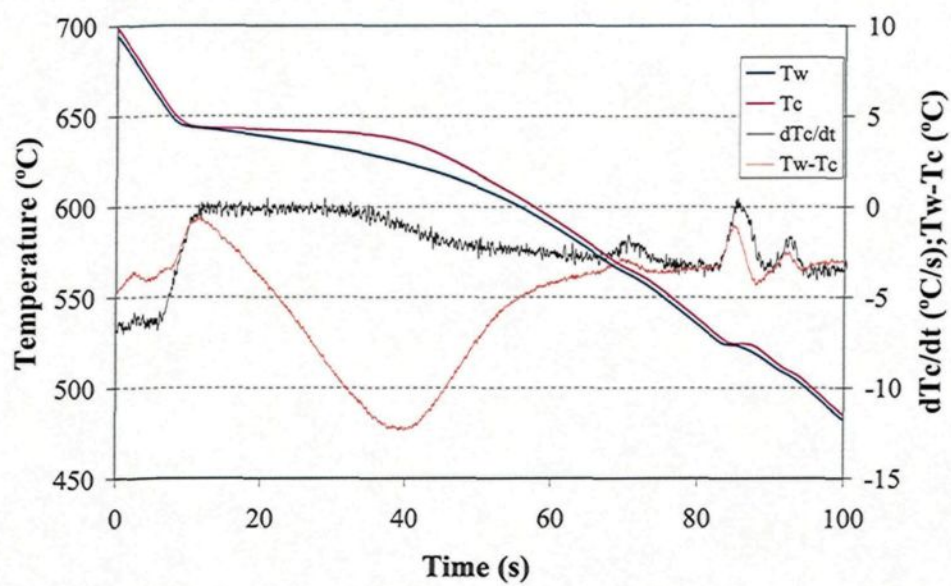
B3128
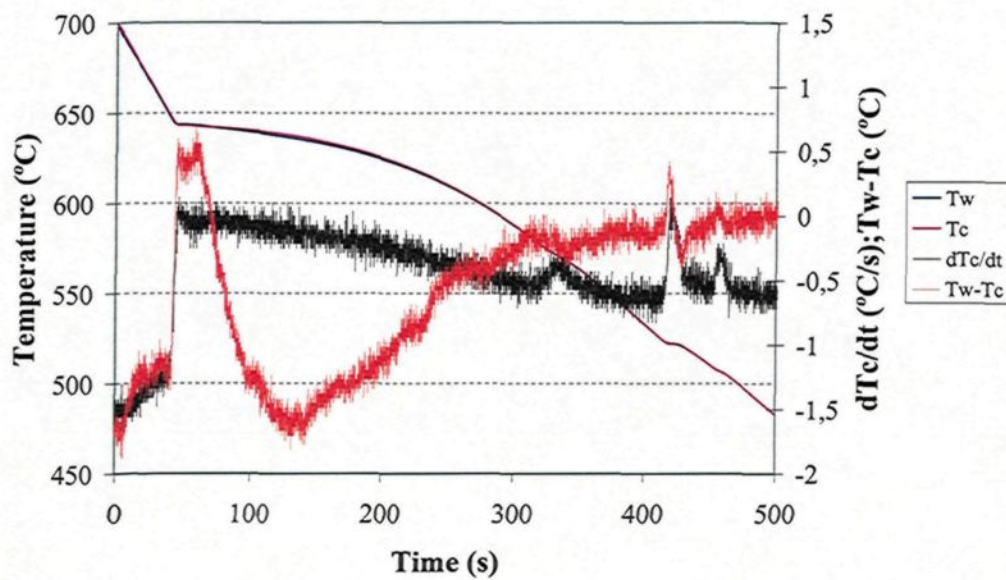
B3128A
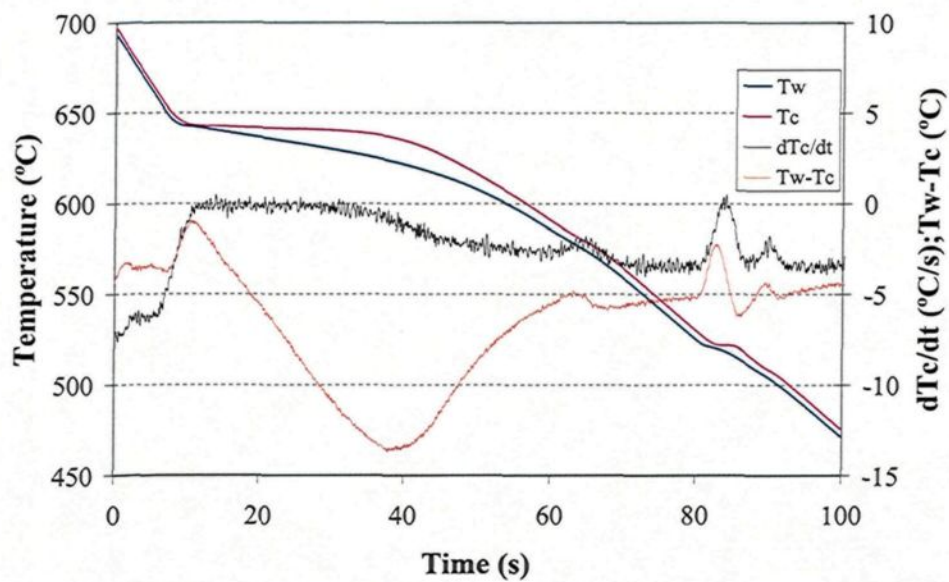
B2328
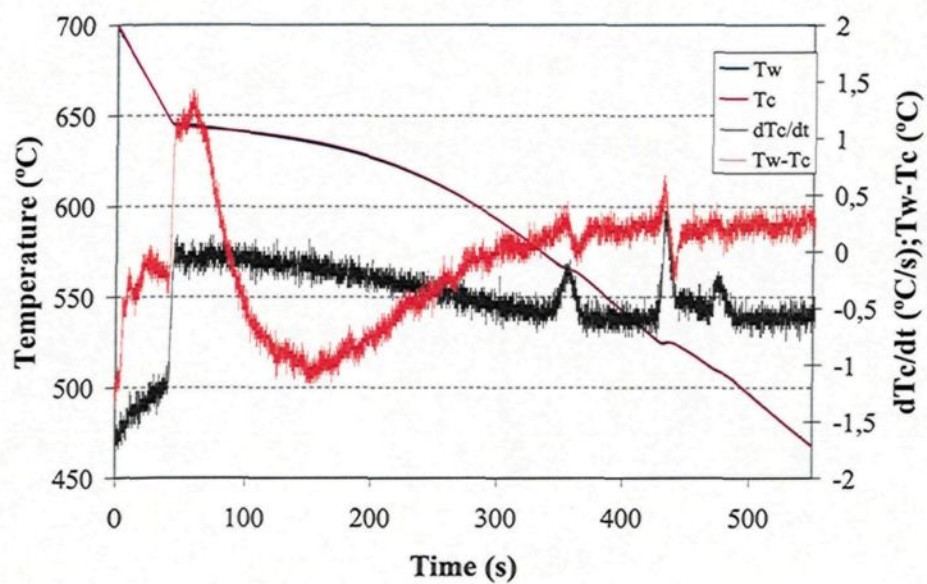
B2328A
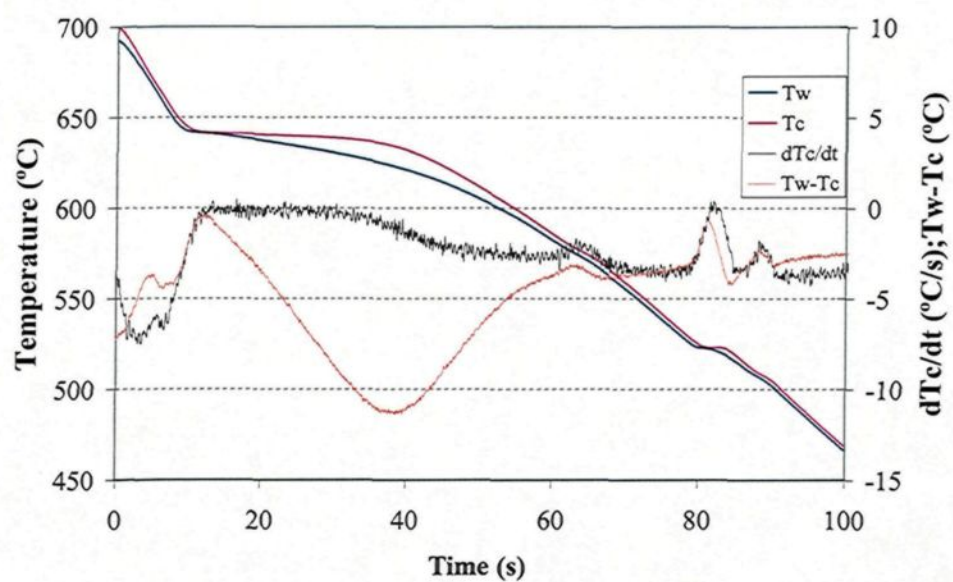
U1206
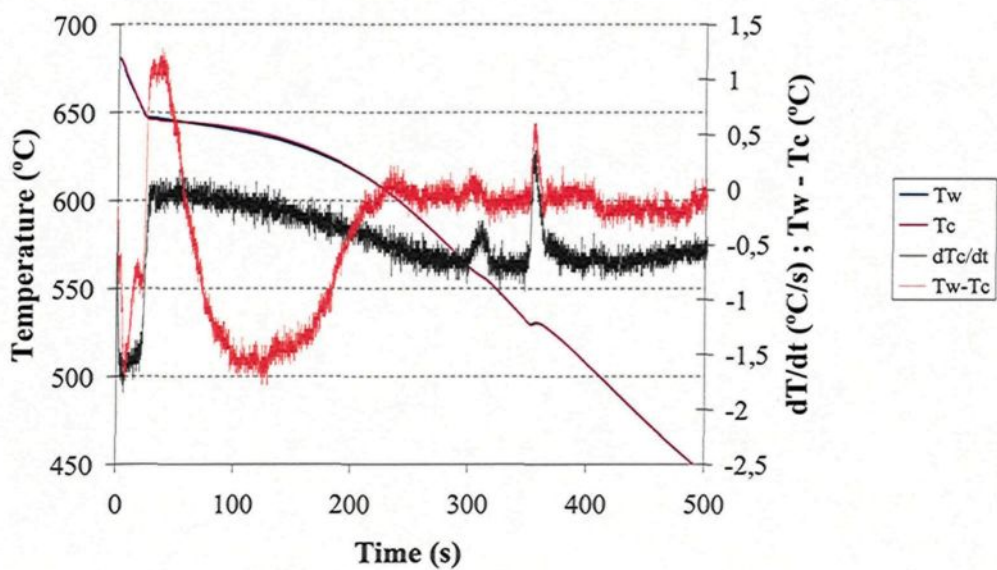
U1206A
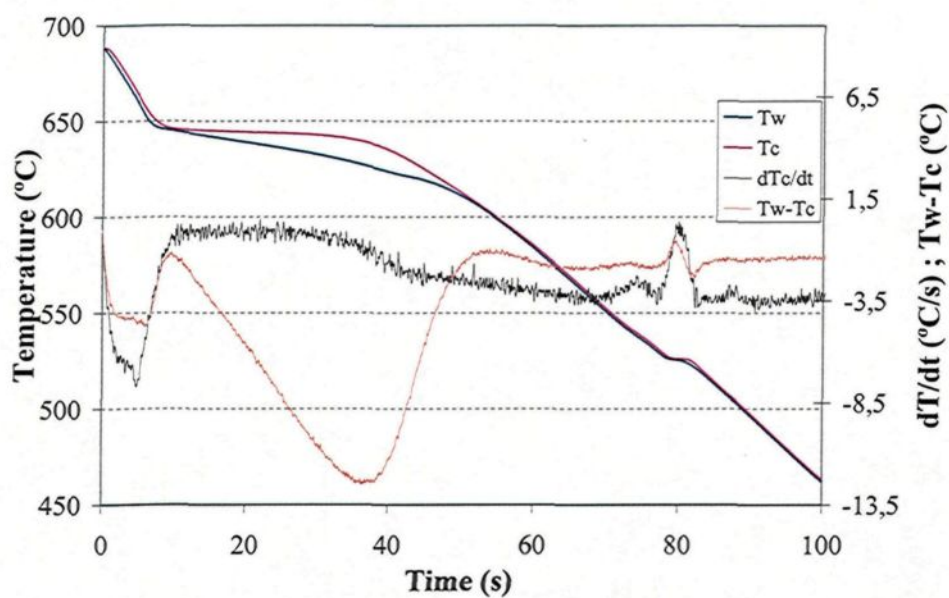
U1710
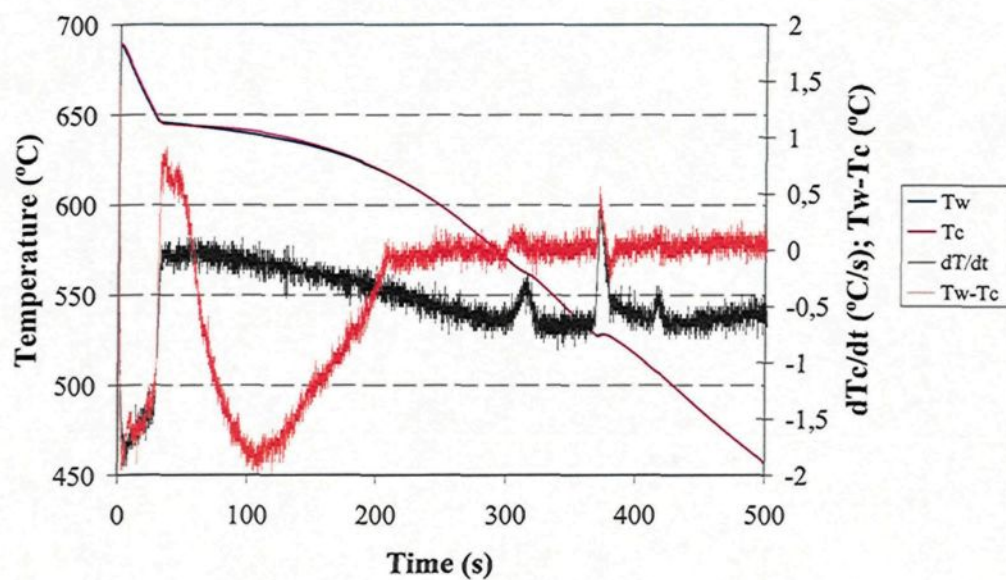
U1710A
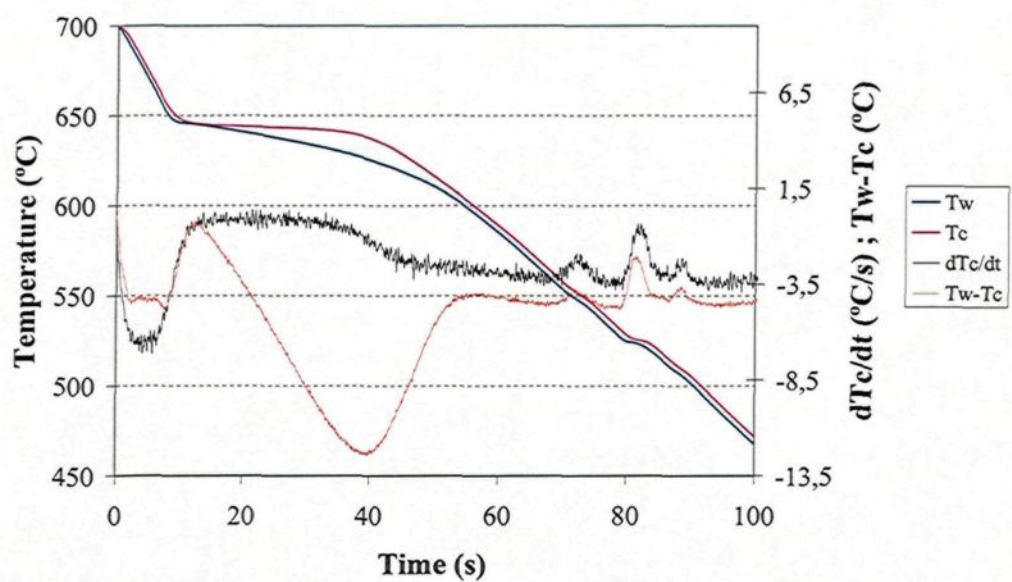
U2410
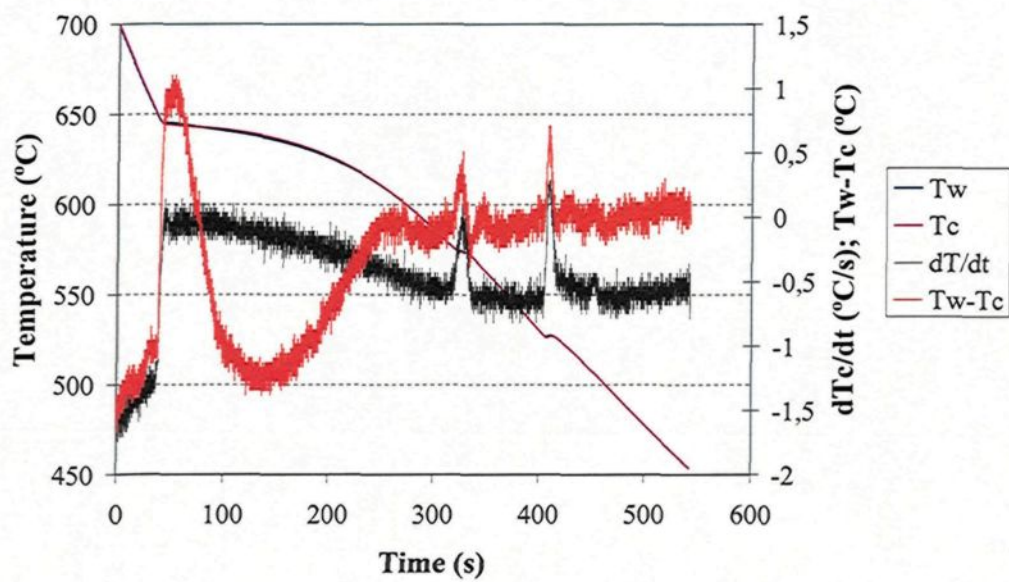
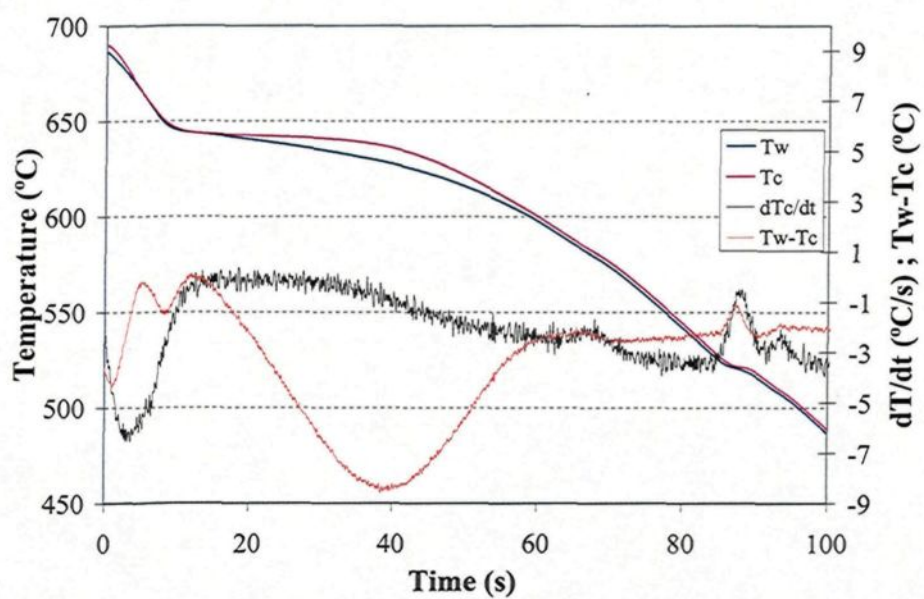**U2410A**
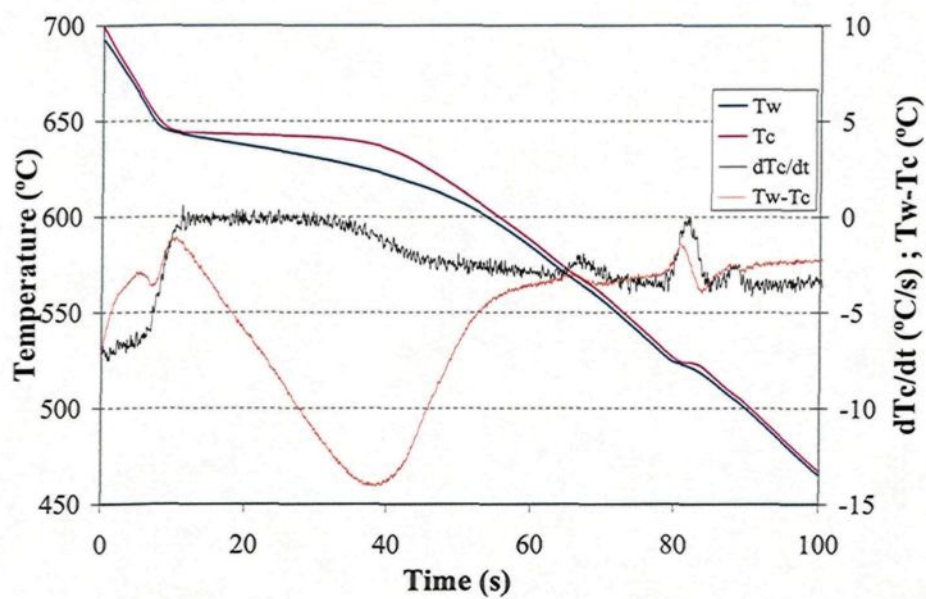
U2320
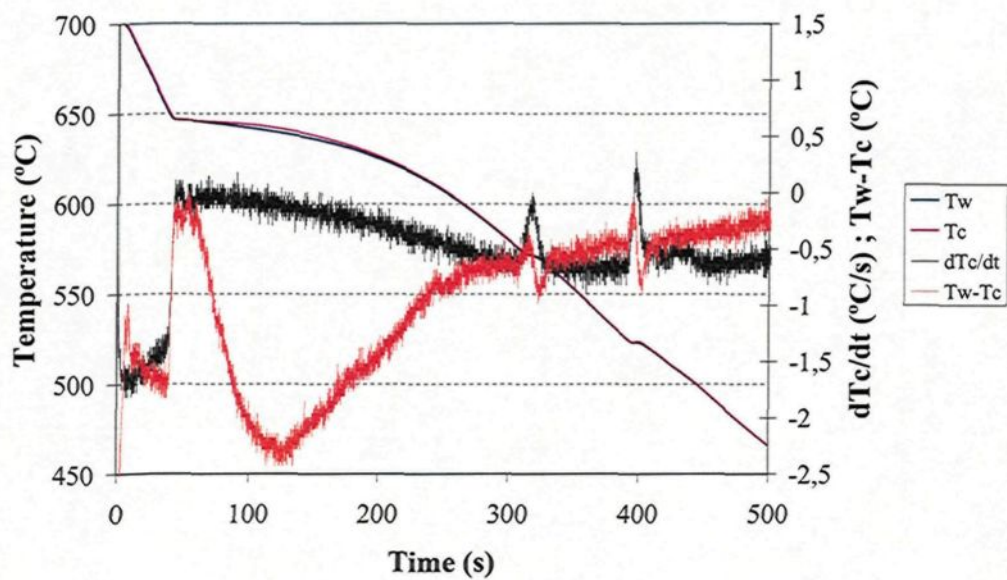
U2320A
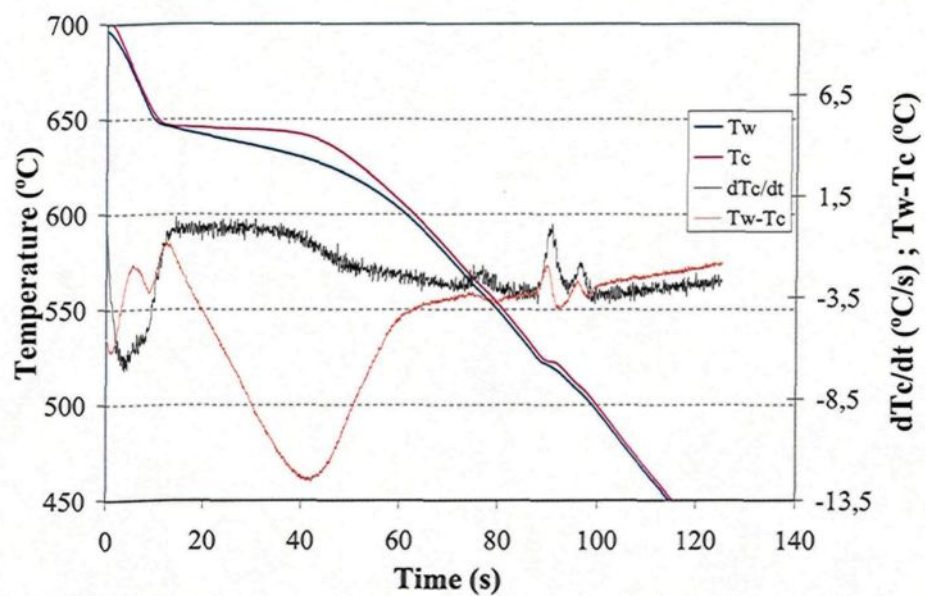
U3420
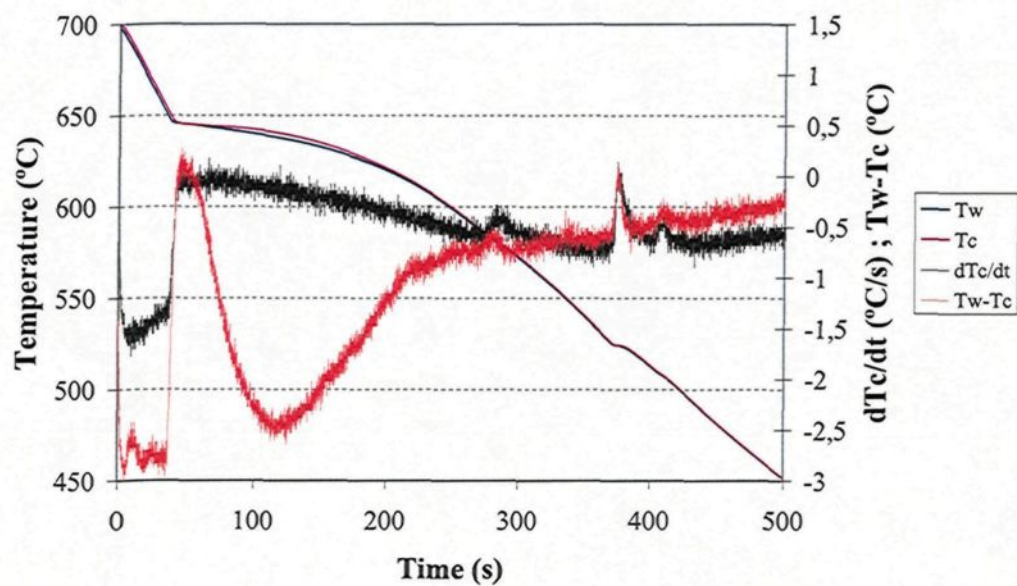
U3420A
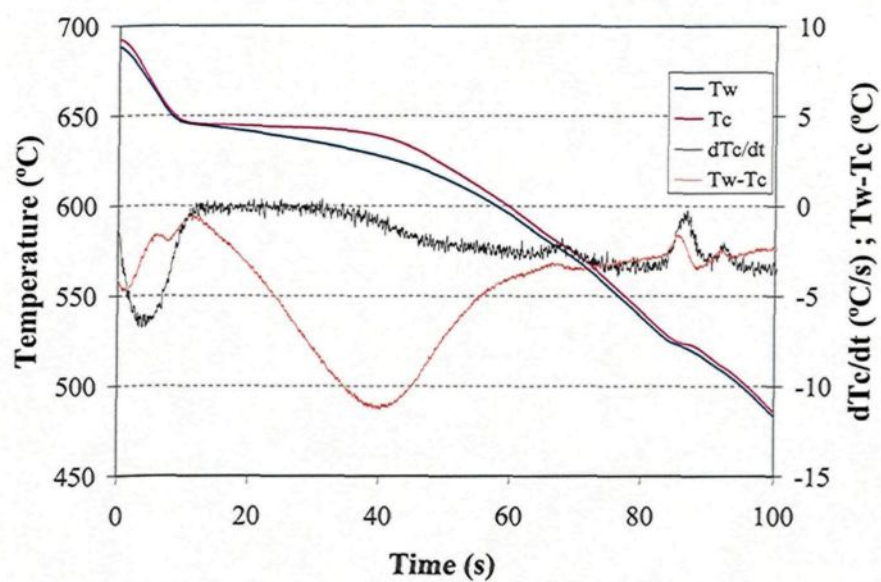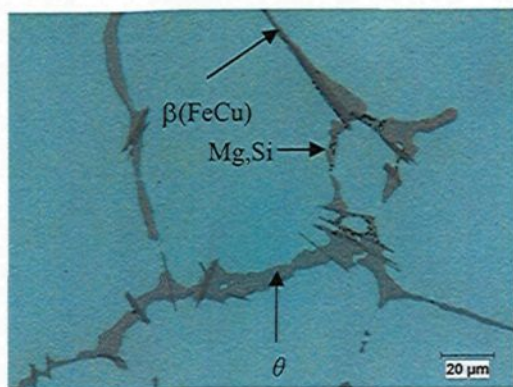
U2430
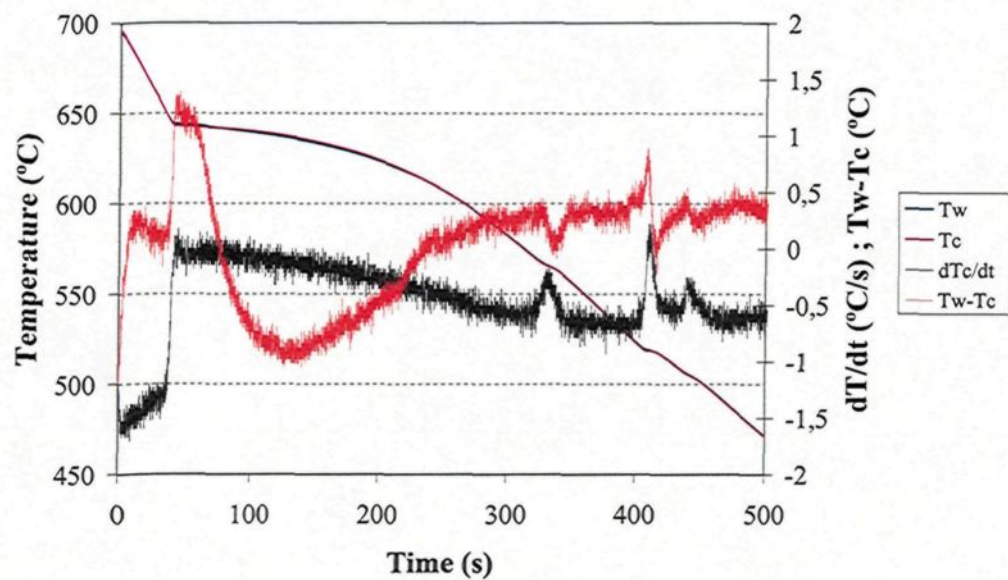
U2430A

Appendix B
Typical microstructure at various iron to silicon ratio and cooling rates

Alloy B1710
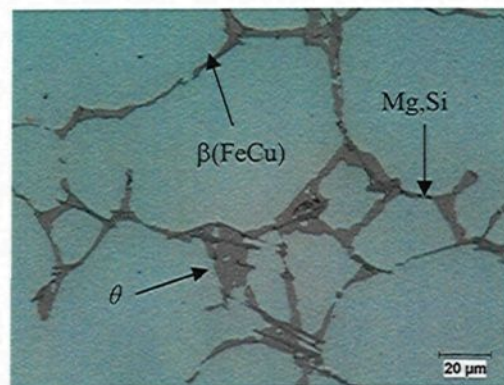
Alloy B1710A
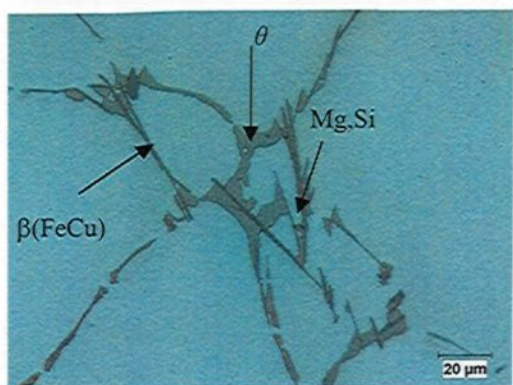
Alloy B2710
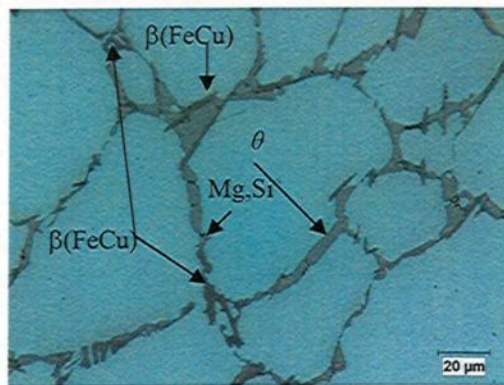
Alloy B2710A
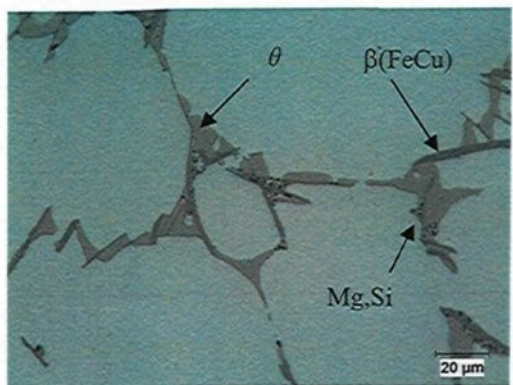
Alloy B2919
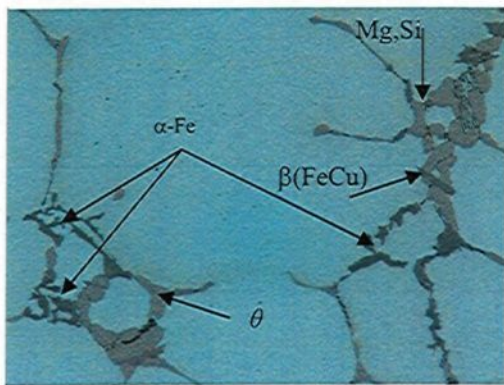
Alloy B2919A
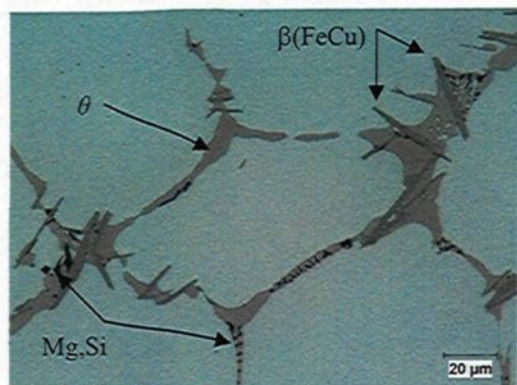
Alloy B2328
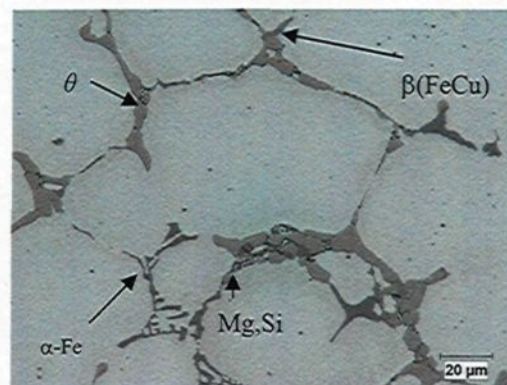
Alloy B2328A

Appendix C
The macroscopic photos of hot tear bars surfaces
of various alloys
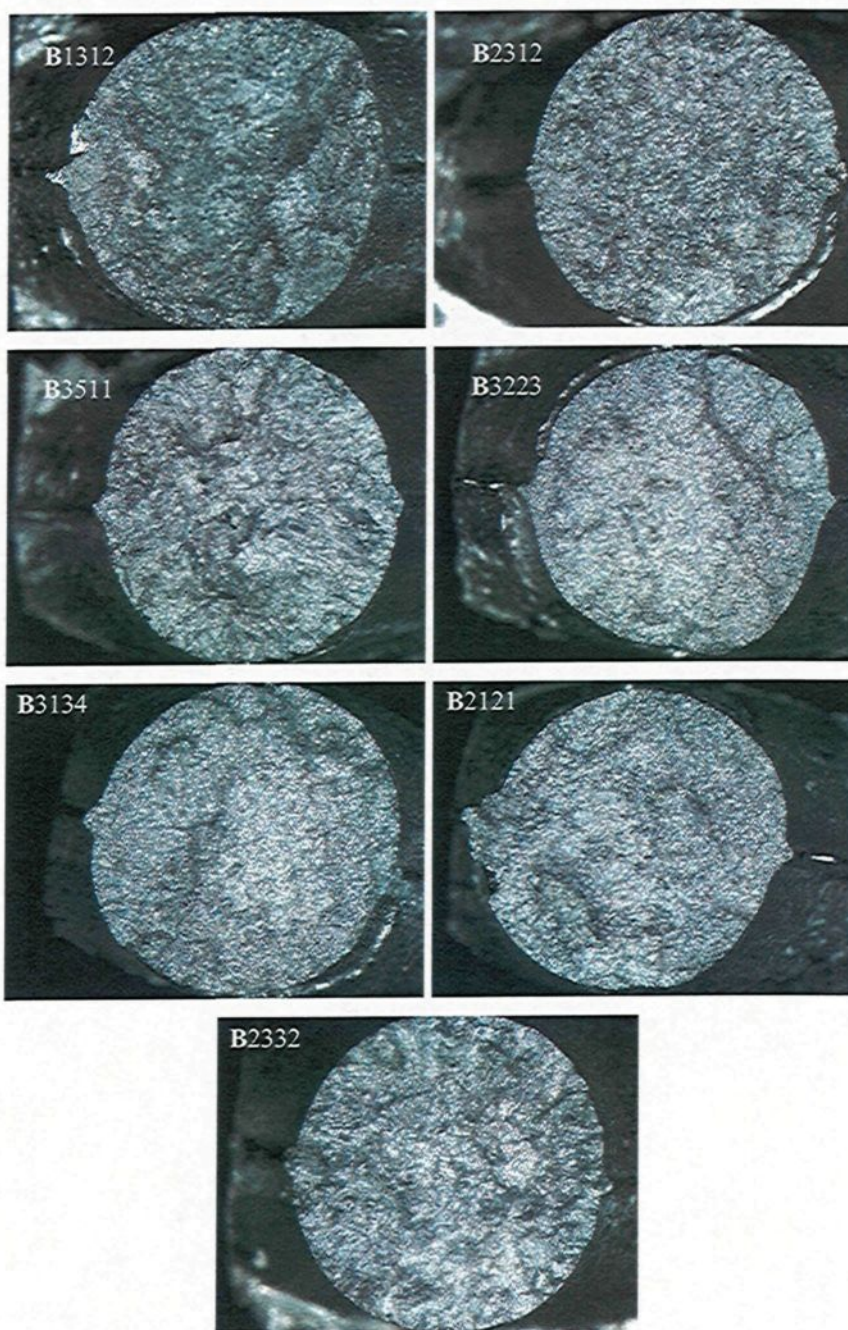
Appendix D:
SEM photos of hot tear surfaces of various alloys

B2312

CNRC-CTA 20.0kV 15.2mm x500 SE(M) 9/22/2009 15:27   100um

B3511

CNRC-CTA 20.0kV 16.1mm x500 SE(M) 9/28/2009 09:24   100um

B3223

CNRC-CTA 20.0kV 13.4mm x500 SE(M) 9/28/2009 09:47   100um

B3134

CNRC-CTA 20.0kV 13.4mm x500 SE(M) 9/28/2009 10:00   100um

196

B2121

CNRC-CTA 20.0kV 13.4mm x500 SE(M) 9/28/2009 10:15   100um

B2332

CNRC-CTA 20.0kV 13.4mm x500 SE(M) 9/28/2009 10:29   100um
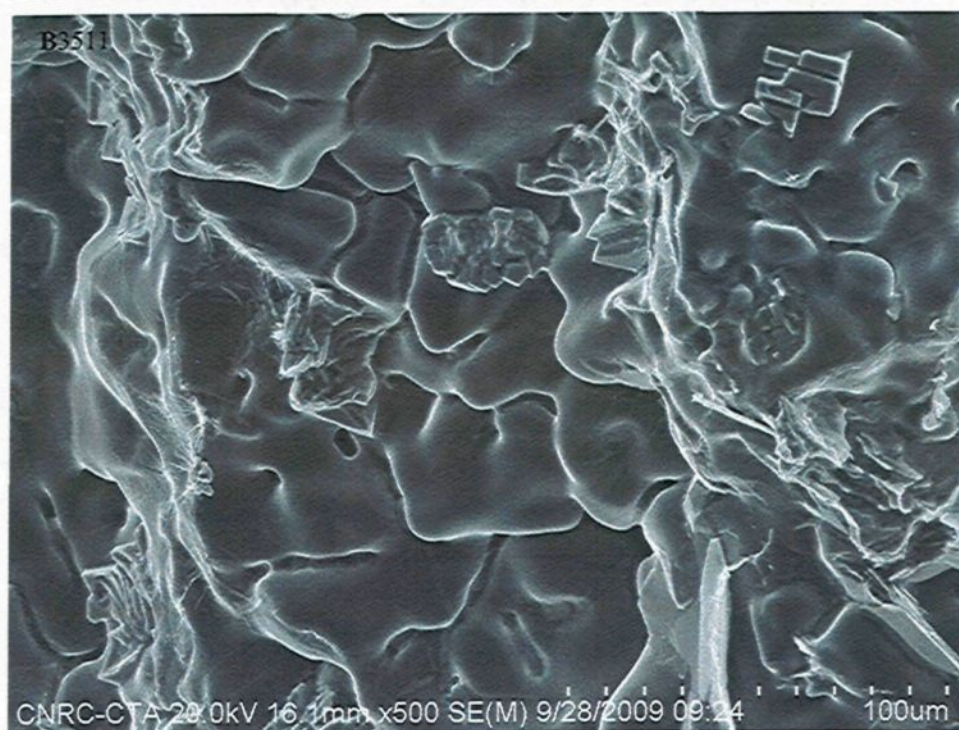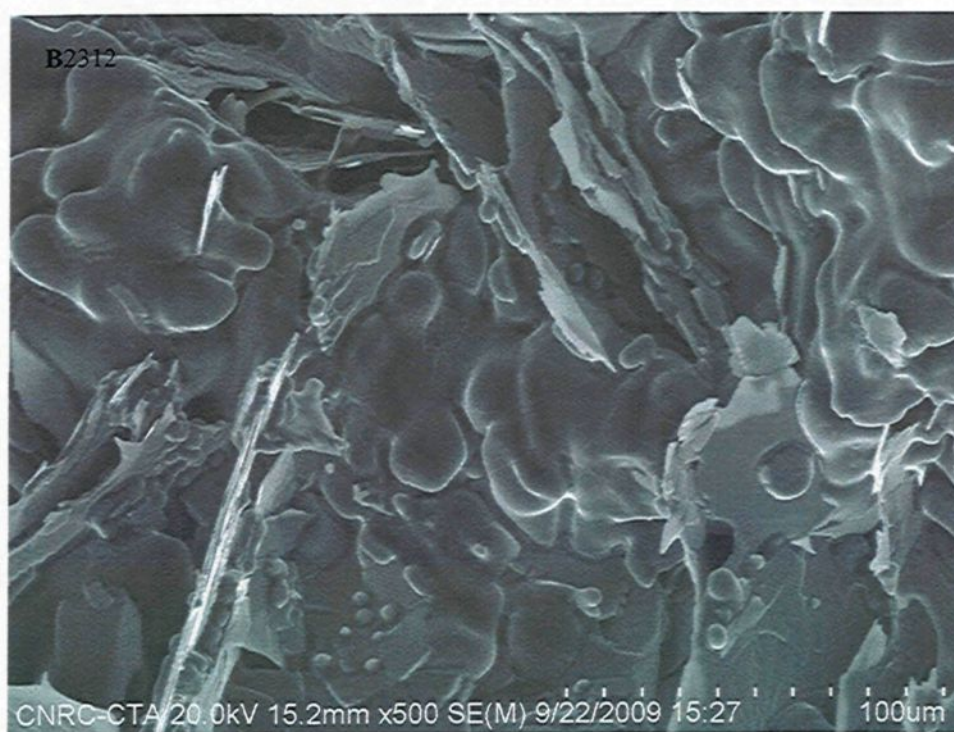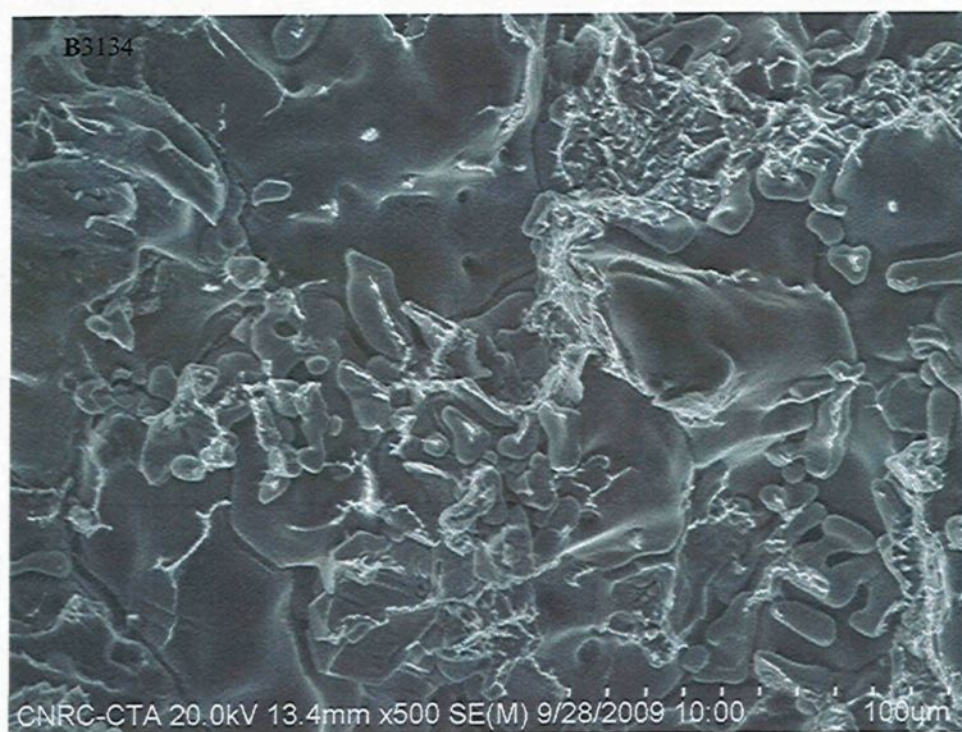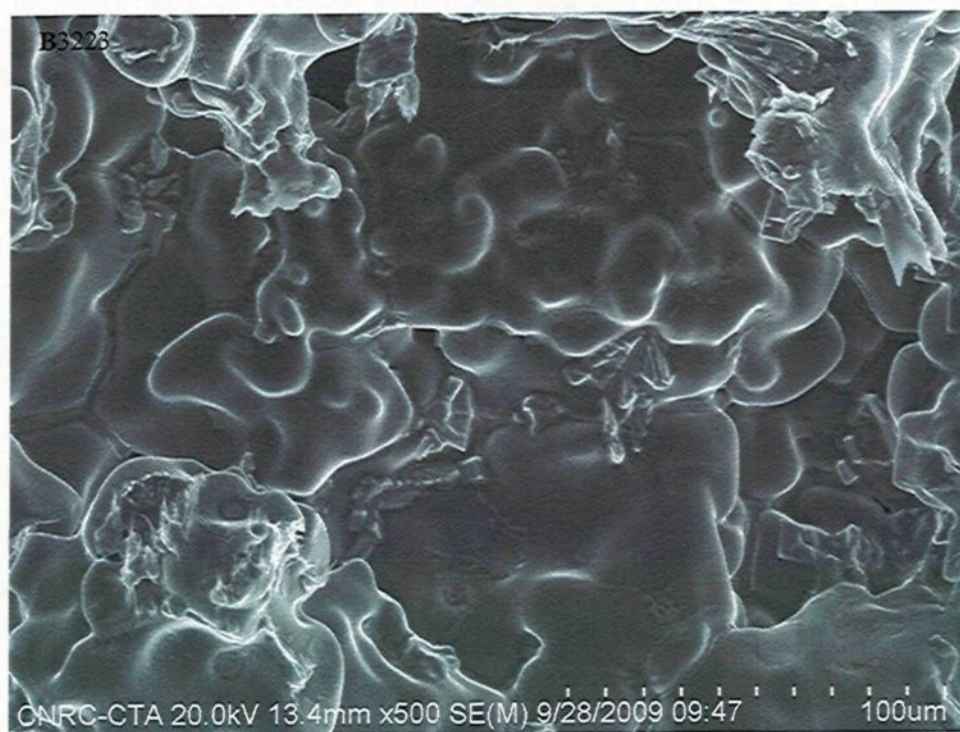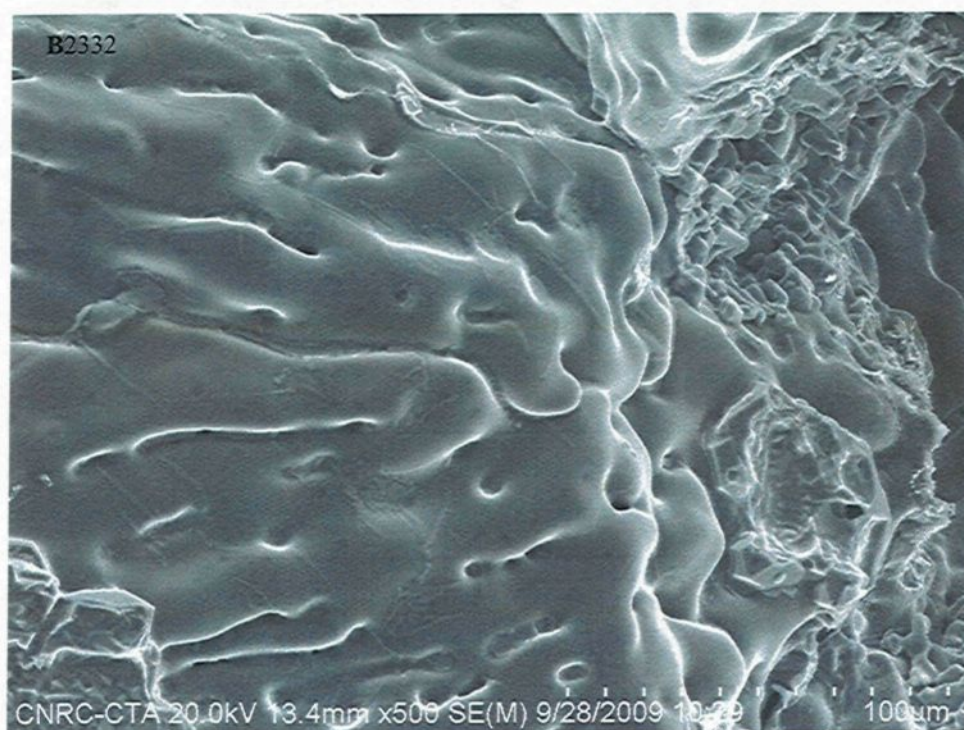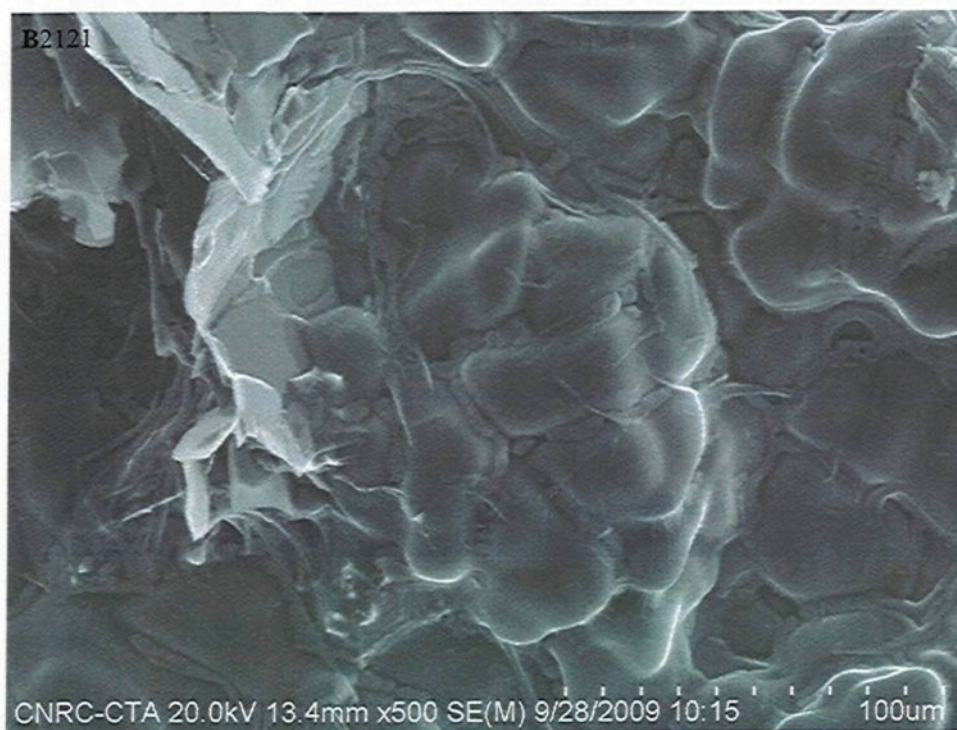
Appendix E:
Hot tear microstructure of various alloys

B206 (Bar D)
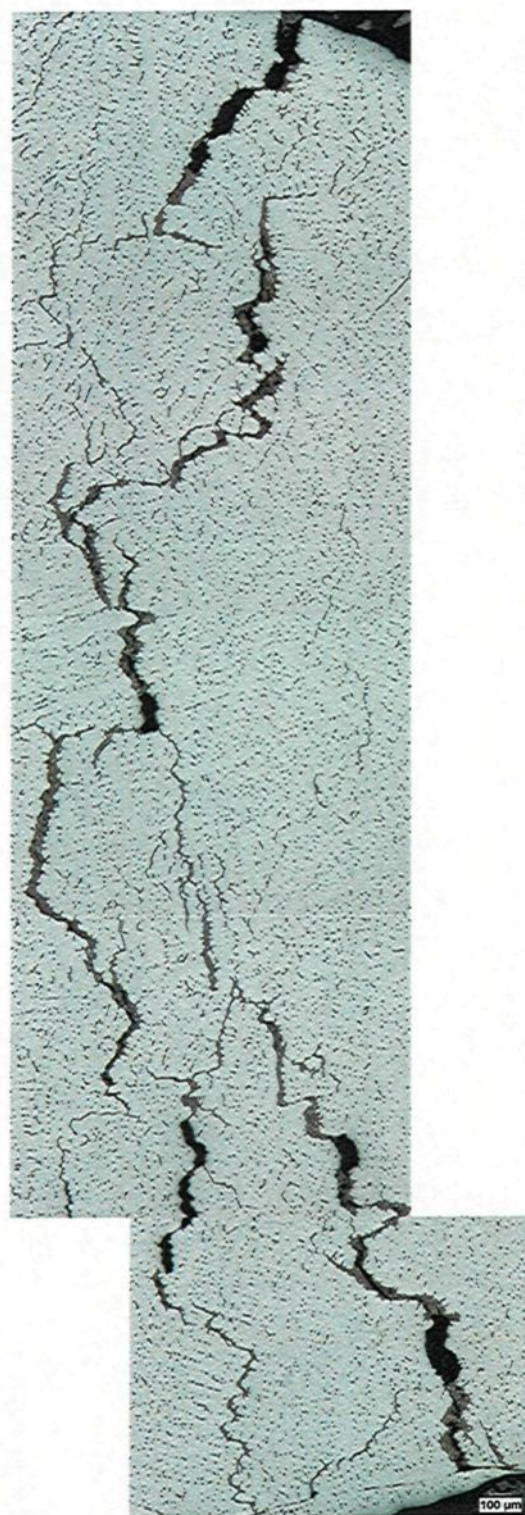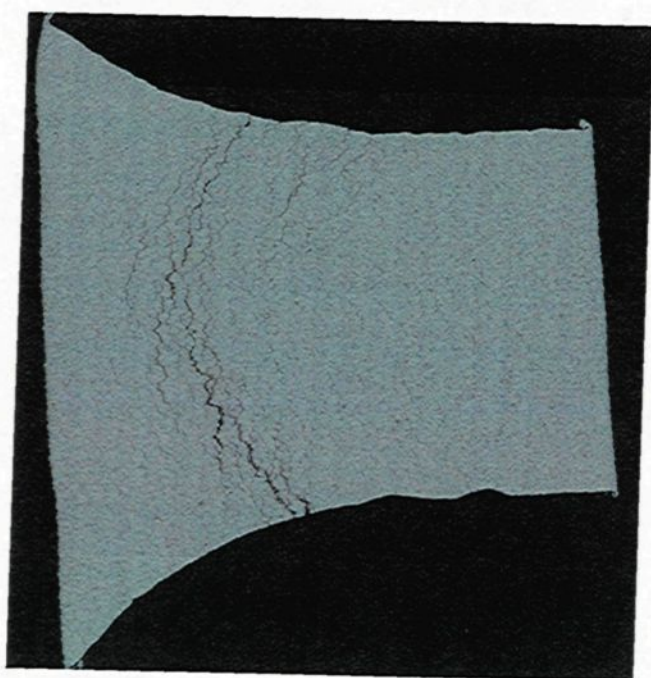
B1213 (Bar D)

B1213 (Bar C)

100 um
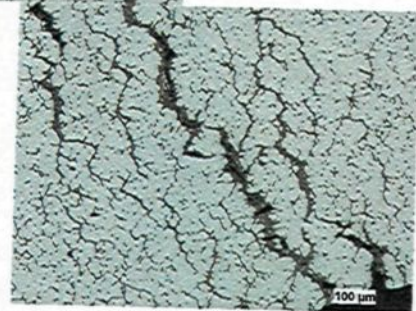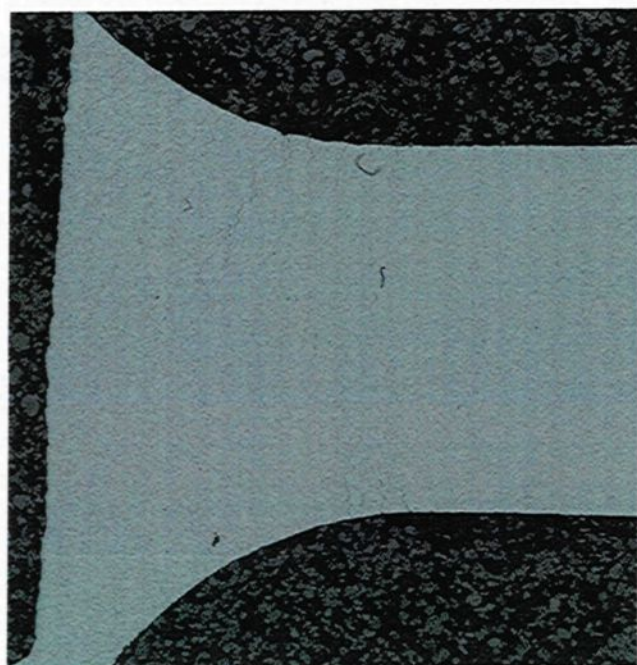
B2312 (Bar D)

B2312 (Bar C)

100 µm
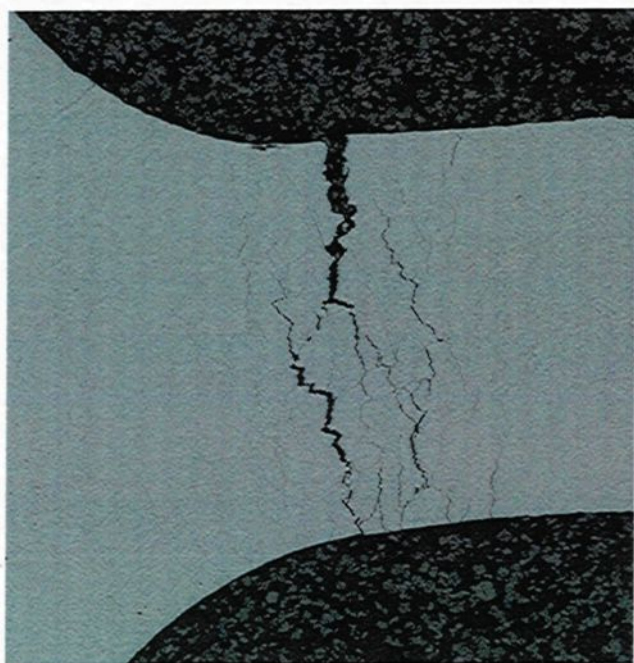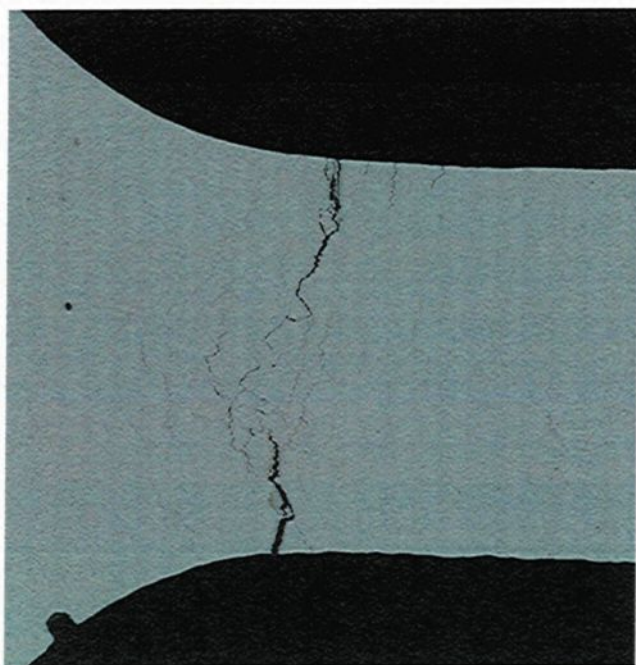
B3511 (Bar D)

B3511 (Bar C)

B3223 (Bar D)

B3134 (Bar D)
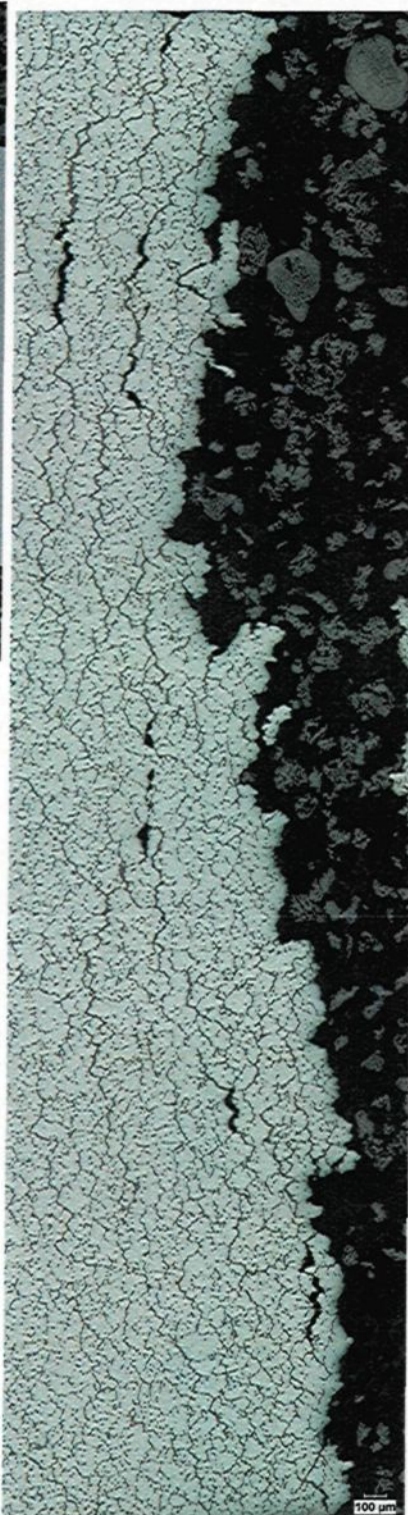
B2121 (Bar D)
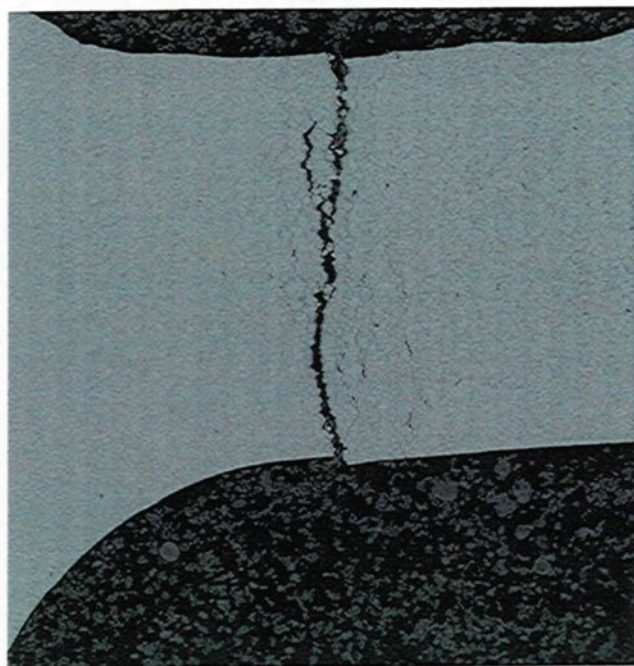
B2121 (Bar D)
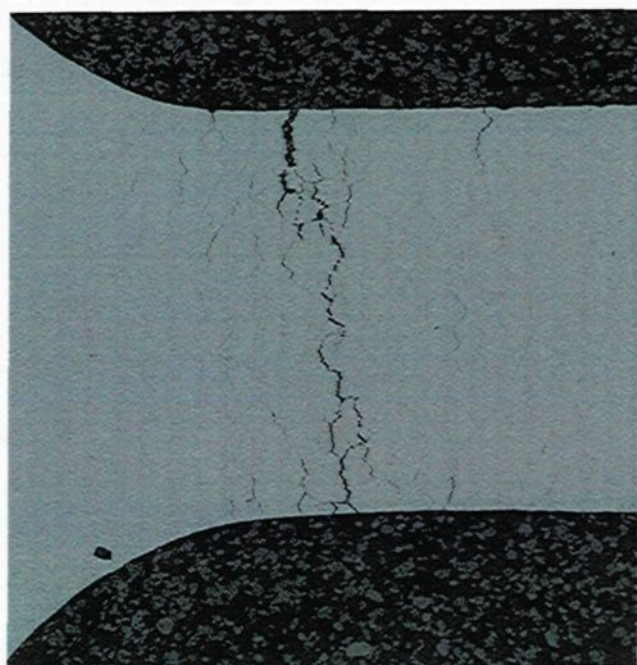
B2332 (Bar D)

Appendix F
Curves and data obtained from tensile tests for various alloys under different heat treatment conditions.

For each condition, the chosen curve was the one that best represented the mean calculated values. Curves are plotted for true values of strength and strain while data given in the table are engineering values. YS is the yield strength, UTS is the ultimate tensile stress and SD is the standard deviation.

As-Cast

Alloy Code	YS , MPa (SD)	UTS, MPa (SD)	Elongation at rupture, % (SD)	Modulus, GPa (SD)
B206	166.34 (±5.62)	244.02 (±10.8)	3.91 (±1.05)	72.03 (±0.41)
B1213	195.00 (±1.20)	263.10 (±3.30)	2.72 (±0.17)	72.70 (±0.36)
B2312	192.30 (±4.80)	252.00 (±9.70)	2.02 (±0.45)	74.10 (±0.87)
B3511	185.60 (±4.40)	238.10 (±7.80)	1.69 (±0.24)	74.66 (±2.00)
B3223	184.00 (±4.10)	227.30 (±9.60)	1.34 (±0.27)	73.58 (±2.15)
B3134	181.10 (±3.10)	239.90 (±4.90)	1.97 (±0.36)	72.48 (±0.62)
B2121	188.00 (±6.60)	237.60 (±6.00)	1.62 (±0.44)	76.26 (±4.24)
B2332	175.30 (±2.60)	224.10 (±5.20)	2.03 (±0.29)	71.55 (±1.90)

2 hours SHT, naturally aged (T4)
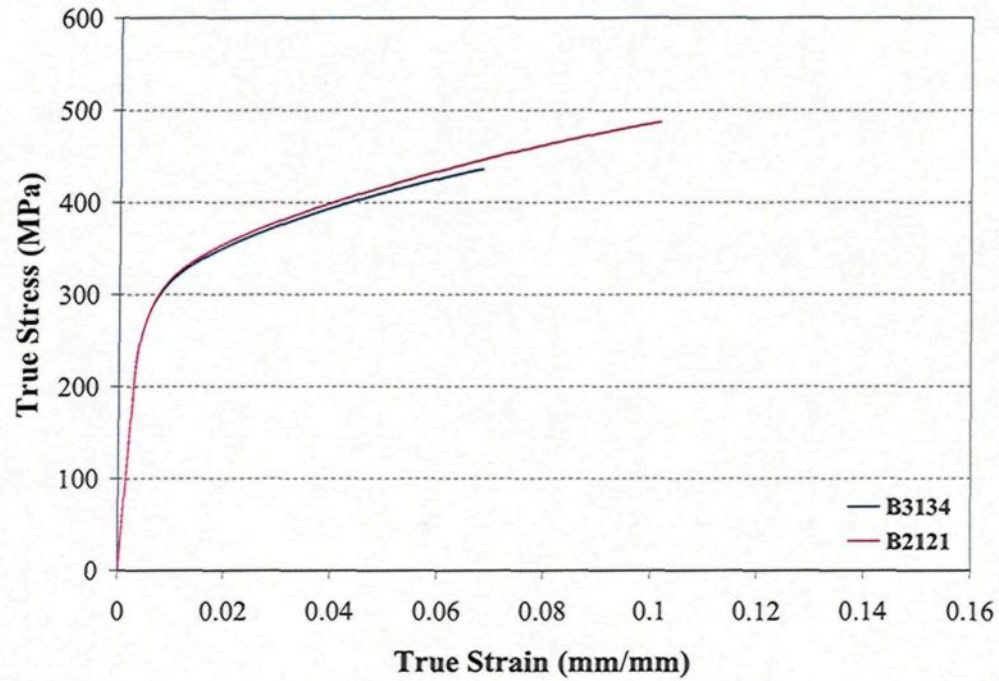
T4 (solution heat treatment time - 2h)

Alloy Code	YS , MPa (SD)	UTS, MPa (SD)	Elongation at rupture, % (SD)	Modulus, GPa (SD)
B3134	279.30 (±5.20)	403.70 (±8.70)	7.10 (±0.01)	70.84 (±1.01)
B2121	275.90 (±7.30)	405.30 (±26.4)	7.70 (±0.02)	71.32 (±0.48)

3 hours SHT, naturally aged (T4)
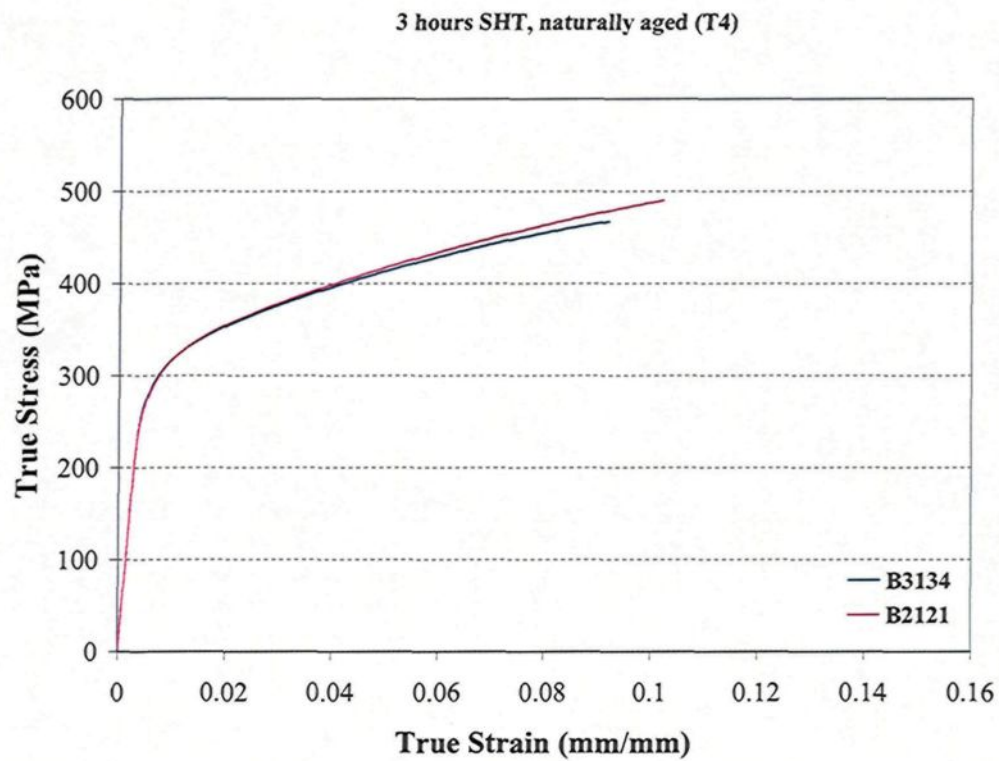
T4 (solution heat treatment time - 3h)

Alloy Code	YS , MPa (SD)	UTS, MPa (SD)	Elongation at rupture, % (SD)	Modulus, GPa (SD)
B3134	278.60 (±6.50)	422.40 (±7.50)	9.19 (±1.16)	71.98 (±1.09)
B2121	280.80 (±2.80)	435.90 (±9.00)	11.08 (±1.63)	70.90 (±1.24)

4 hours SHT, naturally aged (T4)
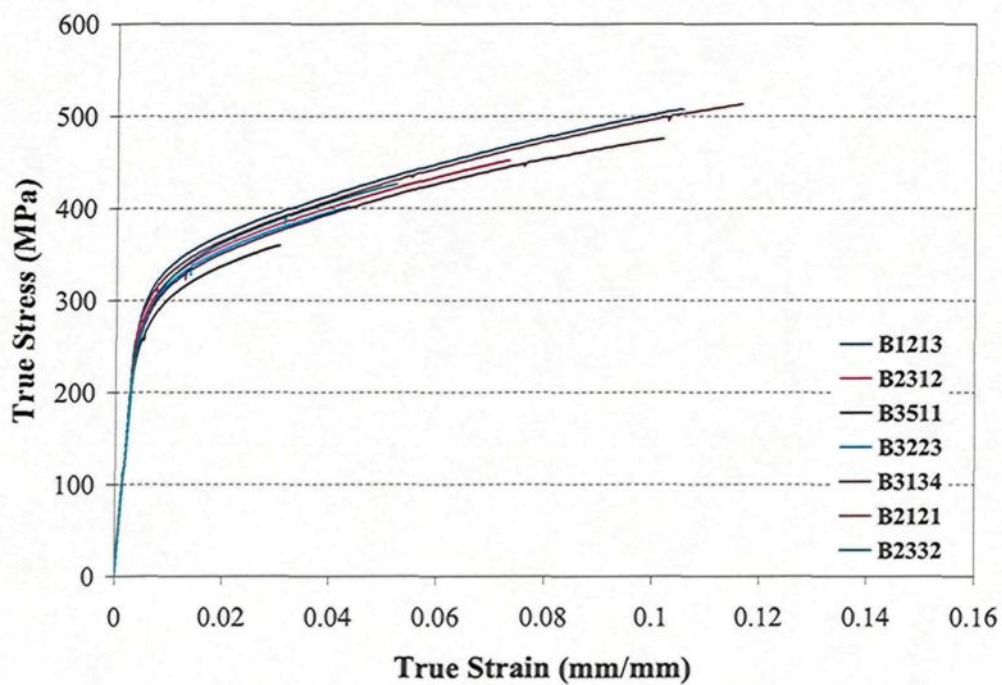
T4 (solution heat treatment time - 4h)

Alloy Code	YS , MPa (SD)	UTS, MPa (SD)	Elongation at rupture, % (SD)	Modulus, GPa (SD)
B1213	302.70 (±3.80)	450.60 (±8.50)	10.74 (±0.57)	72.87 (±2.62)
B2312	290.90 (±3.10)	419.70 (±11.7)	7.61 (±0.78)	71.32 (±1.55)
B3511	273.80 (±4.20)	356.80 (±17.0)	3.46 (±1.24)	72.14 (±0.90)
B3223	288.70 (±4.40)	384.80 (±6.90)	4.17 (±0.80)	72.59 (±1.65)
B3134	287.80 (±4.50)	430.70 (±10.8)	10.42 (±2.03)	71.23 (±0.41)
B2121	297.80 (±5.10)	453.60 (±9.90)	11.78 (±2.20)	73.20 (±1.69)
B2332	286.40 (±1.00)	407.30 (±3.70)	5.87 (±0.58)	72.12 (±2.08)

4 hours SHT, artificially aged (T7)

T7 (solution heat treatment time - 4h)

Alloy Code	YS , MPa (SD)	UTS, MPa (SD)	Elongation at rupture, % (SD)	Modulus, GPa (SD)
B1213	450.60 (±7.10)	468.50 (±10.3)	1.48 (±0.40)	73.89 (±0.75)
B2312	429.75 (±6.63)	447.27 (±10.2)	1.41 (±0.26)	78.18 (±3.75)
B3511	400.60 (±4.30)	404.10 (±1.70)	0.75 (±0.13)	74.69 (±0.73)
B3223	312.10 (±125)	440.60 (±17.5)	0.82 (±0.27)	73.17 (±0.57)
B3134	483.20 (±7.50)	492.4 (±14.4)	1.19 (±0.25)	72.61 (±0.64)
B2121	385.90 (±84.6)	454.80 (±21.2)	1.36 (±0.87)	70.54 (±0.16)
B2332	467.40 (±7.80)	470.40 (±10.4)	0.93 (±0.07)	71.13 (±1.87)

5 hours SHT, naturally aged (T4)

T4 (solution heat treatment time - 5h)

Alloy Code	YS , MPa (SD)	UTS, MPa (SD)	Elongation at rupture, % (SD)	Modulus, GPa (SD)
B3134	285.80 (±6.20)	428.60 (±8.40)	9.96 (±1.44)	72.53 (±1.39)
B2121	290.70 (±2.00)	446.00 (±7.20)	11.68 (±0.30)	71.49 (±2.56)

6 hours SHT, naturally aged (T4)

T4 (solution heat treatment time - 6h)

Alloy Code	YS , MPa (SD)	UTS, MPa (SD)	Elongation at rupture, % (SD)	Modulus, GPa (SD)
B3134	285.6(±2.90)	427.40 (±7.80)	9.82 (±2.37)	72.41 (±1.37)
B2121	293.6 (±4.23)	439.2 (±6.05)	9.83 (±0.32)	71.57 (±1.01)

8 hours SHT, naturally aged (T4)

T4 (solution heat treatment time - 8h)

Alloy Code	YS , MPa (SD)	UTS, MPa (SD)	Elongation at rupture, % (SD)	Modulus, GPa (SD)
B206	268.90 (±4.10)	434.10 (±9.70)	15.38 (±0.76)	70.53 (±1.29)
B1213	298.80 (±4.20)	462.00 (±13.3)	13.90 (±2.79)	70.65 (±9.32)
B2312	291.80 (±2.20)	416.00 (±8.20)	07.24 (±0.85)	69.74 (±1.64)
B3511	272.90 (±2.70)	377.40 (±4.80)	05.20 (±0.29)	70.98 (±1.57)
B3223	283.90 (±3.40)	390.00 (±23.4)	04.66 (±1.59)	69.95 (±0.97)
B3134	280.9 (±2.90)	426.00 (±3.50)	9.82 (±0.92)	69.20 (±1.27)
B2121	289.50 (±3.90)	434.70 (±26.6)	10.41 (±3.01)	69.81 (±2.79)
B2332	289.90 (±2.80)	395.90 (±28.8)	5.56 (±2.81)	70.82 (±1.09)

8 hours SHT, artificially aged (T7)
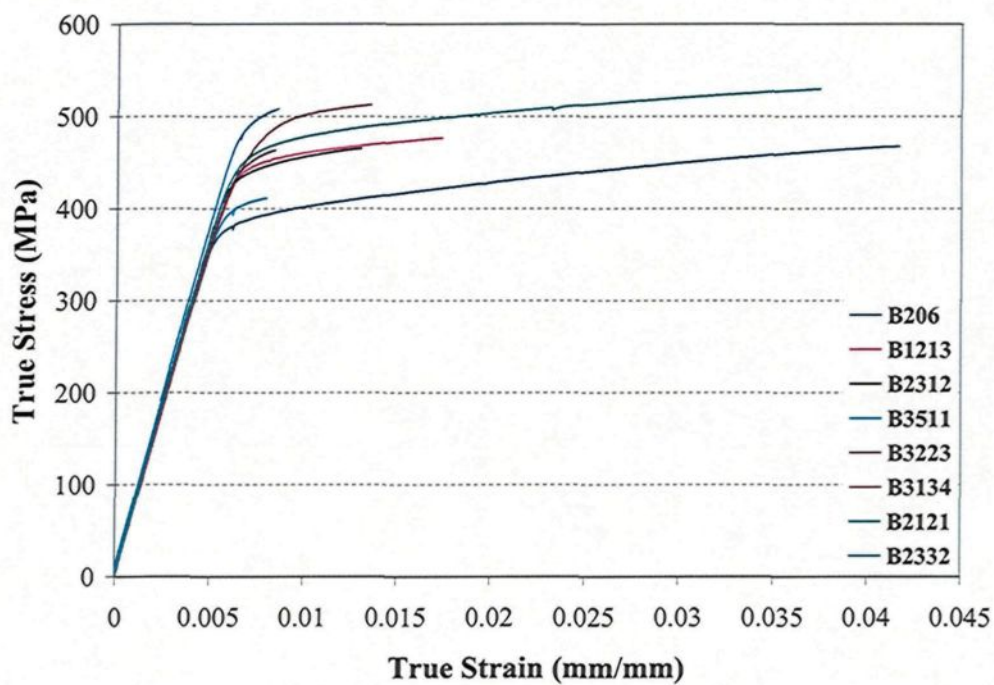
T7 (solution heat treatment time - 8h)

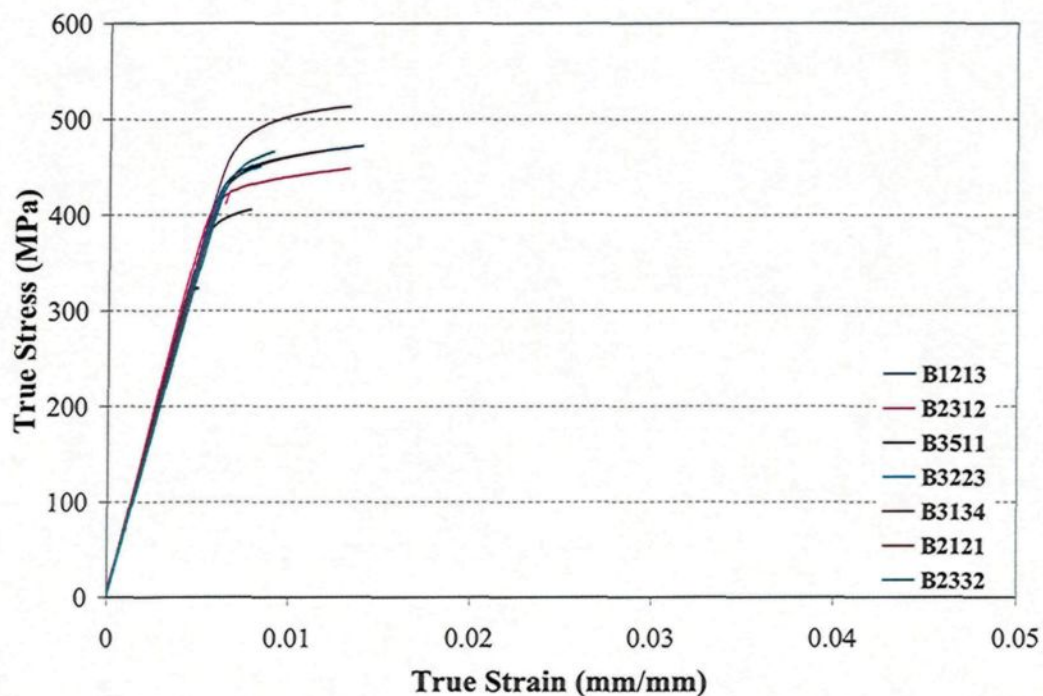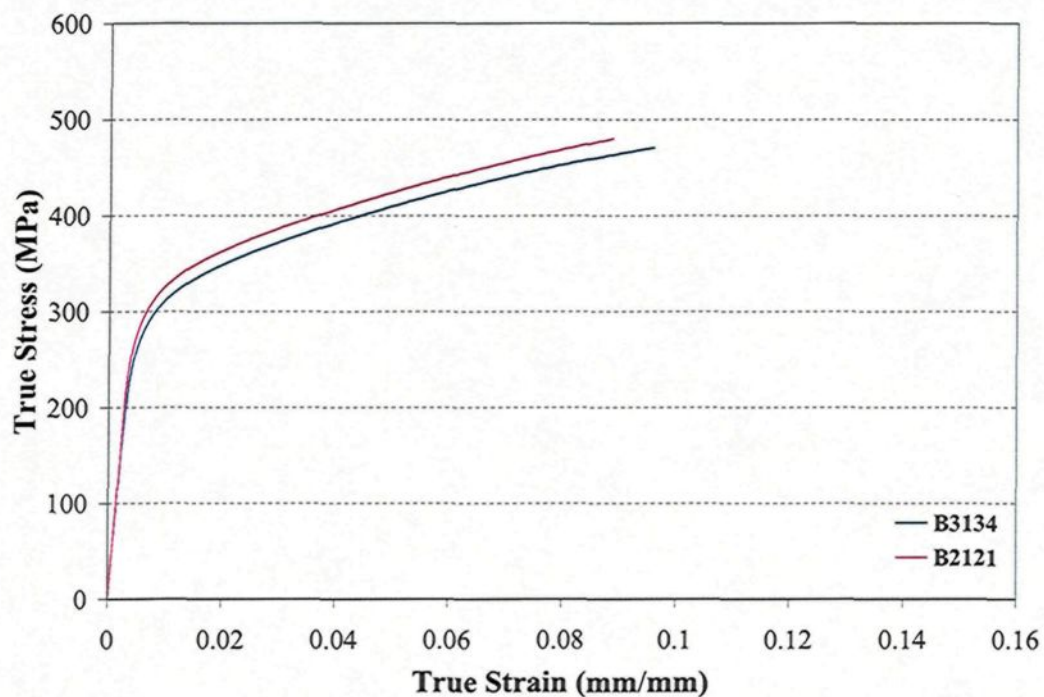| Alloy Code	YS , MPa (SD)	UTS, MPa (SD)	Elongation at rupture, % (SD)	Modulus, GPa (SD)
B206	389.80 (±3.70)	452.90 (±3.60)	4.63 (±0.26)	73.08 (±1.61)
B1213	453.50 (±4.90)	473.30 (±11.9)	1.59 (±0.42)	75.29 (±1.18)
B2312	441.80 (±7.30)	455.90 (±3.30)	1.19 (±0.27)	76.77 (±3.07)
B3511	387.50 (±29.7)	403.20 (±4.00)	0.74 (±0.05)	73.06 (±0.67)
B3223	N.D	446.50 (±12.1)	0.72 (±0.09)	75.27 (±1.93)
B3134	488.10 (±4.10)	506.30 (±5.40)	1.28 (±0.23)	79.61 (±5.51)
B2121	462.90 (±0.80)	495.10 (±21.4)	2.56 (±1.79)	76.26 (±4.24)
B2332	502.30 (±0.00)	503.60 (±0.00)	0.80 (±0.00)	79.06 (±0.00)
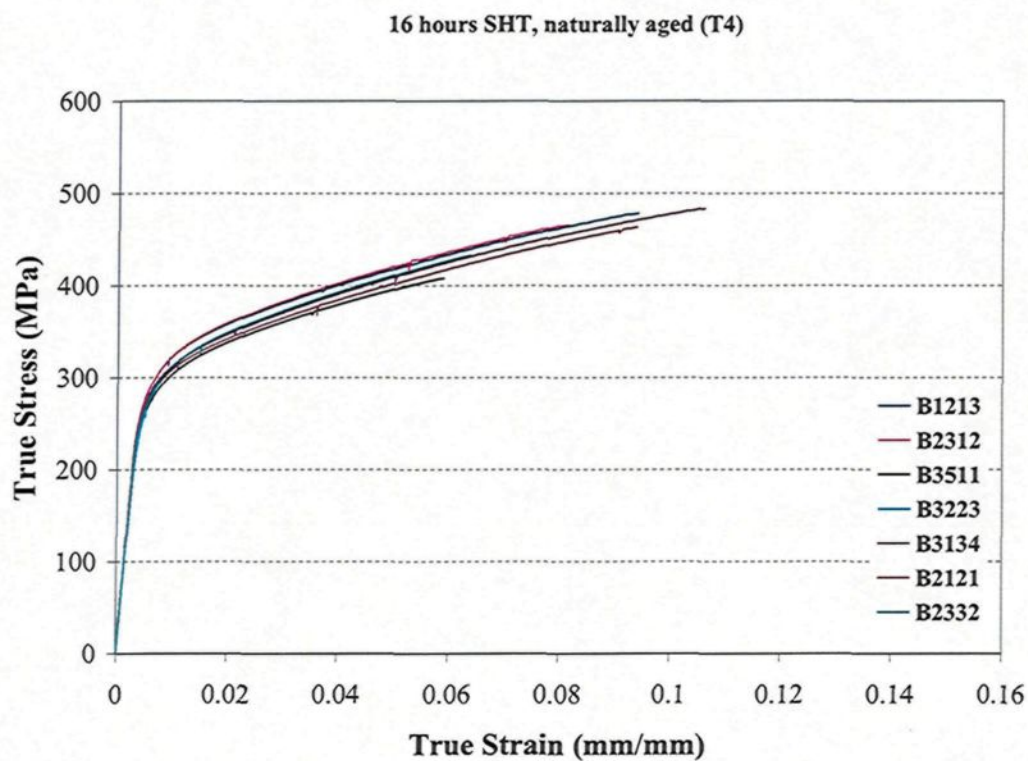
16 hours SHT, naturally aged (T4)

T4 (solution heat treatment time - 16h)

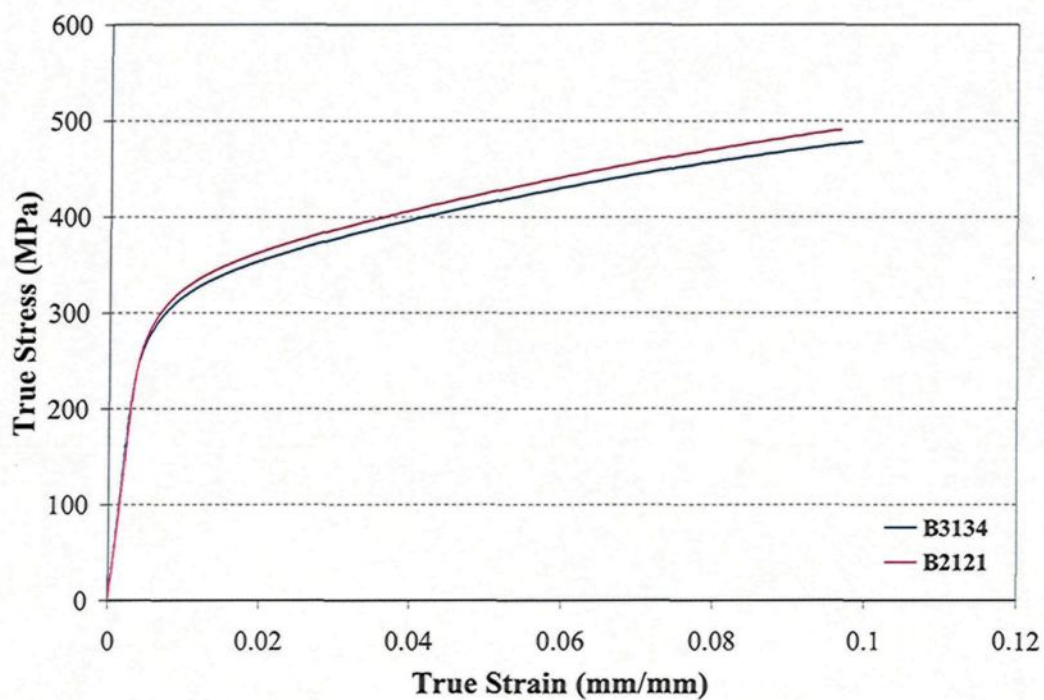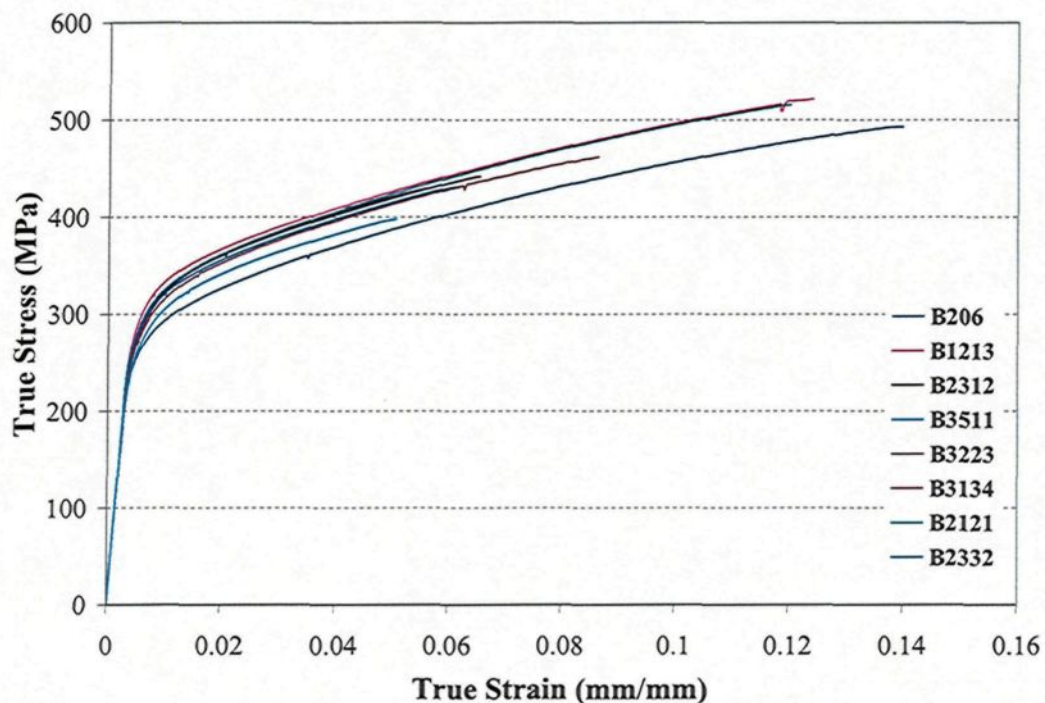| Alloy Code	YS , MPa (SD)	UTS, MPa (SD)	Elongation at rupture, % (SD)	Modulus, GPa (SD)
B1213	291.30 (±4.00)	440.80 (±18.6)	11.58 (±3.00)	71.04 (±1.52)
B2312	284.00 (±4.50)	418.80 (±9.80)	08.15 (±1.00)	71.24 (±1.48)
B3511	267.70 (±3.80)	372.80 (±12.0)	05.14 (±1.16)	72.10 (±1.04)
B3223	278.10 (±2.50)	377.60 (±8.20)	04.61 (±0.86)	70.93 (±0.98)
B3134	280.10 (±3.19)	424.10 (±9.21)	9.67 (±1.07)	69.94 (±0.98)
B2121	282.20 (±6.50)	428.30 (±9.20)	09.60 (±0.38)	73.86 (±1.69)
B2332	277.00 (±1.80)	406.00 (±7.80)	06.86 (±0.97)	72.37 (±0.60)

16 hours SHT, artificially aged (T7)
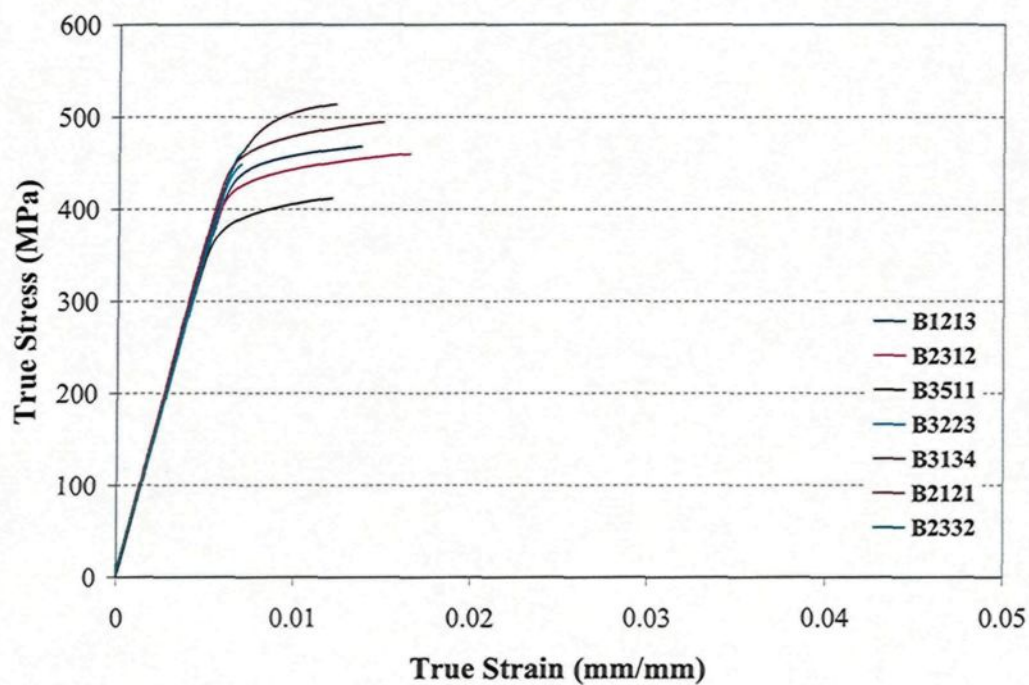
T7 (solution heat treatment time - 16h)

Alloy Code	YS , MPa (SD)	UTS, MPa (SD)	Elongation at rupture, % (SD)	Modulus, GPa (SD)
B1213	449.50 (±6.10)	474.60 (±17.7)	1.97 (±0.79)	72.85 (±0.73)
B2312	433.70 (±4.30)	459.50 (±9.30)	1.76 (±0.34)	73.09 (±0.46)
B3511	389.00 (±2.30)	405.20 (±4.20)	1.23 (±0.16)	72.72 (±0.72)
B3223	331.80 (±19.4)	446.70 (±1.50)	0.72 (±0.03)	72.97 (±0.29)
B3134	489.10 (±4.60)	503.90 (±5.10)	1.26 (±0.14)	73.62 (±1.43)
B2121	456.30 (±9.50)	479.70 (±6.60)	1.63 (±0.26)	72.49 (±3.00)
B2332	N.D	467.20 (±12.4)	0.74 (±0.07)	72.92 (±7.69)

REFERENCES

References

1- Flemings, M.C., "Solidification Processing", McGraw-Hill, New York, 1974.

2- Campbell, J., "Castings", Butterworth-Heinemann Ltd., London, UK, 1991.

3- Sigworth, G.K., "Hot Tearing of Metals", AFS Transactions, 1996, Vol. 106, pp.1053-1069.

4- Suyitno., Eskin, D.G., Savran, V.I., Katgerman, L., "Effects of Alloy Composition and Casting Speed on Structure Formation and Hot Tearing during Direct-Chill Casting of Al-Cu Alloys", Metall. Mater. Trans. A, Nov.2004, Vol. 35A, pp 3551-3561.

5- Wang, L., Makhlouf, M., Apelian, D.,"Effect of A380 Alloy Chemistry on Its Microstructure and Mechanical Properties", AFS Transactions, 1995, Vol. 103, pp 675-681.

6- Li, K-D., Chang, E., "Explanation of the Porosity Distribution in A206 Aluminum Alloy Castings", AFS Transactions, 2003, Vol. 111, pp 267-273.

7- Sigworth, G.K., Frank, D., "Recent Development in the High Strength Aluminum-Copper Casting Alloy A206", AFS Transactions, 2003, Vol. 111, pp 341-354.

8- Kaufman, J.G., Rooy, Elwin.L., AFS., "Aluminum Alloy Castings", ASM International, Ohio, 2004.

9- Kammer, C., "Casting" in Aluminium Handbook, Vol. 2, Aluminium-Verlag, Düsseldorf, 1999.

10- Totten,G.E., Mackenzie,D.S., "Physical Metallurgy and Processes", Handbook of Aluminum,Vol.1, Marcel Dekker Inc, New York, 2003.

11- Arnberg, L., Backerud, L., Dahle, A, "Castability of Aluminum Foundry Alloys", American Foundrymen's Society.Inc, Des Plaines, IL, 1999.

12- Jorstad, J.L., "Understanding Sludge", Die Casting Engineer, (Nov/Dec) 1986, pp 30-36.

13- Sigworth, G.K., Caceres, C.H., "Quality issues in Aluminum Net-Shape Castings", AFS Transactions, Des Plaines, IL, 2004, Vol. 112, pp 373-386.

14- Kearney, A.L., Raffin, J., "Mechanical Properties of Aluminum Casting Alloys X206.0-T4 and XA206.0-T7 vs Comparable Alloys at Various Cooling Rates", AFS Transactions, 1977, Vol. 85, pp 559-570.

15- MacAllister., G.K., "Effects of Cooling Rates on the Mechanical Properties of A206.0-T4 and A206.0-T71 Aluminum Alloy Castings", AFS Transactions, 1987, Vol. 95, pp 775-786.

16- Wannasin, J., Schwam, D., Yurko, J.A., Rohloff, C., Woycik, G., "Hot Tearing Susceptibility and Fluidity of Semi-Solid Gravity Cast Al-Cu Alloy", Solid State Phenomena, Swizerland, 2006, Vols. 116-117, pp 76-79.

17- Oswalt, K.J., "New Generation High-Strength Aluminum Casting Alloys", AFS Transactions, 1967, Vol. 75, p.62.

18- Major, J.F., Sigworth, G.K., "Chemistry/Property Relationships in AA 206 Alloys", AFS Transactions, 2006, Vol. 114, pp 117-128.

19- Tseng, C.J., Lee, S.L., Wu, T.F., Lin, J.C., "Effects of Fe Content on Microstructure and Mechanical Properties of A206 Alloys", Materials Transactions, JIM, 2000, Vol. 41, No.10, pp 708-713.

20- Sigworth, G.K., Major, J.F., "Factors Influencing the Mechanical Properties of B206 Alloys Castings", Light Metals, TMS, 2006.

21- Oswalt, K.J., "The Development and Application of High Strength Aluminum Casting Material Specifications", Current Aluminum Research and Applications: CARA 87. American Foundrymen's Society.Inc, Des Plaines, IL, 1988.

22- Keshavaram, B., Seiler, D., Dewitt, D., "Aluminum Alloys for Automotive Knuckle Castings", SAE Technical Paper, No 2000-01-1291, in Casting Solutions for the Automotive Industry, (SP-1504), 2000.

23- Davis, J.R., "Aluminum and Aluminum Alloys", ASM, Materials Park, Ohio, 1993.

24- Kurz, W and Fisher, D.J., " Fundamentals of Solidification", Trans Tech Publications, Aedermannsdorf, Switzerland, 1999

25- Mullins, W.W and Sekerka, R.F., "Stability of a Planar Interface during Solidification of a Dilute Binary Alloy", J. Applied Physics, 1964, Vol. 35, pp 444-451.

26- Sekerka, R.F., "Morphological Stability", J. Crystal Growth, 1968, Vol. 3, pp 71-81.

27- Shibata, K., Sato, T., Ohira, G., "Morphological Stabilities of Planar Solid-Liquid Interfaces during Unidirectional Solidification of Dilute Al-Ti and Al-Cr Alloys", J. Crystal Growth, 1978, Vol. 44, pp 419-434.

28- Bardes, B.P., Flemings, M.C., "Dendrite Arm Spacing and Solidification Time in a Cast Aluminum-Copper Alloy", AFS Transactions, 1966, Vol. 74, pp 406-412.

29- Kattamis, T.Z., Coughlin, J.C., Flemings, M.C., "Influence of Coarsening on Dendrite Arm Spacing of Aluminum-Copper Alloys", TMS AIME, 1967, Vol. 239, pp 1504-1511.

30- Young, K.P., Kirkwood, D.H., "The Dendrite Arm Spacings of Aluminum-Copper Alloys Solidified under Steady-State Conditions", Metall. Mater. Trans. A, 1975, Vol. 6A, pp 197-205.

31- Hunt, J.D., "Cellular and Primary Dendrites Arm Spacings", Solidification and Casting of Metals, The Metals Society, London, 1979, pp 1-9.

32- Trivedy, R., "Theory of Dendritic Growth during the Directional Solidification of Binary Alloys", J. Crystal Growth, 1980, Vol. 49, pp 219-232.

33- Kurz, W., Fisher, D.J., "Dendrite Growth at the Limit of Stability: Tip Radius and Spacing", Acta Metallurgica, 1981, Vol. 29, pp 11-20.

34- Jackson, K.A., Hunt, J.D., "Lamellar and Rod Eutectic Growth", TMS AIME, 1966, Vol. 236, pp 1129-1142.

35- Mollard, F.R., Flemings, M.C., "Growth of Composites from the Melt-Part I&II", TMS AIME, 1967, Vol. 239, pp 1526-1546.

36- Grugel, R., Kurz, W., "Growth of Interdendritic Eutectic in Directionally Solidified Al-Si Alloys", Metall. Mater. Trans. A, 1987, Vol. 18A, pp 1137-1142.

37- Rosenhain, W., "Introduction into Physical Metallurgy", D. Van Nostrand Co, 1915

38- Jeffries, Z., Archer, R.S., "The Science of Metals", McGraw-Hill Book Co, 1924.

39- Alexander, B.H., Rhines, F.N., "Dendritic Crystallization of Alloys", AIME Transactions, 1950, Vol. 188, p.1267.

40- Flemings, M.C., Uram, S.Z., Taylor, H.F., "Solidification of Aluminum Castings", AFS Transactions, 1960, Vol. 68, pp 670-684.

41- Flemings, M.C., Peckner, D., "Premium Quality Castings", Materials in Design Engineering, Aug.1963, pp 99-106.

42- Flemings, M.C., "Controlled Solidification", Twelfth Sagamore Army Materials Research Conference, Aug.24-27, 1965.

43- Dean, W.A., Spear, R.E., Discussion of "Controlled Solidification" by Flemings, M.C., Twelfth Sagamore Army Materials Research Conference, Aug.24-27, 1965.

44- Flemings, M.C., Strachan, R.W., Poirier, E.J., Taylor, H.F., "Performance of Chills on High Strength Magnesium Alloy Sand Castings of Various Thicknesses", AFS Transactions, 1958, Vol. 66, pp 336-343.

45- Polich, R.F., Flemings, M.C., "Mechanical Properties of Unidirectional Steel Castings", AFS Transactions, 1965, Vol. 73, pp 28-33.

46- Quigley, F.C., Ahearn, P.J., "Homogenization of Steel Castings at 2500°F", AFS Transactions, 1964, Vol. 72, pp 813-817.

47- Passmore, E.M., Flemings, M.C., Taylor, H.F., "Fundamental Studies on Effects of Solution Treatment, Iron Content and Chilling of Sand Cast Aluminum-Copper Alloy", AFS Transactions, 1958, Vol. 66, pp 96-104.

48- Kattamis, T.Z., Flemings, M.C., "Dendrite Morphology, Microsegregation, and Homogenization of Low Alloy Steel", AIME Transactions, 1965, Vol. 233, pp. 992-999.

49- Michael, A.B., Bever, M.B., "Solidification of Aluminum-Rich Aluminum-Copper Alloys", AIME Transactions, 1954, Vol.200, p.47.

50- Reed, M.D., "The Effect of the Time of Solidification on the Dendrite Arm Spacing", S.B Thesis, MIT, Dept. of Metallurgy, 1960.

51- Brown, P.E., Adams, C.M., "Fusion-Zone Structures and Properties in Aluminum Alloys", Welding Journal Research Supplement, Dec.1960.

52- Howarth, J.A., Mondolfo, L.F., "Dendritic Growth", Acta Metallurgica, 1962, No.10, p.1037.

53- Rohatgi, P.K., Adams, C.M., "Dendritic Solidification of Aluminum-Copper Alloys", TMS AIME, 1967, Vol. 239, pp 1737-1746.

54- Spear, R.E., Gardner, G.R., "Dendrite Cell Size", AFS Transactions, 1963, Vol.71, pp 209-215.

55- Hatch, J.E., "Aluminum: Properties and Physical Metallurgy", ASM, Metals Park, Ohio, 1984.

56- Mondolfo, L.F., "Aluminum Alloys: Structure and Properties", London: Butterworths, 1976.

57- Belov, N.A., Eskin, D.G., Aksenov, A.A., "Multicomponent Phase Diagrams: Applications for Commercial Aluminum Alloys", Elsevier, U.K, 2005.

58- Legendre, B., Harmelin, M., "Ternary Alloys", Eds. Petzow.G & Effenberg.G, Vol. 4, VCH, Weinheim, 1991, pp 475-489.

59- Belov, N.A., Eskin, D.G., Aksenov, A.A., "Iron in Aluminum Alloys: Impurity and Alloying Element", Taylor & Francis, London, 2002.

60- Drits, M.E., Kadaner, E.S., Padezhnova, E.M., Rokhlin, L.L., Sviderskaya, Z.A and Turkina, N.I., "Phase Diagrams of Aluminum and Magnesium Based Systems", Ed. AbriKosov, N.Kh., Nanka, Moscou, 1977.

61- Narayan, L.A., Samuel, F.H., Gruzlezki, J.E., Metall. Mater. Trans. A, 1995, 26A, p.2161.

62- Backerud, L., Krol, E, Tamminen, J., "Solidification Characteristics of Aluminum Alloys", Vol.1: Wrought Alloys, Skanaluminium, Olso, 1987.

63- Cao, X., Campbell, J., "The Solidification Characteristics of Fe-Rich Intermetallics in Al-11.5Si-0.4Mg Cast Alloys", Metall. Mater. Trans. A, 2004, Vol. 35A, pp 1425-1435.

64- Mondolfo, L.F., "Manganese in Aluminum Alloys", The Manganese Centre, Neuilly sur Seine, France, 1978.

65- Moustafa, M.A., Samuel, F.H., Doty, H.W., "Effect of Solution Heat treatment and Additives on the Microstructure of Al-Si (413.1) Automotive Alloys", Journal of Materials Science, 2003, Vol. 38, pp 4507- 4522.

66- Backerud, L., Chai, G., Tamminen, J., "Solidification Characteristics of Aluminum Alloys", Vol.2: Foundry Alloys, AFS/Skanaluminium, 1990.

67- Kuo, Y.S., Chang, E., Lin, Y.L., "The Feeding Effect of Risers on the Mechanical Properties of A201 Aluminum Alloy Plate Casting", AFS Transactions, 1989, Vol. 97, pp.777-782.

68- Lee, Y.W., Chang, E., "Correlation of Feeding and Mechanical Properties of A206 Aluminum alloy Plate Casting", AFS Transactions, 1990, Vol. 98, pp.935-941.

69- Kao, S.T., Chang, E., Horng, D., "Effect of Taper Placement on Feeding behaviour in A206 Alloy Plate Castings", AFS Transactions, 1995, Vol. 103, pp.581-586.

70- Rading, G.O., Li, J., Berry, J.T., "Fatigue Crack Growth in Cast Al-Cu Alloy A206 with Different levels of Porosity", AFS Transactions, 1994, Vol. 102, pp.57-61.

71- Fang, Q.T., Granger, D.A., "Porosity Formation in Modified and Unmodified A356 Alloy Castings", AFS Transactions, 1989, Vol. 97, pp 989-1000.

72- Piwonka, T.S., Flemings, M.C., "Pore Formation in Solidification", AIME Transactions. 1966, Vol. 236, pp. 1157-1165.

73- Poirier, D.R., Yeum, K., Maples, A.L., "A Thermodynamic Prediction for Microporosity Formation in Aluminum-Rich Al-Cu Alloys", Metall. Mater. Trans. A, 1987, Vol. 18A, pp.1979-1987.

74- Viswanathan, S., "The Relation of Solidification Parameters to Microporosity in Al-4.5%Cu Alloy Castings", PhD Dissertation, University of Pittsburgh, Pittsburgh, PA, 1990.

75- Chang, E., Kuo, Y.S., "Semi-Empirical Analysis of Thermal Parameters for Porosity Formation in 201 Al Alloy Casting", AFS Transactions, 1994, Vol. 03, pp.167-172.

76- Kao, S.T., Chang, E., Lee, Y.W., "Role of Interdendritic Fluid Flow on the Porosity Formation in A206 Alloy Plate Castings", Mat. Trans., JIM, 1994, Vol. 35, No.9, pp.632-639.

77- Samuel, A.M., Samuel, F.H., "Porosity Factor in Quality Aluminum Castings", AFS Transactions, 1992, Vol. 100, pp.657-666.

78- Charbonnier, J., "Gaz dans les Alliages d'Aluminium de Fonderie", Tech. de l'ing., Traite de Metallurgie, 1991.

79- Talbot, D.E.J., "Effects of Hydrogen in Aluminum, Magnesium, Copper and their Alloys", International Metallurgical Reviews, 1975, Vol. 20, pp.166-184.

80- Edwards, G.A., Sigworth, G.K., Cáceres, C.H., StJohn, D.H., Barresi, J ., "Microporosity Formation in Al-Si-Cu-Mg Casting Alloys", AFS Transactions, 1997, Vol. 105, pp.809-818.

81- Roy, N., Samuel, A.M., Samuel, F.H., "Porosity Formation in Al-9wt Pct Si- 3wt Pct Cu Alloy Systems: Metallographic Observations", Metall. Mater. Trans. A, 1996, Vol. 27A, pp.415-429.

82- Iwahori, H., Yonekura, K., Sugiyama, Y., Yamamoto, Y., Nakamura, M., "Behaviour of Shrinkage Porosity defects and Limiting solid Fraction of Feeding on Al-Si Alloys", AFS Transactions, 1985, Vol. 93, pp.443-452.

83- Chen, X.G., Engler, S., "Hydrogen and Porosity in Al-Si and Al-Mg Alloys, Part 1. Al-Si Alloys", Metall, 1991, Vol. 45, No.10, pp.995-1000.

84- Chen, X.G., Engler, S., "Hydrogen and Porosity in Al-Si and Al-Mg Alloys, Part 2. Al-Mg Alloys and Discussion on Pore Formation", Metall, 1991, Vol. 45, No.12, pp.1225-1231.

85- Norton, A., "Hot Shortness Testing Machine for Aluminum Alloys", ASME Transactions, 1914, Vol. 8, p.124.

86- Archbutt, Grogan and Jenkin., "Properties and Production of Aluminum Alloy Die Castings", Journal of Institute of Metals, 1928, Vol. 40, p219.

87- Vero, J., "The Hot Shortness of Aluminum Alloys", The Metal Industry, 1936, Vol. 48, pp.431-442.

88- Singer, A.R.E., Cottrell, S.A., "Properties of the AL-Si Alloys at Temperatures in the Region of the Solidus", Journal of Institute of Metals, 1946, Vol. 73, pp.33-54.

89- Forest, B., Bercovici, S., "Experimental Study of Mechanical Properties of Aluminum Alloys During Controlled Solidification: Application to Hot Tearing", Solidification Technology in the Foundry and Cast House, Proceed.1980 Conf., Univ. of Warwick, Coventry, U.K, Paper 93, 12 pages.

90- Wisniewski, P., "Tensile Properties of Binary Al-Cu Alloys in Solid plus Liquid State", PhD Thesis, Univ. of Pittsburgh, Pittsburgh, PA, 1990.

91- Borland, J.C., "Generalized Theory of Super-Solidus Cracking in Welds and Casting", British Welding Journal, 1960, Vol. 7, No.8, pp.508-512.

92- Pellini, W.S., "Strain Theory of Hot Tearing", Foundry, Nov.1952, Vol. 80, pp.124-199.

93- Pumphrey, W.I., Jennings, P.H., "A Consideration of the Nature of Brittleness at Temperature above the Solidus in Castings and Welds in Aluminum Alloys", Journal of Institute of Metals, 1948, Vol. 75, p.235.

94- Lees, D.C.G., "The Hot Tearing Tendencies of Aluminum Casting Alloys", Journal of Institute of Metals, 1946, Vol. 72, pp.343-364.

95- Smith, R.W., Sadayappan, M., Sahoo.M., "Influence of Alloying Elements and Melt Treatment on the Hot Tearing Resistance of Aluminum Alloy A201", Light Metals, COM 2001, Met. Soc., pp. 455-466.

96- Warrington, D., McCartney, D.G., "Development of a New Hot Cracking Test for aluminum Alloys", Cast Metals, 1989, Vol.2, pp.134-143.

97- Davies, L., "The Influence of Grain Size on Hot Tearing", The British Foundryman, April 1970, pp.93-101.

98- Lees, D.C.G., "Note on the Effect of Dissolved Gas on Hot Tearing of Aluminum Casting Alloys", Journal of Institute of Metals, 1947, Vol. 73, p.537.

99- Spittle, J.A and Cushway, A.A., "Influence of Superheat and Grain Structure on Hot Tearing Susceptibilities of Al-Cu Alloy Castings", Metals Technology, 1983, Vol. 10, p.6-13.

100- Williams, J.A., Singer, A.R.E., "Deformation, Strength, and Fracture Stress above the Solidus Temperature", Journal of Institute of Metals, 1968, Vol. 96, pp.5-12.

101- Metz, S.A., Flemings, M.C., "A Fundamental Study of Hot Tearing", AFS Transactions 1970, Vol. 78, pp.453-460.

102- Kubota, M., Kitaoka, S., "Solidification Behaviour and Hot Tearing Tendency of Aluminum Casting Alloys", AFS Transactions, 1973, Vol. 81, pp.424-427.

103- Oya, S., Fujii, T., Ohtaki, M., Baba, S ., "Solidification Structure and Hot Tearing of Al-4.5%Cu and Al-4.5%Cu-5%Si Alloys Containing Various Additives", J. Japan Inst. Light Metals, 1984, Vol. 34, pp.511-516.

104- Rosenberg, R.A., Flemings, M.C., Taylor, H.F., "Nonferrous Binary Alloys Hot Tearing", AFS Transactions, 1960, Vol. 68, pp.518-528.

105- Chai, G., Roland, T., Arnberg, L., Backerud, L., "Studies of Dendrite Coherency in Solidifying Aluminum Alloy melts by Rheological Measurements", 2nd Int. Conf. of Semisolid Material Processing, 1992, pp. 193-201.

106- Chai, G., "Dendrite Coherency during Equiaxed Solidification in Aluminum Alloys", Doctoral Dissertation, Chemical Communications, No.1, Stockholm Univ., Stockholm , Sweden, 1994.

107- Davis, J.R., "Aluminum and Aluminum Alloys", ASM, Materials Park, Ohio, 1993.

108- Kaufman, J.G., "Introduction to Aluminum Alloys and Tempers", ASM International, Materials Park, OH, 2000.

109- Talamantes-Silva, M.A., Rodríguez, A., Talamantes-Silva, J., Valtierra, S., Colás, R., "Effect of Solidification Rate and Heat Treating on Microstructure and Tensile Behaviour of an Aluminum-Copper Alloy", Metall. Mater. Trans. B, Dec.2008, Vol. 39B, pp 911-919.

110- Van Horn, K.R., "Aluminum: Properties, Physical Metallurgy and Phase Diagrams", Vol. 1, ASM, Metals Park, Ohio, 1967.

111- Fuchs, E.G., Roosz A., "TTD-Diagrams for the Homogenization of As-Cast Structures", Metallkunde, 1972, Vol. 63, pp.211-214.

112- Jorstad, J.L., Rasmussen, W.M., "Aluminum Casting Technology", 2nd Ed., AFS Inc., Des Plaines, IL, 1997.

113- Apelian, D., Shivkumar, S., Sigworth, G., "Fundamental Aspects of Heat

Treatment of Cast Al-Si-Mg Alloys", AFS Transactions, 1989, Vol. 97, pp.727-742.

114- Zhang, D.L., Zheng, L., "The Quench Sensitivity of Cast Al-7 Wt Pct Si- 0.4Wt Pct Mg Alloy", Metall. Mater. Trans. A, 1996, Vol. 27A, pp.3983-3991.

115- Croucher, T., Butler, B., "Polymer Quenching of Aluminum Castings", 26th National SAMPE Symposium, 1981, pp.527-535.

116- Totten, G.E., Mackenzie, D.S., "Aluminum Quenching Technology: A Review", Materials Science Forum, 2000, Vols. 331-337, pp.589-594.

117- Sverdlin, A.V., Totten, G.E., Vebster, G.M., "Polyalkyleneglycol Base Quenching Media for Heat Treatment of Aluminum Alloys", Metallovedenie Termicheskaya Obrabotka Metallov, 1996, Vol. 6, pp.17-19.

118- Senatorova, O.G., "Low Distorsion Quenching of Aluminum Alloys in Polymer Medium", Materials Science Forum, 2002, Vols. 396-402, pp.1659-1664.

119- Bietz, H., "None-Combustible Water-Based Quenchants in Forging Shops for Automotive Parts Latest Development", The 1st International Automotive Heat Treating Conference, Puerto Vallerta, Mexico, 1998, pp.106-109.

120- Emadi, D., "Optimal Heat Treatment of A356.2 Alloy", Light Metals, TMS, Warrendale, PA, 2003, pp.983-989.

121- Kandil, H.M., "Recent Developments in Age Hardening Behaviour of Aluminum Alloys- A Review Article", in Heat Treating: Proceedings of the 21st Conference, Indianapolis, Indiana, USA: ASM International, 2001, pp.343-351.

122- ASM Handbook., Materials Park, OH, 1995, pp.823-873.

123- Ardel, A.J., "Precipitation Hardening", Metall. Mater. Trans. A, 1985, Vol. 16A, pp.2132-65.

124- Sehitoglu, H., Foglesong, T., Maier, H.J., "Precipitate Effects on the Mechanical Behaviour of Aluminum Copper Alloys: Part I. Experiments", Metall. Mater. Trans. A, March 2005, Vol. 36A, pp.749-761.

125- Caceres, C.H., Din T., Rashid A.K.M.B., Campbell J .,"Effect of Aging on Quality Index of an Al-Cu Casting Alloy" Materials Science and Technology, June 1999, Vol.15, pp.711-716.

126- Hidayetoglu, T.K., Pica, P.N., Haworth, W.L., "Aging Dependence of Bauschinger Effect in Aluminum Alloy 2024", Materials Science and Engineering, 1985, 73, pp.65-76.

127- Lorimer, G.W., Proc. Precipitation Processes in Solids, Proc. Symp., sponsored by TMS-AIME Heat Treatment at TMS Meeting, TMS-AIME, Niagara Falls, NY, 1976, pp.87-97.

128- Martin, J.W., "Micromechanisms in Particle-Hardened Alloys", Cambridge University Press, Cambridge, U.K., 1980.

129- Guinier, A., "Structure of Age-Hardened Aluminum-Copper Alloys", Nature, 1938, Vol. 142, p.569.

130- Preston, G.D., "Structure of Age-Hardened Aluminum-Copper Alloys", Nature, 1938, Vol. 142, p.570.

131- Chiou, C., Herman, H., Fine, M.E., Trans. TMS-AIME, 1960, Vol. 218, pp.299-307.

132- Turnbull, D., Rosenbaum, H.S., Treaftis, H.N., "Kinetics of clustering in some aluminum alloys", Acta Metallurgica, 1960, Vol. 8, pp.277-95.

133- Baker, R.G., Brandon, D.G., Nutting, J., "The growth of precipitates", Philosophical Magazine, 1959, Vol.4 (48), pp.1339-45.

134- Silcock, J.M., Heal, T.J., Hardy, H.K., "Structural ageing characteristics of binary aluminium–copper alloys", Journal of the Institute of Metals, 1953, Vol. 82, pp. 239-48.

135- Byrne, J.G., Fine, M.E., Kelly, A., "Precipitate hardening in an aluminium copper alloy", Philosophical Magazine, 1961, Vol. 6 (69), pp. 1119-45.

136- Silcock, J.M., "A study of elongation and ageing in Al-4% Cu and Al-4% Cu 0.05% In crystals", Acta Metallurgica, 1959, Vol. 8, pp.589-97.

137- Wilsdorf, H., Kuhlmann-Wilsdorf, D., Proc. Defects in Crystalline Solids, The Physical Society, University of Bristol, Bristol, 1954, pp.175-86.

138- Vaughan, D., "Grain boundary precipitation in an Al-Cu alloy", Acta Metallurgica, 1968, Vol. 16, pp. 563-77.

139- Boyd, J.D., Nicholson, R.B., "The coarsening behaviour of θ'' and θ' precipitates in two Al-Cu alloys", Acta Metallurgica, 1971, Vol. 19, pp.1379-91.

140- Weatherly, G.C., "Loss of Coherency of Growing Particles by the Prismatic Punching of Dislocation Loops", Philosophical Magazine, 1968, Vol. 17, pp.791-99.

141- Weatherly, G.C., Nicholson, R.B., "Electron microscope investigation of the interfacial structure of semicoherent precipitates", Philosophical Magazine, 1968, Vol. 17, pp.801-831.

142- Vaughan, D., "The determination of the lattice parameters of the θ' structure formed in an Al-Cu alloy", Philosophical Magazine, 1968, Vol. 18, pp. 1305-08.

143- Sankaran, R., Laird, C., "Interfacial Structure of Platelike Precipitates", Philosophical Magazine, 1974, Vol. 29, pp. 179-215.

144- Stobbs, W.M., Purdy, G.R., "The elastic accommodation of semicoherent θ' in Al-4 wt.%Cu alloy", Acta Metallurgica, 1978, Vol. 26, pp. 1069-81.

145- Nemoto, M., Morishige, N., Oguchi, T., Suto, H., "The Loss of Coherency of θ' Precipitates in an Aluminum-Copper Alloys", Trans. Jpn. Inst. Met., 1971, Vol. 12, pp.429-33.

146- Brown, L.M., Woolhouse, G.R., Valdre, U., "Radiation-induced coherency loss in a copper-cobalt alloy", Philosophical Magazine, 1968, Vol. 17, pp.781-89.

147- Brown, L.M., Woolhouse, G.R., "The loss of coherency of precipitates and the gene ration of dislocation", Philosophical Magazine, 1970, Vol. 21, pp.329-45.

148- Weatherly, G.C., "The structure of ledges at plate-shaped precipitates", Acta Metallurgica, 1971, Vol. 19, pp. 181-92.

149- Sankaran, R., Laird, C., "Kinetics of Growth of Platelike Precipitates", Acta Metallurgica, 1974, Vol. 22, pp. 957-69.

150- Weatherly, G.C., "The Growth of Faceted Precipitates", Can. Metall. Q., 1969, Vol.8 (2), pp. 105-09.

151- Thomas, G., Whelan, M.J., "Observations of precipitation in thin foils of aluminium. 4% copper alloy", Philosophical Magazine, 1961, Vol. 6 (69),

pp. 1103-14.

152- Laird, C., Aaronson, H.I., "Mechanisms of Formation of θ and Dissolution of θ' Precipitates in an Al-4% Cu Alloy", Acta Metallurgica, 1966, Vol. 14, pp. 171-85.

153- Smith, T.J., Maier, H.J., Sehitoglu, H., Fleury, E., Allison, J., "Modeling high-temperature stress strain behaviour of cast aluminum alloys", Metall. Mater. Trans. A, 1999, Vol. 30A, pp.133-46.

154- Schey, J.A., "Introduction to Manufacturing Processes", McGraw Hill, USA, 2000

155- Dreyer, K.L., Hansen, M., "The Influence of Mg, Si, Mn, and Fe on the properties of the Alloy Duralumin Cu 30", Luftfahrtforschung, 1943, Vol. 20, pp.323-331.

156- Entwistle, K.M., Fell, J.H., Koo, K.I., "The Effect of Vacancy/Impurity Interaction on the Rate of Quench-Age-Hardening in Al-Cu Alloys", Journal of Institute of Metals, 1962, Vol. 91, pp.84-88.

157- Phillips, H.W.L., "Annotated Equilibrium Diagrams of Some Aluminum Alloys Systems", Institute of Metals, London, 1959, p.31.

158- Drouzy, M., Jacob, S., Richard, M., "Le Diagramme Charge de Rupture-Allongement des Alliages D'Aluminium : L'Indice de Qualité - Application aux A-S7 G", Fonderie 355, Avril 1976, pp.139-147.

159- Drouzy, M., Jacob, S., Richard, M., " L'Indice de Qualité et la Limite D'élasticité des Alliages A-S7 G", Fonderie 360, Oct. 1975, pp.345-349.

160- Standard Methods of Tension testing of Metallic Materials, ASTM Designation E8-69, "Annual Book of ASTM Standards", American Society for Testing and Materials, Philadelphia, 2004.

161- Dieter, E.G., "Mechanical Metallurgy", McGraw Hill, USA, 1986.

162- Mack, D.J., "Young's Modulus-Its Metallurgical Aspects", AIME Transactions, Vol.166, 1946, pp.68-85.

163- Schaffer, J.P., Saxena, A., Antolovich, S.D., Sanders, Jr.T.H., Warner, S.B., "The Science and Design of Eng. Materials", Richard D. Irwin, Inc., USA, 1995.

164- Drouzy, M., Jacob, S., Richard, M., " Interprétation des Résultats de L'Essai de traction a l'aide de L'Indice de Qualité et la Limite D'élasticité Probable – Application aux Alliages A-Si7 Mg de Fonderie", Journées Métallurgiques d'automne 1976, Société Française de Métallurgie.

165- Din, T., Rashid, M.B., Campbell, J., "High Strength Aerospace Casting Alloys: Quality Factor Assessment", Materials Science and Technology, 1996, 12, pp.269-273.

166- Caceres, C.H., Sokolowski, J.H.,"Effect of Aging and Mg Content on Quality Index of Two Model Al-Cu-Si-Mg Alloys", Materials Science and Engineering A, 1999, Vol. A271, pp.53-61.

167- Gauthier, J., Loucher, P.R., Samuel, F.H., "Heat Treatment of 319.2 Aluminum Automotive Alloy: II. Aging Behaviour", Cast Metals, 1995, Vol.8(2), pp. 107-114

168- Caceres, C.H., "A Rationale for the Quality Index of Al-Si-Mg Casting Alloys",

Int. J. of Cast Metals Research, 1998, Vol. 10, pp.293-299.

169- Caceres, C.H., "A Phenomenological Approach to the Quality Index", Int. J. of Cast Metals Research, 2000, Vol.12, pp.367-375.

170- Jonason, P., " Thermal Fatigue of Cylinder Head Alloys", AFS Transactions, 1992, Vol.100, pp. 601-607.

171- Russ, J.C., "Practical Stereology", Plenum Press, New York, 1986, pp.35-41.

172- Larouche, D, "Computation of Solidification Paths in Multiphase Alloys with Back-Diffusion", CALPHAD, 2007, Vol. 31, pp 490-504.

173- Sundman, B, Jansson, B, Andersson, J-O, CALPHAD, 1985, Vol. 9, pp 153-190.

174- TTAL6, TT Al-based Alloys Database, version 6.0, ThermoTech Ltd, Surrey Technology Center, Guildford, UK.

175- MOBAl1, TCS Al-Alloys Database, version 1.0, Thermo-Calc Software AB.

176- Andersson, J-O, Helander, T, Höglund, L, Shi, P, Sundman, B, CALPHAD, 2002, Vol. 26, pp 273-312.

177- Arnberg, L., Backerud, L., Chai, G., "Solidification Characteristics of Aluminum Alloys", , Vol.3: Dendrite Coherency , AFS Inc, Des Plaines, IL, 1996.

178- Clyne, T.W., Davies, G.J., "Comparison between Experimental Data and Theoretical Predictions Relating to Dependence of Solidification Cracking on Composition", Solidification and Casting of Metals, Proc. Int. Conf., University of Sheffield, July, 1977, pp 275-278, The Metals Society, London, 1978.

179- Clyne, T.W., Davies, G.J., "The Influence of Composition on Solidification Cracking in Binary Alloy Systems", The British Foundryman, 1981, vol 74, pp 65-73.

180- Campbell, J., Clyne, T.W., "Hot Tearing in Al-Cu Alloys", Cast Metals, 1991, Vol. 3, pp224-226.

181- Eskin, D., Du, Q., Ruvalcaba, D. Katgerman, L., " Experimental Study of Structure Formation in Binary Al-Cu alloys at different cooling rates", Materials Science and Engineering A, 2005, vol. 405, pp. 1-10.

182- Source: http://www.instron.co.uk

183- Mohamed, A., "Effect of Additives on the Microstructure and Mechanical Properties of Aluminum-Silicon Alloys", PhD Thesis, UQAC, Chicoutimi, Canada, 2008.